UNIVERSITÀ DI PARMA

UNIVERSITA' DEGLI STUDI DI PARMA

DOTTORATO DI RICERCA IN

"Scienze Chimiche"

CICLO XXXVI

From the genesis to the application: design of cocrystals based on natural ingredients and monitoring of their synthesis and activation

Coordinatore:
Chiar.ma Prof.ssa Alessia Bacchi

Tutore:
Chiar.ma Prof.ssa Alessia Bacchi

Dottorando: Michele Prencipe

Anni Accademici 2020/2021 – 2022/2023

CONTENTS

General abstract

The aim of this thesis is the stabilization of natural active ingredients, such as *essential oils*, into a novel crystalline environment, with the purpose of improving their physical properties and modulating their release. These molecules of interest are directly produced by plants and exhibit antimicrobial, antifungal, and antioxidant properties. According to the strategy of *cocrystallization*, the choice of molecular partners which effectively interacted with essential oils led to the formation of multi-component crystalline materials (*i.e.* cocrystals), with different physical properties. To further influence the release of the active ingredients, the molecular partners were opportunely designed with light responsive properties, thus producing smart materials that could be activated with an external stimulus. The idea was to arbitrarily trigger the release of essential oils using a low energy irradiation, altering the cocrystal structure by exploiting the absorption on behalf of the *photo-responsive* molecular partners. The final cocrystals, based on both essential oils and photo-responsive molecules, were tested in terms of release response upon different irradiation times. The results showed a mild increase of the release for low irradiation times, whilst an evident loss of the active ingredients after 24 h of irradiation. The employment of sustainable procedures for the synthesis of cocrystals aligned with the use of natural active compounds, such as the essential oils.

Beyond the release of active ingredients, another purpose of this thesis is the investigation of the mechanism of cocrystallization, which suggests information on the main interactions among molecules and their reactivity. The cocrystal formation of two cases of study was investigated using an *in situ monitoring*

approach, considering the presence of liquid intermediate species. These systems were analysed with different techniques aiming at tackling the phenomenon from mechanistic, thermal, and spectroscopic points of view. The liquid intermediates were found to be the eutectic binary mixtures of the reactants, whose formation was a crucial step for cocrystals nucleation.

A full comprehension of the role of the intermediate species required a more in-depth analysis of the molecular arrangement, which was performed through the *pair distribution function* (PDF). PDF analysis returns the probability of finding pairs of atoms at a certain distance and gives information about the local structure. Starting from another example of cocrystallization, proceeding through a liquid intermediate, a similarity between the PDFs of cocrystal and liquid intermediate was pointed out. However, the reliability of the data was compromised by the low resolution and poor power of scattering of organic compounds, suggesting the use of a synchrotron radiation.

CHAPTER 1

Introduction

1.1 Essential oils

The human interest in the treatment of diseases has encouraged the research of natural remedies since ancient civilizations. Early investigations were directed at what nature could offer and the spontaneous response was found in medicinal plants. Although there was not sufficient information about the beneficial properties of plants, primitive classifications of medicinal plants were provided based on experience[1]. The first written evidence is a Sumerian clay slab from Nagpur, dated approximately 5000 years ago, in which are mentioned over 250 types of different plants used for the preparation of natural drugs[2]. In the age of

the Old Kingdom, Egyptians started to record their medicinal knowledge in tomb illustrations and on papyrus, such as the valuable "Ebers Papyrus" which reports a collection of 800 treatments with medical herbs[3]. Many other documents concerning the usage of medicinal plants have been found in China, India, and Ancient Greece, however the academics recognize Dioscorides, a military physician of Nero's army, as the father of pharmacognosy[4,5]. From his experience around the Roman empire, he classified a large number of plants, roots, and seeds according to their outward aspect, locality, making of drug preparation, and therapeutic effect. This compendium entitled "*De materia medica"* represents the first example of modern pharmacopeia and constituted the basic *materia medica* until the Renaissance[6,7]. The curative effects of medicinal plants remained unclear until the development of chemical techniques which allowed the extraction of the main components from vegetal matrices. The physician Ibn Sina, also known as Avicenna, and the chemist Ibn al-Baitar derived in the late Middle Ages the essential fragrance of aromatic herbs through a distillation process opportunely described[8,9]. This example represents the first recorded procedure for the preparation of essential oils (EOs), the liquid mixture of natural compounds that define the pharmaceutical properties of aromatic plants[10].

The term "Essential Oil" was first coined by Paracelsus von Hohenheim in the 16th century to indicate the effective components of at that time drug composition[11].

Essential oils are heterogeneous mixtures of volatile compounds produced by plants as secondary metabolites. The role of the EOs is to protect the plants from predators and microbial pathogens exploiting their antimicrobial, antibacterial, antifungal, and antioxidant properties[12]. They also contribute to the livelihood of the plants by attracting pollinators and being involved in defence mechanisms against abiotic stress (*e.g.* UV exposure)[10]. EOs are synthesized in secretory

glandules and can be stored in all the plants' organs. They appear as coloured and limpid liquids at room temperature, even though some of them are solid or resin with low melting points[13,14]. The composition of EOs is extremely variable and may comprehend up to 60 different compounds, depending on the type of plant and its life cycle. Most of these metabolites can be classified into two main groups with respect to their hydrocarbon skeleton[15] (*Figure 1*):

- terpenes/terpenoids, which are obtained by the combination of one or more isoprene units;

- phenylpropanoids, aromatic compounds which derive from phenylpropane.

Monoterpenes (2 isoprene units, C_{10}) represent 90% of EOs and may exhibit different functionalities (*e.g.* esters, aldehydes, ketones, phenols, alcohols, ethers) which influence their solubility and bioavailability. Despite the presence of polar groups, they result barely soluble in water due to the hydrophobic skeleton, underlying a problem in terms of production since they are usually extracted through steam distillation[16].

The mixture of essential oils consists of two or three components at fairly high concentrations compared to the others present in trace amounts. For instance, *Thymus vulgaris* plants contain thymol (48-60 %), p-cymene (11-20 %), and carvacrol (5-10 %) as major components[17]. Several studies have demonstrated that EOs based on phenols and aldehydes ensure a remarkable antibacterial effect, followed by alcohols, ketones, and esters; while hydrocarbon terpenes are often ineffective[18–21]. Thymol and carvacrol are the phenolic components responsible for the high antimicrobial activity of *Thymus* and *Origanum* species[22–26] and eugenol to those of *Eugenia caryophillus*[27], *Syzygium aromaticum*[12,28] and *Ocimum basilicum*[24]. Although the biological properties of EOs arise mainly from

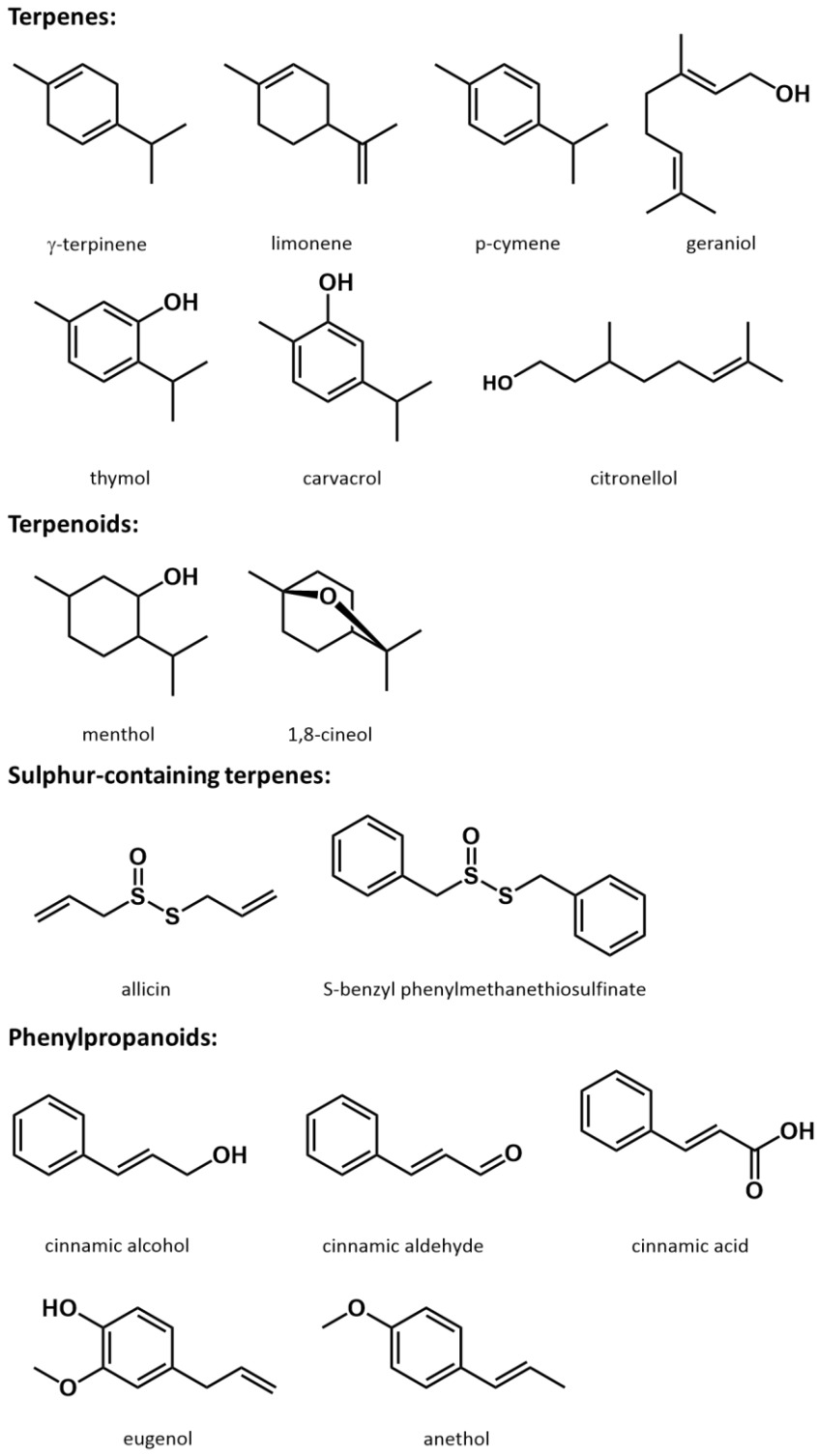

Figure 1. *Classification of the most used components of essential oils.*

the major components, even the minor ones may play a significant role in reinforcing or weakening the biological activity. For instance, the combination of either thymol and carvacrol with eugenol has evidenced a synergistic effect on Escherichia Coli strains, as well as the concomitant use of different EOs mixtures[12]. The lipophilic nature of EOs accounts for their effectiveness against microbial species, especially in the case of fungi which are eukaryotic organisms difficult to ascertain and treat. Thanks to their hydrocarbon skeleton, terpenes and terpenoids might easily penetrate the membrane cells of pathogen agents causing their disruption and death[29,30]. Moreover, EOs have manifested antioxidant properties that prevent or delay the aerobic oxidation of organic compounds. Phenolic terpenes act as *direct* antioxidants and interfere with the chain propagation step of the radical reaction forming peroxyl radicals[31,32]; instead terpenes having cyclohexadiene structure enhance the probability of the chain termination step[33,34], and terpenes with sulphur atoms are *preventive* antioxidants[15].

Over the years, essential oils have been exclusively used for their captivating fragrance in the cosmetic and cleaning industries, or for aromatherapy treatments. In the last few decades, the awareness of their beneficial properties has encouraged their application also in pharmaceutical, agrochemical, and nutraceutical fields as sustainable and environmental alternatives[35,36]. The U.S. Food and Drug Administration (FDA) has included EOs in the list of GRAS (Generally Recognized As Safe) compounds[37] promoting their employment as additives in food products[38,39]. Nevertheless, the usage of EOs is still strongly limited due to their chemical instability, low solubility in water, high volatility, and complications related to their handling since most of them are liquids at room temperature. In particular, EOs are susceptible to degradation processes induced by light, temperature, and oxygen which lead to organoleptic alterations and physical changes. The main reactions of degradation are oxidation, polymerization,

disproportionation, and cyclization. Furthermore, the presence of heavy metals as impurities catalyses oxidation reactions while water contamination determines the occurrence of spoilage events[40]. For these reasons several studies have been proposing alternative methods to deliver the EOs, in order to reduce the interaction with the degradation agents and limit their volatility. These solutions consist of nano-formulations, based on lipidic systems[14,41], or provide the encapsulation of the oil in mesoporous silica nanoparticles[42], cyclodextrins[43], or chitosan[44]. Some examples of application concern the protection of plants from pathogen organisms[45], the increase of the shelf-life of foods[46–48], and the treatment of epilepsy and skin healing[49,50]. In this work of thesis, the drawbacks of the EOs have been approached with the strategy of cocrystallization.

1.2 Cocrystallization

The rate of success in the use of a specific active compound depends on its effectiveness towards the substrate but also on the physical state in which it is administered. That is the reason why, in the pharmaceutical field, only less than 1% of drug leads enter the market[51]. Physical properties such as solubility, permeability, and release are necessary requirements for the formulation of drugs[52–54]. Therefore, in the last decades the research has also shifted to the possibility of changing the physical properties of well-known active compounds. Pharmaceutical industry first moved with this purpose[55], most recently followed by agrochemical[56], nutraceutical[57], food preserving[58], and energetic[59] fields.

Liquid active ingredients are hardly used as pure compounds due to their low stability, and often their application requires a dissolution in a solvent to reduce

their concentration. On the other hand, solid active compounds are more stable and exhibit defined physical properties, which rely on the molecular arrangement; they are classified as crystalline or amorphous materials. Drug formulations are developed towards an amorphous or crystalline product depending on the physical properties to be exploited. Amorphous solids usually provide a higher solubility and permeability but can convert unexpectedly into the more stable crystalline phase[60,61], instead crystalline solids are stable and their physical properties are reproducible and easier to monitor for the industry[51,62]. In addition, the same active molecule may generate different crystal arrangements and thereby different crystalline solids with distinctive physical properties. This phenomenon is renowned as polymorphism[63], but it is still challenging to predict in advance the existence and the number of polymorphic phases[64].

Amorphous or crystalline formulations of single component drugs are frequently not definitive solutions to obtain the desired physical properties. For these reasons, multi component drugs have been finding large applications in virtue of their versatility and easiness in manufacturing. The category of multi component crystals includes solvates, hydrates, salts, and cocrystals[65,66]. Multi component crystals are the result of intermolecular interactions established among two or more different entities in a defined stoichiometric ratio. In particular, solvates are formed by at least one solvent entity, specifically water in case of hydrates, while salts are constituted by ionic species. Cocrystal definition has long been debated[67] since they are constituted by neutral/ionic molecular entities (*i.e.* coformers), none of these acting as a solvent. Only recently it has been introduced the concept of ionic cocrystals[68], whereby one of the coformer is a salt.

For well over half a century, it has been a common place to consider salts and solvates as the only multi component strategies to modify the physical properties of active compounds[69]. Salts and solvates have the advantage of being cost-

effective, easy to prepare, and increase the solubility and bioavailability of active ingredients[54,70]. However, solvates are limited by the number of usable solvents, and salts require pairs of acid-base with appropriate pka values to induce a proton exchange. In the last two decades, the interest in developing of cocrystals has gradually increased in all fields[71–74], especially for the opportunity to use a large number of potential coformers selected from the list of GRAS compounds.

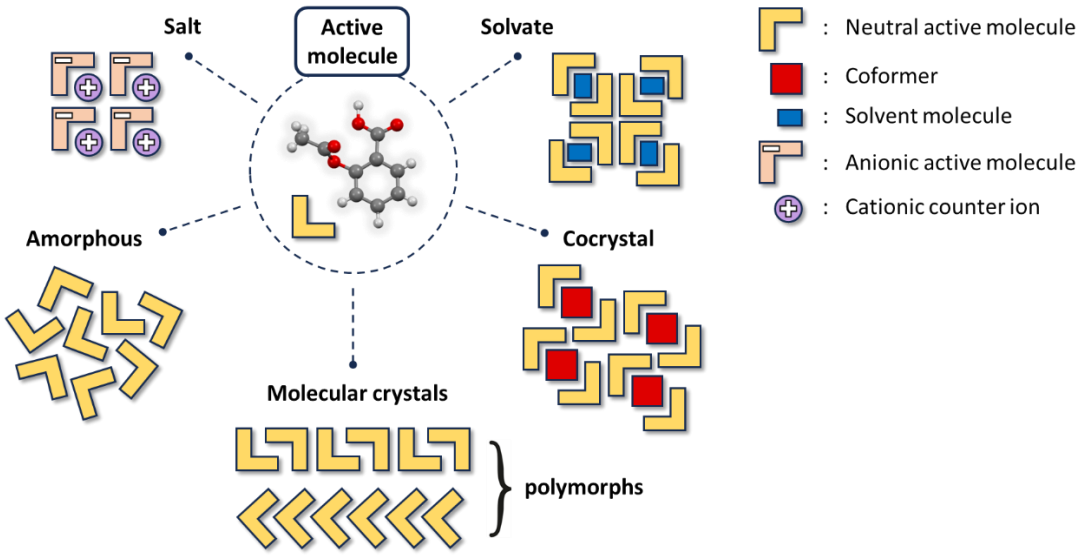

Figure 2. *Solid-state formulations of active ingredients.*

Given an active molecule, the main obstacle in forming cocrystals is the choice of coformers with suitable chemical structures. The design of the supramolecular interactions that are supposed to form within the cocrystal structure is at the basis of crystal engineering[75]. In general, crystal engineering considers crystals as the result of kinetical steps whereby molecules interact using *supramolecular synthons* (*Figure 3*)[76]. Supramolecular synthons are the ensemble of functional groups which generate the intermolecular interactions[77]. At the early stages of crystallization, the strongest synthons are formed and tend to persist until the end of the crystal formation, therefore the final crystal can be regarded as the gathering

of the most robust synthons. According to crystal engineering, the cocrystal formation thus requires the choice of coformers with functional groups capable of establishing robust synthons with the functional groups of the active molecule. The interactions that coordinate the strong synthons are extremely directional, such as hydrogen bond[78,79], σ-hole and π-hole interactions (*e.g.* halogen bond, chalcogen, tetrel, and pnictogen bonds)[80–82], and dipole-dipole interactions. Instead, the weaker van der Waals forces and π···π interactions usually contribute to the stabilization of the crystal packing[83,84]. From a survey on the Cambridge Structural Database (CSD)[85], the most recurrent synthon in cocrystals structures involves the carboxylic functional group and the N-containing heterocycle[86]. Another study confirmed that the carboxylic-pyridine hetero synthons is more favourable than the carboxylic-carboxylic homo synthon[87]. Crystal engineering represents a powerful strategy that facilitates the prediction of supramolecular networks and the design of multi component crystals; however the competition between alternative synthons and the complexity of organic crystals underlie some limitations and failures. Nowadays, it is still not possible to definitely predict the formation of a cocrystal starting from its coformers since cocrystallization is a complex phenomenon. Nevertheless, more and more performing computational methods have been developing that are based on structure or energy calculations. In the last years, the Cambridge Crystallographic Data Center (CCDC)[88] has implemented several tools, available in their software Mercury[89], that adopt structure-based approaches. For example, the tool "Molecular Complementarity"[90] exploits molecular descriptors related to the size and the shape of the molecules, and the magnitude of their dipole moment, to predict the likelihood of cocrystal formation. The tool "Hydrogen Bond Propensity"[91], instead, estimates the possibility of forming a cocrystal through the difference between the strongest heteromeric and homomeric hydrogen bond interactions[92]. The last frontier in structure-based

methods regards the use of Artificial Intelligence (AI): thanks to the rising number of cocrystal structures, machine learning approaches have been spread out by using different training algorithms (*e.g* QSAR/QSPR, multivariate adaptive regression spline, artificial neural network, and so) and extrapolating opportune molecular descriptors to figure out the propensity to cocrystallization[93,94].

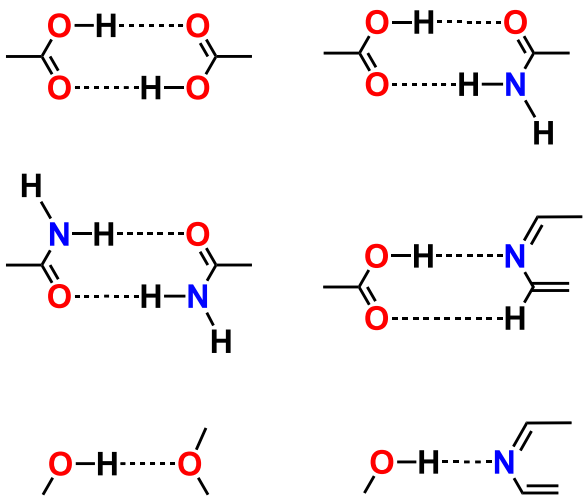

Figure 3. *Representation of the most frequent supramolecular synthons in the CSD database.*

Energy-based methods consist of energy calculations in gas phase, solution, or even in a crystalline environment. The simplest calculation is the determination of the Molecular Electrostatic Potential (MEP) that is used to rank donor and acceptor groups involved in the strongest intermolecular interactions, such as hydrogen and halogen bonds[95,96]. With this approach, it is possible to estimate the energy of homo and hetero interactions and correlate their difference to the chance of cocrystal formation[97]. Multi techniques approaches have also paired MEP calculations with structure-based methods[98–100]. Different from MEP calculations, crystal structure prediction (CSP) methods are more rigorous approaches and calculate the energy landscape for a given crystal structure. In the case of cocrystals,

the presence of more than one molecule in the asymmetric unit complicate the calculations as reason of the higher number of degrees of freedom to be explored in identifying all the low-energy crystal structures. Calculations thus result highly expensive in terms of CPU time and many hypothetical cocrystal structures are predicted. Comparing the free energy of the more stable cocrystal structure with those of coformers is possible to evaluate the probability of existence of that cocrystal[101–104].

Cocrystallization has found widespread success especially in the pharmaceutical field[105], in which most of the active pharmaceutical ingredients (API) exhibit poor solubility in water, and low permeability, dissolution rate, and bioavailability. Beyond these properties, several studies have demonstrated that cocrystals may also modulate other API's properties such as their melting point, hydration, photo and thermal stability, and mechanical properties[51,62,70]. Although the clear evidence of cocrystals physical improvements, the regulatory guidance for pharmaceutical cocrystals have limited their employment for many years. The first example of cocrystal approved by FDA was Entresto[106] and dates back only in 2015. Entresto is a Novartis drug used for the treatment of chronic heart failure and combines sacubitril, a neprilysin inhibitor, with valsartan, an angiotensin receptor inhibitor[62]. Steglatro is another pharmaceutical cocrystal, used for the treatment of diabetes and developed with the collaboration between Pfizer and Merk. This cocrystal represents the first commercial form of ertuglifozin, which is the active ingredient and belongs to the class of SGLT-2 inhibitors[71].

As seen previously, active ingredients are not always in solid-state and many of those manifest chemical and thermal instability. Cocrystals have already offered a valid alternative improving such physical properties, for instance in the case of energetic[59] or volatile compounds[107,108]. In the last years, the problem of

stabilizing liquid or low melting solid active ingredients has been successfully addressed using cocrystallization[109–112]. However, the coformers adopted as molecular partners of the active ingredients are usually selected from the list of safe compounds (*i.e.* GRAS) and most of them do not show relevant properties. This means that the release of the active ingredients is affected only by the new intermolecular network of the cocrystal structure; hence, it cannot be further activated by external triggers. Within this perspective, the choice of photo-responsive molecular partners aims at stimulating the release and changing the availability of the active molecules, according to the need. Moreover, the process of cocrystallization involves the concomitance of many chemical species and often leading to complexities in understanding the outcomes. Approaching the phenomenon from different points of view have allowed a wider comprehension of the molecular reactivity and found out the involving of intermediate species. The deepening of these aspects represents the core of this thesis.

1.3 Cocrystallization techinques

The synthesis of cocrystals requires the creation of new arrangements where different entities coexist within the same crystal lattice. This molecular coexistence can be achieved by many cocrystallization techniques, classified either in terms of the driving force of the process, or in terms of the amount of solvent used[113]. Cocrystallization methods driven by kinetics involve non-equilibrium states and may generate metastable products with higher Gibbs free energies. These methods include grinding, slurry sonification, spray drying, and surpercritical fluid technologies. On the other hand, cocrystallization methods influenced by thermodynamics act in equilibrium conditions consuming a large amount of time.

Some examples of thermodynamic methods are slow solvent evaporation and cocrystallization from melt. Another classification of cocrystallization methods regards the use of solvents[113,114]. Solvent-based methods require large amounts of solvent, often hazardous, which limit their application to the academic field due to the high disposal costs and the low performance of the processes. However, solvent-based methods are also extremely versatile thanks to the possibility of changing solvent and temperature, and thus influencing the morphology and the size of the final crystals. The sustainable answer to the use of bulk solvents has been the development of solvent-free methods of cocrystallization. Solvent-free methods have been largely finding application in industry and comprehend mechanochemical processes, matrix-assisted cocrystallizations, and generic thermal methods which take advantage of melted phases. The drawbacks of these methods are the poor control on crystal properties, such as the degree of crystallinity and the morphology, the possibility to obtain amorphous products, and the consumption of energy during the processes; nevertheless the overall costs of solvent-free methods are significantly lower than the corresponding solvent-based ones. Among solvent-free methods, mechanochemistry has recently stood out for the high versatility and the huge scale-up potential.

1.3.1 Mechanochemistry

The International Union of Applied Chemistry (IUPAC) defined a mechanochemical reaction as a "chemical reaction that is induced by the direct absorption of mechanical energy"[115]. Mechanochemical methods are solid-state techniques that generate mechanical energy through the action of contact forces such as

compression, friction, shearing, and stretching. Although there are no records, mechanochemistry probably took its first steps in the Stone Age when foodstuffs were prepared using mortar and pestle[116]. This starting unintentional approach became full conscious when in the 19th century the potential of grinding to induce chemical transformations was understood[117,118]. In the last decades, mechanochemistry has returned to the fore as a sustainable strategy of synthesis and phase transformations, extending its early domain in inorganic chemistry and metallurgy even to organic, organometallic, supramolecular, and pharmaceutical chemistry[119,120]. Many examples were reported of covalent reactions[121–124], metal catalysed transformations[125–127], synthesis of inclusion[128], supramolecular and multi components compounds[129,130], all performed by means of mechanochemical methods. The rising popularity of mechanochemistry has been built on the continuous research of innovative procedures that erase the concept of massive usage of solvents and seek for safer chemicals[131]. This perspective, along with the principles of atom economy and the reduction of energy costs, has encouraged IUPAC to identify mechanochemistry as one of the 10 world-changing technologies[132].

Mechanochemical reactions are performed either manually or with automated instruments. Grinding by means of mortar and pestle represents the easiest mechanochemical method but it has a limited application when high mechanical energies, accurate reproducibility, or long reaction time are requested. The automated instruments are of different types but can be grouped into two main categories: mills and extruders. Mills are constituted by closed vessels of different materials (*e.g.* stainless steel, zirconia, tungsten carbide) which are subjected to oscillations during the mechanochemical process. The presence of spheres within the vessels increases the mechanical energy provided during the reaction. These mills are commonly named ball mills and usually represent the most used

automated instruments. On the other hand, mills that shake without the use of spheres are considered mixers and lead to soft mechanical impacts. The nature of the oscillation determines a wide range of mills, such as vibrational, planetary, magnetic, and gravity, but also resonant mixers[133]. Beyond the type of mill or mixer, it is worth noting that many other factors strongly influence the outcomes of a mechanochemical reaction: the material of the assembly (*i.e* vessels and spheres), the filling of the vessels, the size and number of the spheres, the oscillation or rotation frequency, the temperature, and the time of grinding or mixing.

Different from mills, extruders are long barrels in which the chemical compounds are inserted and then grounded through the inner rotating screws. The barrel has three different sections dedicated respectively to the introduction of the samples, the compression, and the metering. Extrusion systems are divided into single screw and twin screw extruders, with the latter providing a higher mixing of the components[113].

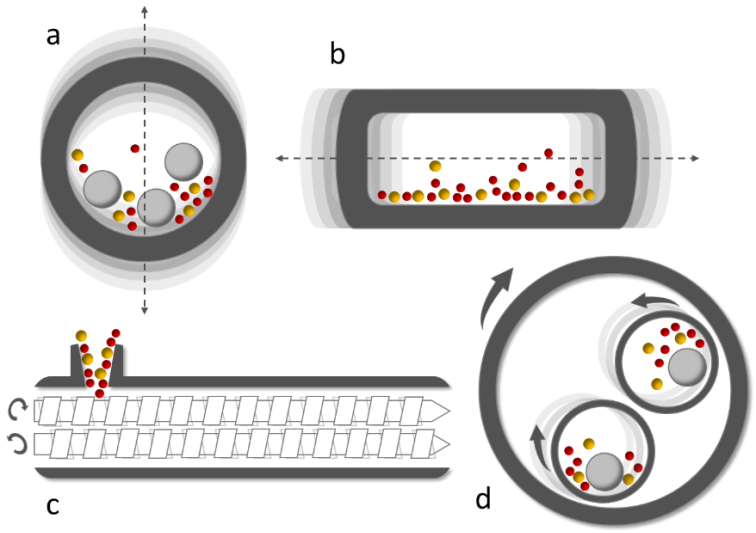

Figure 4. *Representation of mechanochemical methods: a) vibrational ball milling; b) mixing; c) twin screw extrusion; d) planetary ball milling.*

The versatility of mechanochemistry consists in the high number of parameters that can be modulated during the setup of the reaction. Apart from the equipment, the experimental conditions of mechanochemical reactions might also include the presence of additives. The simplest case is the total absence of solvent or other agents, performing the solid-state reactions in "neat" or "dry" conditions. Liquid-assisted (LA) methods, instead, use a small amount of solvent to drastically improve the speed and the yield of the reactions, eventually bringing to different crystalline phases[130,134]. The benefits of liquid-assisted methods are due to the increase in molecular mobility, thanks to the role of solvent which acts as a lubricant. The amount of solvent used in liquid-assisted methods is opportunely evaluated through the η parameter[135], which is defined as follows:

$$\eta = \frac{V_{liquid}}{m_{sample}}$$

where V_{liquid} is the volume of solvent in mL and m_{sample} is the weight of all reactants in mg. Liquid-assisted reactions correspond to values of $0 < \eta < 2$, while $\eta = 0$ represents dry conditions and $\eta > 2$ slurry conditions[136].

In the last years, especially grinding methods have developed new techniques that take advantage of polymers, ions, or vapor as additives, respectively polymer-assisted grinding (POLAG), ion- and liquid-assisted grinding (ILAG), and vapor-assisted grinding (VAG)[137]. The presence of additives has been shown to further stimulate the reactivity of the species and avoid the formation of undesirable products (*e.g.* solvates, hydrates).

Although it is well-known the correlation between contact forces and mechanical energy to induce chemical transformations, the mechanism through which it develops is still a source of debate. The theories of magma-plasma or "hotspots" suppose that the action of mechanical forces may generate short-lived (10^{-9} s)

microscopic areas where the temperature reaches extremely high values (>1000 °C)[138]. However, these models were proposed for inorganic materials and fail for mechanochemical reactions that involve organic or supramolecular materials. Indeed, organic compounds are highly sensitive to the temperature of the reaction, and this should have had a significant effect on the kinetics of the process. These considerations are in accordance with a recent finding[139], where the temperature of Diels-Alder reactions performed through ball milling was evaluated. The results showed that the temperature of hotspots during the reactions was likely to be below 100 °C. Another theory about mechanical reactions explains their high reactivity through the formation of liquid intermediates, such as low melting eutectic mixtures or melted phases generated by energetic impacts. In literature there are many examples of mechanical reactions mediated by liquid intermediates[140], however, also examples of gas phase mediation or pure solid-state reactions are found[141,142]. Hence, there are not enough results to completely understand the mechanism of mechanical impacts for all kind of reactions.

So far, ex-situ analyses have offered the possibility to characterize the products of mechanochemical synthesis either at the end or during the reaction, in the latter case by interrupting the grinding. This approach has some drawbacks since intermediate species with short lifetimes could not be determined or, even if enough stable, may convert into other species after grinding. Moreover, the interruption of the reaction might lead to different final products rather than not stopping. For these reasons, in the last decade there has been a boost towards the development of in-situ monitoring setups[143]. Mechanochemical reactions are suited for in-situ monitoring analysis and a broad range of techniques can be used. For instance, structural investigations can be performed by means of X-ray powder diffraction[144], X-ray absorption spectroscopy[145], Raman spectroscopy[146], and more recently solid-state-NMR spectroscopy[147].

In conclusion, mechanochemistry represents a “green” alternative to solution chemistry and a versatile method to deeply understand the evolution of a reaction through the employment of in-situ investigations.

1.4 Release of active ingredients

Among the properties which more influence the effectiveness of active ingredients, the release assumes a key role since it is directly correlated with bioavailability. “Release” is a general term that acquires a specific meaning depending on the kind of drug and its activation mode. For instance, pesticides are spread over the plants by way of solutions or solids, while pharmaceutical drugs can be either taken orally in the form of tablets/pills or directly injected as solutions. In particular, pharmaceutical drugs usually require to be assimilated through the blood in order to reach the substrate of interest. In those cases, the release coincides with the dissolution of the active ingredient. Therefore, the kinetics of the release of active ingredients is related to the conditions of the environment where they have to operate and to the physical properties of the formulation drug. As mentioned, cocrystallization represents a valid strategy to alter the physical properties of active compounds, and many examples of cocrystals have evidenced an improvement in terms of release[62]. Cocrystals of meloxicam, a non-steroidal anti-inflammatory drug, showed a faster dissolution rate and higher oral absorption[148], while danazol-vanillin cocrystal[149] revealed a 10-fold higher bioavailability compared to pure danazol. Moving to the agrochemical field, sustainable pesticides based on essential oils cocrystals showed a controlled release rather than the pure active molecules[150], instead urea cocrystals with different hydroxybenzoic acids exhibited an increasing release over the days[151]. A large number of other studies

concerning cocrystals release have been published, however the a-priori changing of physical properties is not the only way to affect the release of a drug. Stimuli-responsive materials have been proposed as smart materials that can be activated when subjected to an opportune stimulus. The compelling advantage of these systems is the high site selectivity, consequently their main application is the delivery of active compounds. In medicine, polymeric carrier drugs were developed for cancer treatments exploiting pH stimuli[152], while liposome carriers were used for different employments and could be activated by pH, enzymes, redox reactions, and light[153]. Moreover, several examples of carrier pesticides have been proposed with pH, thermal, redox, enzyme, and photo-responsive properties[154–156].

Cocrystals are not so different from the concept of carriers, since the presence of coformers drives the active ingredient towards its substrate, thanks to the new physical properties of the crystal structure. Therefore stimuli-responsive cocrystals are usually not developed for the delivery of drugs but rather to activate some properties, such as mechanical[157–161], optical[162], fluorescent[163], and luminescent[164]. A few examples of cocrystals based on volatile compounds also showed photo-carving, chromic, and mechanical responses[165,166]. However, there are no studies so far on the activation of cocrystals materials with the purpose of altering the release profile.

1.5 Aim of the thesis

The organization of United Nations has encouraged the research of sustainable solutions aiming at safeguarding the environment from rising pollution and climate change. Over the years, the chemical industry has significantly contributed to the

technological development but always putting in the foreground the economic returns to the sustainability of the processes. The principles of “Green Chemistry” have paved the way to the finding of less impactive strategies, promoting the selection of safer compounds along with the reduction of undesirable by-products. Within this perspective, the core of this thesis has focused on the formulation and synthesis of activating materials containing natural active ingredients, such as essential oils. These molecules of interest represent a promising solution to the alarming issues of soil contamination and food waste; however, their application has been limited because of their adverse physical properties. The strategy used in this thesis to alter their physical properties will be the cocrystallization, which consists of introducing the active ingredients into a novel crystalline environment by establishing interactions with opportune molecular partners. The synthesis of cocrystals does not provide for the formation of by-products since all the reactants are contained in the final crystalline material, respecting the principles of atom economy. In addition, the synthetic procedures of cocrystallization were performed by means of mechanochemical methods, that exploit the mechanical forces to induce chemical transformations without the use of large amounts of solvents.

The release of essential oils from the cocrystalline matrix depends on the strength of intermolecular interactions between the active ingredients and the molecular partners. In literature, a few examples of cocrystals have been proposed capable of stimulating the loss of volatile components, none of these using active ingredients whose release is activated through low energy radiation. In this thesis, the design and synthesis of photo-responsive molecular partners have the purpose of triggering the release of a larger amount of active ingredient from the cocrystalline matrix, thus modulating the release properties through an external stimulus. In this way, cocrystals can be managed as smart materials at the same time improving the chemical and thermal stability of the essential oils. The activating properties of the

photo-responsive molecular partners and cocrystals will be tested using UV-vis spectroscopy and X-ray powder diffraction, while the thermal stability will be evaluated by differential scanning calorimetry. A quantitative measurement of the effective release of essential oils will be shown on the most promising cocrystals.

A full comprehension of cocrystallization processes would be useful in understanding the reactivity between the molecular partners. However, cocrystallizations often involve the presence of intermediate species which influence the mechanism of cocrystals formation. In this thesis, the process of cocrystallization will be investigated with an in situ monitoring approach, evaluating the role of intermediate species. The use of several techniques will propose a global view of the phenomenon showing a successful strategy to address a complex problem. Indeed, the mechanism of cocrystallizations will provide the formation of metastable liquid intermediates which rapidly convert into cocrystals. The mechanisms of cocrystallization will be clarified by the analysis of the mechanochemical reactions through synchrotron X-ray powder diffraction. Instead, the nature of liquid intermediates will be determined by constructing the binary phase diagram of the reactants.

The composition of liquid intermediates is accessible from thermodynamics, nevertheless the information concerning their molecular aggregation is not a straightforward task since it depends on the strength of interactions that can be established in the liquid phase. The molecular organization of metastable intermediates might be indicative of the arrangement within the cocrystal structure, such as the starting point of cocrystal nucleation. In this thesis, a deepening into the molecular organization will be proposed using the pair distribution function analysis (PDF), trying to compare the similarities between a metastable liquid intermediate and its corresponding cocrystal. The selling point of

this approach consists in the potential determination of the local structure, and the easiness of discriminating between amorphous and crystalline compounds.

Bibliography

[1] H. M. A. Hassan, H. Mutlak, A. Hassan, *Chimia (Aarau).* **2015**, *69*, 622.

[2] K. K., *History of Medicine*, Facts On File, New York, **2009**.

[3] Glesinger L., *Medicine through Centuries*, Zora, Zagreb, **1954**.

[4] H. E. Sigerist, *A History of Medicine*, Oxford University Press, New York, **1955**.

[5] A. A. Elkordy, R. R. Haj-Ahmad, A. S. Awaad, R. M. Zaki, *J. Drug Deliv. Sci. Technol.* **2021**, *63*, 102459.

[6] B. B. Petrovska, *Pharmacogn. Rev.* **2012**, *6*, 1–5.

[7] A. Rooney, *The History of Medicine*, The Rosen Publishing Group, **2012**.

[8] Jordan Rubin, *Essential Oils: Ancient Medicine for a Modern World*, Destiny Image Publishers, **2017**.

[9] O. Essa, Ahmed; Ali, *Studies in Islamic Civilization: The Muslim Contribution to the Renaissance*, **2010**.

[10] H. Schäfer, M. Wink, *Biotechnol. J.* **2009**, *4*, 1684.

[11] E. Guenther, *The EssentialOils*, DavidvanNostrand Co.Inc., New York, NY, USA, **1948**.

[12] I. H. N. Bassolé, H. R. Juliani, *Mol. 2012, Vol. 17, Pages 3989-4006* **2012**, *17*, 3989–4006.

[13] F. Bakkali, S. Averbeck, D. Averbeck, M. Idaomar, *Food Chem. Toxicol.* **2008**, *46*, 446–475.

[14] A. El Asbahani et al., *Int. J. Pharm.* **2015**, *483*, 220–243.

[15] R. Amorati, M. C. Foti, L. Valgimigli, *J. Agric. Food Chem.* **2013**, *61*, 10835–10847.

[16] P. Masango, *J. Clean. Prod.* **2005**, *13*, 833–839.

[17] L. Galovičová et al., *Plants* **2021**, *10*, 1959.

[18] V. K. Bajpai, K. H. Baek, S. C. Kang, *Food Res. Int.* **2012**, *45*, 722–734.

[19] K. A. Hammer, C. F. Carson, T. V. Riley, *J. Appl. Microbiol.* **1999**, *86*, 985–990.

[20] H. J. D. Dorman, S. G. Deans, *J. Appl. Microbiol.* **2000**, *88*, 308–316.

[21] A. Ben Arfa, S. Combes, L. Preziosi-Belloy, N. Gontard, P. Chalier, *Lett. Appl. Microbiol.* **2006**, *43*, 149–154.

[22] I. Manou, L. Bouillard, M. J. Devleeschouwer, A. O. Barel, *J. Appl. Microbiol.* **1998**, *84*, 368–376.

[23] S. Cosentino et al., *Lett. Appl. Microbiol.* **1999**, *29*, 130–135.

[24] I. H. N. Bassolé et al., *Mol. 2010, Vol. 15, Pages 7825-7839* **2010**, *15*, 7825–7839.

[25] M. D. Soković et al., *Mol. 2009, Vol. 14, Pages 238-249* **2009**, *14*, 238–249.

[26] M. Hazzit, A. Baaliouamer, A. R. Veríssimo, M. L. Faleiro, M. G. Miguel, *Food Chem.* **2009**, *116*, 714–721.

[27] A. Ait-Ouazzou et al., *Innov. Food Sci. Emerg. Technol.* **2011**, *12*, 320–329.

[28] Y. J. Fu et al., *Phyther. Res.* **2007**, *21*, 989–994.

[29] F. Nazzaro, F. Fratianni, R. Coppola, V. De Feo, *Pharm. 2017, Vol. 10, Page 86* **2017**, *10*, 86.

[30] F. Diánez et al., *Lett. Appl. Microbiol.* **2018**, *67*, 400–410.

[31] G. W. Burton et al., *J. Am. Chem. Soc.* **1985**, *107*, 7053–7065.

[32] M. C. Foti, *J. Pharm. Pharmacol.* **2010**, *59*, 1673–1685.

[33] M. C. Foti, K. U. Ingold, *J. Agric. Food Chem.* **2003**, *51*, 2758–2765.

[34] M. C. Foti, R. Amorati, *J. Pharm. Pharmacol.* **2010**, *61*, 1435–1448.

[35] C. M. Franz, *Flavour Fragr. J.* **2010**, *25*, 112–113.

[36] R. Pavela, G. Benelli, *Trends Plant Sci.* **2016**, *21*, 1000–1007.

[37] R. L. Smith et al., *Food Chem. Toxicol.* **2005**, *43*, 345–363.

[38] S. Burt, *Int. J. Food Microbiol.* **2004**, *94*, 223–253.

[39] C. Boutekedjiret, A. Hellal, A. S. Fabiano-Tixier, M. Abert-Vian, F. Chemat, *Green Food Process. Tech. Preserv. Transform. Extr.* **2019**, 369–390.

[40] C. Turek, F. C. Stintzing, *Compr. Rev. Food Sci. Food Saf.* **2013**, *12*, 40–53.

[41] I. Corrado, R. Di Girolamo, C. Regalado-González, C. Pezzella, *Polymers (Basel).* **2022**, *14*, 166.

[42] Q. Hao et al., *Chinese Chem. Lett.* **2022**, *33*, 320–323.

[43] G. Wadhwa, S. Kumar, L. Chhabra, S. Mahant, R. Rao, *J. Incl. Phenom. Macrocycl. Chem.* **2017**, *89*, 39–58.

[44] A. Negi, K. K. Kesari, *Micromachines 2022, Vol. 13, Page 1265* **2022**, *13*, 1265.

[45] M. B. Isman, S. Miresmailli, *ACS Symp. Ser.* **2011**, *1090*, 67–77.

[46] K. S. Landry, S. Micheli, D. J. McClements, L. McLandsborough, *Food Microbiol.* **2015**, *51*, 10–17.

[47] Z. Wu et al., *Food Chem.* **2019**, *295*, 16–25.

[48] M. Guidotti-Takeuchi et al., *Microorg. 2022, Vol. 10, Page 1504* **2022**, *10*, 1504.

[49] H. J. Moon, L. P. Xiang, M. K. Jong, W. K. Sung, H. P. Jeong, *Phyther. Res.* **2008**, *22*, 544–549.

[50] G. E. Guilherme et al., *Mater. Today Commun.* **2021**, *27*, 102169.

[51] N. Qiao et al., *Int. J. Pharm.* **2011**, *419*, 1–11.

[52] D. J. Good, R. H. Naír, *Cryst. Growth Des.* **2009**, *9*, 2252–2264.

[53] R. Thakuria et al., *Int. J. Pharm.* **2013**, *453*, 101–125.

[54] D. P. Elder, R. Holm, H. L. De Diego, *Int. J. Pharm.* **2013**, *453*, 88–100.

[55] S. M. Berge, L. D. Bighley, D. C. Monkhouse, *J. Pharm. Sci.* **1977**, *66*, 1–19.

[56] E. Nauha, M. Nissinen, *J. Mol. Struct.* **2011**, *1006*, 566–569.

[57] S. J. Bethune, N. Schultheiss, J. O. Henck, *Cryst. Growth Des.* **2011**, *11*, 2817–2823.

[58] F. Bianchi et al., *Food Chem.* **2021**, *347*, 129051.

[59] X. Zhao, W. Zhu, *CrystEngComm* **2022**, *24*, 6119–6136.

[60] B. C. Hancock, G. Zografi, *J. Pharm. Sci.* **1997**, *86*, 1–12.

[61] L. Yu, *Adv. Drug Deliv. Rev.* **2001**, *48*, 27–42.

[62] G. Bolla, A. Nangia, *Chem. Commun.* **2016**, *52*, 8342–8360.

[63] J. Haleblian, W. McCrone, *J. Pharm. Sci.* **1969**, *58*, 911–929.

[64] J. Bernstein, *Polymorphism in Molecular Crystals*, Oxford University Press, New York, **2002**.

[65] S. Aitipamula, et all., *Cryst. Growth Des.* **2012**, *12*, 2147–2152.

[66] E. Grothe, H. Meekes, E. Vlieg, J. H. Ter Horst, R. De Gelder, *Cryst. Growth Des.* **2016**, *16*, 3237–3243.

[67] L. J. Barbour, D. Das, T. Jacobs, G. O. Lloyd, V. J. Smith, *Supramol. Chem.* **2012**, DOI 10.1002/9780470661345.SMC108.

[68] D. Braga et al., *Chem. Commun.* **2010**, *46*, 7715–7717.

[69] J. W. Steed, *Trends Pharmacol. Sci.* **2013**, *34*, 185–193.

[70] A. M. Healy, Z. A. Worku, D. Kumar, A. M. Madi, *Adv. Drug Deliv. Rev.* **2017**, *117*, 25–

46.

[71] N. K. Duggirala, M. L. Perry, Ö. Almarsson, M. J. Zaworotko, *Chem. Commun.* **2015**, *52*, 640–655.

[72] J. Zhang, J. M. Shreeve, *CrystEngComm* **2016**, *18*, 6124–6133.

[73] D. J. Berry, J. W. Steed, *Adv. Drug Deliv. Rev.* **2017**, *117*, 3–24.

[74] P. P. Mazzeo et al., *ACS Sustain. Chem. Eng.* **2019**, *7*, 17929–17940.

[75] G. R. Desiraju, *Angew. Chemie Int. Ed. English* **1995**, *34*, 2311–2327.

[76] J. D. Dunitz, A. Gavezzotti, *Cryst. Growth Des.* **2012**, *12*, 5873–5877.

[77] G. R. Desiraju, *J. Am. Chem. Soc.* **2013**, *135*, 9952–9967.

[78] M. C. Etter, J. C. MacDonald, J. Bernstein, *urn:issn:0108-7681* **1990**, *46*, 256–262.

[79] B. K. Saha, A. Nangia, M. Jaskólski, *CrystEngComm* **2005**, *7*, 355–358.

[80] P. Politzer, J. S. Murray, T. Clark, G. Resnati, *Phys. Chem. Chem. Phys.* **2017**, *19*, 32166–32178.

[81] P. Politzer, J. S. Murray, *Cryst. 2019, Vol. 9, Page 165* **2019**, *9*, 165.

[82] A. Daolio, P. Scilabra, G. Terraneo, G. Resnati, *Coord. Chem. Rev.* **2020**, *413*, 213265.

[83] C. A. Hunter, J. K. M. Sanders, *J. Am. Chem. Soc.* **1990**, *112*, 5525–5534.

[84] P. P. Mazzeo, S. Canossa, C. Carraro, P. Pelagatti, A. Bacchi, *CrystEngComm* **2020**, *22*, 7341–7349.

[85] F. H. Allen, IUCr, *urn:issn:0108-7681* **2002**, *58*, 380–388.

[86] C. B. Aakeröy, D. J. Salmon, *CrystEngComm* **2005**, *7*, 439–448.

[87] T. Steiner, IUCr, *urn:issn:0108-7681* **2001**, *57*, 103–106.

[88] C. R. Groom, I. J. Bruno, M. P. Lightfoot, S. C. Ward, *urn:issn:2052-5206* **2016**, *72*, 171–179.

[89] C. F. Macrae et al., *urn:issn:0021-8898* **2008**, *41*, 466–470.

[90] L. Fábián, *Cryst. Growth Des.* **2009**, *9*, 1436–1443.

[91] P. T. A. Galek, F. H. Allen, L. Fábián, N. Feeder, *CrystEngComm* **2009**, *11*, 2634–2639.

[92] N. Sarkar, A. S. Sinha, C. B. Aakeroÿ, *CrystEngComm* **2019**, *21*, 6048–6055.

[93] T. Heng et al., *ACS Omega* **2021**, *6*, 15543–15550.

[94] M. E. Mswahili et al., *Appl. Sci. 2021, Vol. 11, Page 1323* **2021**, *11*, 1323.

[95] C. A. Hunter, *Chem. Sci.* **2013**, *4*, 1687–1700.

[96] M. C. Storer, C. A. Hunter, *Chem. Soc. Rev.* **2022**, *51*, 10064–10082.

[97] T. Grecu et al., *Cryst. Growth Des.* **2014**, *14*, 1749–1755.

[98] B. Sandhu et al., *Cryst. Growth Des.* **2018**, *18*, 466–478.

[99] N. Sarkar, N. C. Gonnella, M. Krawiec, D. Xin, C. B. Aakeröy, *Cryst. Growth Des.* **2020**, *20*, 7320–7327.

[100] S. Ahmadi et al., *Cryst. Growth Des.* **2021**, *21*, 5862–5872.

[101] P. G. Karamertzanis et al., *J. Chem. Theory Comput.* **2009**, *5*, 1432–1448.

[102] H. C. S. Chan, J. Kendrick, M. A. Neumann, F. J. J. Leusen, *CrystEngComm* **2013**, *15*, 3799–3807.

[103] A. M. Reilly, et all., *Acta Crystallogr. Sect. B Struct. Sci. Cryst. Eng. Mater.* **2016**, *72*, 439–459.

[104] I. J. Sugden, D. E. Braun, D. H. Bowskill, C. S. Adjiman, C. C. Pantelides, *Cryst. Growth Des.* **2022**, *22*, 4513–4527.

[105] G. Bolla, B. Sarma, A. K. Nangia, *Chem. Rev.* **2022**, *122*, 11514–11603.

[106] "Novartis Entresto® granted expanded indication in chronic heart failure by FDA," https://www.novartis.com/news/media-releases/novartis-entresto-granted-expanded-indication-chronic-heart-failure-fda.

[107] P. P. Mazzeo, D. Balestri, A. Bacchi, P. Pelagatti, *CrystEngComm* **2021**, *23*, 7262–7269.

[108] F. Montisci et al., *ACS Sustain. Chem. Eng.* **2022**, DOI 10.1021/ACSSUSCHEMENG.2C01257.

[109] A. Bacchi et al., *Cryst. Growth Des.* **2016**, *16*, 6547–6555.

[110] D. Capucci et al., *Cryst. Growth Des.* **2017**, *17*, 4958–4964.

[111] A. Bacchi, P. P. Mazzeo, *https://doi.org/10.1080/0889311X.2021.1978079* **2021**, *27*, 102–123.

[112] C. Caro Garrido, K. Robeyns, D. P. Debecker, P. Luis, T. Leyssens, *Crystals* **2023**, *13*, 808.

[113] M. Rodrigues, B. Baptista, J. A. Lopes, M. C. Sarraguça, *Int. J. Pharm.* **2018**, *547*, 404–420.

[114] N. Pawar, A. Saha, N. Nandan, J. V. Parambil, *Cryst. 2021, Vol. 11, Page 303* **2021**,

11, 303.

[115] D. McNaught, A., A. Wilkinson, *IUPAC. Compendium of Chemical Terminology*, Blackwell Scientific Publications, Oxford, **1997**.

[116] A. J. Lynch, C. A. Rowland, *The History of Grinding*, Metallurgy And Exploration, Inc., Littleton, CO, **2005**.

[117] A. R. Ling, J. L. Baker, *J. Chem. Soc. Trans.* **1893**, *63*, 1314–1327.

[118] L. Takacs, *Chem. Soc. Rev.* **2013**, *42*, 7649–7659.

[119] D. Tan, T. Friščić, *European J. Org. Chem.* **2018**, *2018*, 18–33.

[120] S. L. James et al., *Chem. Soc. Rev.* **2011**, *41*, 413–447.

[121] J. M. Harrowfield, R. J. Hart, C. R. Whitaker, *Aust. J. Chem.* **2001**, *54*, 423–425.

[122] Z. Zhang, Y. W. Dong, G. W. Wang, K. Komatsu, *https://doi.org/10.1246/cl.2004.168* **2004**, *33*, 168–169.

[123] W. C. Shearouse, J. MacK, *Green Chem.* **2012**, *14*, 2771–2775.

[124] C. Falenczyk, B. Pölloth, P. Hilgers, B. König, *Synth. Commun.* **2015**, *45*, 348–354.

[125] D. Braga, D. D'Addario, M. Polito, F. Grepioni, *Organometallics* **2004**, *23*, 2810–2812.

[126] R. Thorwirth, A. Stolle, B. Ondruschka, *Green Chem.* **2010**, *12*, 985–991.

[127] A. P. Amrute, J. De Bellis, M. Felderhoff, F. Schüth, *Chem. – A Eur. J.* **2021**, *27*, 6819–6847.

[128] T. Friščič, A. V. Trask, W. D. S. Motherwell, W. Jones, *Cryst. Growth Des.* **2008**, *8*, 1605–1609.

[129] M. Klimakow, P. Klobes, A. F. Thünemann, K. Rademann, F. Emmerling, *Chem. Mater.* **2010**, *22*, 5216–5221.

[130] D. Braga, L. Maini, F. Grepioni, *Chem. Soc. Rev.* **2013**, *42*, 7638–7648.

[131] K. J. Ardila-Fierro, J. G. Hernández, *ChemSusChem* **2021**, *14*, 2145–2162.

[132] F. Gomollón-Bel, *Chem. Int.* **2019**, *41*, 12–17.

[133] D. Tan, T. Friščić, *European J. Org. Chem.* **2018**, *2018*, 18–33.

[134] P. Ying, J. Yu, W. Su, *Adv. Synth. Catal.* **2021**, *363*, 1246–1271.

[135] T. Friščić, S. L. Childs, S. A. A. Rizvi, W. Jones, *CrystEngComm* **2009**, *11*, 418–426.

[136] T. Friščić, C. Mottillo, H. M. Titi, *Angew. Chemie Int. Ed.* **2020**, *59*, 1018–1029.

[137] T. Friščić, C. Mottillo, H. M. Titi, *Angew. Chemie Int. Ed.* **2020**, *59*, 1018–1029.

[138] F. K. Urakaev, V. V. Boldyrev, *Powder Technol.* **2000**, *107*, 93–107.

[139] K. S. McKissic, J. T. Caruso, R. G. Blair, J. Mack, *Green Chem.* **2014**, *16*, 1628–1632.

[140] K. Chadwick, R. Davey, W. Cross, *CrystEngComm* **2007**, *9*, 732–734.

[141] R. Kuroda, K. Higashiguchi, S. Hasebe, Y. Imai, *CrystEngComm* **2004**, *6*, 464–468.

[142] C. Bolm, J. G. Hernández, *Angew. Chemie Int. Ed.* **2019**, *58*, 3285–3299.

[143] A. A. L. Michalchuk, F. Emmerling, *Angew. Chemie Int. Ed.* **2022**, *61*, e202117270.

[144] I. Halasz et al., *Angew. Chemie* **2013**, *125*, 11752–11755.

[145] P. F. M. de Oliveira et al., *Chem. Commun.* **2020**, *56*, 10329–10332.

[146] L. Batzdorf, F. Fischer, M. Wilke, K. J. Wenzel, F. Emmerling, *Angew. Chemie - Int. Ed.* **2015**, *54*, 1799–1802.

[147] J. G. Schiffmann, F. Emmerling, I. C. B. Martins, L. Van Wüllen, *Solid State Nucl. Magn. Reson.* **2020**, *109*, 101687.

[148] D. R. Weyna et al., *Mol. Pharm.* **2012**, *9*, 2094–2102.

[149] S. L. Childs, P. Kandi, S. R. Lingireddy, *Mol. Pharm.* **2013**, *10*, 3112–3127.

[150] F. Montisci et al., *ACS Sustain. Chem. Eng.* **2022**, *10*, 8388–8399.

[151] T. Rajbongshi et al., *RSC Sustain.* **2023**, *1*, 1416–1422.

[152] H. Lou et al., *ACS Appl. Polym. Mater.* **2021**, DOI 10.1021/ACSAPM.1C01502.

[153] G. Liu, J. F. Lovell, L. Zhang, Y. Zhang, *Int. J. Mol. Sci. 2020, Vol. 21, Page 6380* **2020**, *21*, 6380.

[154] M. C. Camara et al., *J. Nanobiotechnology* **2019**, *17*, 1–19.

[155] Y. Liang et al., *Colloids Surfaces B Biointerfaces* **2022**, *219*, 112796.

[156] J. Zhou et al., *Chem. Eng. J.* **2023**, *455*, 140167.

[157] O. S. Bushuyev et al., *Chem. Commun.* **2016**, *52*, 2103–2106.

[158] P. Gupta, D. P. Karothu, E. Ahmed, P. Naumov, N. K. Nath, *Angew. Chemie Int. Ed.* **2018**, *57*, 8498–8502.

[159] S. Li, D. Yan, *ACS Appl. Mater. Interfaces* **2018**, *10*, 22703–22710.

[160] S. Saha, M. K. Mishra, C. M. Reddy, G. R. Desiraju, *Acc. Chem. Res.* **2018**, *51*, 2957–2967.

[161] S. Li, B. Lu, X. Fang, D. Yan, *Angew. Chemie Int. Ed.* **2020**, *59*, 22623–22630.

[162] J. C. Christopherson, F. Topić, C. J. Barrett, T. Friščić, *Cryst. Growth Des.* **2018**, *18*, 1245–1259.

[163] S. Li, D. Yan, *Sci. China Chem.* **2018**, *61*, 215–221.

[164] Y. Zhang et al., *Sci. China Mater.* **2022**, *65*, 1320–1328.

[165] T. H. Borchers et al., *Nat. Chem. 2022 145* **2022**, *14*, 574–581.

[166] T. H. Borchers et al., *J. Am. Chem. Soc.* **2023**, *145*, 51.

CHAPTER 2

Materials and methods

All the reagents and solvents were purchased from Sigma Aldrich Chemical Co. and used as such in the synthetic procedures and crystallization experiments.

2.1 Thermal analysis

Differential scanning calorimetry (DSC) analyses were performed by means of a PerkinElmer Diamond equipped with a model ULSP 90 ultracooler. Samples were

prepared in closed Al-pans of 10 or 50 µL, depending on the easiness of the handling. General measurements were performed using the following mode: heating – cooling – heating, with a temperature gradient of 5 °C/min. In the case of samples that undergo decomposition, a single heating was carried out. The temperature range was variable according to the different reagents used. The measurements were performed at atmospheric pressure under a constant flow of nitrogen (20 mL/min). The enthalpy of endothermic or exothermic events is determined by the integration of the area under the DSC peak, which is reported in J/g.

2.2 Single Crystal X-ray Diffraction

Crystal structures were obtained by collecting the diffracted intensities with a CMOS Photon II 2D detector on a Bruker D8 Venture diffractometer, equipped with a kappa goniometer and an Oxford Cryostream. Data collections were performed either by a microfocused Cu Kα radiation (λ = 1.54178 Å) or microfocused Mo Kα radiation (λ = 0.71073 Å). All the measurements were carried out under nitrogen flux at 200 K, except for **2b** (150 K) and **6b** (194 K). Lorentz polarization and absorption correction were applied, while data reduction was performed using APEX v3 software.

All the structures were solved by direct methods using SHELXT and refined by full-matrix least-squares on all F2 using SHELXL as implemented in Olex2, using anisotropic thermal displacement parameters for all non-hydrogen atoms. Hydrogens atoms were added as a model. Crystal structure of **3**-CAR **b** cocrystal was refined by splitting the isopropyl group of CAR(1) molecule into two parts (*Figure*

56), both with 50% of occupancy. Crystal data and structure refinement parameters are reported in Appendix A4, B3, C2.

2.3 Powder X-ray Diffraction

Powder X-ray Diffraction (PXRD) analyses were performed to verify the cocrystals formation and check the purity of the samples. PXRD data were collected in Bragg-Brentano geometry with Cu Kα radiation on a Rigaku SmartLab XE diffractometer equipped with a solid-state Hypix3000 2D detector. The samples were placed on glass supports and exposed to radiation (1.5° ≤ 2θ ≤ 40°) with a scan of 20°/min. A length-limiting slit of 15 mm was used to exploit the maximum loading of the sample holder; 5° Soller slits allowed to improve the peak profile and limit the overlapping of reflections.

2.3.1 Variable Temperature Powder X-ray Diffraction

In situ variable temperature (VT) measurements were carried out on a Rigaku SmartLab XE diffractometer equipped with an Anton-Paar TTK600 nonambient chamber with a flat copper sample holder. Data were collected in Bragg-Brentano geometry with the radiation source fixed at ω = 4° and the Hypix3000 2D solid-state detector at 2θ = 13°. A thermal profile comparable with the calorimetric analyses was applied. Data collection was performed while the temperature was ramped out, with a step of ∼1 °C for each pattern. A solid-state detector was used in 2D mode with an acquisition time of 10 s. Powder patterns were extrapolated

integrating the resulting images between 163°< β >197° along β direction to obtain a 2θ range of 5-19.

2.4 Time-Resolved In Situ Powder X-ray Diffraction

Time-Resolved In Situ (TRIS) PXRD monitoring was performed at the μSpot beamline of BESSY-II synchrotron (Helmholtz Centre Berlin for Materials and Energy) using a low energy incident beam (0.729 Å, 17 keV) of ø 150 μm. Data collection took place in transmission geometry using a double crystal monochromator (Si 111). During the experiment, the samples were shaken within a Perspex poly (methyl methacrylate) (PMMA) jar with two stainless steel balls by using a Fritsch Pulverisette 23 vibration mill. Shaking occurred vertically with a frequency of 50 Hz. The diffracted beams were collected through an EIGER X 9M 2D detector with an acquisition time of 500 ms per frame. Sequential multi-phase Rietveld refinement was performed with TOPAS v.6[167] software to extrapolate the relative amount of the chemical species involved in the mechanochemical reaction.

2.5 X-ray Total Scattering

Total scattering measurements were carried out with a STOE STADI P diffractometer in transmission geometry with a curved Ge (111) monochromator yielding pure Ag Kα1 radiation (λ = 0.5594 Å). The beam was focused on a Dectris MYTHEN2 4K detector at 260 mm of distance and with the sample in a halfway position. The detector was used in "moving" mode reaching a range of 0° < 2θ < 130°. The

samples were ground and filled in quartz capillaries with a diameter of 5 mm. Air scattering was limited by means of a collimator ending with a slit that was close to the capillary. The total measurement time was 6 h for the standard LaB_6, 24 h for the solid organic compounds, and 40 h for the metastable liquid eutectic composition.

Total scattering data were processed using the tool GetX3 included in xPDFsuite software[168], and PDF analysis was performed with TOPAS v.6 software.

2.6 UV-vis spectroscopy

UV-vis absorption spectra were collected using a PerkinElmer UV/vis/NIR Lambda 750 spectrometer, equipped with a D2 lamp for the UV region and a slum halogen lamp for the vis-NIR region. Measurements were performed in double beam mode with a wavelength range from 270 to 600 nm and a spectral resolution of 1 nm. Samples for solution measurements were prepared in $CHCl_3$ at 10^{-5} M and analysed in quartz cuvettes with optical beam of 1 cm. Solid-state measurements were instead carried out on a quartz plate, vertically inserted in a self-made support, and orthogonal to the incident beam. Solid-state samples were prepared by grinding the bulk compound and spreading the resulting fine powder on the quartz plate, obtaining a thin film.

2.7 Raman spectroscopy

The Raman spectra were measured with a Horiba LabRAM HR Evolution spectrometer equipped with 600 gr/mm grating in order to collect a wider spectral region in a single shot. The excitation light comes from a 633 nm He-Ne laser and the scattered radiation was filtered by an ultra low-frequency Bragg filter to reject the elastic scattering.

2.8 HotStage Microscopy

Cocrystallizations were monitored by placing a few crystals (µm order of magnitude) of the two coformers on a glass slide and bringing them into contact with a spatula. The whole process was recorded through a Euromex 10 MP video camera equipped with a trinocular optic microscope with a magnification of up to 100x. Thermal treatments were performed by means of a Linkam LTS420 hot stage.

2.9 Density calculations

Density values were calculated using the cell volume obtained through a Pawley refinement of the powder patterns collected at 293 K. For metastable polymorphs, cell volumes were obtained from single crystal samples. Close packing coefficients were extrapolated using molecular volumes calculated by means of Olex2 tool.

2.10 Energy calculations

Intermolecular interactions and lattice energies were calculated using CrystalExplorer17[169–171] at CE-B3LYP/6-31G (d,p) level of theory, considering for each molecule all the other surrounding molecules in a sphere of radius 3.80 Å and 20 Å, respectively. The lattice energy of **11** required a sphere of 25 Å for the presence of zwitterionic molecules[172]. The pair interaction energies were averaged according to the number of independent molecules in the asymmetric unit (Z').

2.11 Radiative treatment

The photo-responsive behaviour of coformers and cocrystals was induced using a UV Spectroline® Serie-E 6W lamp at 365 nm, on average corresponding to the λ_{max} of absorption of the azopyridinic coformers. During the irradiation, samples were placed at a 5 cm distance from the lamp resting on an aluminium support which provided efficient heat dissipation.

2.12 Release of active compounds (EOs)

The release of EOs was evaluated by preparing two sets of samples using 10 mL glass vials. One set was exposed to a radiation of 365 nm for different amounts of time (treated set) while the other set was not irradiated (control set). Before the measurements, samples were equilibrated for 5 min at constant temperature.

Headspace GC-MS analyses were carried out by injecting 1 mL of the headspace above the sample into the gas chromatograph by using a PAL COMBI-xt autosampler. A HP 6890 Series Plus gas chromatograph equipped with an MSD 5973 mass spectrometer was used. The carrier gas was helium at a constant flow of 1.3 mL/min. The injection port was held at 270 °C and the injection was carried out in split mode (split ratio 10:1). Chromatographic separation was performed on a 30 m × 0.25 mm, df 0.25 µm Rxi-17Sil MS capillary column using the following temperature program: initial temperature 70 °C, 10 °C/min up to 140 °C, 5 °C/min up to 170 °C. The transfer line and source were maintained at the temperatures of 270 and 150 °C, respectively. Full scan electron ionization (EI) data were acquired under the following conditions: ionization energy: 70 eV; mass range: 40-200 amu; scan time: 3 scan/s; electron multiplier voltage: 1400 V. Signal acquisition and data handling were performed using the HP Chemstation software. Two independent replicated measurements were always performed.

Bibliography

[1] A. A. Coelho, *J. Appl. Crystallogr.* **2018**, *51*, 210–218.

[2] P. Juhás, T. Davis, C. L. Farrow, S. J. L. Billinge, *urn:issn:0021-8898* **2013**, *46*, 560–566.

[3] C. F. Mackenzie, P. R. Spackman, D. Jayatilaka, M. A. Spackman, *IUCrJ* **2017**, *4*, 575–587.

[4] S. L. Tan, M. M. Jotani, E. R. T. Tiekink, *urn:issn:2056-9890* **2019**, *75*, 308–318.

[5] P. R. Spackman et al., *urn:issn:1600-5767* **2021**, *54*, 1006–1011.

[6] S. P. Thomas, P. R. Spackman, D. Jayatilaka, M. A. Spackman, *J. Chem. Theory Comput.* **2018**, *14*, 1614–1623.

CHAPTER 3

Photo-responsive cocrystals

3.1 Photo-responsive azopyridinic coformers

The category of stimuli-responsive materials comprises a broad spectrum of molecules which differ in the type of activating stimulus and chemical structure. Often, it is crucial that the activation process occurs in solution phase since it allows the molecules to be more reactive in virtue of the higher mobility, as in the case of pH, enzyme, or redox stimuli. Activations through temperature or light irradiation are more suitable for solid-state materials, even though the performances may be influenced by the particle shape, crystallinity, and amount of solid. In particular,

light irradiation exhibits relevant advantages including noncontact control, cost effectiveness, and the possibility of using different kinds of sources. In the last decades, photo-responsive molecules have been attracting attention for the capability of performing chemical reactions triggered by light[1,2], or inducing physical[3,4], and mechanical changes[5,6]. They have shown potential applications as molecular machines[7–9], mechanical actuators[10], and smart switches[11,12]. Photochemical reactions include dimerization, cyclization, and decomposition, with the result of completely changing the chemical and physical properties of the material thanks to the new chemical connectivity. Another way to obtain the same results, without changing connectivity, is the triggering of photo-isomerization processes. The preservation of the chemical connectivity has the advantage to prevent the formation of undesirable by-products, making photo-isomerization a sustainable reaction in accordance with the principles of atom economy[13]. The isomerization consists of a reversible conversion between geometric isomers (*i.e.* trans-cis, E-Z) and can be carried out by means of irradiation or thermal activation. Geometric isomers have different physical properties and therefore can be separated if stable enough. The most effective compounds that display photo-isomerization processes are azo compounds, stilbene derivates, hydrazones, hemiindigos, and indigos[12]. In particular, azo compounds exploit the isomerization of the azo bond and have been the most studied for their versatility and efficiency. Azo compounds are mainly divided into azobenzene and azopyridinic derivates. They have found applications as adhesives[14], or for photon energy storage[15] and lithography[16]; even showing significant optical[17] and mechanical properties[18–22]. Although the isomerization of azo compounds has been widely investigated in solution[23–27], only a few studies have approached the issue in solid-state[28]. In general, the isomerization process can take place through two different mechanisms: the *inversion* of one nitrogen atom or the *rotation* around the azo

bond[29] (*Figure 5*). These mechanisms occur depending on the rotational freedom of the system and develop along the S_1 (n-π*) or S_2 (π-π*) excited states, which involve respectively the non-bonding orbital of a nitrogen atom (n) and the π-symmetry bonding orbital (π) with the π-symmetry antibonding orbital (π*). The π-π* transition is symmetry allowed and has its maximum around 360 nm, while the n-π* transition has a maximum around 445 nm but it is not allowed for symmetry thus has a lower intensity. During the trans-to-cis isomerization, the n-π* band increases, due to the cis formation, while the π-π* band decreases. Whichever the mechanism, the isomerization of azo bonds requires a quite large "free volume" to occur in solid-state, contrasting the need of close packing in the crystalline materials. At this purpose, it has been demonstrated that the presence of alkyl chains and methyl substituents facilitates the isomerization process in solid-state with respect to non-substituted precursors[3].

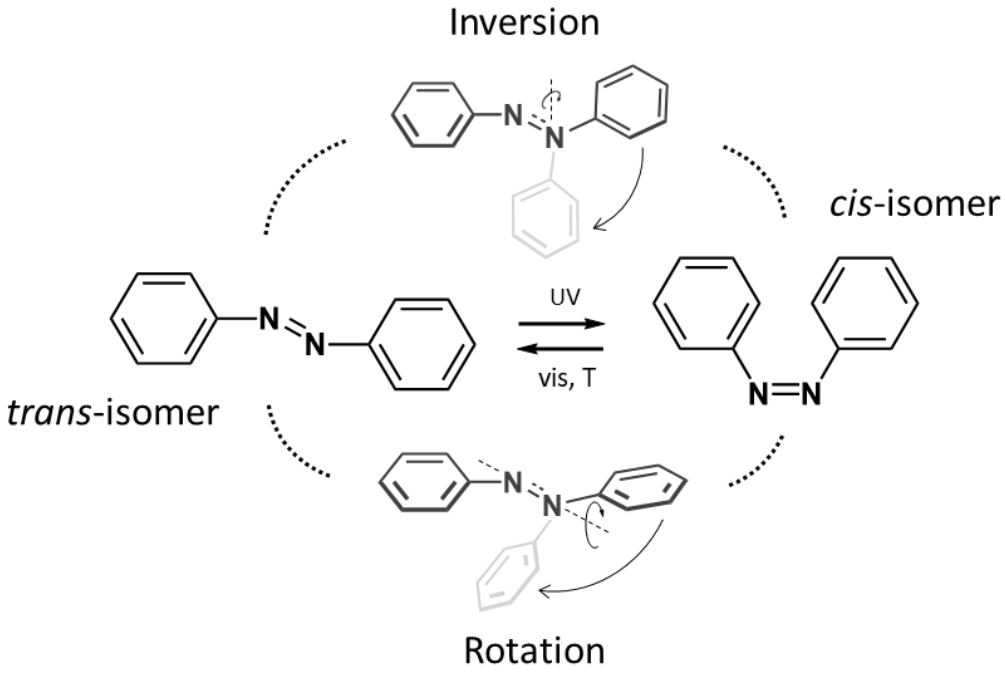

Figure 5. *Schematic mechanism of isomerization between trans and cis isomers of azobenzene.*

The design of photo-responsive coformers has moved from these considerations leading to the synthesis of azopyridinic derivates opportunely functionalized with alkyl chains of different length and/or methyl substituents on the aromatic rings. The choice of azopyridinic derivates mainly arises for the presence of a free nitrogen atom on the pyridine ring that may interact with the phenolic groups of EOs, according to the principles of crystal engineering, driving to the formation of cocrystals. Moreover, azopyridines have shown a higher rate constant of cis-to-trans isomerization than azobenzenes, which is a potential advantage as photoswitchers[27].

3.1.1 Synthesis

Azopyridinic (AZP) coformers were synthesized through an azo-coupling reaction between a diazonium salt, formed by the reaction of 4-aminopyridine with $NaNO_2$, and different phenol derivates as electrophilic substituents (*Scheme 1-2*). AZP coformers with alkyl chains of 6, 8, and 10 carbon atoms (**2**, **3**, **4**, and **6**, **7**, **8**) were obtained with a further nucleophilic substitution (SN2 mechanism) respectively on AZP coformers **1** and **5** with different alkyl bromides.

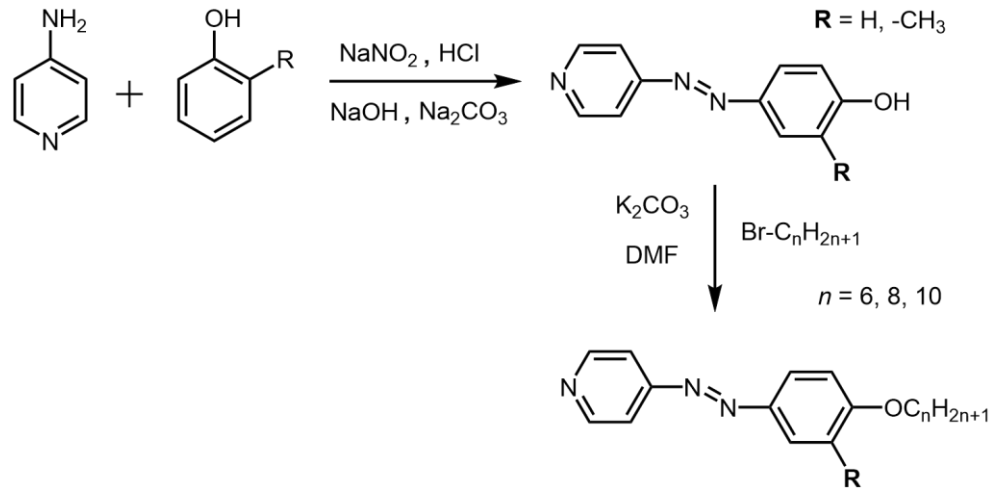

Scheme 1. *Synthesis of AZP coformers with different alkyl chain length.*

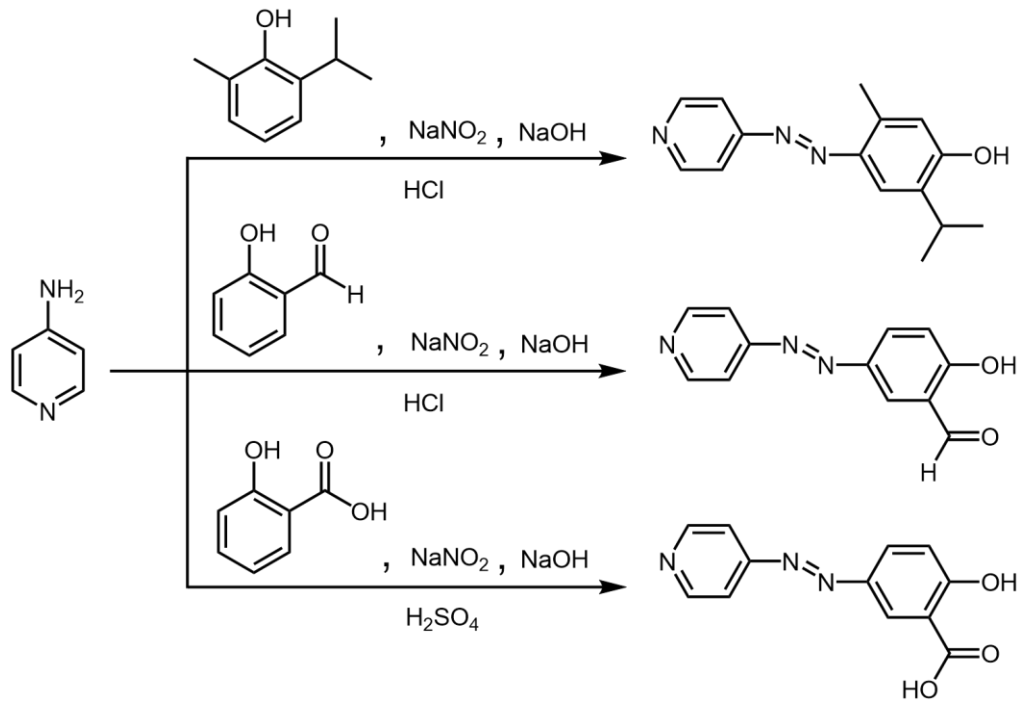

Scheme 2. *Synthesis of AZP coformers with different orto-substituents on the phenolic ring.*

Table 1. *Nomenclature of synthesized AZP coformers.*

AZP coformer	**R**	*n (alkyl chain)*
1	H	/
2	H	6
3	H	8
4	H	10
5	-CH_3	/
6	-CH_3	6
7	-CH_3	8
8	-CH_3	10
9	-iPr	/
10	-CHO	/
11	-COOH	/

AZP **1** and AZP **5**[30]

A solution of $NaNO_2$ (2.00 g, 29.00 mmol, 1.45 eq) in 50 mL of distilled H_2O was added dropwise to a solution of 4-aminopyridine (1.88 g, 20.00 mmol, 1.00 eq), 50 mL of distilled H_2O and 8.50 mL of 7 M HCl (aq). The resulting mixture was stirred at -5 °C for 15 min in an ice-salt bath. A basic solution of NaOH (1.04 g, 26.00 mmol), Na_2CO_3 (9.60 g, 90 mmol), and phenol (**1**, 2.70 g, 28.70 mmol, 1.43 eq) or cresol (**5**, 3.14 g, 29.00 mmol, 1.43 eq) in 50 mL of distilled H_2O was added slowly to the previous diazonium salt solution and the final mixture kept at 0 °C for 1 h under N_2 atmosphere. Then, the mixture was brought to room temperature and acidified to pH 6-7. An orange precipitate was obtained, filtered off through a Buchner filter and washed with distilled H_2O. The resulting orange powder was dried by vacuum for 2 h.

1: (1.72 g, yield = 43%)

Single crystal of **1b** polymorph were obtained by dissolving ~5 mg in ~2 mL of EtOH. Yellow needles crystallized in a few days through slow solvent evaporation under chemical hood.

^{1}H NMR (400 MHz, DMSO): δ 10.60 (s, 1H), 8.77 (d, J = 6.0 Hz, 2H), 7.88 (d, J = 8.8 Hz, 2H), 7.68 (d, J = 6.0 Hz, 2H), 6.98 (d, J = 8.8 Hz, 2H).

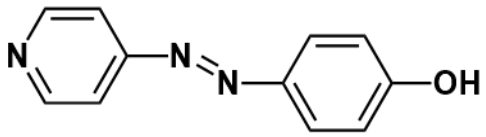

5: (1.93 g, yield = 45%)

Single crystals of **5** were obtained by dissolving ~5 mg in ~3.5 mL of a solution $CHCl_3$/hexane 1:1 (v/v). Yellow prisms crystallized in a week through slow solvent evaporation under chemical hood.

^{1}H NMR (400 MHz, DMSO): δ 10.54 (s, 1H), 8.77 (d, J = 6.4 Hz, 2H), 7.77 (s, 1H), 7.74 (d, J = 2.8 Hz, 1H), 7.67 (d, J = 6.4 Hz, 2H), 7.00 (d, J = 8.4 Hz, 1H), 2.23 (s, 3H).

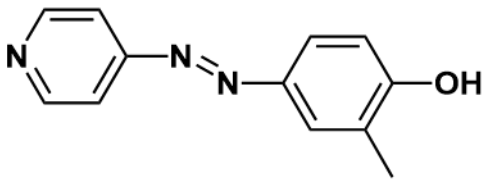

AZP **2**-**4** and AZP **6**-**8**[31]

1 (0.35 g, 1.76 mmol, 1.00 eq.) or **5** (0.37 g, 1.76 mmol, 1.00 eq) and K_2CO_3 (0.36 g, 2.64 mmol, 1.50 eq) were dissolved in 18 mL of DMF. Then, alkyl bromide (1.76 mmol, 1.00 eq) was added and the mixture was kept in reflux at 90 °C for 2 h, monitoring the proceeding of the reaction through TLC. The reaction mixture was poured into 50 mL of distilled H_2O and the suspension was extracted with 20 mL of ethyl acetate for two times. The organic layers were combined and washed with 5%

$NaHCO_3$ (aq), brine, and two times with a saturated solution of LiCl. The organic phase was then dried with $MgSO_4$, and the solvent was removed under reduced pressure. The products were recrystallized from distilled H_2O and dried by vacuum for 2 h obtaining a red precipitate.

2: (0.32 g, yield = 64%)

Single crystals of **2a** were obtained by synthesis, while single crystals of **2b** were obtained by dissolving ~5 mg in ~2 mL of EtOH. Orange prisms crystallized in a few days through slow solvent evaporation under chemical hood.

^{1}H NMR (400 MHz, DMSO): δ 8.79 (d, J = 6.0 Hz, 2H), 7.95 (d, J = 9.2 Hz, 2H), 7.70 (d, J = 6.0 Hz, 2H), 7.15 (d, J = 9.2 Hz, 2H), 4.09 (t, J = 6.4 Hz, 2H), 1.75 (m, 2H), 1.43 (m, 2H), 1.31 (m, 4H), 0.88 (t, J = 6.8 Hz, 3H).

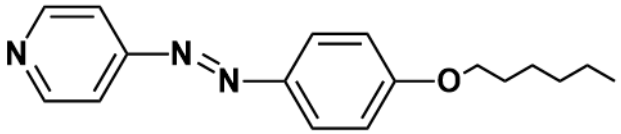

3: (0.34 g, yield = 61%)

Single crystals of **3** were obtained by dissolving ~5 mg in ~1 mL of acetone, up to saturation, and then adding a few drops of distilled H_2O. Yellow thin plates crystallized in a week through slow solvent evaporation under chemical hood.

^{1}H NMR (400 MHz, DMSO): δ 8.80 (d, J = 6.4 Hz, 2H), 7.95 (d, J = 8.8 Hz, 2H), 7.71 (d, J = 6.4 Hz, 2H), 7.16 (d, J = 8.8 Hz, 2H), 4.11 (t, J = 6.8 Hz, 2H), 1.76 (m, 2H), 1.44 (m, 2H), 1.28 (m, 8H), 0.87 (t, J = 6.8 Hz, 3H).

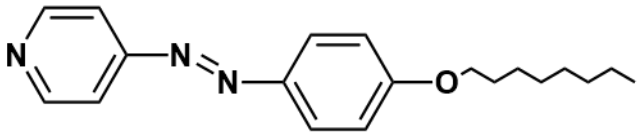

4: (0.31 g, yield = 53%)

Single crystals of **4** were obtained by dissolving ~5 mg in ~3 mL of acetonitrile. Orange needles crystallized in a few days through slow solvent evaporation under chemical hood.

^{1}H NMR (400 MHz, DMSO): δ 8.80 (d, J = 6.0 Hz, 2H), 7.96 (d, J = 8.8 Hz, 2H), 7.71 (d, J = 6.0 Hz, 2H), 7.16 (d, J = 8.8 Hz, 2H), 4.11 (t, J = 6.4 Hz, 2H), 1.76 (m, 2H), 1.43 (m, 2H), 1.26 (m, 12H), 0.86 (t, J = 6.8 Hz, 3H).

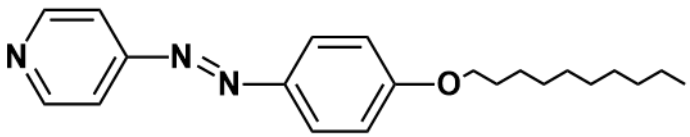

6: (0.24 g, yield = 47 %)

Single crystals of **6a** were obtained by synthesis, while single crystals of **6b** were obtained by recrystallization from melting using the experimental conditions reported in VT-PXRD experiments. Orange prisms of **6c** were instead obtained by dissolving ~5 mg in ~3 mL of acetonitrile, through a slow solvent evaporation in a few days under chemical hood.

^{1}H NMR (400 MHz, DMSO): δ 8.79 (d, J = 6.0 Hz, 2H), 7.87 (d, J = 8.8 Hz, 2H), 7.80 (s, 1H), 7.70 (d, J = 6.0 Hz, 2H), 7.18 (d, J = 8.8 Hz, 2H), 4.12 (t, J = 6.4 Hz, 2H), 2.25 (s, 3H), 1.78 (m, 2H), 1.47 (m, 2H), 1.34 (m, 4H), 0.89 (t, J = 7.2 Hz, 3H).

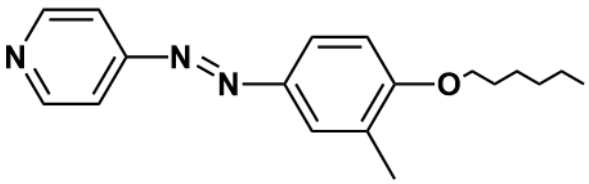

7: (0.37 g, yield = 66%)

Single crystals of **7a** were obtained by synthesis, while single crystals of **7b** and **7c** were obtained by dissolving ~5 mg in ~2 mL of acetonitrile. Orange prisms

crystallized in a few days through respectively slow solvent evaporation or cooling in the fridge at 5°C.

^{1}H NMR (400 MHz, DMSO): δ 8.79 (d, J = 6.4 Hz, 2H), 7.87 (d, J = 8.8 Hz, 2H), 7.80 (s, 1H), 7.70 (d, J = 6.0 Hz, 2H), 7.18 (d, J = 8.8 Hz, 2H), 4.12 (t, J = 6.4 Hz, 2H), 2.25 (s, 3H), 1.78 (m, 2H), 1.47 (m, 2H), 1.32 (m, 8H), 0.87 (t, J = 7.2 Hz, 3H).

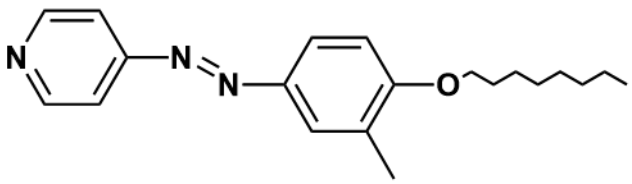

8: (0.30 g, yield = 49%)

Single crystals of **8** were obtained by dissolving ~5 mg in ~3 mL of acetonitrile. Orange prisms crystallized in a few days through slow solvent evaporation under chemical hood.

^{1}H NMR (400 MHz, DMSO): δ 8.79 (d, J = 6.4 Hz, 2H), 7.86 (d, J = 8.8 Hz, 2H), 7.80 (s, 1H), 7.70 (d, J = 6.4 Hz, 2H), 7.18 (d, J = 8.8 Hz, 2H), 4.12 (t, J = 6.4 Hz, 2H), 2.25 (s, 3H), 1.78 (m, 2H), 1.46 (m, 2H), 1.31 (m, 12H), 0.86 (t, J = 7.2 Hz, 3H).

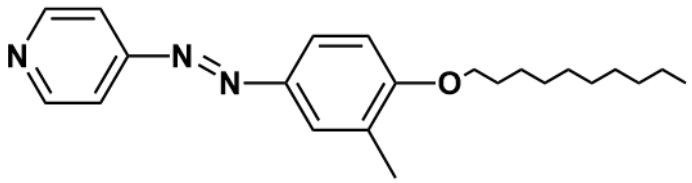

AZP **9**[32]

4-aminopyridine (1.25 g, 13.30 mmol, 1.20 eq) was dissolved in 10 mL of 7 M HCl (aq) and stirred at -5 °C for 30 min in an ice-salt bath. A basic solution of $NaNO_2$ (0.83 g, 12.10 mmol, 1.10 eq) and thymol (1.65 g, 11.00 mmol, 1.00 eq) was prepared in 15 mL of 10% w/w NaOH and cooled at 0°C for 30 min. The basic solution was added dropwise keeping the overall temperature in the range of -5°C

/ 0 °C. Adjusting the pH to 6-7 with 10% w/w NaOH solution, an orangish precipitate was obtained, filtered off through a Buchner filter and dried for 2 h. The crude product was purified by means of column chromatography (SiO_2, ethyl acetate/hexane 1:1) obtaining an orange solid with a yield of 17 % (0.46 g).

Single crystals of **9** were obtained by dissolving ~5 mg in ~3 mL of a solution THF/acetonitrile 1:1 (v/v). Orange prisms crystallized in a week through slow solvent evaporation under chemical hood.

^{1}H NMR (400 MHz, $CDCl_3$): δ 8.79 (d, J = 6.4 Hz, 2H), 7.71 (d, J = 6.0 Hz, 2H), 6.75 (s, 1H), 5.60 (s, 1H), 4.15 (q, J = 6.0 Hz, 1H), 3.22 (h, J = 6.8 Hz, 1H), 2.70 (s, 3H), 1.31 (m, 6H).

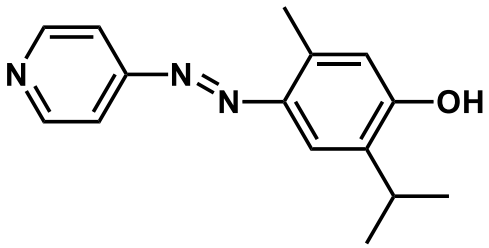

AZP **10**[33]

A solution of 4-aminopyridine (1.50 g, 15.94 mmol, 1.20 eq) in 37.5 mL of 4 M H_2SO_4 (aq) and $NaNO_2$ (1.50 g, 21.74 mmol, 3.00 eq) in 7.5 mL of distilled H_2O were prepared and cooled at -5 °C for 30 min in an ice-salt bath. The two solutions were mixed in less than 30 s and the resulting mixture was stirred at -5 °C for 5 min. A basic solution of salicylaldehyde (0.88 g, 7.21 mmol, 1.00 eq), NaOH (12.50 g, 312.50 mmol) and borax (3.73 g, 9.78 mmol) in 73.5 mL of distilled H_2O was prepared and cooled at 0°C for 15 min. Then, the basic solution was added to the mixture in 30 s, meanwhile providing a homogenous stirring and keeping the temperature in the range of -5°C / 0 °C. The pH was adjusted to 6-7 with a diluted HCl solution, obtaining a brown precipitate which was filtered off through a

Buchner filter and dried for 2 h. The crude product was recrystallized in a mixture of dichloromethane/hexane 1:1 obtaining an orange powder with a yield of 24% (0.38 g).

Single crystals of **10** were obtained by dissolving ~5 mg in ~4 mL of a solution THF/hexane 1:2 (v/v). Orange prisms crystallized in a few days through slow solvent evaporation under chemical hood.

^{1}H NMR (400 MHz, $CDCl_3$): δ 11.48 (s, 1H), 10.08 (s, 1H), 8.84 (d, J = 6.0 Hz, 2H), 8.30 (d, J = 2.4 Hz, 1H), 8.23 (dd, J1 = 2.4 Hz, J2 = 2.4 Hz 1H), 7.72 (d, J = 6.4 Hz, 2H), 7.18 (d, J = 9.2 Hz, 1H).

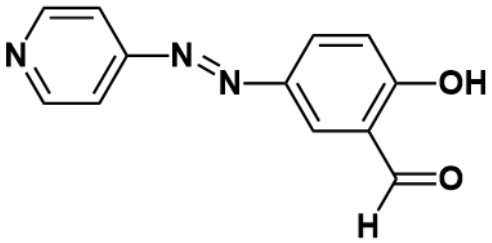

AZP **11**[34]

A solution of 4-aminopyridine (0.85 g, 9.03 mmol, 1.00 eq) in 5.5 mL of 7 M HCl (aq) and a solution $NaNO_2$ (0.65 g, 9.42 mmol, 1.05 eq) in 7 mL of distilled H_2O were prepared and cooled at -5 °C for 30 min in an ice-salt bath. The two solutions were mixed and stirred at -5 °C for 5 min. A basic solution of salicylic acid (1.24 g, 8.97 mmol, 1.00 eq) in 17 mL of 10% w/w NaOH was prepared and cooled at 0°C for 15 min. Then, the basic solution was added to the mixture within 5–10 s obtaining an orange precipitate. The resulting mixture was kept stirring for 1 h at -5 °C and then kept overnight at 4°C in a refrigerator. On the following day, the orange precipitate was filtered off through a Buchner filter and repeatedly washed with hot distilled H_2O, methanol, and hexane, then the crude product was dried for 2 h. The dried solid was dissolved in 10% w/w $NaHCO_3$ (aq) and after precipitated by adding a few

mL of diluted CH_3COOH (aq). The resulting solid was filtered off by a Buchner filter, washed with distilled H_2O until neutralized and dried for 3 h at room temperature. The crude product was crystallized from a mixture DMSO/H_2O 3:1 obtaining a red solid (0.32 g, 15%).

Single crystals of **11** were obtained by dissolving ~5 mg in ~2 mL of THF, up to saturation, and then adding a few drops of distilled H_2O. Orange prisms crystallized in a few days through slow solvent evaporation under chemical hood.

^1H NMR (400 MHz, DMSO): δ 8.84 (d, J = 6.4 Hz, 2H), 8.41 (d, J = 2.4 Hz, 1H), 8.11 (dd, J1 = 8.8 HZ, J2 = 2.4 Hz, 1H), 7.81 (d, J = 6.4 Hz, 2H), 7.13 (d, J = 8.8 Hz, 1H).

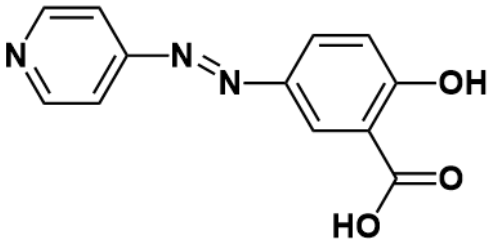

3.1.2 Trans-to-cis isomerization

The isomerization process of AZP coformers was investigated through UV-vis spectroscopy to compare the efficiency of AZP molecules as a function of the different substituents on the phenyl ring. Photoisomerization was induced by irradiating the sample at 365 nm for different times (1.5 h, 3 h, and 24 h) and monitoring the π-π* and n-π* bands of trans and cis isomers respectively. Measurements were performed in solution ($CHCl_3$) and even on thin films proving a promising response with low irradiation energy.

All the samples in $CHCl_3$, except for AZP **9**, achieved the photostationary state after 24 h. As expected, symmetry allowed π-π* bands of trans isomers gradually

decrease meanwhile symmetry forbidden n-π* bands of cis isomers increase (*Figure 6*). The isomerization process is further confirmed by the presence of isosbestic points as reported in *Table 2*.

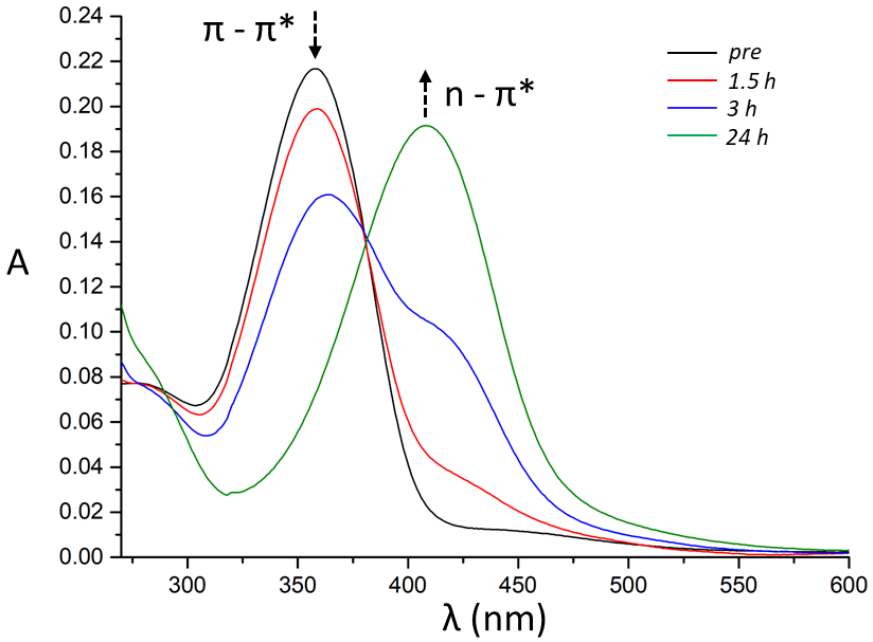

Figure 6. *UV-vis absorption spectra of* ***4*** *in $CHCl_3$ before and after different times of irradiation as example of trans-to-cis isomerization.*

The partial overlap between the π-π* and n-π* bands is emphasized by the presence of hydroxyl and alkoxyl groups which shift the π-π* transition of trans isomers to higher wavelengths via electron donor effect. On the other hand, **10** and **11** exhibit electron withdrawing groups which lead to a blue shift according to the ipsocromic effect (*Figure 7*).

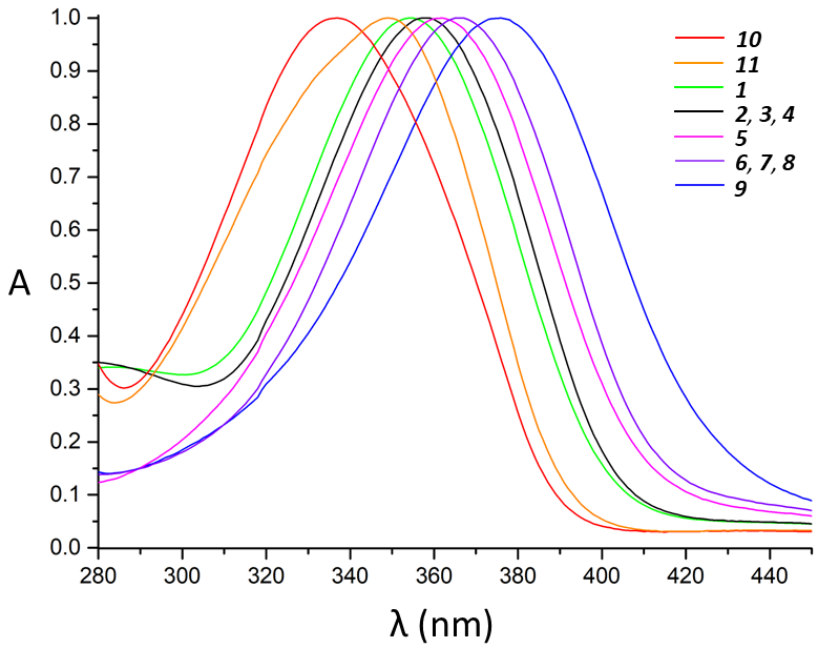

Figure 7. *UV-vis absorption spectra of AZP coformers in $CHCl_3$ before irradiation. Each spectrum was normalized [0,1] to compare the π-π* bands of trans isomers and was depicted with different colours as reported in the caption.*

The trans-cis isomerization efficiency was evaluated by determining the cis population in the photostationary state upon different irradiation times[35]:

$$\%\, cis = 100 \cdot (A_{trans}\,(i) - A_{trans}\,(t))/A_{trans}\,(i)$$

where $A_{trans}\,(i)$ and $A_{trans}\,(t)$ are the absorbances of π -π* band of trans isomer before the irradiation and after a certain time of irradiation.

In $CHCl_3$, AZP derivates overall showed a significant degree of conversion after 24 h, reaching a maximum of 77.98 % in the case of AZP **5** (*Table 1*). AZP **9** exhibited a partial conversion until 3 h but then disappeared after 24 h probably due to a competitive decomposition process involving the azo bond (*Figure 16*). Indeed, the presence of a methyl group in ortho respect to the azo bond might hamper the

mechanisms of isomerization, favouring alternative pathways for long time exposures.

Table 2. *Spectroscopic information of trans-cis isomerization process of AZP coformers in $CHCl_3$.*

AZP	π-π* (λ_{MAX})	n-π* (λ_{MAX})	Isosbestic point (nm)	% cis (1.5 h)	% cis (3 h)	% cis (24 h)
1	354	404	383	2.26	6.47	72.23
2	358	407	382	/	5.77	67.32
3	358	408	384	5.80	15.42	64.71
4	358	408	381	8.26	26.86	66.59
5	361	406	396	4.38	6.71	77.98
6	366	414	386	4.07	18.46	52.80
7	366	418	387	5.94	16.68	56.61
8	366	417	387	2.00	10.63	60.04
9	376	/	413	/	/	/
10	337	387	368	2.39	9.72	72.42
11	349	391	373	/	15.08	64.90

Comparing **1** and **5** with their alkylated derivates, respectively **2**, **3**, **4**, and **6**, **7**, **8**, the former ones achieved a higher conversion after 24 h of irradiation even though revealed a lower conversion rate after 3 h and 4 h. Moreover, among the alkylated derivates, the presence of the methyl group in the molecular structure has proven to not further improve the isomerization process since the most promising results were obtained for **2**, **3**, **4**.

Solid-state measurements require different considerations from solution since whenever the wavelength of radiation is similar to the dimension of the solid particles, scattering occurs. Scattering strongly affects the baseline of UV-vis spectra and increases with the amount of solid; in addition a large amount of solid may lead to self-absorption phenomena. To limit these issues, the amount of sample spread on the quartz plate was minimum, obtaining thin film depositions. However, the

measured absorbance is proportional to the concentration of the sample, according to Lambert-Beer law[36,37], therefore absorbance values for solid-state measurements result lower than for solutions.

As general observation, solid-state measurements of AZP coformers also showed the decrease of π-π* band related to the trans isomer despite no clear evidence of cis formation can be appreciated. In fact, even after the shortest irradiation time (1.5 h), the scattering contribution often increased along with the baseline, likely due to a particle rearrangement. In these conditions, neither isosbestic points nor definite bands could be seen. In particular, AZP coformers with alkyl chains seem to be more susceptible to physical changes since their spectra show an extremely different baseline after the irradiation (*Figure 8-18*, right). A reasonable explanation can be found in the non-radiative processes which occur after the absorption in competition with the emission processes (*i.e.* fluorescence or phosphorescence) and the photo-isomerization. AZP coformers with alkyl chains exhibit lower melting points rather than the other coformers, below 70°C (Appendix A.3), therefore the increase of temperature due to the non-radiative processes could more affect their physical state changing the scattering contribution in the UV-vis spectra.

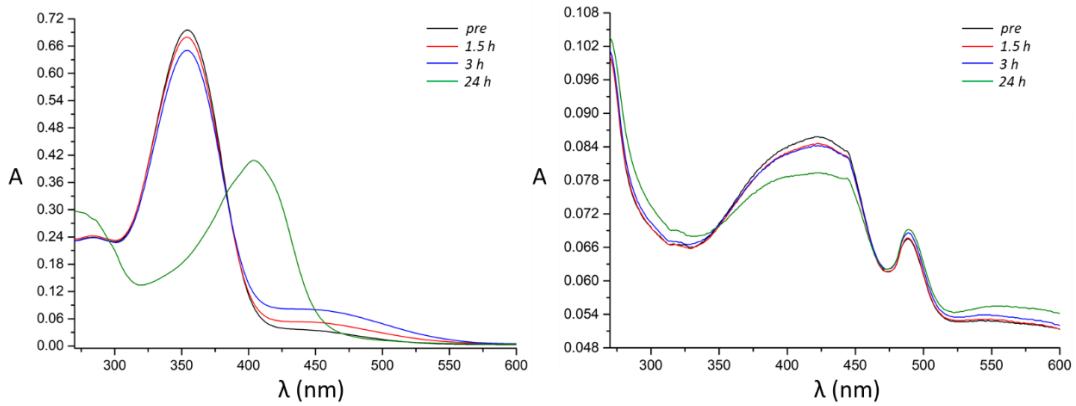

Figure 8. *UV-vis spectra of AZP* ***1*** *in $CHCl_3$ (left) and as thin film (**1a**) (right).*

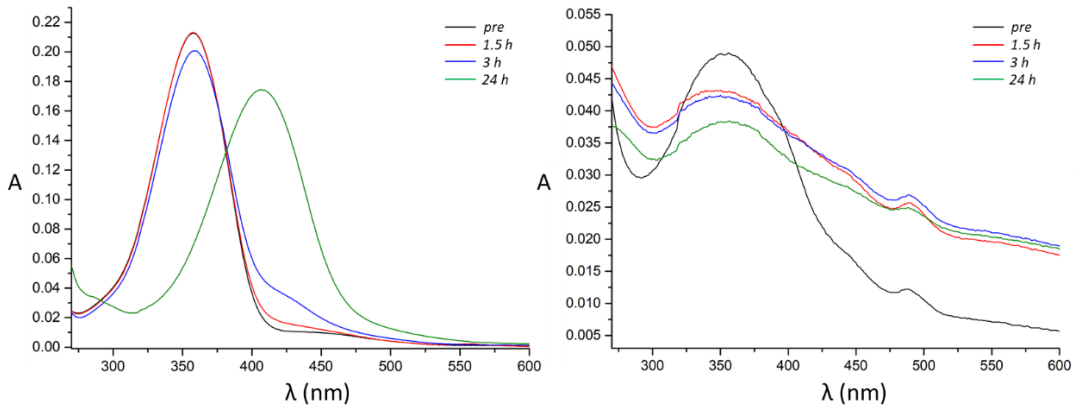

Figure 9. *UV-vis spectra of AZP* ***2*** *in $CHCl_3$ (left) and as thin film (****2a****) (right).*

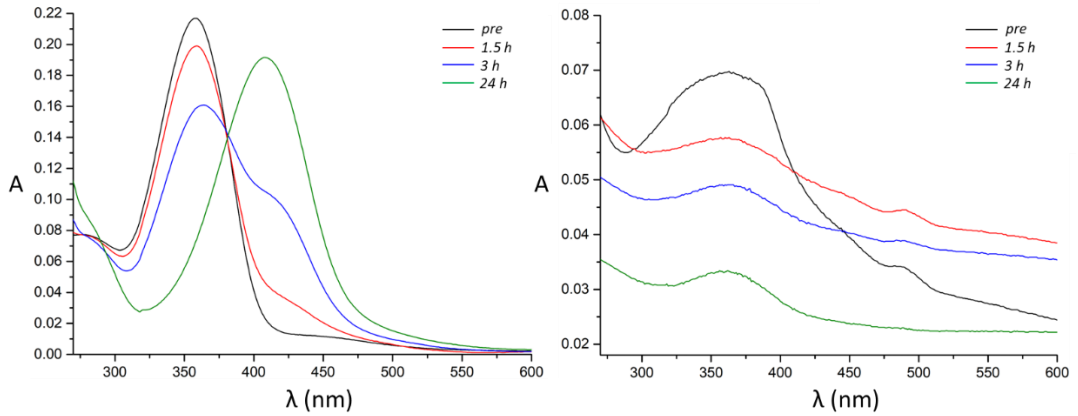

Figure 10. *UV-vis spectra of AZP* ***3*** *in $CHCl_3$ (left) and as thin film (right).*

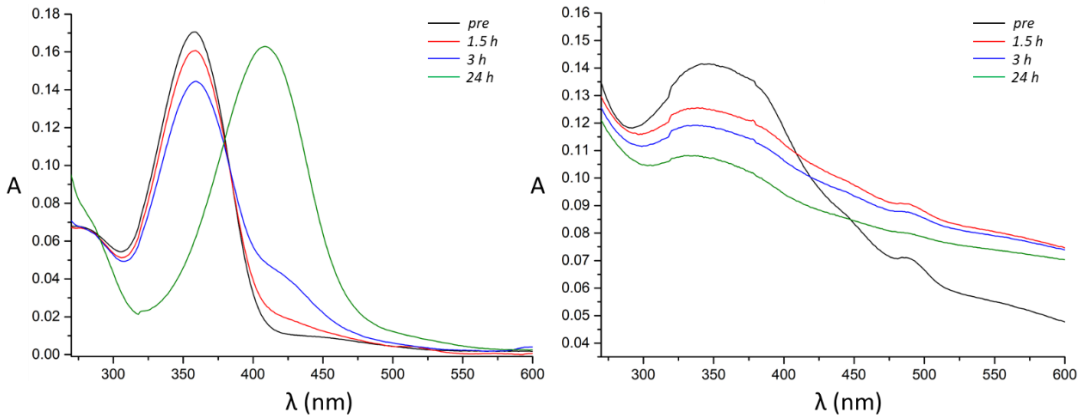

Figure 11. *UV-vis spectra of AZP* ***4*** *in $CHCl_3$ (left) and as thin film (right).*

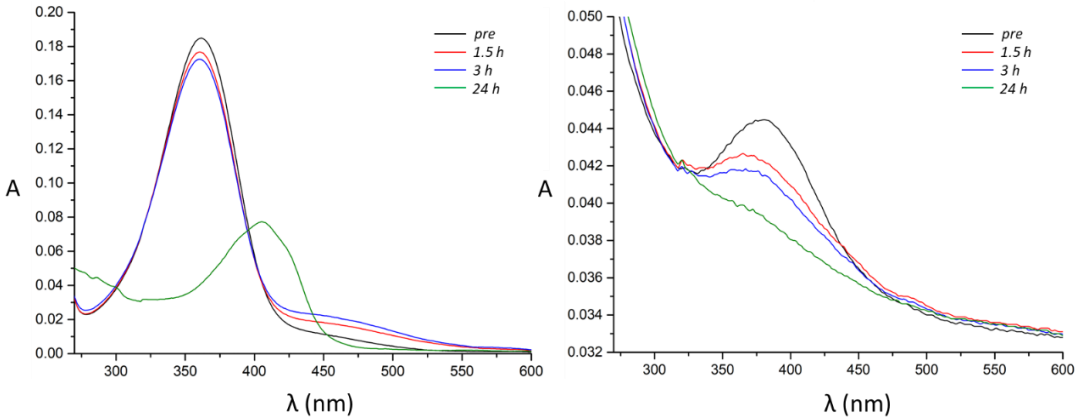

***Figure 12**. UV-vis spectra of AZP **5** in $CHCl_3$ (left) and as thin film (right).*

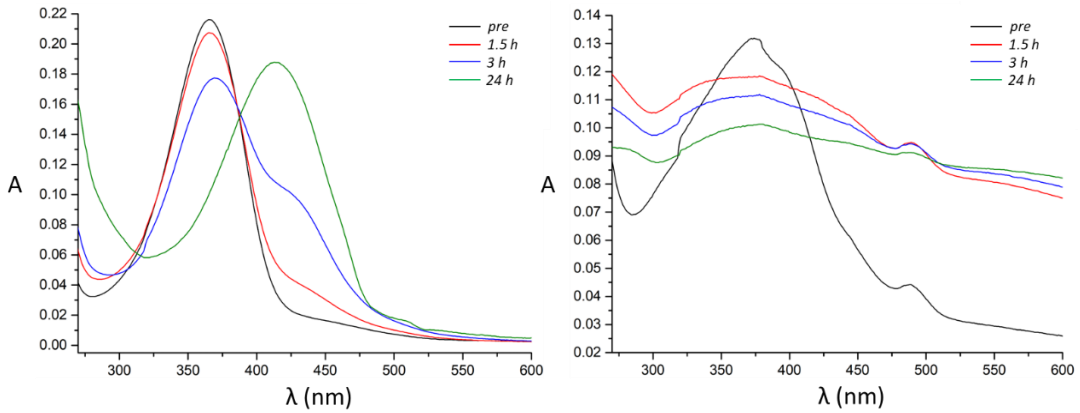

***Figure 13.** UV-vis spectra of AZP **6** in $CHCl_3$ (left) and as thin film (**6b**) (right).*

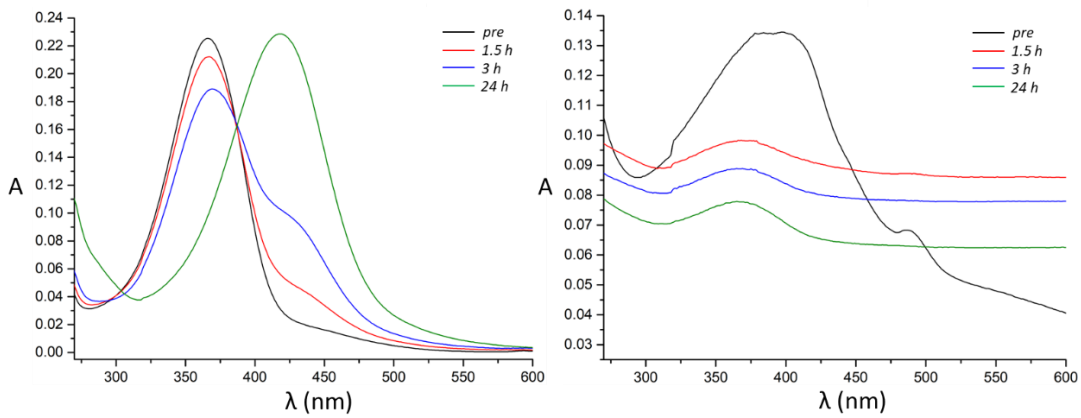

***Figure 14.** UV-vis spectra of AZP **7** in $CHCl_3$ (left) and as thin film (**7c**) (right).*

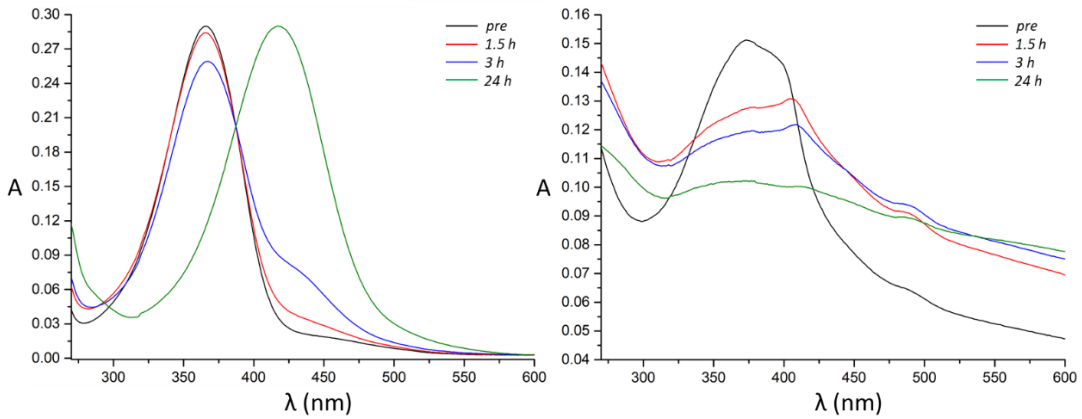

Figure 15. *UV-vis spectra of AZP* ***8*** *in $CHCl_3$(left) and as thin film (right).*

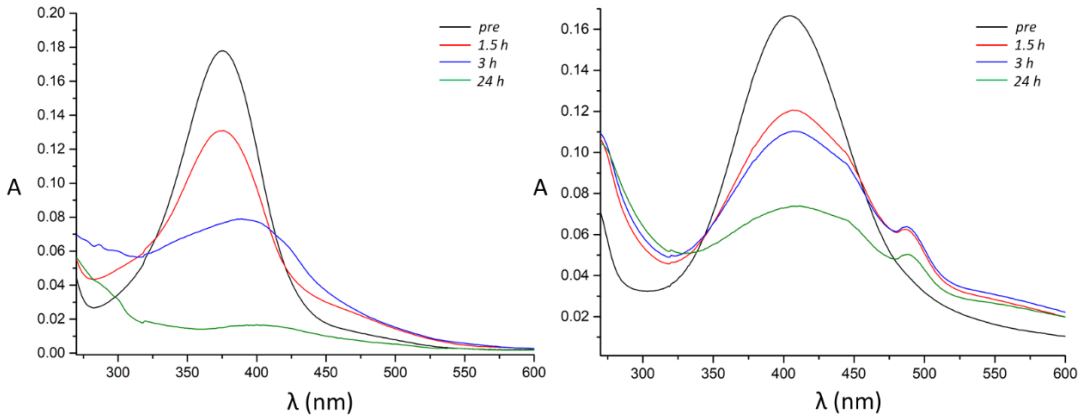

Figure 16. *UV-vis spectra of AZP* ***9*** *in $CHCl_3$ (left) and as thin film (right).*

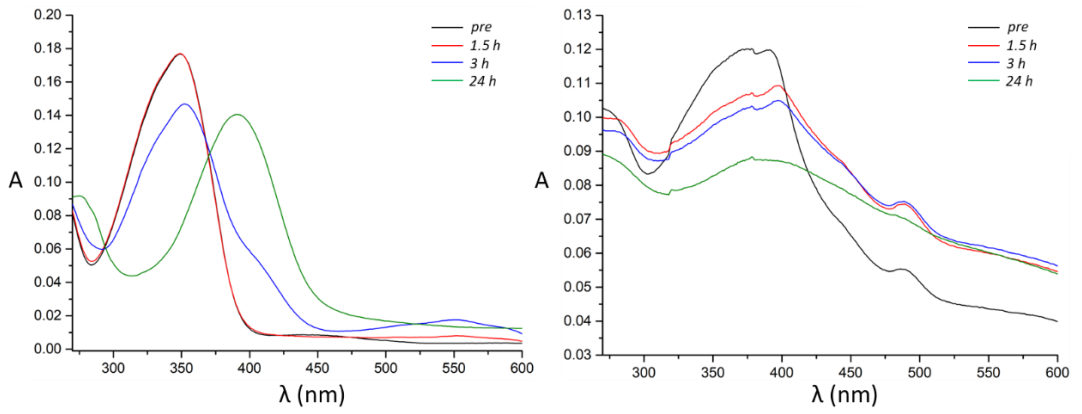

Figure 17. *UV-vis spectra of AZP* ***10*** *in $CHCl_3$ (left) and as thin film (right).*

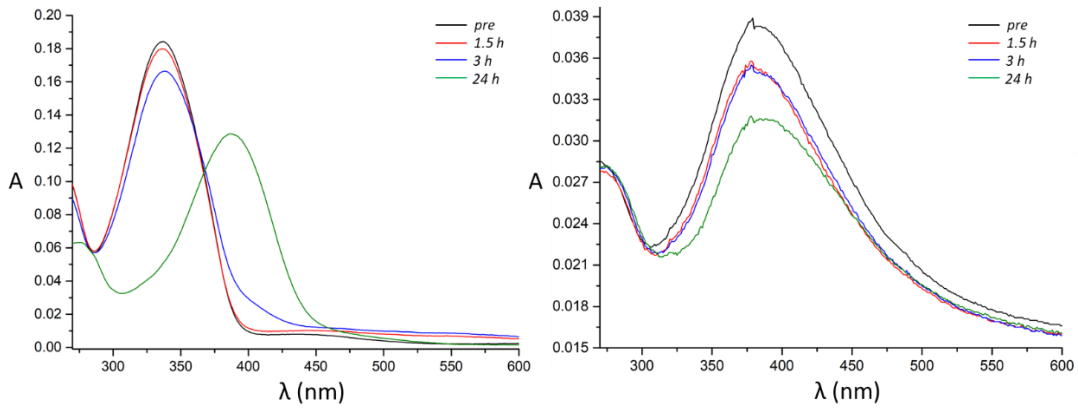

Figure 18. *UV-vis spectra of AZP **11** in $CHCl_3$ (left) and as thin film (right).*

3.1.3 Crystal structures

The crystallographic information concerning the crystal structures of AZP coformers and the refinement details is reported in Appendix A.4.

AZP **1**

A crystalline phase of AZP **1** (polymorph **a**) is already reported in the CSD[38] as a monoclinic form with space group P21/n (a: 5.592 Å, b: 11.313 Å, c: 15.439 Å, α: 90°, β: 97.6°, γ: 90°; CSD Refcode: AXUYOJ). Here, it is reported a new crystalline phase (polymorph **b**), obtained as single crystals, which crystallizes in P-1 space group. **1b** has two formula units in the asymmetric unit (Z = 4, Z' = 2), against one formula unit of **1a** (Z = 4, Z' = 1). The crystal structures of both polymorphs are driven by head-to-tail hydrogen bonds (HBs) between the phenolic groups and the nitrogen atoms of the pyridine rings (**1a**: O···N: 2.670(3) Å; O-H···N = 164.0(3)°; **1b**: O···N: 2.678(3) Å; O-H···N = 168.9(1)°) (*Figure 19*, up). These head-to-tail motifs generate chains of molecules that are stacked in pillars through π···π interactions: **1a** exhibits pillars with two different orientations alternated along the a-direction,

instead **1b** pillars run along the c-direction and are formed by chains of molecules with inverted head-to-tail orientation (*Figure 19*, up and down). Head-to-tail HBs are rather strong and represent the most stabilizing interactions for the crystal packing, with a molecule-molecule energy of -47.4 kJ/mol (**1a**) and -49.2/-47.0 kJ/mol (**1b**), as calculated by Crystal Explorer at CE-B3LYP/6-31G(d,p) level of theory. The synergistic effect between HBs and stacking interactions contributes to high crystal density values of 1.358 (**1a**) and 1.385 (**1b**) g/cm^3.

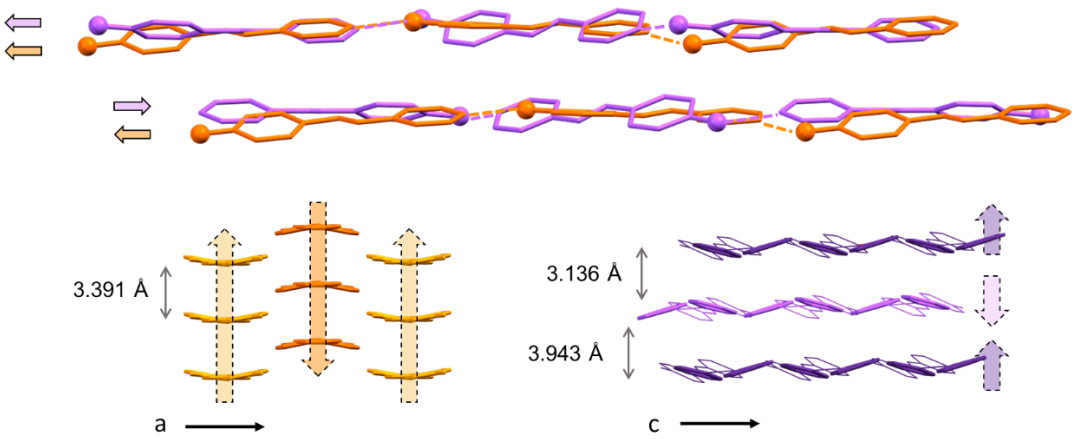

Figure 19. *Up: overlap of **1a** (orange) and **1b** (purple) crystal structures with the emphasis on head-to-tail O-H···N hydrogen bonds. Down: arrangement of the molecular chains generated by the HBs and stacked by π-π interactions in **1a** (left) and **1b** (right) crystal structures. Hydrogen atoms are omitted for sake of clarity.*

AZP **2**

AZP **2** crystallizes in the P-1 space group with two different polymorphic forms **2a** and **2b**, both with one formula unit in the asymmetric unit (Z = 2, Z' = 1). The alkylation of the phenolic group no longer allows to build HB networks, therefore the main contributions to the crystal packing are π···π and C-H···π interactions. The molecular arrangement is organized in offset stacked pillars, where the aromatic

bones are stacked over the alkyl chains (*Figure 20*). The strength and the number of π···π and C-H···π interactions determine the efficiency of the overlap, showing differences within a range of 10 kJ/mol in terms of molecule-molecule energies (A: -64.7 kJ/mol; B: -56.1 kJ/mol; C: -58.8 kJ/mol; D: -60.2 kJ/mol). It is worth noting that **2b** molecules show a torsion angle of 18.21° between the aromatic rings while **2a** molecules are almost planar. Overall, the presence of alkyl chains remarkably reduces the crystal density with respect to the polymorphs of **1**, leading to values of 1.220 g/cm^3 for **2a**, and 1.193 g/cm^3 for **2b**.

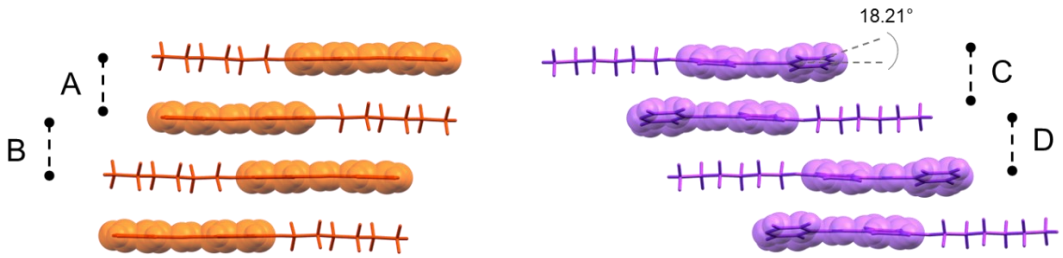

Figure 20. *Molecular arrangements due to the stacking interactions in **2a** (orange) and **2b** (purple) crystal structures. A, B, and C, D are the pairs of molecules that give the largest molecule-molecule interaction energies respectively in the crystal structures of **2a** and **2b**.*

AZP **3**

AZP **3** crystallizes in P-1 space group with one formula unit in the asymmetric unit (Z = 2, Z' = 1). Cell parameters (Appendix A.4, Table A4.1)) suggest a structural similarity with **2a** polymorph, which was confirmed through the overlap of **2a** and **3** crystal structures (*Figure 21*, up). By superimposing the molecules included in both asymmetric units, the molecular arrangements appear analogous but oriented in different directions, with a tilt angle of 2.92° (*Figure 21,* up). Molecules are organized driven by π···π and C-H···π interactions, forming stacked offset pillars

oriented in a head-to-tail motif (*Figure 21*, down). The highest molecule-molecule interaction energy of **3**, indicated by A and B pairs in *Figure 21* (down) (A: -71.4 kJ/mol; B: -66.9 kJ/mol), are comparable with those of **2a**, bringing out differences due to the longer alkyl chains that establish a higher number of dispersive interactions. These considerations are reflected in the crystal density values of **3** (1.158 g/cm^3), which result more similar to **2** than **1** polymorphs.

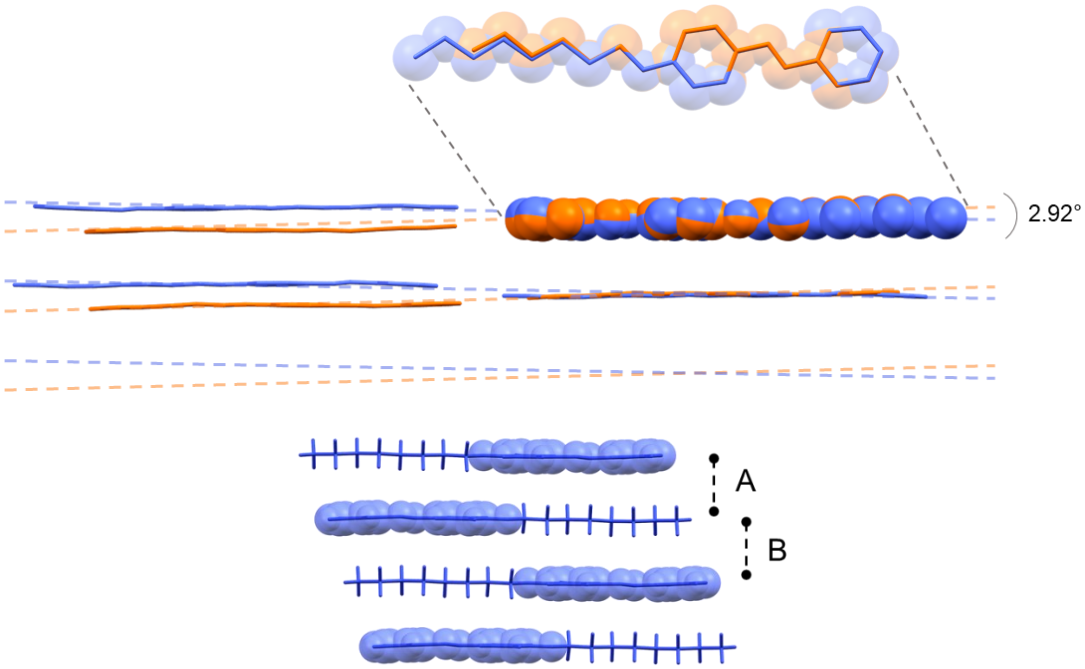

Figure 21. *Up: overlap of **2a** (orange) and **3** (blue) crystal structures. Hydrogen atoms are omitted for sake of clarity. Down: molecular arrangements due to the stacking interactions in **3** crystal structure. A, B are the pairs of molecules that give the largest molecule-molecule interaction energies in the crystal structure.*

AZP **4**

AZP **4** crystallizes in P-1 space group with one formula unit in the asymmetric unit (Z = 2, Z' = 1). From a comparison of the unit cell parameters with AZP **3** (Appendix A.4, Table A4.1), the two crystalline phases exhibit analogous cell axes, except for the c-axis of **4** which is a bit longer due to the alkyl chain containing two more carbon atoms; while the cell angles are *de facto* complementary (*Figure 22*, down, left). These properties find confirm by the overlap of **3** and **4** crystal structures, as shown in *Figure 22* (up). Accordingly, also the crystal structure of **4** is driven by π···π and C-H···π interactions, leading to the formation of stacked offset pillars that run along the b-direction (*Figure 22,* down, right). Energy calculations further validate the role of π···π stacking interactions by reason of the highest molecule-molecule energies (A: -75.8 kJ/mol; B: -77.7 kJ/mol). The crystal density of **4** (1.125 g/cm^3) is in line with the values of alkylated AZP coformers (**2**, **3**).

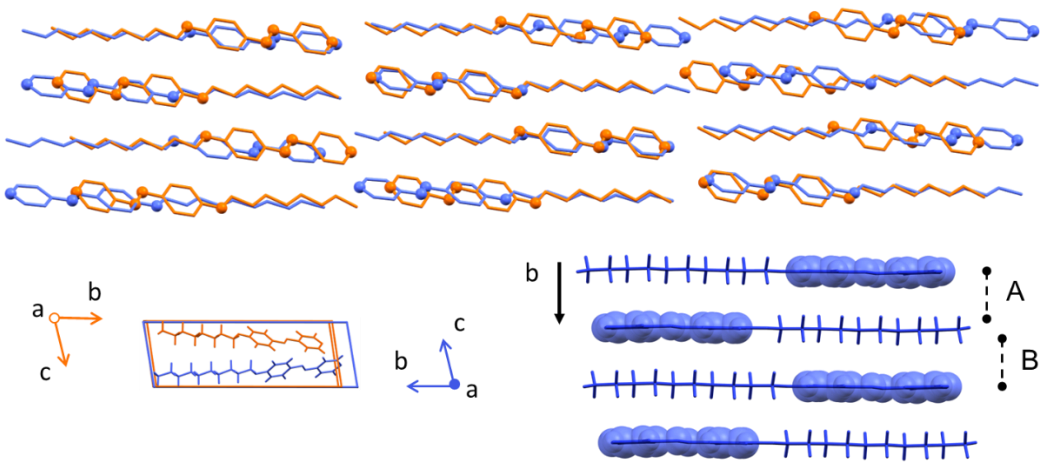

Figure 22. *Up: overlap of **3** (orange) and **4** (blue) crystal structures. Hydrogen atoms are omitted for sake of clarity. Down, left: superimposition of **3** and **4** unit cells. Down, right: molecular arrangements due to the stacking interactions in **4** crystal*

structure. A, B are the pairs of molecules that give the largest molecule-molecule interaction energies in the crystal structure.

AZP **5**

The crystal structure of AZP **5** exhibits a non-centrosymmetric space group P212121 with one formula unit in the asymmetric unit (Z = 4, Z' = 1). As seen for **1** polymorphs, head-to-tail HB interactions are established between the phenolic groups and the nitrogen atoms of the pyridine rings (**5**: O···N: 2.746(4) Å; O-H···N = 146.5(2)°), mainly contributing to the strength of the molecular network (*Figure 23*, left). Compared to **1** polymorphs, however, the presence of a methyl substituent on the phenolic ring completely alters the stacking arrangement, leading to T-shape C-H···π interactions between the aromatic C-H groups with the phenolic and pyridinic rings (*Figure 23*, right). The steric hindrance due to the methyl groups also influences the energy of the HBs, which result less stable (-44.4 kJ/mol) and with lower O-H···N angles. Nevertheless, the crystal density of **5** is only slightly affected (1.352 g/cm^3) and the value is comparable with the ones of **1a** and **1b** polymorphs.

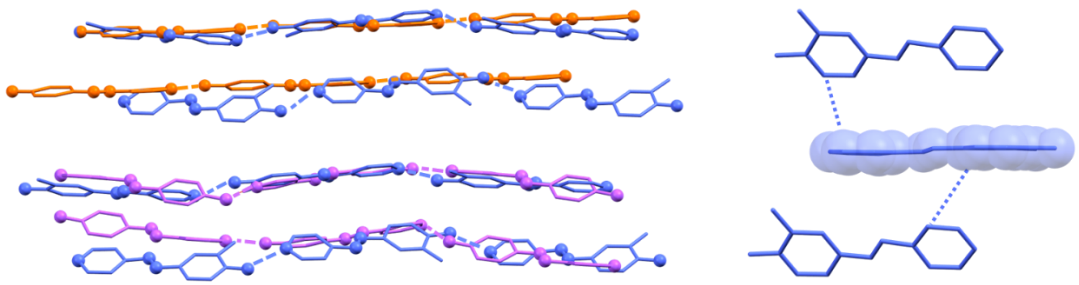

Figure 23. *Left: overlap of **1a** (orange) and **1b** (purple) with **5** (blue) crystal structure, highlighting head-to-tail O-H···N hydrogen bonds. Right: molecular arrangements in **5** (blue) crystal structures due to T-shape C-H···π interactions. Hydrogen atoms are omitted for sake of clarity.*

AZP **6**

AZP **6** presents three different polymorphic forms which crystallize all in P-1 space group with one formula unit in the asymmetric unit (Z = 2, Z' = 1) for **6a** and **6b**, and two formula units (Z = 4, Z' = 2) for **6c**. Similarly to polymorphs **2a** and **2b**, which differ for the absence of a methyl substituent, the main interactions within the crystal structure are represented by π···π and C-H···π interactions. The molecular arrangements of **6a** and **6b** resemble that of **2b** polymorph: stacked offset pillars are formed through the alternation of molecules which differently head-to-tail overlap, establishing either π···π and C-H···π interactions or merely C-H···π interactions (*Figure 24*, depicted in orange and purple). Torsion angles of 17.36° (**6a**) and 23.23° (**6b**) between the aromatic rings further confirm the similarity with **2b**, whilst differences in terms of molecule-molecule interaction energies are observed due to the methyl substituent and the different overlaps (A: -53.5 kJ/mol; B: -73.7 kJ/mol; C: -66.3 kJ/mol; D: -50.2 kJ/mol).

Instead, the crystal structure of **6c** is comparable with **2a** polymorph since pairs of molecules exactly overlap head-to-tail forming offset pillars (*Figure 24*, depicted in teal). However, the two largest molecule-molecule interactions in **6c** polymorph are rather different in energies (E: -73.9 kJ/mol; F: -28.5 kJ/mol), unlike to **2a** polymorph, because of the more efficient molecular overlap in pair E against the mere overlap of aromatic bones in pair F.

The molecular arrangements are also influenced by methyl substituents, which opportunely display on opposite sides either for neighbouring molecules (**6a**, **6b**) or for neighbouring pairs (**6c**) in order to minimize their steric hindrance. The overall effect due to the presence of methyl substituents is thus to slightly decrease the density of the crystal structure (**6a**: 1.153 g/cm^3, **6b**: 1.131 g/cm^3, **6c**: 1.177 g/cm^3).

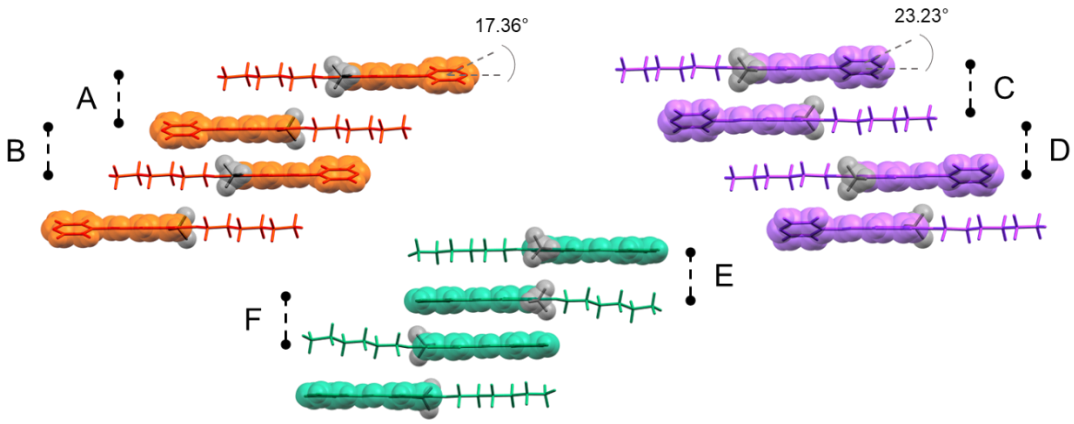

Figure 24. *Molecular arrangements due to the stacking interactions in* ***6a*** *(orange),* ***6b*** *(purple) and* ***6c*** *(teal) crystal structures. A, B, C, D, and E, F are the pairs of molecules that give the largest molecule-molecule interaction energies respectively in the crystal structures of* ***6a***, ***6b*** *and* ***6c****.*

AZP **7**

AZP **7** exhibits three different polymorphic forms, **7a** and **7c** which crystallize in P-1 space group with one formula unit in the asymmetric unit (Z = 2, Z' = 1), and **7b** which crystallizes in C2/c space group with one formula unit in the asymmetric unit (Z = 8, Z' = 1). The molecular arrangement of the three polymorphs is substantially different, however the driving forces of the packings dwell in the π···π and C-H···π interactions. The crystal structure of **7a** evidences a similarity with **3** since molecules form offset pillars where the alkyl chains are overlapped to the aromatic bones in an alternating way (*Figure 25*, depicted in orange). On the other hand, the torsion angle between the aromatic rings (11.14°) resembles the conformations assumed in **2b**, **6a**, and **6b** crystal structures. The molecular arrangement of **7b** has no similarities with the other crystalline phases of AZP coformers and consists of dimeric head-to-tail overlaps interspersed by two molecules that display head-to-head in the same plane (*Figure 25*, depicted in purple). The dimers exhibit the

methyl substituents on the same side, while the on-plane two molecules alternate their methyl groups with respect to the neighbouring molecules. Also the molecular arrangement of **7c** is quite singular, indeed molecules are overlapped head-to-head by forming offset stacked pillars (*Figure 25*, depicted in teal). The methyl substituents are exhibited on the same side and the torsion angles between the aromatic rings measure 17.33°. From a comparison of the molecule-molecule interaction energies, **7a** and **7b** polymorphs revealed similar highest values (A: -69.8 kJ/mol; B: -76.0 kJ/mol; C: -72.3 kJ/mol; D: -42.0 kJ/mol; E: -23.3 kJ/mol), instead the energies in **7c** crystal structures result lower but comparable (-58.0 kJ/mol). The energy values of pairs D and E are consequence of the limited overlaps, as seen for pair F in **6c** polymorph. Finally, the crystal density values are slightly below the values of **6** polymorphs due to the longer alkyl chains (7**a**: 1.113 g/cm^3, **7b**: 1.115 g/cm^3, **7c**: 1.116 g/cm^3).

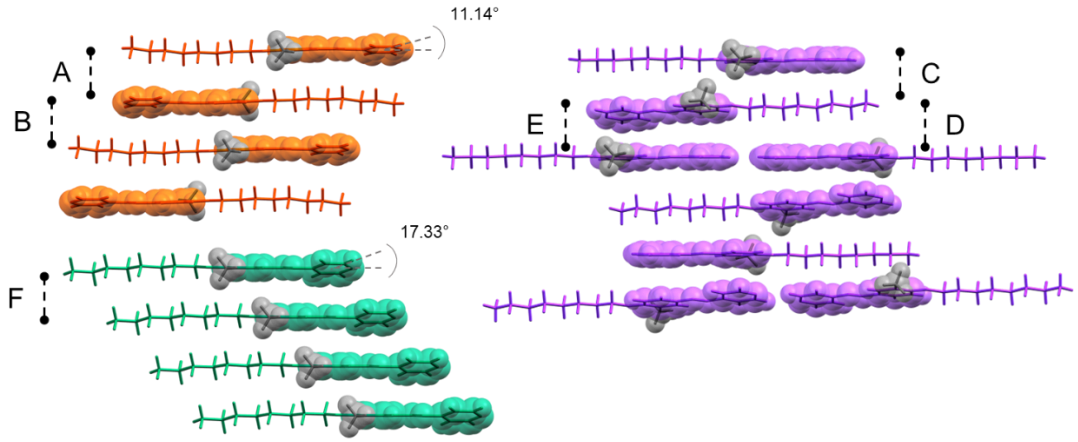

Figure 25. *Molecular arrangements due to the stacking interactions in **7a** (orange), **7b** (purple) and **7c** (teal) crystal structures. A, B, C, D, E, and F are the pairs of molecules that give the largest molecule-molecule interaction energies respectively in the crystal structures of **7a**, **7b** and **7c**.*

AZP **8**

AZP **8** crystallizes in P-1 space group with one formula unit in the asymmetric unit (Z = 2, Z' = 1). The comparison with **4** crystal structure brings out that the molecular arrangements of the two phases are analogous, even though no correlation is found between the unit cells. Molecules are stacked in offset pillars by means of π···π and C-H···π interactions, maintaining the same orientation along the pillars in AZP **4** (*Figure 26*, left, orange) or alternating their orientation in AZP **8** (*Figure 26*, left, blue). A different molecular orientation is also found comparing consecutive pillars, whose molecules retain their orientation in **8** crystal structure while invert in **4** crystal structure (*Figure 26*, left). The similarity of arrangements is reflected even in the molecule-molecule interaction energies, with the two highest values (-84.8 kJ/mol (A), -73.9 kJ/mol (B)) both referring to stacking interactions. The crystal density (1.113 g/cm^3) of **8** is also close to the value of **4**, and in agreement with the other alkylated AZP coformers.

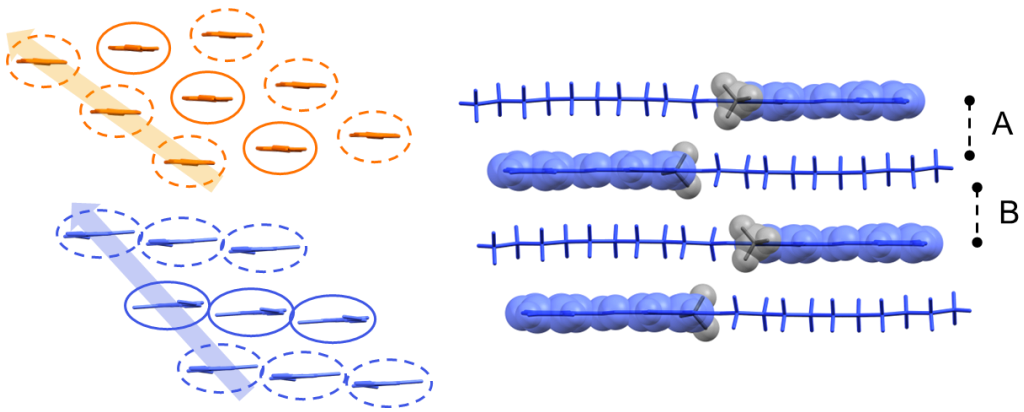

Figure 26. *Left: comparison of **4** (orange) and **8** (blue) crystal structures constituted by alternating pillars (dotted lines). Molecules are oriented orthogonally with respect to the sheet, with incoming (dashed circles) or outgoing (solid circles) alkyl chains. Hydrogen atoms are omitted for sake of clarity. Right: molecular arrangements due to the stacking interactions in **8** crystal structure. A, B are the*

pairs of molecules that give the largest molecule-molecule interaction energies in the crystal structure.

AZP **9**

AZP **9** crystallizes in C2/c space group with one formula unit in the asymmetric unit (Z = 8, Z' = 1). Similarly to **1** polymorphs and **5**, the molecular arrangement is influenced by head-to-tail HBs between the phenolic groups and the nitrogen atoms of the pyridinic ring (**9**: O···N: 2.717(5) Å; O-H···N = 165.8(2)°). Molecules are thus organized in a hierarchic way (*Figure 27*), which begins with the formation of chains whereby the isopropyl substituents are alternated to reduce their steric hindrance. All the chains along the b-direction are then held together through dispersive interactions forming parallel sheets, which complete the hierarchic arrangement by establishing π···π interactions between their aromatic bones. These parallel sheets result superimposed to the crystallographic planes {101} (*Figure 27*). Energy calculations revealed that π···π interactions are the strongest interactions, with molecule-molecule energies of -62.9 kJ/mol and -52.7 kJ/mol, even more than HBs (-49.4 kJ/mol). Nevertheless, the crystal density of **9** (1.123 g/cm^3) is mainly affected by the presence of alkyl substituents, in particular isopropyl groups, which thus have a similar effect as the alkyl chains.

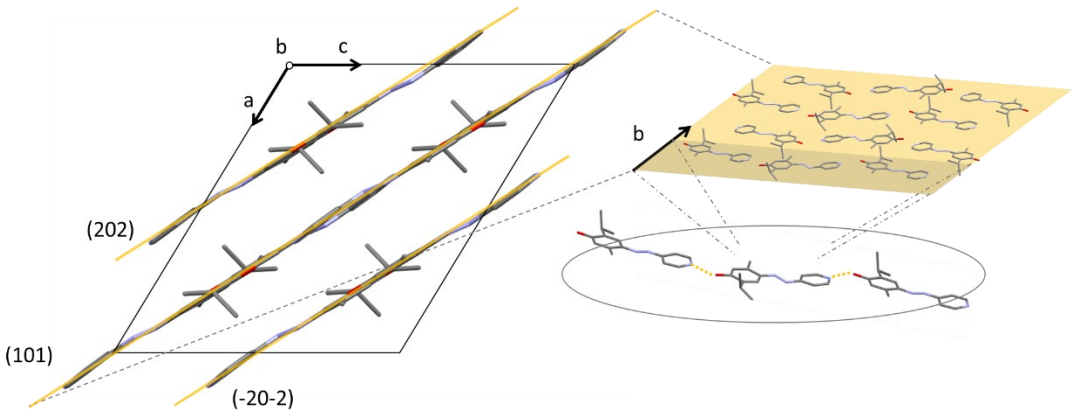

Figure 27. *Hierarchic molecular arrangements in* ***9*** *crystal structure due to π···π and hydrogen bonds interactions, the latter emphasised by yellow dotted lines. Hydrogen atoms are omitted for sake of clarity.*

AZP **10**

AZP **10** crystallizes in P21/c space group with one formula unit in the asymmetric unit (Z = 4, Z' = 1). Although the presence of the aldehyde group, in ortho position with respect to the phenolic group, might suggest the formation of dimers, exploiting HBs with $R_2^2(12)$ geometry, instead the intramolecular HBs are significantly favoured due to the more stable $S(6)$ geometry (O···O: 2.653(2) Å; O-H···O = 145.4(5)°), accordingly to the Etter's rules[39](*Figure 28*). Indeed, the energy value of HBs with $R_2^2(12)$ geometry is definitively low (-12.7 kJ/mol), even more than the weak HBs that involve the pyridinic rings (-16.1 kJ/mol). As a further confirmation, even the distances and angles of $R_2^2(12)$ HBs are in the range of weak HBs (O···O: 2.999(2) Å; O-H···O = 123.6(5)°). The molecular arrangement is thus ruled by π···π interactions that generate stacked offset pillars oriented along the a-axis (*Figure 28*). The stacking distances are repeated with a scheme AAB (A: 3.474 Å, B: 3.288 Å), while energy calculations confirmed π···π interactions as the most stabilizing for the crystal packing, with values of -28.3/-28.5 kJ/mol. The absence of

alkyl groups increases the crystal density (1.413 g/cm^3) of **10**, which is comparable with **1** polymorphs and **5**.

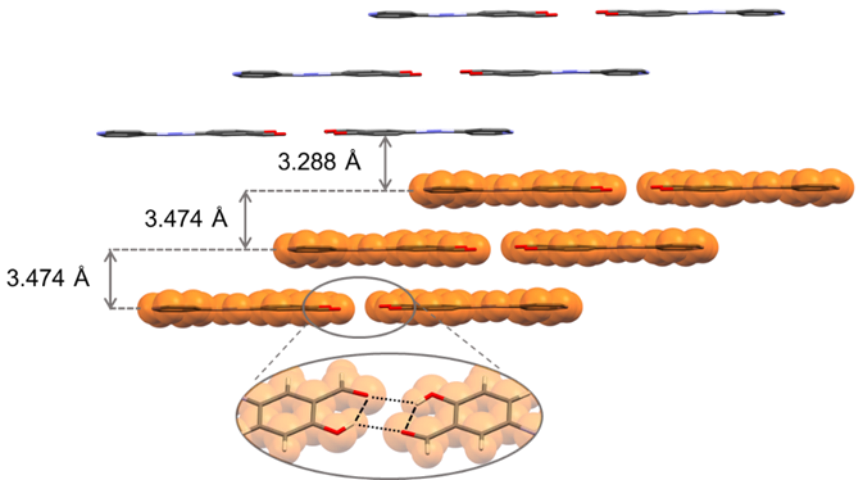

Figure 28. *Molecular arrangements in **10** crystal structure driven by π···π and hydrogen bond interactions. The intramolecular hydrogen bonds are emphasized with black dashed lines, while the weaker intermolecular hydrogen bonds with black dotted lines.*

AZP **11**

AZP **11** crystallizes in P-1 space group with two formula units in the asymmetric unit (Z = 4, Z' = 2). The acidic nature of the carboxylic group combined with the basic one of the pyridinic ring provide a zwitterion character to all the molecules in **11** crystal structure. Therefore, the main interactions which drive the molecular arrangement are the pure ionic interactions between the carboxylates and the pyridiniums groups of following molecules, by forming chains with head-to-tail motifs. (*Figure 29*, left). It is worth noting that, similarly to **11**, the carboxylate groups are also involved in intramolecular HBs with $S(6)$ geometry together with the phenolic groups (O···O: 2.520(2) Å; O-H···O = 147.9(5)°). The ionic interactions, in combination with π···π interactions, are also responsible for the formation of

stacked offset pillars, which run along the (011) crystallographic planes (*Figure 29*, right). Energy calculations evidence much stronger molecule-molecule interactions, compared with the other AZP coformers, as expected for the presence of pure ionic interactions. For instance, the energies between consecutive molecules in chain motifs are -153.6 kJ/mol, while the energies between stacked molecules result in the range -158.7/-163.8 kJ/mol. In this case, the strong interactions even influence the crystal density (1.503 g/cm^3), which reaches the highest value among AZP coformers.

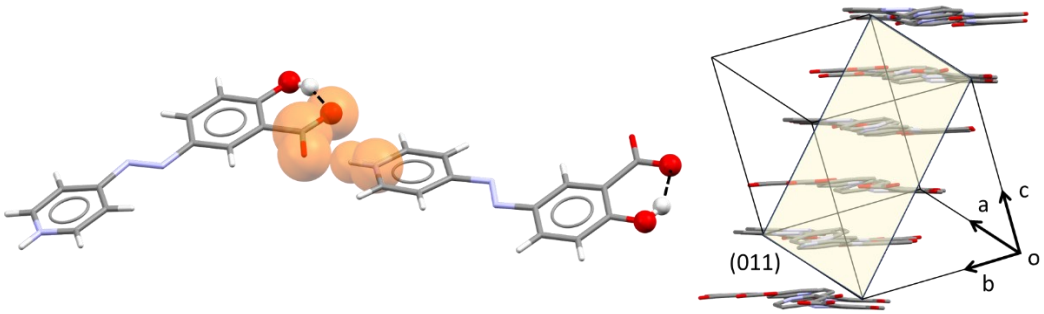

Figure 29. *Left: representation of the main intermolecular interactions between two consecutive molecules in* ***11*** *crystal structure. Pure ionic interactions are emphasised by superimposing van der Waals surfaces on the carboxylate and pyridinium groups. The intramolecular hydrogen bonds are emphasized with black dashed lines, while the weaker intermolecular hydrogen bonds with black dotted lines. Right: molecular arrangements in* ***11*** *crystal structure oriented along the crystallographic plane (011). Hydrogen atoms are omitted for sake of clarity.*

3.1.4 Crystal lattice energy and polymorphs stability

The existence of different polymorphic phases is an important aspect to take into account for defining the physical properties of solid-state materials. The competition between supramolecular synthons, molecular flexibility, or enhanced thermal motion are some of the most relevant factors that raise the probability of having different polymorphic phases for a certain molecule. For AZP coformers, the presence of alkyl chains certainly contributes to the existence of several polymorphic phases, such as in the case of AZP **2**, **6**, and **7** (see paragraph 3.1.3 "Crystal structures"). Instead, the two polymorphs of AZP **1**, which do not have any alkyl chain, differ for the formation of π···π networks or T-shape C-H···π interactions (*Figure 23*, right). The stability of AZP coformers was thus evaluated comparing the lattice energies with the results of thermal analyses and variable-temperature powder X-ray diffraction (VT-PXRD) experiments.

Table 3. *Calculated crystal lattice energies for AZP coformers.*

AZP	Lattice energy (kJ/mol)
1a	-140.35
1b	-142.50
2a	-151.00
2b	-157.05
3	-162.45
4	-178.75
5	-151.40
6a	-154.65
6b	-145.25

6c	-137.87
7a	-166.20
7b	-163.95
7c	-170.15
8	-188.05
9	-148.90
10	-126.60
11	-176.20

The analysis of the lattice energies of AZP coformers shows an increase in stability (lower values of lattice energy) in step with the increase either of the number of alkyl substituents or with the length of alkyl chains (*Table 3*). For instance, AZP coformers with alkyl chains of 10 carbon atoms (**4**, **8**) are more stable than AZP with 8 carbon atoms alkyl chains (**3**, **7**), in their turn more stable than 6 carbon atoms alkyl chains (**2**, **6**). Also, AZP coformers **6**, **7**, **8** have a further methyl group than respectively AZP **2**, **3**, **4**, and thus lower lattice energies. This effect is the consequence of the higher number of weak interactions that can be established among the alkyl groups. Instead, the high stability of AZP **11** is rather due to the strong ionic interactions between the carboxylate and pyridinium groups (*Figure 29, left*).

AZP **1a** crystallized from H_2O at the end of the synthetic procedure but did not show any conversion towards the **1b** phase upon heating. The thermogram showed an exothermic event at 161.93 °C, probably due to a partial recrystallization of the amorphous content, followed by the decomposition of the sample around 250 °C (*Figure 30*).

Table 4. *Summary of the thermal event that occurred during the DSC measurement of AZP* ***1a****.*

AZP	*Run*		*Thermal event*	*Temperature (°C)*	*ΔH (J/g)*
1a	First heating	1st peak	Exothermic	161.93	-82.78
		2nd peak	Endothermic	--	--

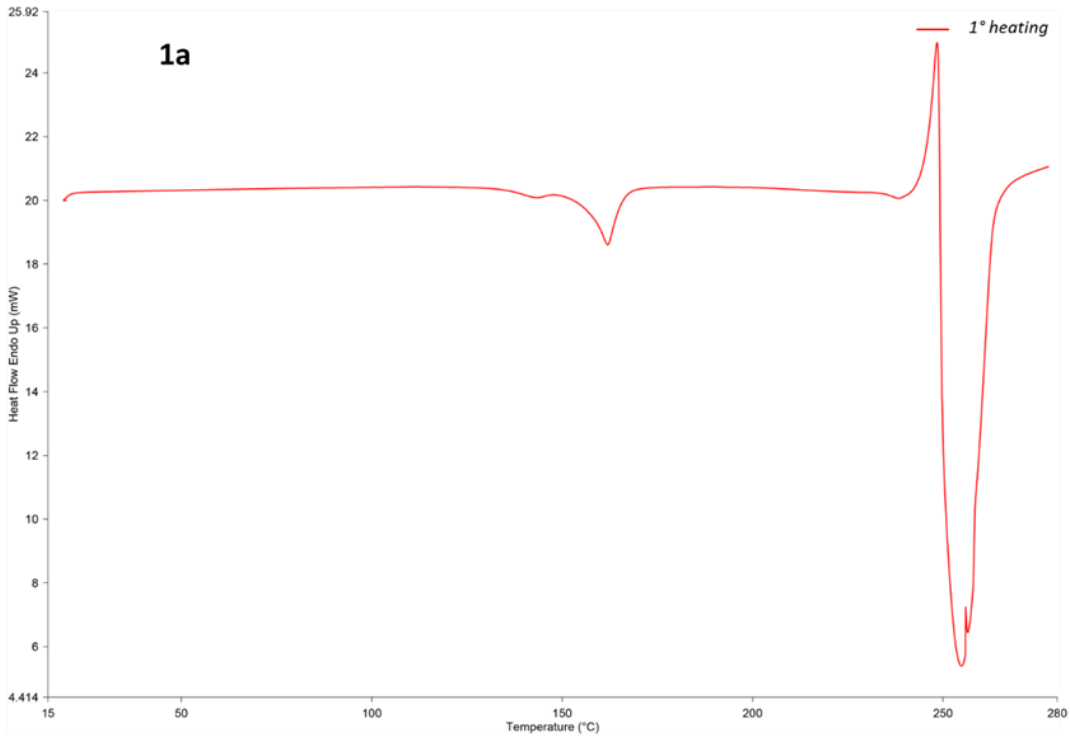

Figure 30. *Thermogram of AZP* ***1a****.*

AZP **2a** crystallized from ethyl acetate and showed a melting point of 56.22 °C (*ΔH = 114.14 J/g*), due to the endothermic peak in the first heating of its thermogram (*Figure 31*). During the cooling run, the melted phase recrystallized into **2a** polymorph (*ΔH = -110.94 J/g*), as confirmed by the endothermic peak in the second heating that referred to the melting of **2a** (T_m *= 55.40 °C, ΔH = 109.48 J/g*). To validate this hypothesis, a VT-PXRD analysis was performed by heating the sample

up to 100 °C, cooling it down to 5 °C, and then thermalizing at 20 °C. The powder pattern collected at 20 °C demonstrated that the crystalline phase was effectively AZP **2a**, as shown by the Pawley refinement (*Figure 32*). The recrystallization of **2a** pointed out that the experimental conditions favoured the metastable polymorph since a more stable polymorph **2b** was found (*Table 3*).

Table 5. *Summary of the thermal events that occurred during the DSC measurement of AZP* ***2a****.*

AZP	*Run*		*Thermal event*	*Temperature (°C)*	*ΔH (J/g)*
	First heating	1st peak	Endothermic	56.22	114.14
2a	First cooling	1st peak	Exothermic	43.90	-110.94
	Second heating	1st peak	Endothermic	55.40	109.48

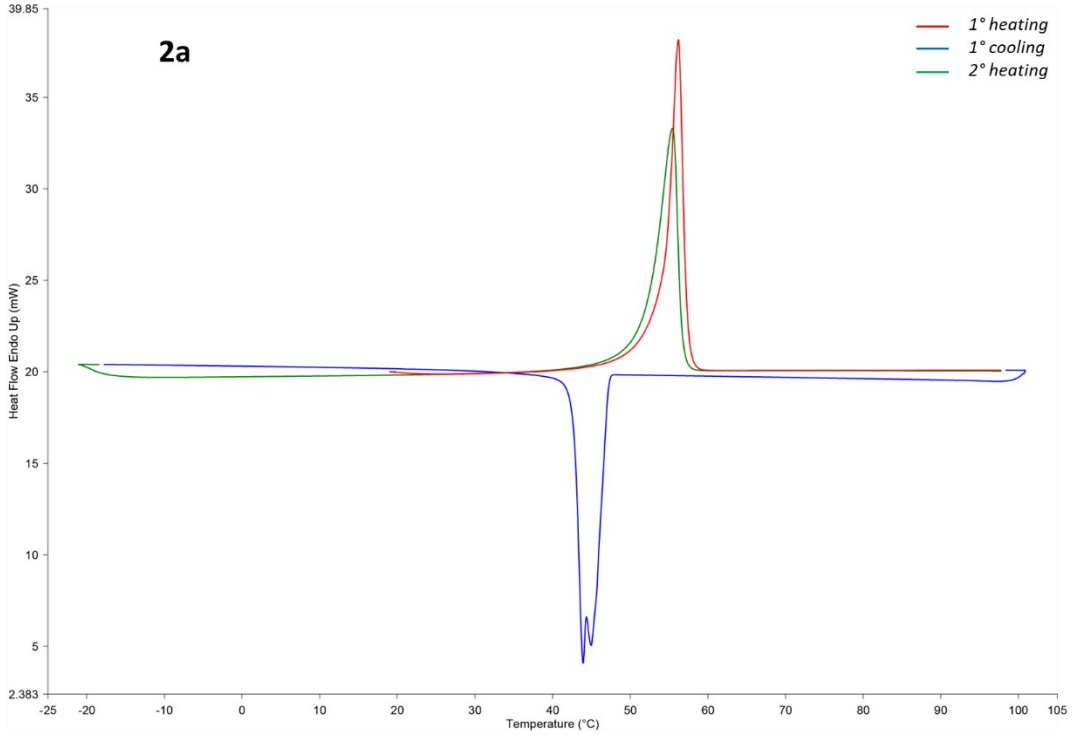

Figure 31. *Thermogram of AZP* ***2a****.*

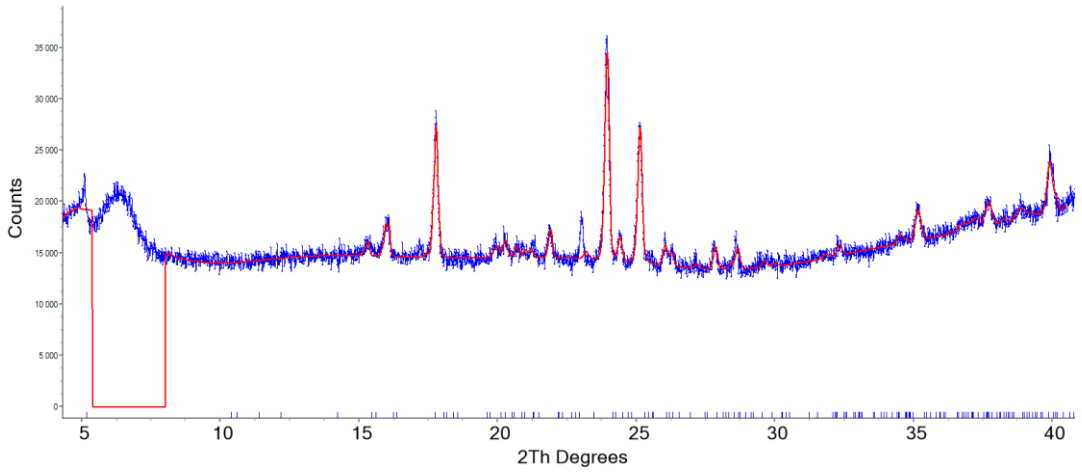

Figure 32. *Pawley fit of AZP* ***2a*** *(red line) against experimental data (blue dots). The powder pattern was collected at 20°C during the VT-PXRD measurement. Tick marks indicate calculated reflection positions. The 2θ region from 5.40 to 8 was excluded from the refinement due to the presence of an amorphous contribution from the experimental setup.*

AZP **6b** crystallized from H_2O and showed a melting point of 55.83 °C (*ΔH = 114.14 J/g*), due to the endothermic peak in the first heating of its thermogram (*Figure 33*). In this case, the crystallization of another polymorph occurred in the cooling run (*ΔH = -113.97 J/g*), confirmed by the melting of this polymorph in the second heating run at 40.72 °C (*ΔH = 45.51 J/g*). Meanwhile to the melting of the new polymorph, an exothermic event took place related to the recrystallization of **6b** polymorph, followed by an endothermic peak due to the melting of **6b** at 55.72 °C (*ΔH = 91.51 J/g*). To identify the unknown polymorphic phase, a VT-PXRD experiment was performed in the same conditions used for **2a** polymorph, since the purpose was to best replicate the experimental conditions of their thermal analyses. The powder pattern collected at 20 °C, at the end of the firing profile, corresponded to the **6c** polymorph (*Figure 34*). Lattice energies underlined that

both **6b** and **6c** were metastable polymorphs (*Table 3*) since a more stable phase (**6a**) was obtained by synthesis.

Table 6. *Summary of the thermal events that occurred the during DSC measurement of AZP* ***6b****.*

AZP	*Run*		*Thermal event*	*Temperature (°C)*	*ΔH (J/g)*
6b	First heating	1st peak	Endothermic	55.83	123.89
	First cooling	1st peak	Exothermic	23.56	-113.97
	Second heating	1st peak	Endothermic	40.72	45.51
		2nd peak	Exothermic	42.83	-18.38
		3rd peak	Endothermic	55.72	91.51

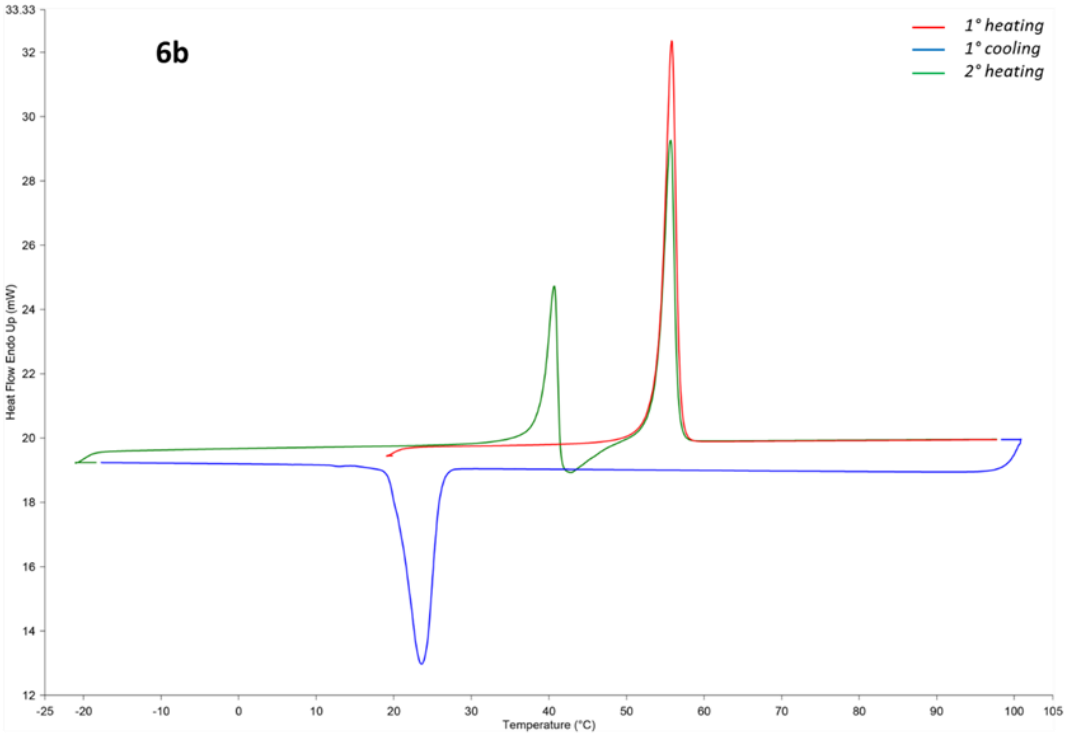

Figure 33. *Thermogram of AZP* ***6b****.*

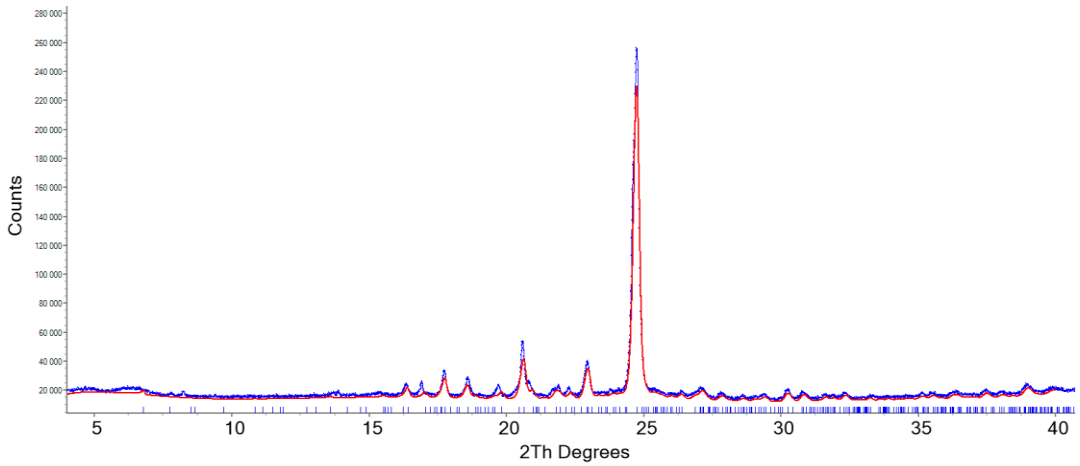

Figure 34. *Pawley fit of AZP* ***6c*** *(red line) against experimental data (blue dots). The powder patter was collected at 20°C during the VT-PXRD measurement. Tick marks indicate calculated reflection positions.*

AZP **7c** crystallized from acetonitrile and showed a melting point of 47.67 °C (*ΔH = 156.54 J/g*), due to the endothermic peak in the first heating of its thermogram (*Figure 35*). During the cooling run, the crystallization of another polymorph occurred, as shown by the exothermic peak (*ΔH = -120.90 J/g*), followed by the melting of this new polymorph in the second heating run at 44.68 °C (*ΔH = 134.93 J/g*). As done for AZP **6b**, a VT-PXRD analysis was carried out to identify the unknown polymorphic phase, by employing the same firing profile. The Pawley refinement of the final powder pattern, collected at 20 °C, revealed the presence of **7b** polymorph (*Figure 36*). Although **7c** was the more stable polymorph, the kinetics of the thermal analyses favoured the crystallization of the metastable phase **7b**. Moreover, another metastable phase (**7a**) was obtained by slow evaporation from acetonitrile.

Table 7. *Summary of the thermal events that occurred during the DSC measurement of AZP* ***7c****.*

AZP	*Run*		*Thermal event*	*Temperature (°C)*	*ΔH (J/g)*
	First heating	1st peak	Endothermic	47.67	156.54
7c	First cooling	1st peak	Exothermic	20.59	-120.90
	Second heating	1st peak	Endothermic	44.68	134.93

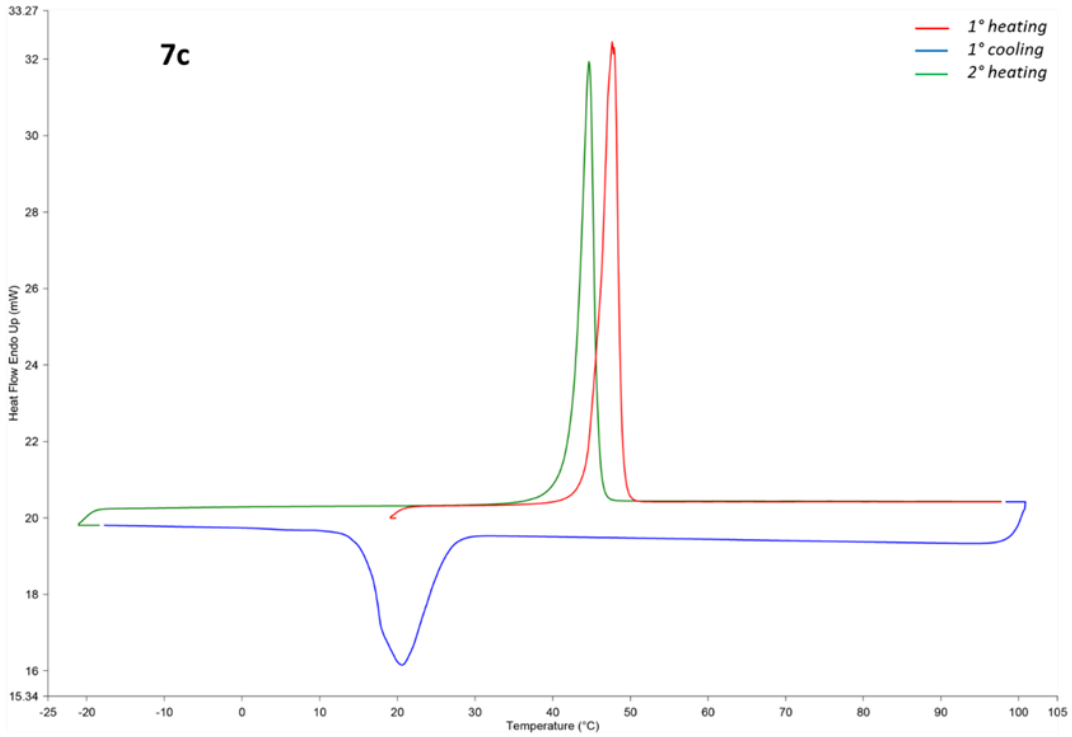

Figure 35. *Thermogram of AZP* ***7c****.*

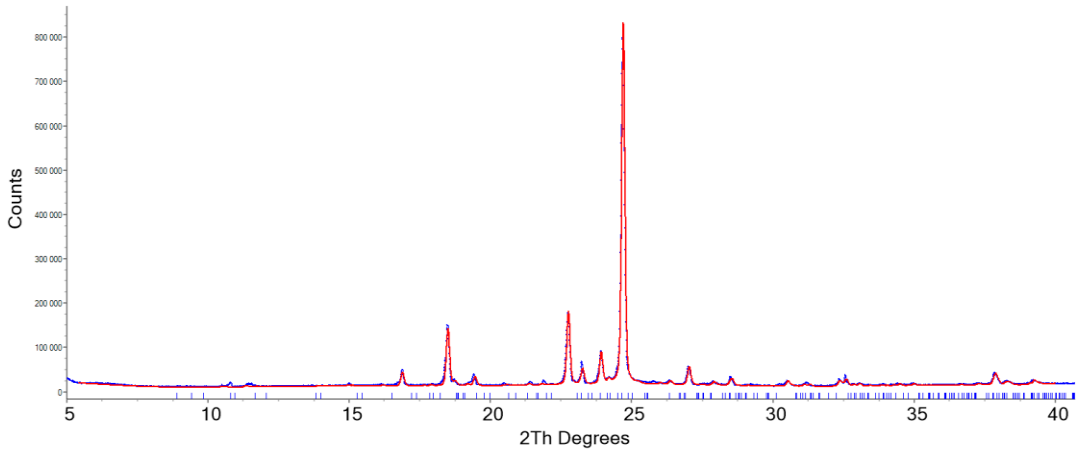

Figure 36. *Pawley fit of AZP* ***7b*** *(red line) against experimental data (blue dots). The powder patter was collected at 20°C during the VT-PXRD measurement. Tick marks indicate calculated reflection positions.*

3.1.5 Density and close packing

The isomerization of azo bonds in solid-state occurs whether a certain "free volume" is accessible for rotation or inversion mechanisms. Crystalline materials are characterized by efficient arrangements that tend to reduce the free volume, maximising the intermolecular interactions. These conflicting aspects were balanced by designing AZP coformers with alkyl chains and methyl substituents on the aromatic rings. In order to evaluate the effective "free volume" within the crystal structure of AZP coformers, density and close packing calculations were carried out.

A typical misconception concerning density assumes that higher densities arise from efficient close packing. Actually, density depends on the weight of the atoms and the number of covalent bonds they are able to establish[40]. Indeed, covalent

bonds are a straightforward and successful way to bring atoms closer than the sum of their van der Waals radii. The "free volume" within the crystal structure is thus better related to the close packing concept. Close packing C_K is defined as the ratio between the crystal density D_C and the intrinsic density D_M:[41]

$$D_C = \frac{Z \cdot M_W}{V_{cell}}, \qquad D_M = \frac{M_W}{V_M}, \qquad \frac{D_C}{D_M} = \frac{Z \cdot V_M}{V_{cell}} = C_K$$

where Z is the number of formula units in the unit cell, V_{cell} is the volume of the unit cell, M_W the molecular weight, and V_M the molecular volume.

From accurate statistics on the CSD, experimental packing coefficients are usually very close to 0.7, independently from the chemical composition. However, the presence of alkyl or nitrile groups has shown a reduction of the packing coefficient[42]. The same behaviour is observed for AZP cofomers, where the lowest values of packing coefficient are achieved by coformers with alkyl chains (*Figure 37*). The presence of a further methyl group on the AZP **5**, **6**, **7**, **8**, instead, does not give significant differences with respect to the corresponding AZP **1**, **2**, **3**, **4** without the methyl group. It is noteworthy that AZP **9** exhibits the lowest packing coefficient ($C_K = 0.60$) even though it does not have any alkyl chain. In this case, the decrease in close packing is due to the combination of isopropyl and methyl substituents on the phenolic ring. These considerations on close packing efficiency are thus in agreement with the designed properties of AZP coformers.

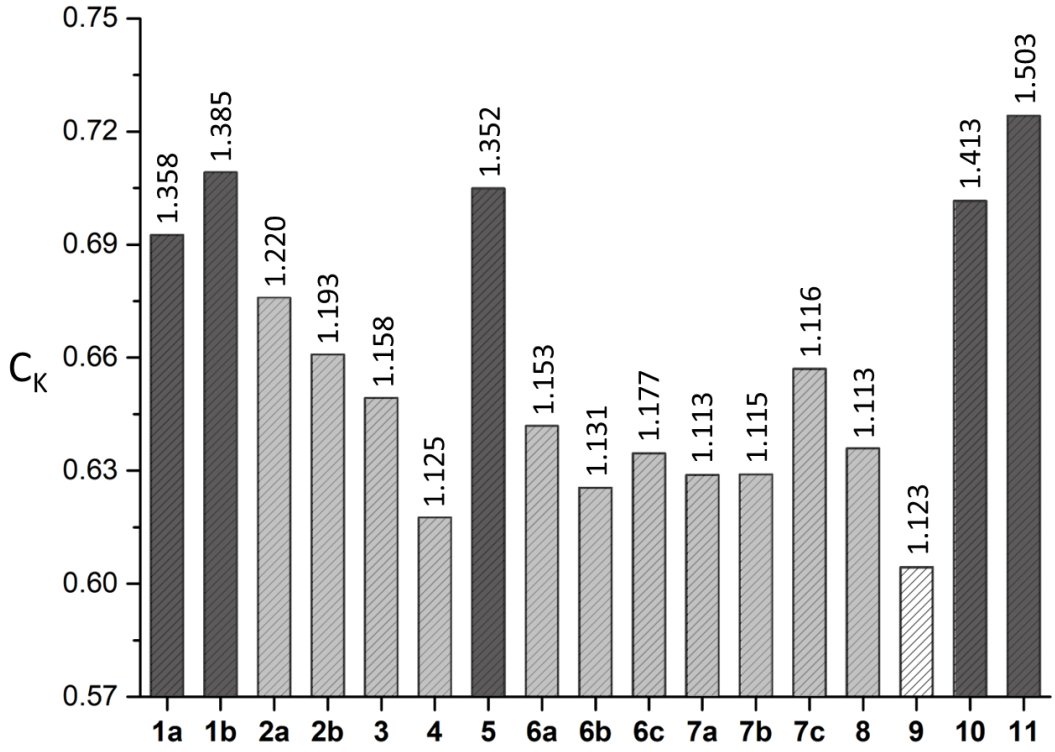

Figure 37. *Plot of packing coefficients C_K for AZP coformers. Bars are depicted in light grey for AZP coformers with alkyl chains, dark grey for not alkylated AZP coformers, and white for AZP* ***9****. On each bar is reported the density value at 293 K, except for AZP* ***2b*** *at 150 K.*

3.2 Synthesis of cocrystals with essential oils

Cocrystals were obtained by reacting AZP coformers with five selected active ingredients extracted from the complex mixtures of essential oils: thymol (THY), carvacrol (CAR), eugenol (EUG), vanillin (VAN), and β-thujaplicin (TJP) (*Figure 38*). These natural ingredients, named as EOs for the sake of simplicity, were chosen for their antimicrobic and antioxidant properties, as well as for the presence of HB

acceptor and donor groups. Each EO was combined with all the AZP coformers in a stoichiometric ratio of 1:1. Indeed, the selected EOs had only the phenolic group as a strong HB donor to potentially interact with the pyridinic nitrogen of AZP, acting as HB acceptor. Cocrystals syntheses were carried out through mechanochemical methods, such as mortar and pestle, vibrational ball mill, or planetary ball mill. Liquid-assisted grinding was also performed to obtain more fast and complete conversions into cocrystals. Grinding reactions took from 15 to 30 min and the resulting powders were analysed through PRXD in order to confirm the formation of cocrystals (*Appendix B.1*). The results of the cocrystals screening were reported in *Table 8*.

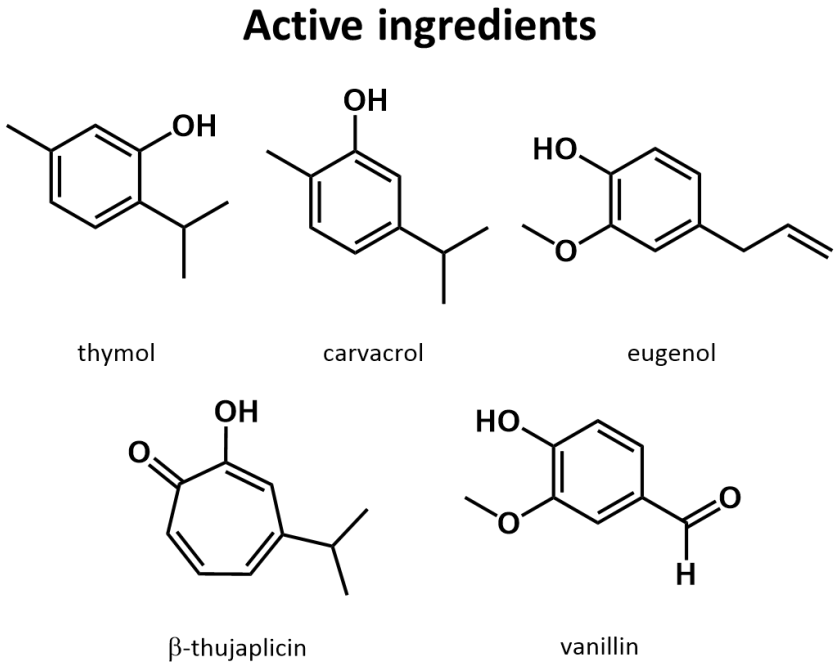

Figure 38. *Chemical structure of the selected active ingredients of essential oils.*

Table 8. *Results of the mechanochemical cocrystallizations between essential oils and azopyridinic coformers.*

AZP	THY	CAR	EUG	VAN	TJP
1	✗	✗	✗	✗	✗
2	✓	✓	✓	✓	✓
3	✓	✓	✓	✓	✓
4	✓	✓	✓	✓	✓
5	✗	✗	✗	✗	✗
6	✓	✓	✗	✓	✗
7	✓	✗	✓	✓	✗
8	✓	✓	✗	✓	✗
9	✓	✗	✗	✗	✗
10	✓	✗	✗	✗	✗
11	✗	✗	✗	✗	✗

To summarize, 23 combinations gave origin to 1:1 cocrystals and the AZP coformers **2**, **3**, and **4** were able to form cocrystals with all the EOs. **6**-CAR, **7**-EUG, and **8**-CAR cocrystals showed 1:2 stoichiometry instead. It is also worth of noting that all the combinations including **1**, **5**, and **11** did not bring to the formation of cocrystals. The reason has to be found in the crystal structures of the AZP coformers, in particular their homomeric synthons: crystal structures of **1** and **5** exhibit strong HB interactions between the phenolic groups and the pyridinic nitrogen atoms, which were the main interactions of the crystal packing (see "*3.1.3 Crystal structures*"). These HB synthons have been already proven as one of the most recurrent among the cocrystal structures collected by the CSD[43], symptomatic of their high stability. Moreover, the likelihood of cocrystallization strongly depends on the mismatch between homomeric and heteromeric interactions, with the latter ones that should be more favourable. In this case EOs present the same phenolic group of **1** and **5**, therefore there is no further stabilization. The same conclusions can be drawn for **11**, whose crystal structure evinces the presence of strong homomeric ionic

interactions between the carboxylates and pyridinium groups, by far more stable than the potential phenolic-pyridinic ones[44]. Finally, AZP **10** might suggest a high potential in forming cocrystals due to its low lattice energy, however the strong intramolecular HBs between the aldehyde and phenolic groups limited the establishment of heteromeric interactions.

The release of pure EOs relies upon the thermal stability and the melting point/vapour pressure of the oils, both contributing to their volatility. The first purpose of cocrystallization was to improve these physical properties, even considering that the EOs carvacrol and eugenol are liquid at room temperature. Within the cocrystal structure, indeed, EOs establish reticular interactions with coformers and their release is affected by these novel heteromeric interactions. For this reason, DSC measurements were performed on the cocrystals obtained by grinding (Appendix B.2). The results pointed out that generally the melting points of the cocrystals were intermediate between the two coformers, in particular the cocrystals containing eugenol and carvacrol revealed a significant stabilization obtaining melting points in the range of 33-47 °C (*Table 9*), compared to the melting points of the pure EOs (*i.e.* respectively -7.5°C and 1.0°C). Also the cocrystal **2**-THY 1:1 exhibited a considerable stabilization with a melting point of 71.8 °C, rather than pure thymol at 50.2 °C, and it was the only case whereby the melting point was higher with respect to both the coformers (*Table 9*, depicted in green). Instead, several cocrystals presented a lower melting point than their coformers (*Table 9*, depicted in red), in particular for solid essential oils. Cocrystals result stable upon thermal cycles of heating until 100 °C and cooling to -20°C, showing the recrystallization of the same crystalline phase or sometimes polymorphic phases.

Table 9. *Melting point of the pure coformers (EOs, AZP) and the synthesized cocrystals. Cocrystals with melting points higher or lower than both coformers are depicted respectively in green or red.*

	pure	THY	CAR	EUG	VAN	TJP
pure		50.2 °C	1.0 °C	-7.5 °C	80.8 °C	52.5 °C
2	56.2 °C	71.8 °C	44.2 °C	36.9 °C	65.7 °C	42.7 °C
3	61.0 °C	41.9 °C	33.6 °C	36.7 °C	67.2 °C	54.13 °C
4	59.2 °C	41.4 °C	44.3 °C	43.4 °C	50.8 °C	52.5 °C
6	55.8 °C	53.1 °C	45.6 °C	/	42.3 °C	/
7	47.7 °C	46.4 °C	/	47.7 °C	60.8 °C	/
8	50.4 °C	41.6 °C	39.8 °C	/	45.6 °C	/
9	dec.	47.1 °C	/	/	/	/
10	166.6 °C	95.2 °C	/	/	/	/

A screening of cocrystallization experiments was performed using several solvents and employing different crystallization techniques (slow solvent evaporation, anti-solvent vapour diffusion, etc.) aiming to obtain suitable single crystals for X-ray diffraction. The crystal structure of six cocrystals was accomplished: **2**-THY 1:1, **3**-THY 1:1, **7**-THY 1:1, **7**-CAR 1:1, **2**-EUG 1:1, and **4**-EUG 1:1.

3.3 Thymol-based cocrystals

2-THY 1:1

AZP **2**-THY cocrystal was obtained by grinding 0.1 mmol of **2** (28 mg) and 0.1 mmol of THY (15 mg) with mortar and pestle for 15 min. The synthesis was also performed using a vibrational ball mill in the following conditions: stainless steel vessel (volume = 5 mL), two stainless steel spheres (diameter = 7 mm), overall loading of 200 mg, 30 Hz of frequency, 20 min of grinding.

The resulting powder was analysed through PXRD to check the purity of the phase (Appendix B1), supported by a Pawley refinement based on the crystal structure collected via SCXRD (*Figure 39*). The cocrystal resulted as the only phase, with no residual peaks detected.

Single crystals of **2**-THY 1:1 were obtained by dissolving ~5 mg of the grinded powder into ~1 mL of CH_2Cl_2. Orange prisms crystallized in a few days through slow solvent evaporation under chemical hood.

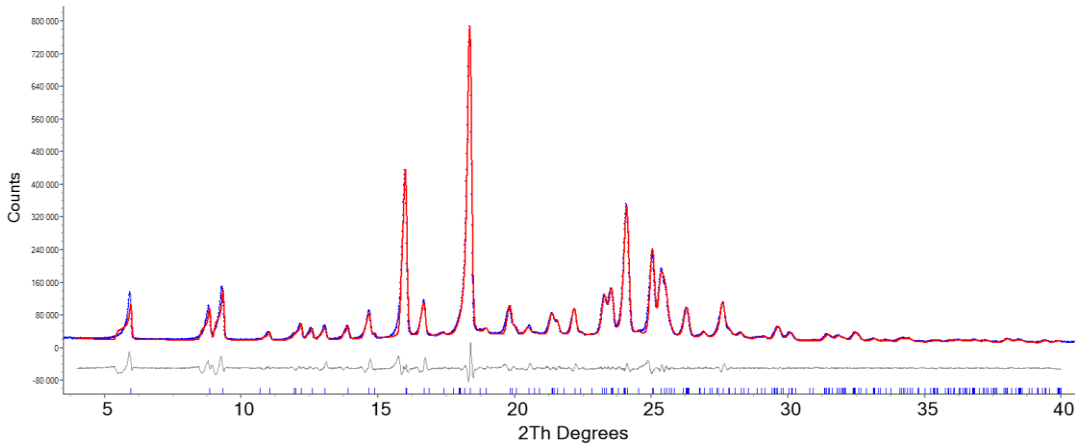

Figure 39. *Pawley fit of **2**-THY 1:1 cocrystal (red line) against experimental data (blue dots). Tick marks indicate calculated reflection positions. Ycalc-Yobs residual curve is reported in grey.*

The thermal behaviour of **2**-THY cocrystal was evaluated performing a DSC measurement. The thermogram showed an endothermic peak at 71.78 °C (*ΔH = 121.59 J/g*) in the first heating, which referred to the melting of the cocrystal, followed by an exothermic peak (*ΔH = -89.52 J/g*) in the cooling run due to its recrystallization. In the second heating a glass transition occurred at 44.55 °C, due to the increase of the specific heat (c_s), while the endothermic peak at 71.80 °C (*ΔH = 120.37 J/g*) confirmed the melting of the cocrystal. Moreover, the cocrystal exhibited a significant higher melting point than the pure thymol (*m.p.* 50.2 °C), confirming the successful stabilization of the essential oil.

Table 10. *Summary of the thermal events that occurred during the DSC measurement of **2**-THY 1:1 cocrystal.*

Cocrystal	*Run*		*Thermal event*	*Temperature (°C)*	*ΔH (J/g)*
2-THY 1:1	First heating	1st peak	Endothermic	71.78	121.59
	First cooling	1st peak	Exothermic	11.74	-89.52
	Second heating	inflection	Increasing of c_s	44.55	/
		1st peak	Endothermic	71.80	120.37

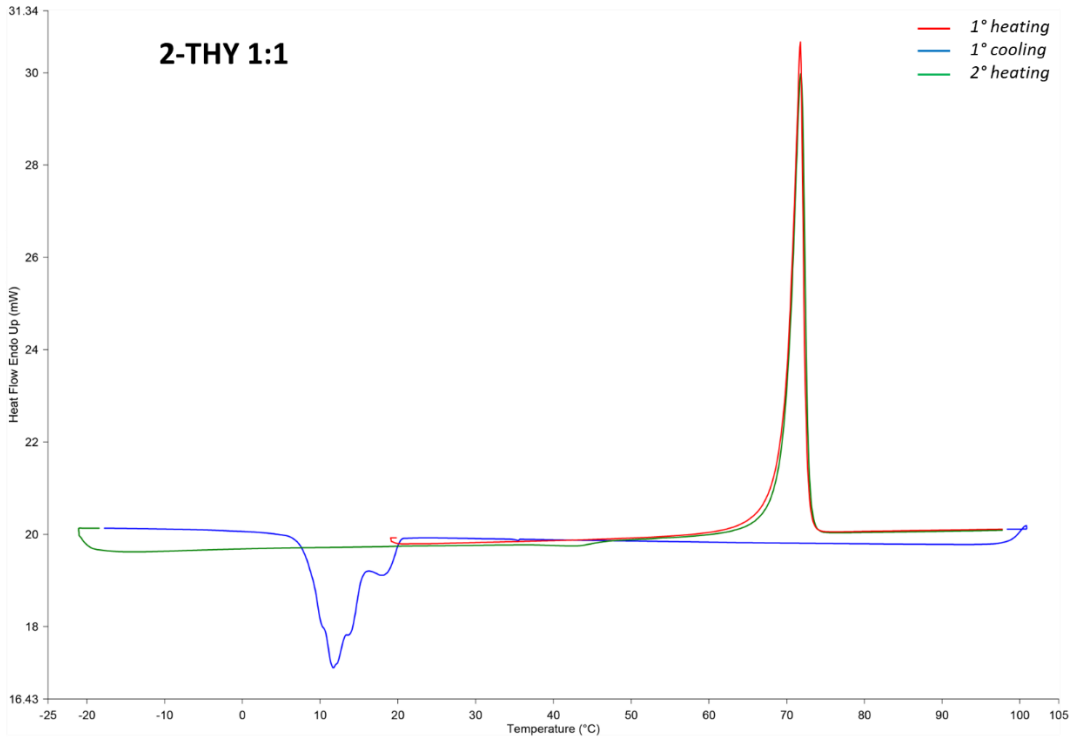

Figure 40. *Thermogram of* ***2****-THY 1:1 cocrystal.*

The crystal structure of **2**-THY cocrystal exhibits P21/c space group, with one formula unit in the asymmetric unit (Z = 4, Z' = 1, Z'' = 2). The two coformers mainly interact through an HB interaction between the phenolic group of THY and the pyridinic nitrogen of **2** (O···N: 2.786(3) Å; O-H···N = 174.1(1)°) (*Figure 41*, left), by forming a dimeric unit. Dimers are thus organized in stacked pillars through the formation of π···π interactions between **2** molecules, which overlap in a head-to-tail configuration (*Figure 41*, right). The so-formed pillars are differently oriented and interact by establishing CH···π interactions among the external THY molecules (*Figure 41*, right). These interactions also contribute to create a V-shape motif among the molecular pillars, in virtue of the dihedral angle (88.34°) between the phenolic ring of THY and the pyridinic ring of **2** in the dimeric unit. The energy calculations confirmed HBs as the driving force of the molecular arrangement together with the π···π interactions, showing molecule-molecule interaction

energies respectively of -65.1 kJ/mol and -67.6 kJ/mol, calculated by Crystal Explorer at CE-B3LYP/6-31G(d,p) level of theory.

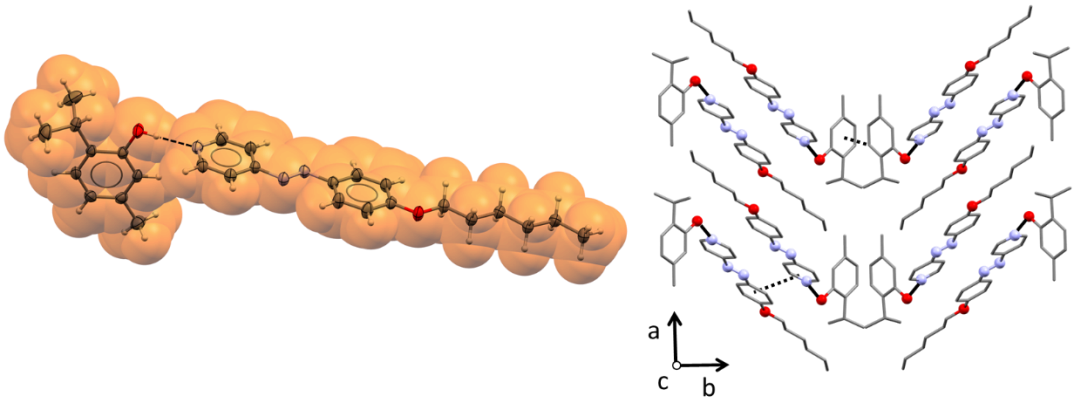

Figure 41. *Left: representation of the asymmetric unit of **2**-THY 1:1 cocrystal. The hydrogen bond is depicted with a black dashed line. Right: molecular arrangements in **2**-THY cocrystal structure driven by hydrogen bonds (solid black lines), π···π, and CH···π interactions (dotted black lines). Hydrogen atoms are omitted for sake of clarity.*

The stimulus-responsive properties of **2**-THY cocrystal were determined by irradiating the sample at 365 nm for different times and measuring the variations in terms of spectroscopic and structural properties. UV-vis measurements were performed as for solid AZP coformers, showing a considerable decrease in terms of absorbance already after 1.5 h, and then a slight decrease until 24 h (*Figure 42*). The shape of the starting spectrum significantly changed after 1.5 h, with a shift of the λ_{max} towards lower values (374 nm → 357 nm). The spectra recorded after irradiation corresponded to **2a** spectra (*Figure 9*, right), demonstrating the release of THY and the remaining of **2a** coformer. It was not possible to conclude that trans-to-cis isomerization occurred since the spectra were not overlapped to appreciate the increasing of cis band, in particular due to the loss of THY contribution after irradiation.

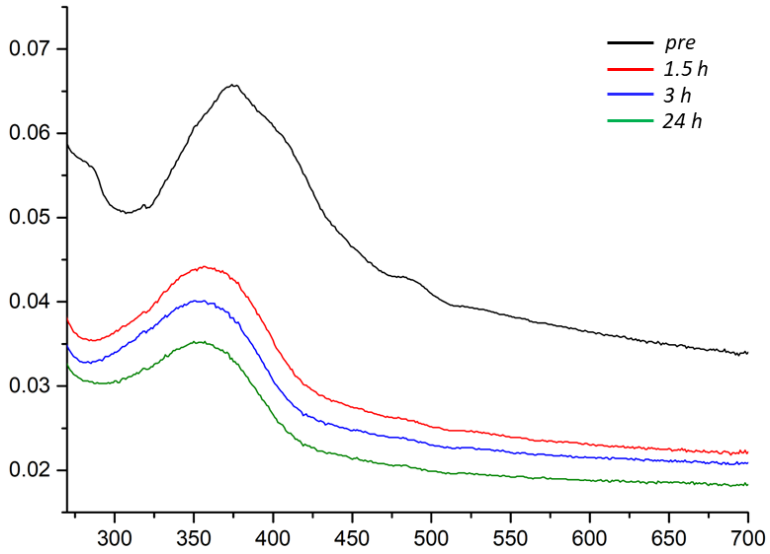

Figure 42. *UV-vis spectra of* ***2****-THY 1:1 cocrystal as thin film.*

The structural changes of **2**-THY cocrystal were evaluated performing PXRD measurements before and after 24 h of irradiation. Samples were prepared on a glass slide and homogeneously distributed on its surface. A higher amount of solid was used with respect to UV-vis spectroscopy to increase the peak intensities and improve the signal to noise ratio.

Powder patterns confirmed the presence of the cocrystal after irradiation, however new peaks appeared at 5.07 and 15.39 2θ, as shown in *Figure 43*. These Bragg reflections corresponded to the trans AZP **2a** coformer, which recrystallized after the irradiation due to a partial release of THY, indeed never detected. The presence of only two peaks was symptomatic of the minimal recrystallization of trans **2a**, while the absence of the other reflections was due to the preferred orientations, that are caused by the oriented glass slide surface and the unit cell of **2a**, characterized by a long c-axis. Preferred orientations also affected the cocrystal intensities.

As well as for the UV-vis measurement, there was no trace of a new phase related to cis isomer.

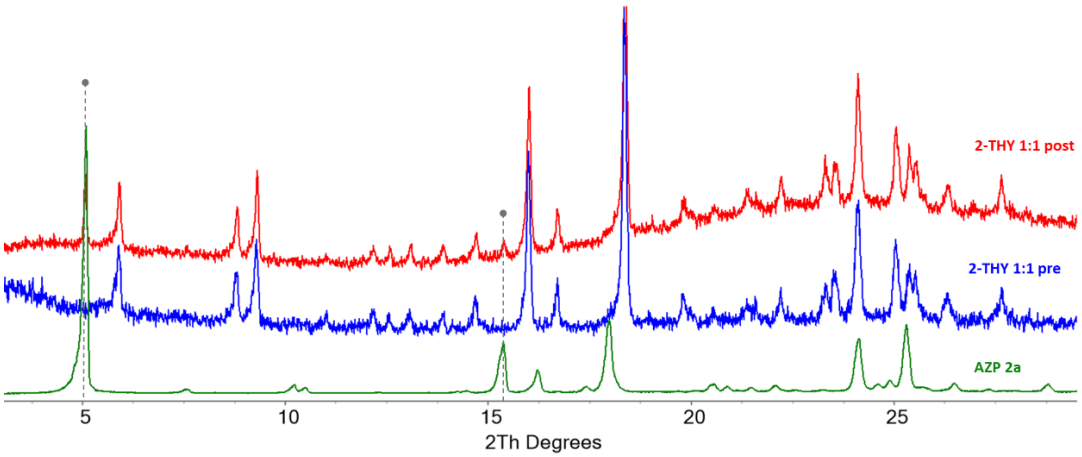

Figure 43. *Comparison of the experimental powder patterns of **2**-THY 1:1 cocrystal before and after 24 h of irradiation at 365 nm with respect to AZP **2a**. Grey arrows highlight the presence of peaks referred to AZP **2a** into **2**-THY cocrystal pattern after the irradiation.*

3-THY 1:1

AZP **3**-THY cocrystal was obtained by grinding 0.1 mmol of **3** (31 mg) and 0.1 mmol of THY (15 mg) with mortar and pestle for 15 min. The synthesis was also performed using a vibrational ball mill, in the same conditions employed for **2**-THY cocrystal.

The resulting powder was analysed through PXRD to check the purity of the phase (Appendix B1), supported by a Pawley refinement based on the crystal structure collected via SCXRD (*Figure 44*). The cocrystal resulted as the only phase, with no residual peaks detected.

Single crystals of **3**-THY 1:1 were obtained by dissolving ~5 mg of the grinded powder first into ~1 mL of acetone, up to saturation, and then adding a few drops of H_20. Orange prisms crystallized in a week through slow solvent evaporation under chemical hood.

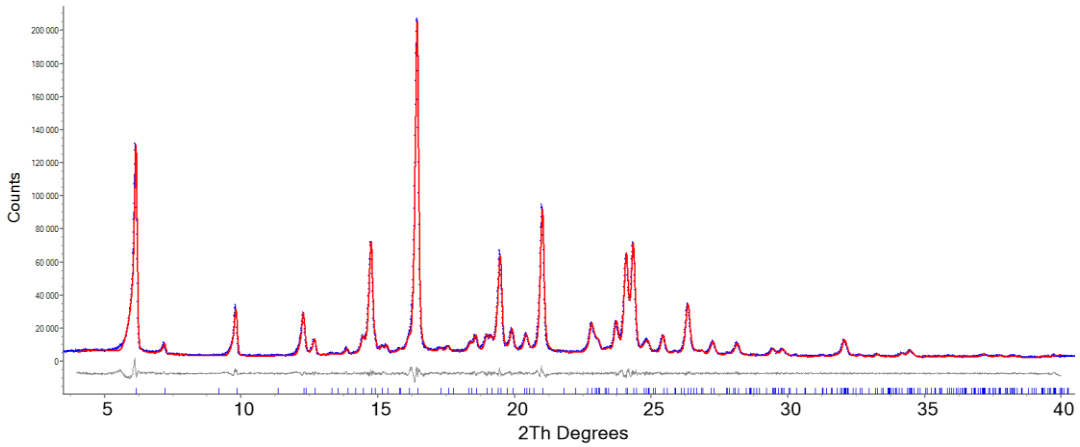

Figure 44. *Pawley fit of **3**-THY 1:1 cocrystal (red line) against experimental data (blue dots). Tick marks indicate calculated reflection positions. Ycalc-Yobs residual curve is reported in grey.*

The thermal behaviour of **3**-THY cocrystal was evaluated performing a DSC measurement. The thermogram showed an endothermic peak at 41.94 °C (*ΔH = 98.07 J/g*) in the first heating, which referred to the melting of the cocrystal. During the cooling run and afterwards in the second heating, two exothermic peaks occurred at 6.41 °C and 35.85 °C (*ΔH = -94.40 J/g*) that were related to the crystallization of a polymorphic phase of **3**-THY cocrystal. This polymorph melted at a higher temperature, as confirmed by the endothermic peak in the second heating at 50.95 °C (*ΔH = 93.53 J/g*). Comparing the enthalpies, the crystallization of the new polymorphic phase from the melt was total.

In this case, the first polymorph evidences a lower melting point than its coformers, while the second phase has a higher melting point than THY, but not than **3**. It is likely that the second polymorph is a more stable phase, however its crystal structure has not been determined yet.

Table 11. *Summary of the thermal events that occurred during the DSC measurement of* ***3****-THY 1:1 cocrystal.*

Cocrystal	*Run*		*Thermal event*	*Temperature (°C)*	*ΔH (J/g)*
3-THY 1:1	First heating	1st peak	Endothermic	41.94	98.07
	First cooling	1st peak	Exothermic	6.41	-69.62
	Second heating	1st peak	Exothermic	35.85	-24.78
		2nd peak	Endothermic	50.95	93.53

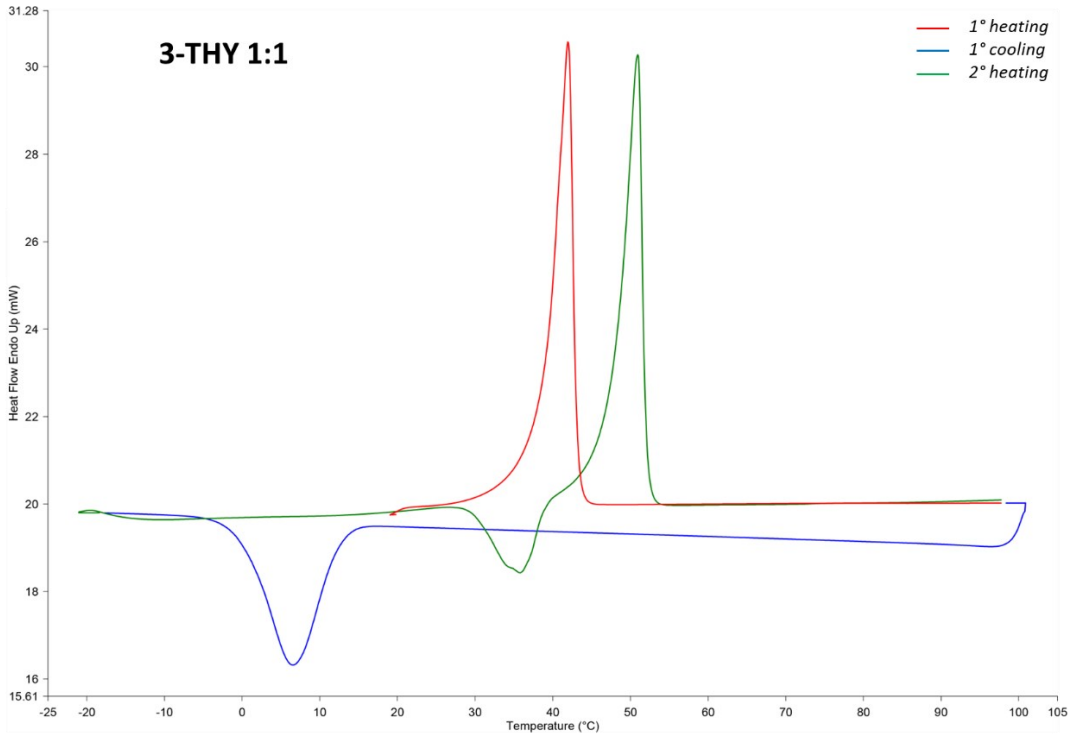

Figure 45. *Thermogram of* ***3****-THY 1:1 cocrystal.*

The crystal structure of **3**-THY cocrystal exhibits P-1 space group, with one formula unit in the asymmetric unit (Z = 2, Z' = 1, Z'' = 2). Similarly to **2**-THY cocrystal, the coformers establish an HB between the phenolic group of THY and the pyridinic nitrogen of **3** (O···N: 2.775(2) Å; O-H···N = 172.8(4)°) (*Figure 46*, left). Even in this case, the molecular arrangement develops through the formation of π···π interactions between **3** molecules, which generate stacked pillars. However, the so-

formed pillars interact mainly by exploiting the π···π interactions among the external THY molecules (*Figure 46*, right). Therefore, the final arrangement is defined by shifted molecular pillars.

The dihedral angles between the phenolic rings of THY and the pyridinic rings of **3** results almost orthogonal (89.81°), as also already observed for **2**-THY dimers. The stacking interactions between **3** molecules mainly contribute to the crystal packing of **3**-THY cocrystal with a value of -70.9 kJ/mol, supported by HB interactions of -61.4 kJ/mol.

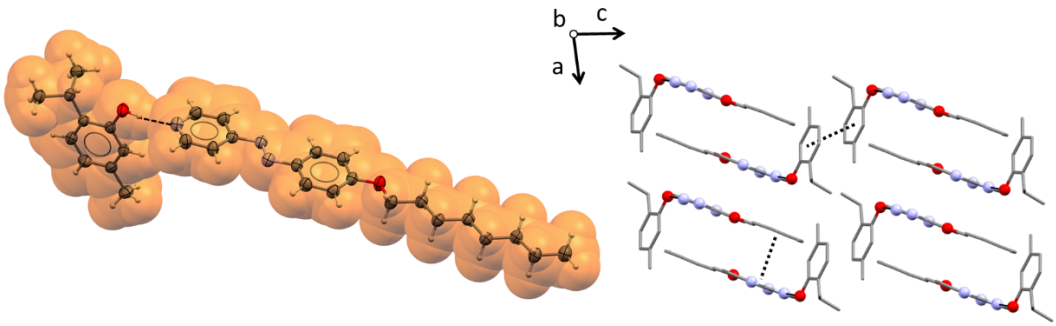

Figure 46. *Left: representation of the asymmetric unit of **3**-THY 1:1 cocrystal. The hydrogen bond is depicted with a black dashed line. Right: molecular arrangements in **3**-THY cocrystal structure driven by hydrogen bonds (solid black lines), and π···π interactions (dotted black lines). Hydrogen atoms are omitted for sake of clarity.*

The stimulus-responsive properties of **3**-THY cocrystal were determined by irradiating the sample at 365 nm for different times and measuring the variations in terms of spectroscopic and structural properties. UV-vis measurements showed a different behaviour rather than **2**-THY cocrystal: the band associated with the trans isomer (π-π*), at 345 nm, slightly decreased meanwhile to the increasing of the absorption in the region above 400 nm (*Figure 47*). It was not completely evident the formation of the cis band (n-π*), likewise the release of THY.

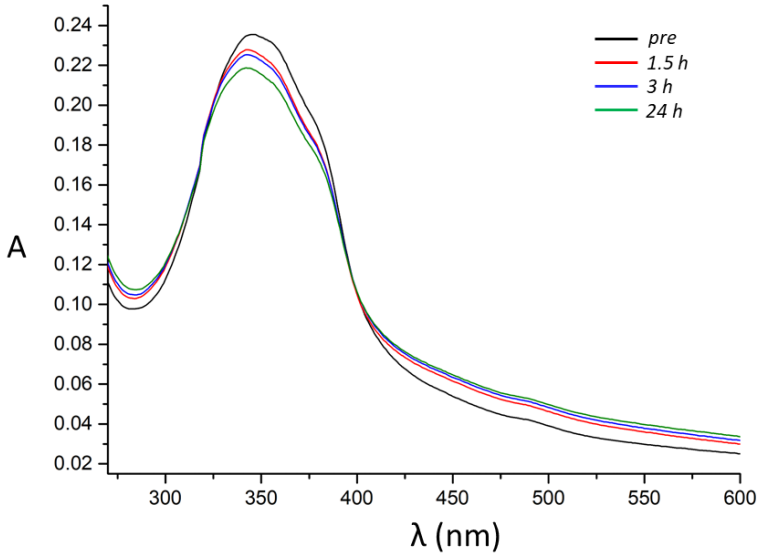

Figure 47. *UV-vis spectra of **3**-THY 1:1 cocrystal as thin film.*

The structural changes of **3**-THY cocrystal were evaluated performing PXRD measurements before and after 24 h of irradiation. Samples were prepared in the same way as **2**-THY cocrystal.

Powder patterns confirmed the presence of the cocrystal after irradiation, as shown in *Figure 48*, as well as the presence of several peaks related to the trans AZP **3** coformer. In this case, almost all the peaks of the AZP coformer are detected, due to a higher starting concentration of the sample and recrystallization upon irradiation. The partial release of thymol from the cocrystal was also confirmed by its lower concentration after the treatment, measured comparing the backgrounds of the powder patterns, as well as for the absence of THY reflections. Moreover, no traces of potentially new phases related to the cis isomer or other species were observed.

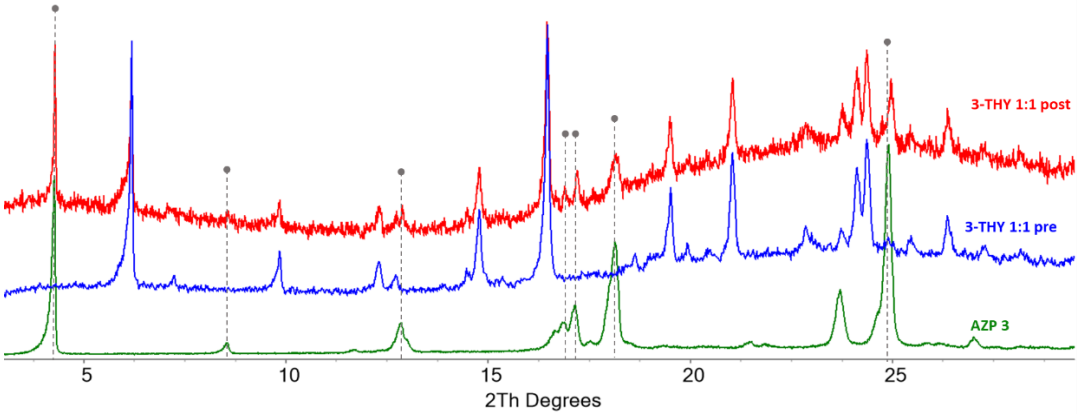

Figure 48. *Comparison of the experimental powder patterns of **3**-THY 1:1 cocrystal before and after 24 h of irradiation at 365 nm with respect to AZP **3**. Grey arrows highlight the presence of peaks referred to AZP **3** into **3**-THY cocrystal pattern after the irradiation.*

7-THY 1:1

AZP **7**-THY cocrystal was obtained by grinding 0.1 mmol of **7** (32 mg) and 0.1 mmol of THY (15 mg) with mortar and pestle for 15 min. The synthesis was also performed using a vibrational ball mill, in the same conditions employed for **2**-THY cocrystal.

The resulting powder was analysed through PXRD to check the purity of the phase (Appendix B1), supported by a Pawley refinement based on the crystal structure collected via SCXRD (*Figure 49*). The cocrystal resulted as the only phase, with no residual peaks detected.

Single crystals of **7**-THY 1:1 were obtained by dissolving ~5 mg of the grinded powder into ~1.5 mL of acetonitrile. Orange prisms crystallized in a few days through slow solvent evaporation under chemical hood.

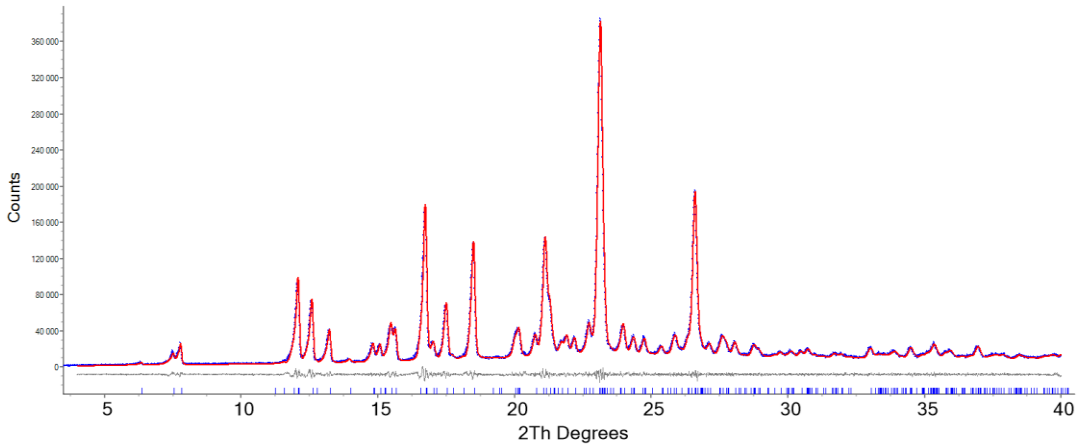

Figure 49. *Pawley fit of **7**-THY 1:1 cocrystal (red line) against experimental data (blue dots). Tick marks indicate calculated reflection positions. Ycalc-Yobs residual curve is reported in grey.*

The thermal behaviour of **7**-THY cocrystal was evaluated performing a DSC measurement. The thermogram showed only an endothermic peak at 46.45 °C (*ΔH = 107.68 J/g*) in the first heating, which referred to the melting of the cocrystal. No crystallization occurred in the following runs. Even in this case, the melting point of cocrystal is lower than the melting point of coformers.

Table 12. *Summary of the thermal event that occurred during the DSC measurement of **7**-THY 1:1 cocrystal.*

Cocrystal	*Run*		*Thermal event*	*Temperature (°C)*	*ΔH (J/g)*
7-THY 1:1	First heating	1st peak	Endothermic	46.45	107.68

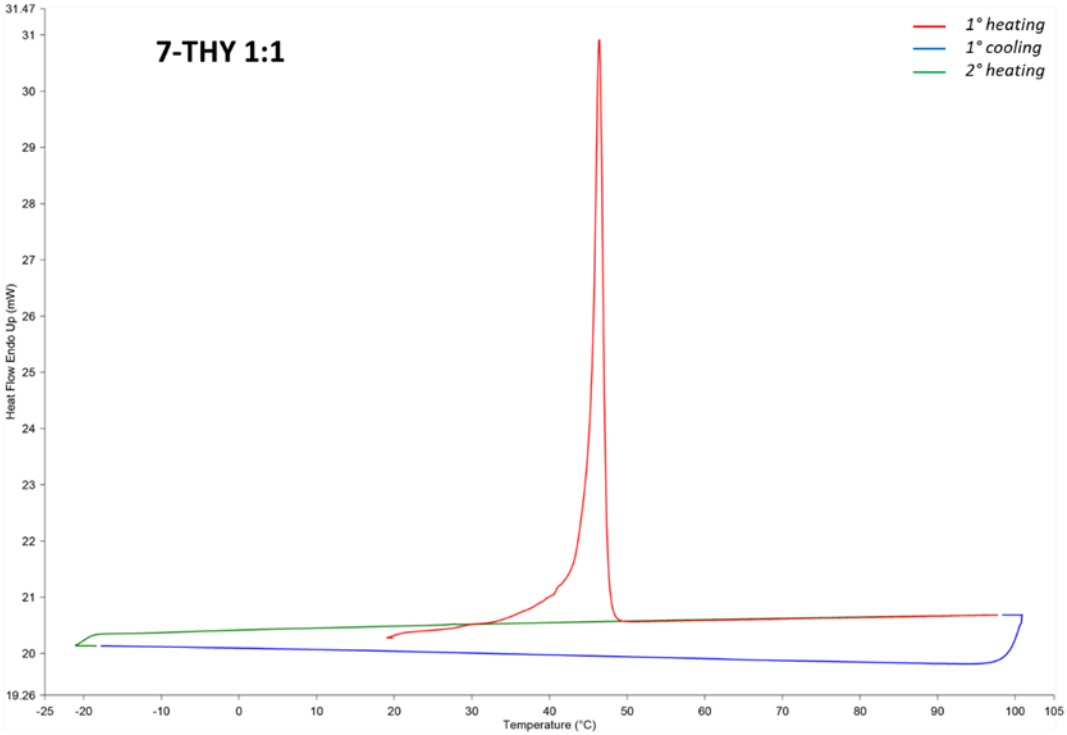

Figure 50. *Thermogram of **7**-THY 1:1 cocrystal.*

The crystal structure of **7**-THY cocrystal exhibits P-1 space group, with one formula unit in the asymmetric unit (Z = 2, Z' = 1, Z'' = 2). As the two previous cocrystals containing THY, a dimeric unit is formed by means of the HB between the phenolic group of THY and the pyridinic nitrogen of **7** (O···N: 2.769(2) Å; O-H···N = 169.5(2)°) (*Figure 51*, left). The molecular organization evidences a great similarity with the crystal structure of **3**-THY cocrystal, also arguably for the difference of only a methyl substituent between **3** and **7** AZP coformers. Indeed, **7** molecules result displayed on the same plane and form stacked pillars by establishing π···π interactions (*Figure 51*, right). The overall arrangement is also constituted by shifted pillars, however in this case they mutually interact through CH···π interactions between the aromatic C-H of **7** molecules and the aromatic rings of THY ones (*Figure 51*, right). A slight difference is observed also in the dihedral angles (83.86°), calculated between the phenolic rings of THY and the pyridinic ring of **7** molecules. Energy calculation

confirmed that the driving force of the crystal packing was a combined effect between HBs (-62.4 kJ/mol) and π···π interactions (-60.3 kJ/mol), which have comparable values.

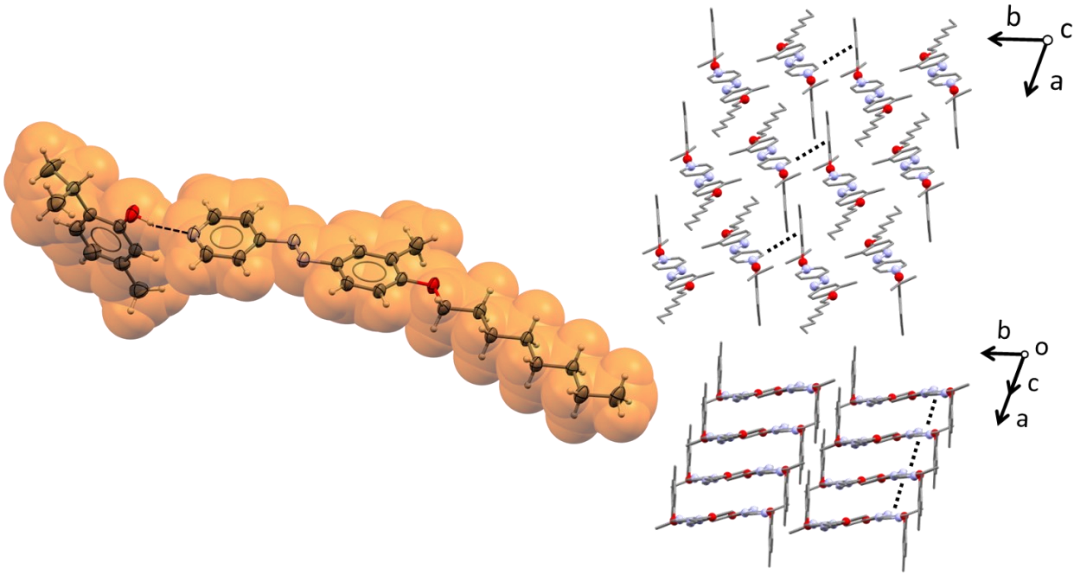

Figure 51. *Left: representation of the asymmetric unit of **7**-THY cocrystal. The hydrogen bond is depicted with a dashed black line. Right: molecular arrangements in **7**-THY cocrystal structure with the emphasis of π···π and C-H···π interactions (dotted black lines). Hydrogen atoms are omitted for sake of clarity.*

The stimulus-responsive properties of **7**-THY cocrystal were determined by irradiating the sample at 365 nm for different times and measuring the variations in terms of spectroscopic and structural properties. UV-vis measurements revealed a similar behaviour with respect to **3**-THY cocrystal, as confirmed by the decrease of the trans isomer band around 369 nm and the increase of the absorption in the region above 413 nm (*Figure 52*). Also the comparison of cocrystal spectra with those of pure AZP **7** coformer (*Figure 14*, left) highlighted some similarities, however while in the case of coformer the trans isomer bands clearly decreased, in the case of cocrystal the whole spectra were shifted towards lower values of

absorbance, due to reduced concentration of the sample. This lower concentration suggests THY release and was more pronounced particularly after 24 h of irradiation.

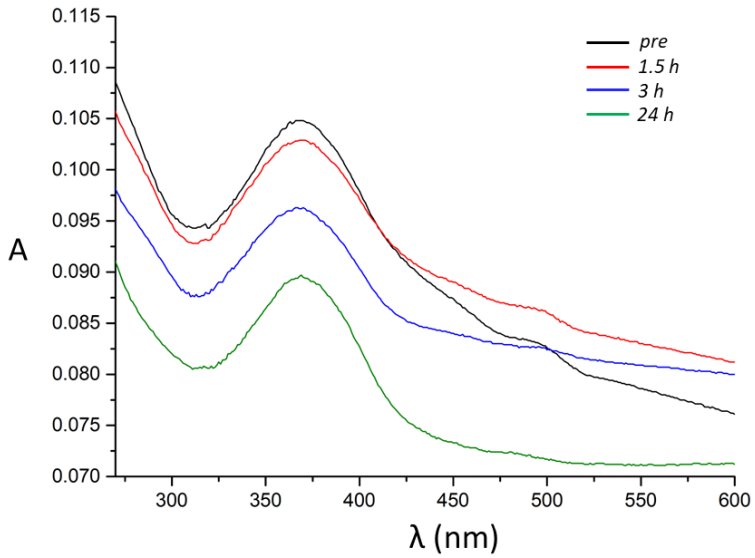

Figure 52. *UV-vis spectra of **7**-THY 1:1 cocrystal as thin film.*

The structural changes of **7**-THY cocrystal were evaluated performing PXRD measurements before and after 24 h of irradiation. Samples were prepared in the same way as **2**-THY cocrystal.

Powder patterns confirmed the presence of the cocrystal after irradiation, as shown in *Figure 53*, and the evidence of new crystalline peaks referring to the trans isomer of AZP **7**, which recrystallized during the irradiation. All the new peaks accounted to the trans form and no proof of other species were detected.

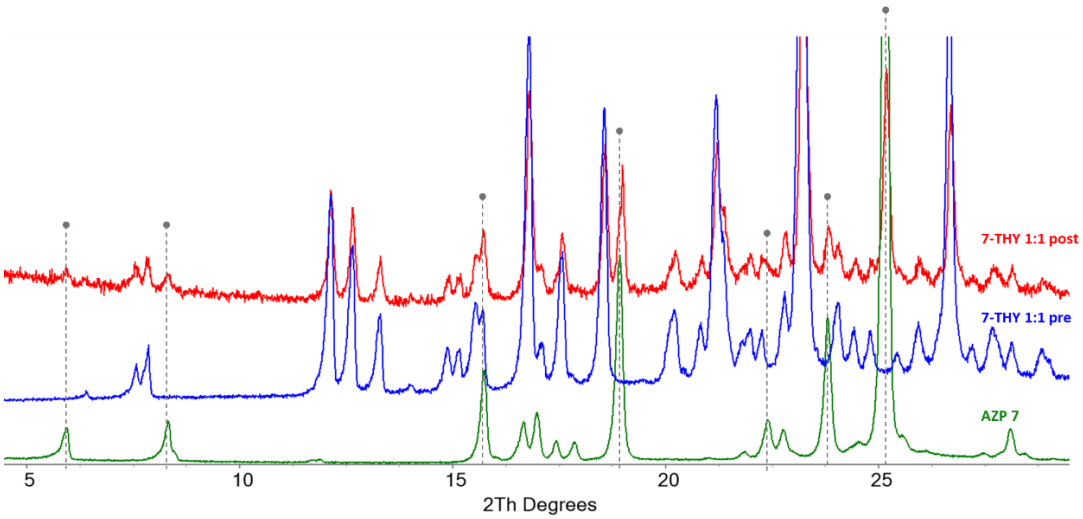

Figure 53. *Comparison of the experimental powder patterns of **7**-THY 1:1 cocrystal before and after 24 h of irradiation at 365 nm with respect to AZP **7**. Grey arrows highlight the presence of peaks referred to AZP **7** into **7**-THY cocrystal pattern after the irradiation.*

3.4 Carvacrol-based cocrystals

3-CAR 1:1

AZP **3**-CAR cocrystal was obtained by direct mixing 0.1 mmol of **3** (32 mg) and 0.1 mmol of CAR (~15 µL) with mortar and pestle for 15 min. The synthesis was also performed using a vibrational ball mill in the following conditions: stainless steel vessel (volume = 5 mL), two stainless steel spheres (diameter = 7 mm), overall loading of 300 mg, 30 Hz of frequency, 20 min of grinding.

The resulting powder was analysed through PXRD to check the purity of the phase, turning out that no residual peaks of coformers were detected thus a cocrystal

phase was obtained (*Figure 54*). However, this crystalline phase did not correspond to the cocrystal phase obtained through SCXRD, therefore it was a new polymorph with 1:1 stoichiometry (**3**-CAR **b**).

Single crystals of **3**-CAR 1:1 **a** were obtained by dissolving ~5 mg of the grinded powder into ~2 mL of EtOH. Orange prisms crystallized in a few days through slow solvent evaporation under chemical hood.

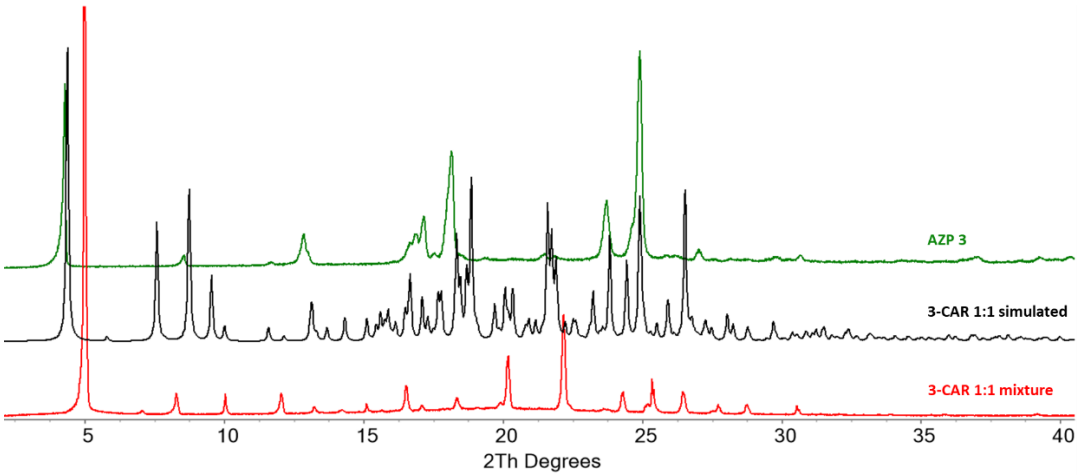

Figure 54. *Comparison of the experimental powder patterns of AZP **3** and the mixture **3**-CAR 1:1 obtained after grinding with the simulated pattern at 200 K of **3**-CAR 1:1 **a** cocrystal obtained through SCXRD.*

The thermal behaviour of **3**-CAR **b** cocrystal was evaluated performing a DSC measurement. The thermogram showed an endothermic peak at 34.45 °C (*ΔH = 37.12 J/g*) in the first heating, which referred to the melting of the cocrystal. The shape of the peak was influenced by the low melting point of the sample, which was close to the starting experimental temperature. In the second heating an exothermic peak occurred (*ΔH = -43.98 J/g*), that was related to the crystallization of a polymorphic phase of **3**-CAR **b** cocrystal. This polymorph melted at a lower temperature, as confirmed by the endothermic peak in the second heating at 33.28 °C (*ΔH = 37.20 J/g*), and totally crystallized from melt. The higher melting points of

both polymorphs rather than the pure CAR (m.p. 1°C) contribute to the stabilization of the essential oil.

Table 13. *Summary of the thermal event that occurred during the DSC measurement of* ***3****-CAR* ***b*** *cocrystal.*

Cocrystal	*Run*		*Thermal event*	*Temperature (°C)*	*ΔH (J/g)*
3-CAR 1:1	First heating	1st peak	Endothermic	34.45	37.12
	Second heating	1st peak	Exothermic	5.35	-43.98
		2nd peak	Endothermic	33.28	37.20

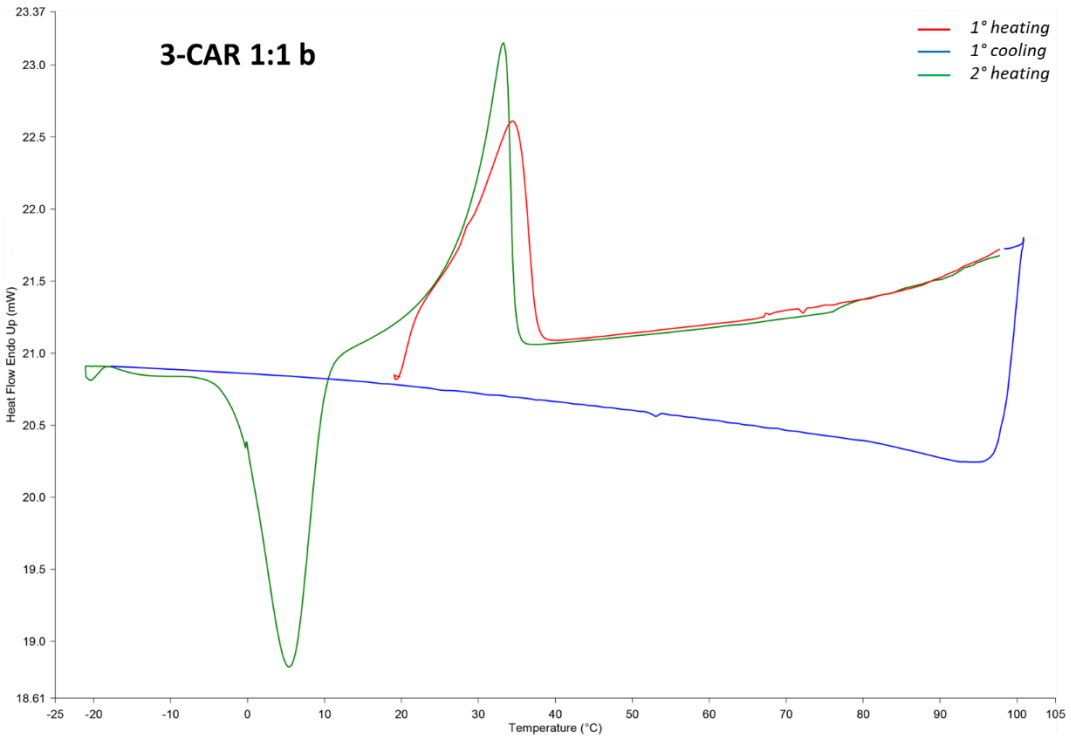

Figure 55. *Thermogram of* ***3****-CAR 1:1* ***b*** *cocrystal.*

The crystal structure of **3**-CAR **a** cocrystal exhibits P21/n space group, with two formula units in the asymmetric unit (Z = 8, Z' = 2, Z'' = 4). As expected, the coformers mainly interact exploiting the HB interaction between the phenolic group of CAR and pyridinic nitrogen of **3** (HB_1: O···N: 2.787(4) Å; O-H···N = 168.1(4)°;

HB_2: O···N = 2.738(4) Å, O-H···N = 169.8(4)°) (*Figure 56*), forming a dimeric unit. The presence of two dimers in the asymmetric unit are significative of some difficulty in optimize all the intermolecular interactions by CAR and **3** molecules. This is also supported by the higher thermal motion of the isopropyl groups and the alkyl chains. Nevertheless, dimers are organized in tetramers by establishing π···π interactions among **3** molecules, which overlap in a head-to-tail configuration (*Figure 57*). Tetramers develop along the a-direction through dispersive interactions, while result displayed in interlocked motifs on the (011) crystallographic planes (*Figure 57*). These motifs are mostly stabilized thanks to π···π and C-H···π interactions among the aromatic ring of THY molecules and respectively the aromatic bone or the C-H alkyl group of **3** molecules. Even in this case, HB and π···π interactions evinced similar values in terms of molecule-molecule interaction energies (HB_1: -61.2 kJ/mol, HB_2: -65.1 kJ/mol, stacking: -61.6 kJ/mol), mostly contributing to the crystal packing. Moreover, the dihedral angles between the phenolic rings of CAR and the pyridinic rings of **3** molecules are lower than the previous cocrystals (θ_1: 67.58°, θ_1: 74.94°).

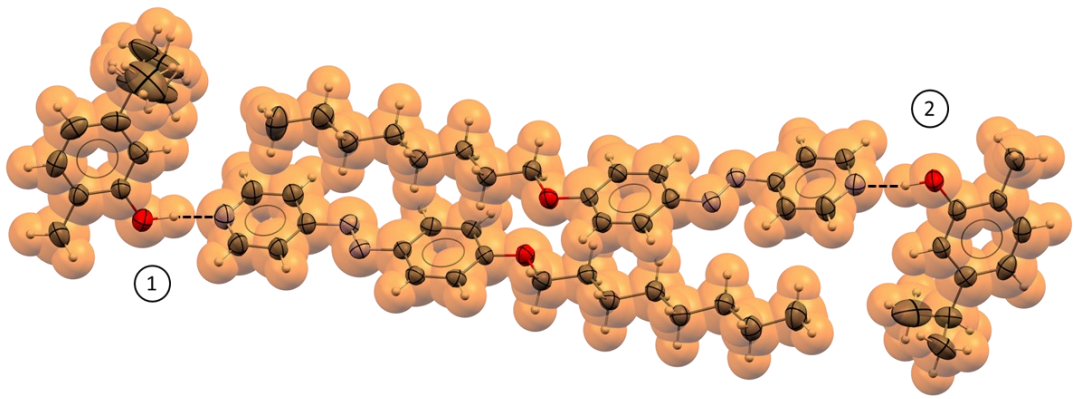

Figure 56. *Representation of the asymmetric unit of **3**-CAR **a** cocrystal. The two hydrogen bonds are depicted with a black dashed line.*

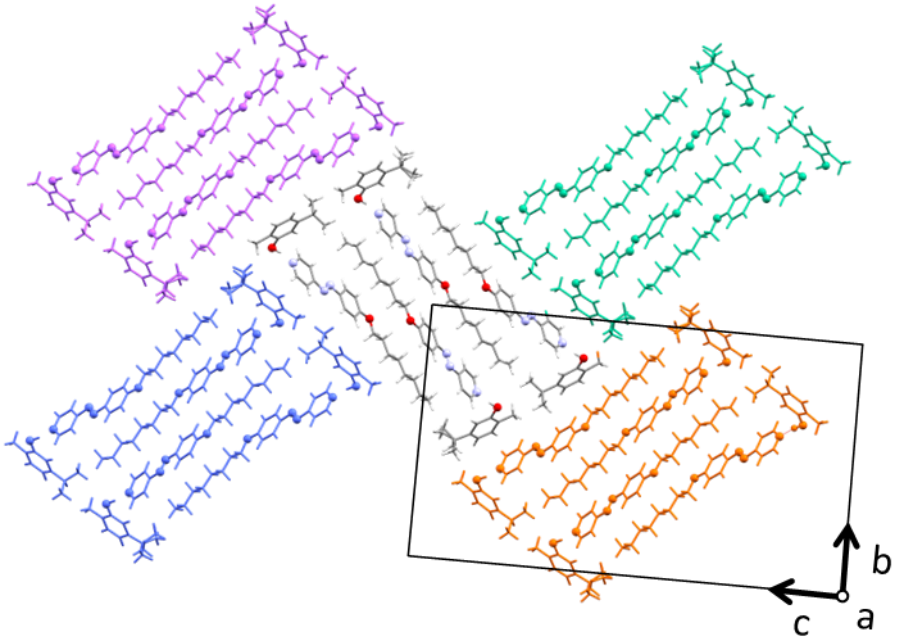

Figure 57. *Molecular arrangements in **3**-CAR **a** cocrystal structure highlighting the interlocked motif generated through the interaction of tetramers.*

The stimulus-responsive properties of **3**-CAR **b** cocrystal were determined by irradiating the sample at 365 nm for different times and measuring the variations in terms of spectroscopic and structural properties. UV-vis measurements evidenced a considerable decrease in absorbance already after 1.5 h, in a similar way to **2**-THY cocrystal (*Figure 58*). Also the shape of the trans isomer band changed after the irradiation, however in this case there was no clear correspondence with the spectra of AZP **3** coformer. Nevertheless, this evidence may be correlated with a diminishing of cocrystal concentration and thus the release of CAR, which was the volatile component.

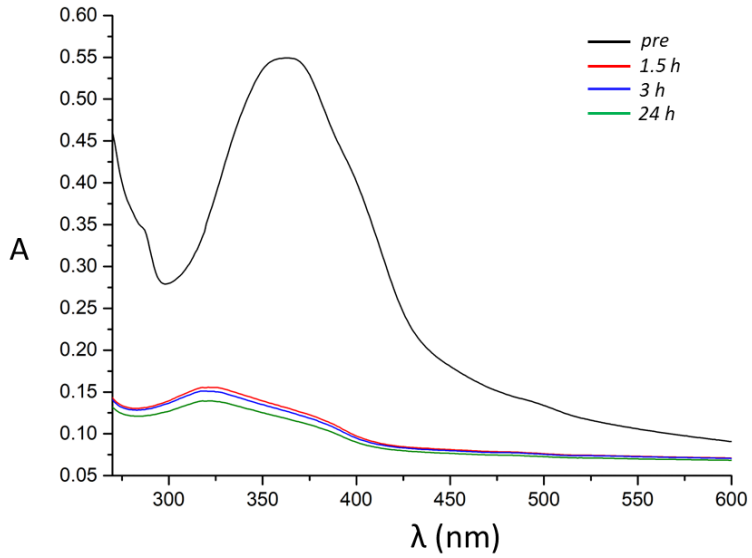

Figure 58. *UV-vis spectra of **3**-CAR 1:1 **b** cocrystal as thin film.*

The structural changes of **3**-CAR **b** cocrystal were evaluated performing PXRD measurements before and after 24 h of irradiation. Samples were prepared in the same way as **2**-THY cocrystal.

Powder patterns confirmed the presence of the cocrystal after irradiation, as shown in *Figure 59*, and the recrystallization of trans AZP **3** coformer. All the new peaks found are referable exclusively to **3** coformer, which recrystallized after the irradiation due to a partial release of CAR.

The activated release of CAR is confirmed also by the visual comparison of the sample, prepared for PXRD measurement, before and after 24 h of irradiation (*Figure 60).* The smaller crystals of **3**-CAR **b** cocrystal disappear and new drops are formed, attributed to carvacrol. There was no definitive evidence of **3** cis isomer formation, which could be formed just in a transient step triggering the release of the active ingredient, and then rapidly recovering the trans configuration. Other mechanisms of activation could also be envisaged, that anyway require the absorption of the radiation.

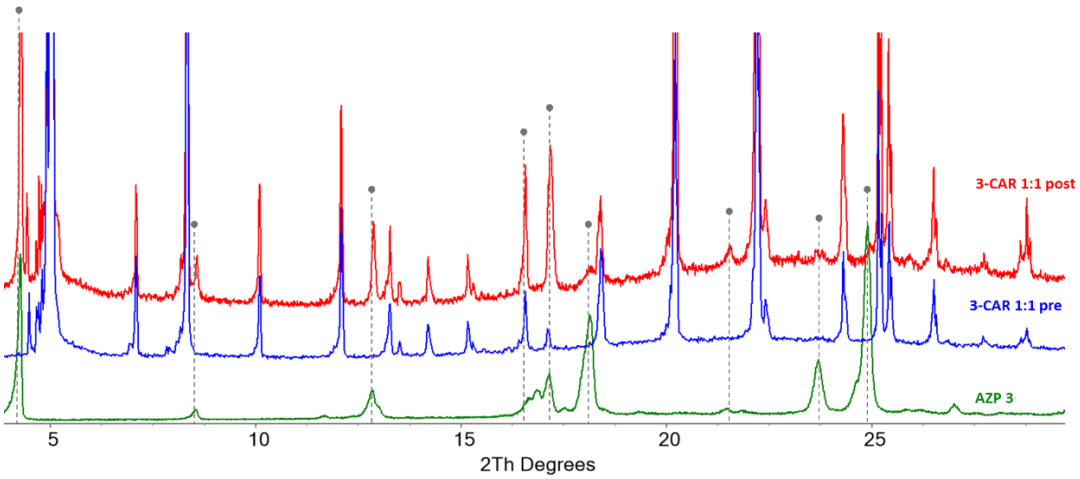

Figure 59. *Comparison of the experimental powder patterns of **3**-CAR **b** cocrystal before and after 24 h of irradiation at 365 nm with respect to AZP **3**. Grey arrows highlight the presence of peaks referred to AZP **3** into **3**-CAR **b** cocrystal pattern after the irradiation.*

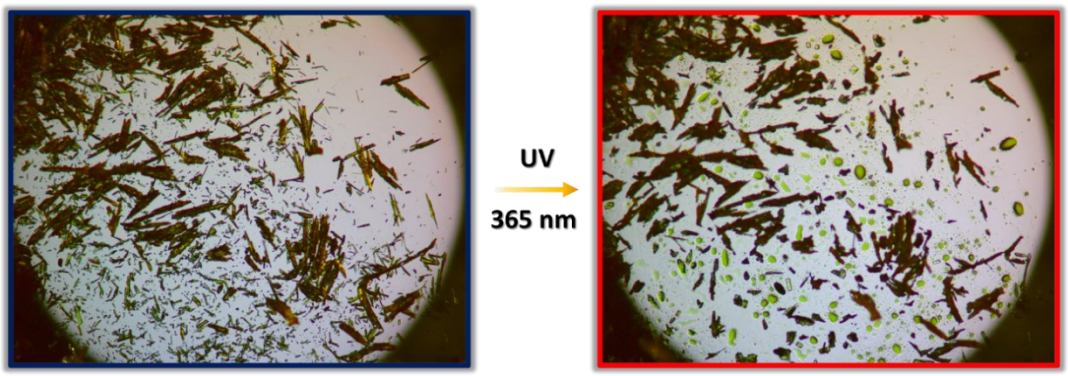

Figure 60. *Images of **3**-CAR1:1 **b** cocrystal before and after 24 h of irradiation at 365 nm captured with a magnification of 30x.*

3.5 Eugenol-based cocrystals

2-EUG 1:1

AZP **2**-EUG cocrystal was obtained by direct mixing 0.1 mmol of **2** (28 mg) and 0.1 mmol of EUG (~15 µL) with mortar and pestle for 15 min. The synthesis was also performed using a vibrational ball mill, in the same conditions employed for **3**-CAR cocrystal.

The resulting powder was analysed through PXRD to check the purity of the phase (Appendix B1), supported by a Pawley refinement based on the crystal structure collected via SCXRD (*Figure 61*). The cocrystal resulted as the only phase, with no residual peaks detected.

Single crystals of **2**-EUG 1:1 were obtained by dissolving ~5 mg of the grinded powder into ~1.5 mL of EtOH. Orange thin plates crystallized in a few days through slow solvent evaporation under chemical hood.

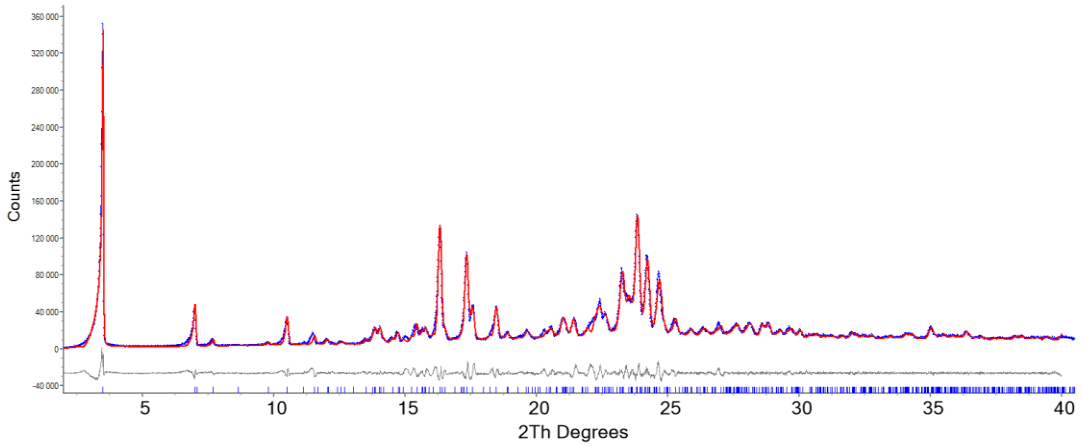

Figure 61. *Pawley fit of **2**-EUG 1:1 cocrystal (red line) against experimental data (blue dots). Tick marks indicate calculated reflection positions. Ycalc-Yobs residual curve is reported in grey.*

The thermal behaviour of **2**-EUG cocrystal was evaluated performing a DSC measurement. The thermogram showed an endothermic peak at 36.89 °C (*ΔH = 111.39 J/g*) in the first heating, which referred to the melting of the cocrystal, followed by an exothermic peak (*ΔH = -103.36 J/g*) in the cooling run due to its recrystallization. In the second heating the endothermic peak at 36.85 °C (*ΔH = 107.43 J/g*) confirmed the melting of the cocrystal and the total recrystallization from melt. Even in this case, the cocrystal results as more stable form than the pure essential oil (EUG, m.p. -7.5 °C), due to its higher melting point.

Table 14. *Summary of the thermal event that occurred during the DSC measurement of **2**-EUG 1:1 cocrystal.*

Cocrystal	*Run*		*Thermal event*	*Temperature (°C)*	*ΔH (J/g)*
2-EUG 1:1	First heating	1st peak	Endothermic	36.89	111.39
	First cooling	1st peak	Exothermic	16.88	-103.36
	Second heating	1st peak	Endothermic	36.85	107.43

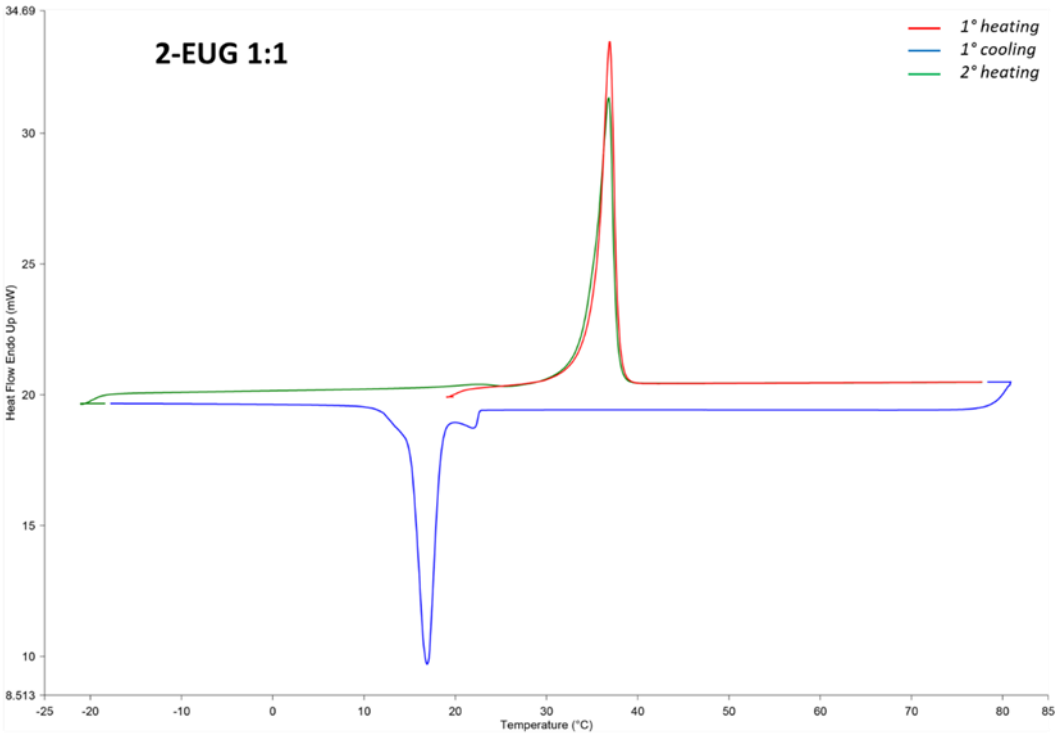

Figure 62. *Thermogram of **2**-EUG 1:1 cocrystal.*

The crystal structure of **2**-EUG cocrystal exhibits P21/c space group, with two formula units in the asymmetric unit (Z = 8, Z' = 2, Z'' = 4). In line with the other cocrystals, the coformers generate a dimer through the HB between the phenolic group of EUG and the pyridinic nitrogen of **2** ((HB_1: O···N: 2.749(1) Å; O-H···N = 145.3(4)°; HB_2: O···N = 2.760(1) Å, O-H···N = 151.6(2)°) (*Figure 63*). However, in this case, the two dimers in the asymmetric unit present the molecules of the essential oil on the same side, which interact through offset π···π interactions. In addition, the AZP coformer molecules are no longer parallel and establish T-shape C-H···π interactions (*Figure 63*). The molecular organization consists in stacked pillars formed by dimeric units which run along the a-direction (*Figure 64*). These pillars mutually interact either by facing their EUG molecules, therefore connecting with π···π and C-H···π interactions, or their alkyl chains, so through dispersive

interactions. The final result is the alternation of stacked pillar such to create a V shape motif, similarly to **2**-THY cocrystal.

Different dihedral angles are assumed between the phenolic rings of EUG and the pyridinic rings of **2** (θ_1: 3.45°, θ_1: 39.13°), with the purpose to best optimize the intermolecular interactions. Energy calculations revealed that the driving forces of the crystal packing are the π···π interactions between **2** molecules, which assumed values of -70.3 kJ/mol and -62.1 kJ/mol. HB interactions also contributed to the crystal arrangement with molecule-molecule energy values of -52.3 kJ/mol (HB_1) and -54.2 kJ/mol (HB_2).

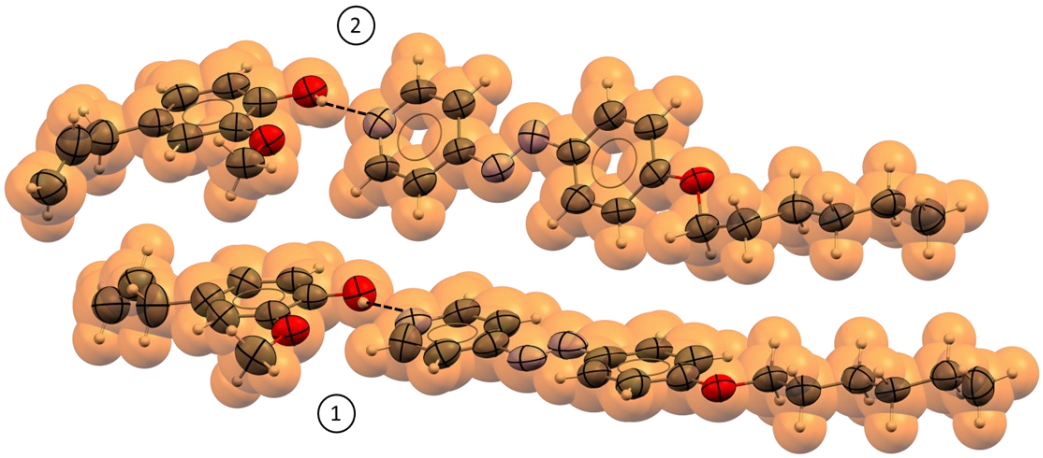

Figure 63. *Representation of the asymmetric unit of **2**-EUG cocrystal. The two hydrogen bonds are depicted with a black dashed line.*

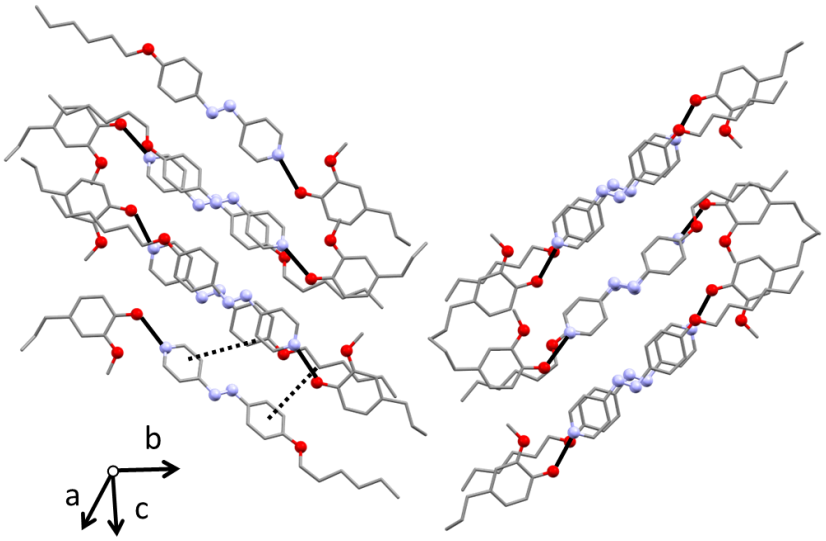

Figure 64. *Molecular arrangements in **2**-EUG cocrystal structure driven by hydrogen bonds (solid black lines), π···π, and CH···π interactions (dotted black lines). Only two examples of π···π and CH···π interactions were reported for simplicity. Hydrogen atoms are omitted for sake of clarity.*

The stimulus-responsive properties of **2**-EUG cocrystal were determined by irradiating the sample at 365 nm for different times and measuring the variations in terms of spectroscopic and structural properties. UV-vis measurements evidenced a similarity with **7**-THY cocrystal, that consisted in the decrease of the trans isomer band at 360 nm, mainly after 1.5 h and 3 h of irradiation, followed by the diminishing of cocrystal concentration after 24 h (*Figure 65*). As seen for the previous cocrystals, there was no evident proof of the cis isomer band, however it was possible to conclude that the reduced cocrystal concentration was a consequence of the essential oil release upon irradiation.

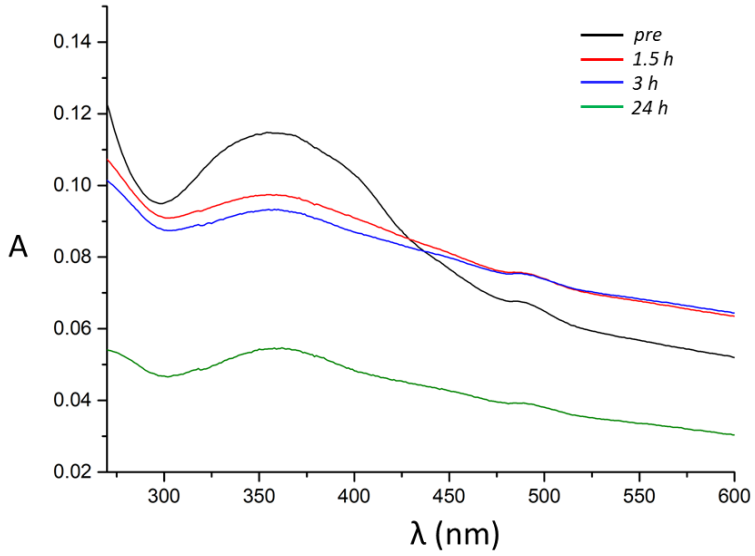

Figure 65. *UV-vis spectra of **2**-EUG 1:1 cocrystal as thin film.*

The structural changes of **2**-EUG cocrystal were evaluated performing PXRD measurements before and after 24 h of irradiation. Samples were prepared in the same way as **2**-THY cocrystal.

As seen for the previous systems, powder patterns confirmed the presence of the cocrystal after irradiation (*Figure 66*), even though in a lower concentration, due to the partial release of EUG. The new peaks detected were related to the recrystallization of trans AZP **2a** coformer, which was more quantitative rather than in **2**-THY cocrystal.

Similarly to **3**-CAR **b** cocrystal, the visual comparison of the sample before and after 24 h of irradiation showed the formation of drops (*Figure 67*). In addition, some of these drops contained thin plate crystals, which were morphologically different from the other crystals presented on the glass slide. These thin crystals corresponded to the recrystallized trans AZP **2a** coformer, confirmed by measuring their melting points, and the morphology justified the presence of preferred orientations for **2a** peaks.

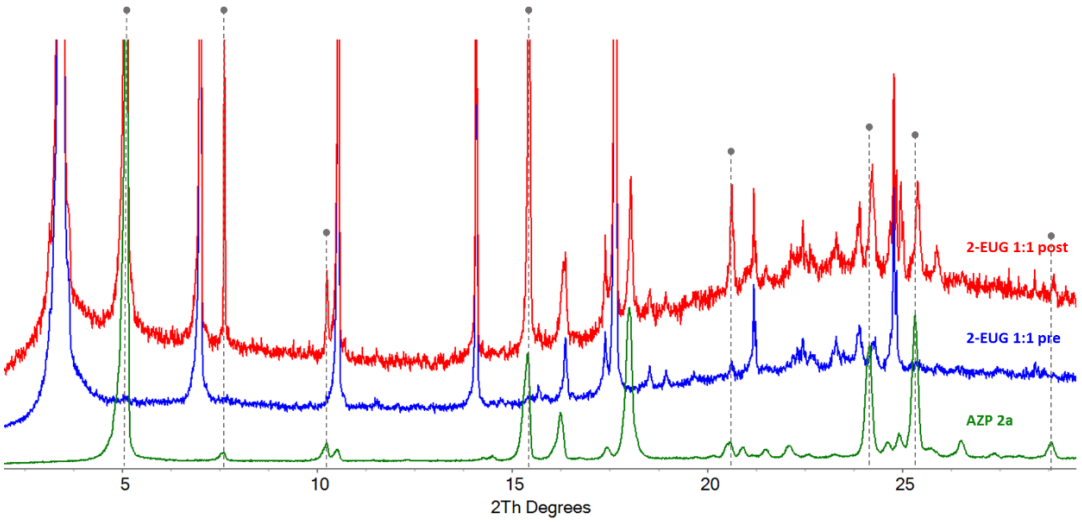

Figure 66. *Comparison of the experimental powder patterns of **2**-EUG 1:1 cocrystal before and after 24 h of irradiation at 365 nm with respect to AZP **2**. Grey arrows highlight the presence of peaks referred to AZP **2** into **2**-EUG cocrystal pattern after the irradiation.*

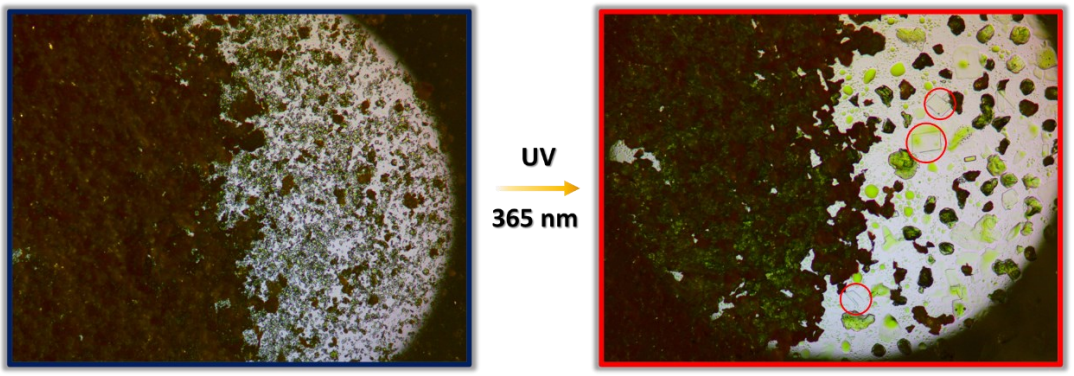

Figure 67. *Images of **2**-EUG 1:1 cocrystal before and after 24 h of irradiation at 365 nm captured with a magnification of 30x. The thin plate crystals which recrystallized after the irradiation were highlighted by red circles (left).*

4-EUG 1:1

AZP **4**-EUG cocrystal was obtained by direct mixing 0.1 mmol of **4** (34 mg) and 0.1 mmol of EUG (~15 µL) with mortar and pestle for 15 min. The synthesis was also performed using a vibrational ball mill, in the same conditions employed for **3**-CAR cocrystal.

The resulting powder was analysed through PXRD to check the purity of the phase, turning out that no residual peaks of coformers were detected thus a cocrystal phase was obtained (*Figure 68*). However, this crystalline phase did not correspond to the cocrystal phase obtained through SCXRD, therefore it was a new polymorphic phase (**b**).

Single crystals of **4**-EUG 1:1 **a** were obtained by dissolving ~5 mg of the grinded powder into ~2 mL of EtOH. Orange prisms crystallized in a week through slow solvent evaporation under chemical hood.

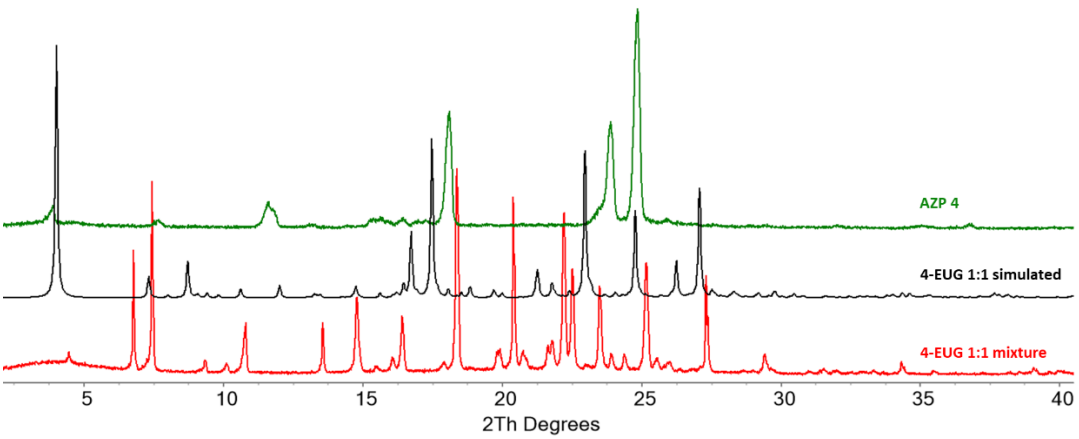

Figure 68. *Comparison of the experimental powder patterns of AZP* ***4*** *and the mixture* ***4****-EUG 1:1 obtained after grinding with the simulated pattern at 150 K of* ***4****-EUG 1:1* ***a*** *cocrystal obtained through SCXRD.*

The thermal behaviour of **4**-EUG cocrystal was evaluated performing a DSC measurement. The thermogram showed an endothermic peak at 43.43 °C (*ΔH = 94.05 J/g*) in the first heating, which referred to the melting of the cocrystal. In the cooling run, an exothermic peak (*ΔH = -81.39 J/g*) occurred due to the crystallization of a polymorphic phase of **4**-EUG cocrystal (**b**). This polymorph exhibited a lower melting temperature, as confirmed by the endothermic peak in the second heating at 34.24 °C (*ΔH = 78.19 J/g*). As seen for **3**-CAR and **2**-EUG, the melting temperature of the cocrystal is significantly higher with respect to the pure essential oil.

Table 15. *Summary of the thermal event that occurred during the DSC measurement of **4**-EUG 1:1 **b** cocrystal.*

Cocrystal	*Run*		*Thermal event*	*Temperature (°C)*	*ΔH (J/g)*
	First heating	1st peak	Endothermic	43.43	94.05
4-EUG 1:1 b	First cooling	1st peak	Exothermic	12.64	-81.39
	Second heating	1st peak	Endothermic	34.24	78.19

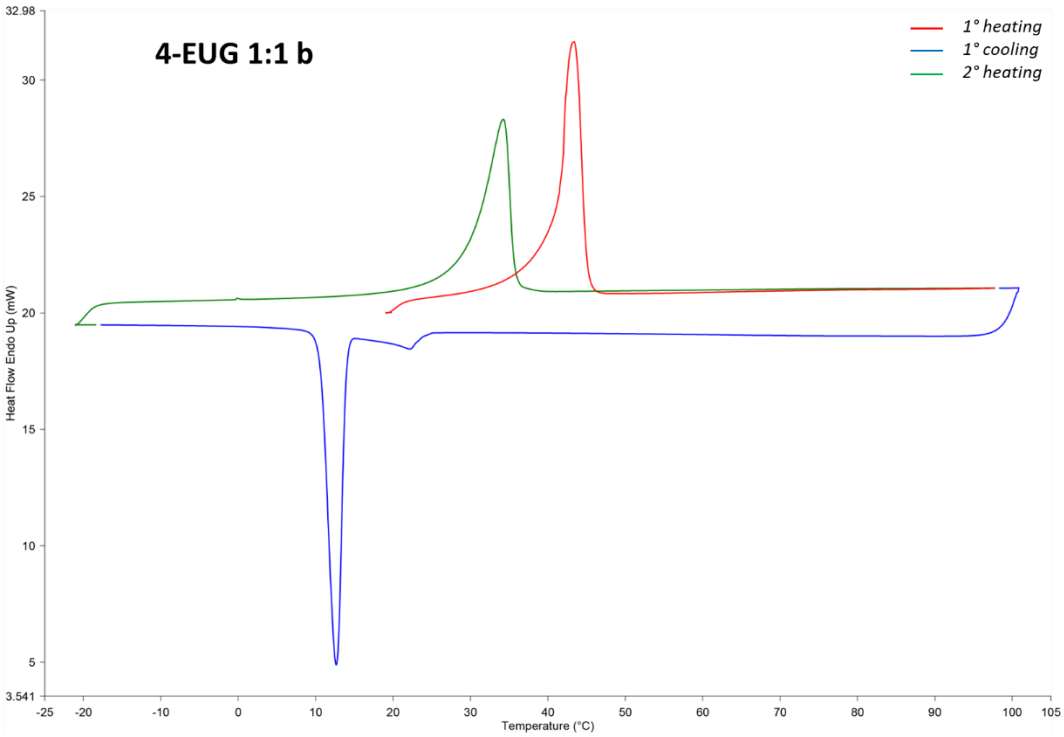

Figure 69. *Thermogram of* ***4****-EUG 1:1* ***b*** *cocrystal.*

The crystal structure of **4**-EUG **a** cocrystal exhibits P-1 space group, with two formula units in the asymmetric unit (Z = 4, Z' = 2, Z'' = 4). Also in this case, dimers are formed through an HB interaction between the phenolic group of EUG and the pyridinic nitrogen of **4** ((HB_1: O···N: 2.750(7) Å; O-H···N = 146.0(1)°; HB_2: O···N = 2.747(7) Å, O-H···N = 149.0(1)°) (*Figure 70*). Differently from **2**-EUG cocrystal, the two dimers in the asymmetric unit weakly interact since they are not overlapped, in addition the dihedral angles between the phenolic rings of EUG and the pyridinic ring of **4** are extremely low (θ_1: 16.33°, θ_1: 4.74°). On the other hand, each dimer results the starting point for the formation of stacked pillars by head-to-tail overlap with other dimers, thanks to π···π and C-H···π interactions (*Figure 71*). Pillars are instead kept together through the π···π interactions among the propylenic groups of EUG molecules. The importance of π···π interactions was also proved by the molecule-molecule interaction energies, with the highest values of -74.5 kJ/mol and

-68.0 kJ/mol referred to the stacking of **4** molecules. As seen for **2**-EUG cocrystal, the HBs involving EUG molecules assumed lower values (HB_1: -50.9 kJ/mol, HB_2: -47.8 kJ/mol) with respect to the other cocrystals based on THY and CAR.

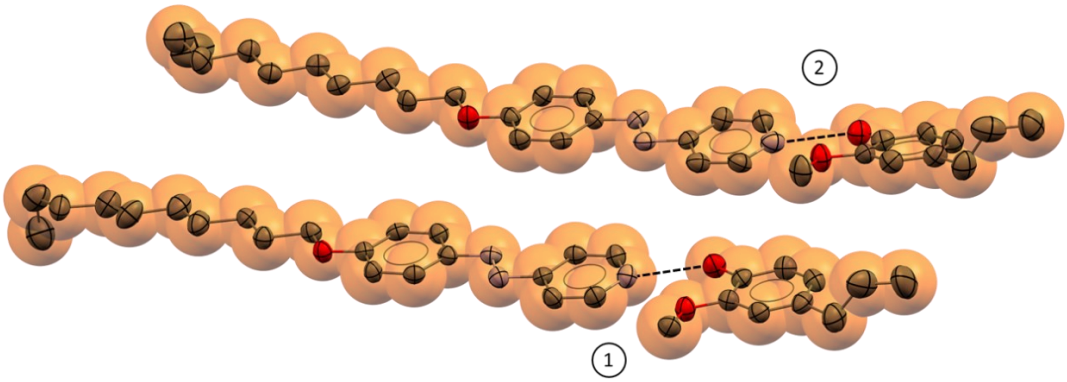

Figure 70. *Representation of the asymmetric unit of **4**-EUG **a** cocrystal. The two hydrogen bonds are depicted with a black dashed line.*

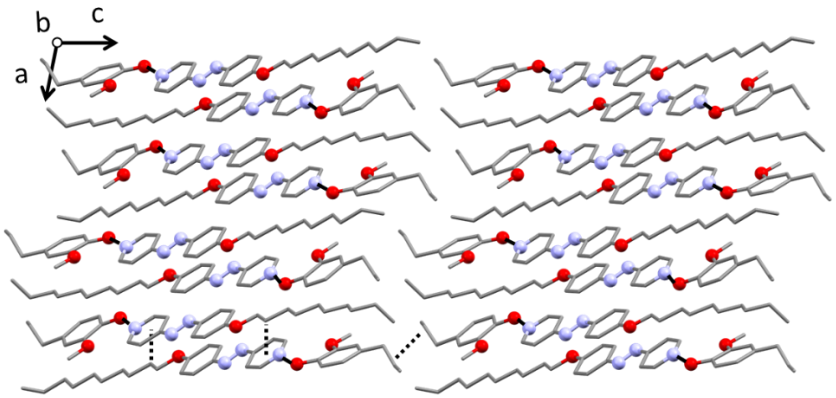

Figure 71. *Molecular arrangements in **4**-EUG **a** cocrystal structure driven by hydrogen bonds (solid black lines) and π···π interactions (dotted black lines). Hydrogen atoms are omitted for sake of clarity.*

The stimulus-responsive properties of **4**-EUG **b** cocrystal were determined by irradiating the sample at 365 nm for different times and measuring the variations in terms of spectroscopic and structural properties. UV-vis measurements showed a similarity with **3**-THY cocrystal, due to the decrease of the trans isomer band at

357 nm and the increase of the region above 422 nm (*Figure 72*). Also in this case, there was no clear evidence of cis coformer as well as the release of EUG.

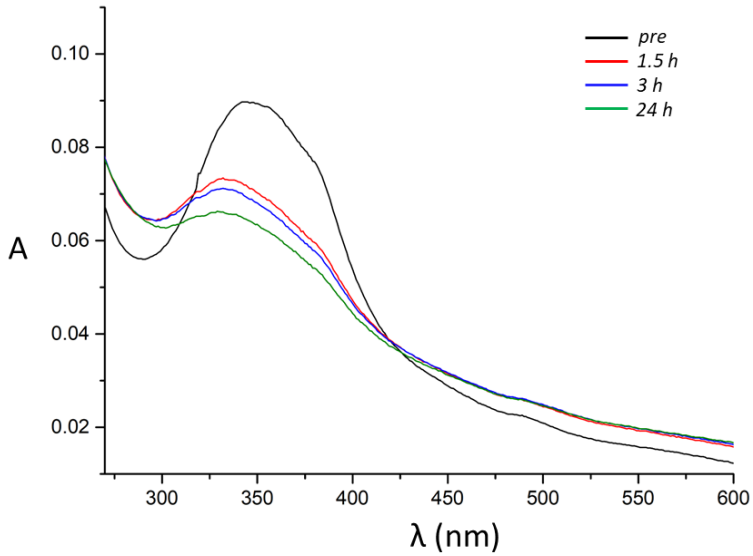

Figure 72. *UV-vis spectra of* ***4****-EUG 1:1* ***b*** *cocrystal as thin film.*

The structural changes of **4**-EUG **b** cocrystal were evaluated performing PXRD measurements before and after 24 h of irradiation. Samples were prepared in the same way as **2**-THY cocrystal.

Powder patterns confirmed the presence of the cocrystal after irradiation, as shown in *Figure 73*, however some peaks appeared at 3.96 and 24.97 2θ which referred to the trans AZP **4** coformer. The intensity of these peaks was very low and the other reflections of **4** were barely appreciable. This was significant of a lower release of EUG from the cocrystal, in agreement with the results of spectroscopic measurement.

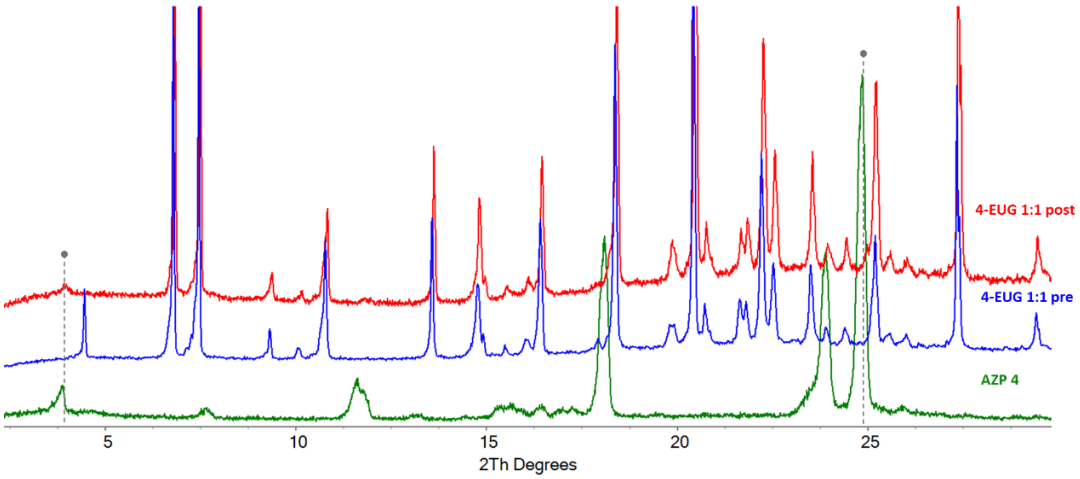

Figure 73. *Comparison of the experimental powder patterns of **4**-EUG 1:1 **b** cocrystal before and after 24 h of irradiation at 365 nm with respect to AZP **4**. Grey arrows highlight the presence of peaks referred to AZP **4** into **4**-EUG **b** cocrystal pattern after the irradiation.*

3.6 Triggering the cocrystals release

The investigation of the spectroscopic and structural alterations of photo-responsive cocrystals led to the conclusion that the treatment with opportune UV radiation influenced the cocrystal release. It turned out that the trans AZP coformers recrystallized after the irradiation consequently to the loss of the essential oil. Even though the use of PXRD helped with the comprehension of cocrystal consumption after the irradiation, by means of a qualitative comparison of peak intensities and background, it was necessary to estimate the quantitative release of the cocrystals. The quantitative release of photo-responsive cocrystals was evaluated comparing the response of two sets of samples: one treated with the UV radiation (treated set), and the other one not irradiated (control set). The

radiative treatment was performed in the same conditions used for the other solid-state characterizations (see paragraph 2.11 “Radiative treatment”), with the following irradiation times: 1 h, 3 h, 5 h, 7 h, 9 h, and 24 h. The release of the cocrystals was determined in terms of the active ingredients concentration by performing headspace gas chromatography/mass spectrometry (HS-GC/MS) analyses. The cocrystals responses were normalized on the basis of the acute release of the pure ingredient (after 5 min at 30 °C). Considering the high number of cocrystals obtained, the measurements were carried out only on the most promising ones, at the same time trying to understand the correlation between release properties and active ingredients. The selected cocrystals were **2**-THY 1:1, **2**-CAR 1:1, and **2**-EUG 1:1.

2-THY cocrystal showed a significant release of THY in the range between 1 h and 3 h, independently from the treatment, which reached a plateau only after 7 h (*Figure 74*). Comparing the two sets of samples (treated and control sets), there were no differences induced by the irradiation, even after 24 h. A reasonable explanation may be related to the shape of cocrystal release profile, indeed the major loss of THY occurred in the first hours and no more points were recorded in that range. After that, the quantity of released THY was so limited that no differences were appreciated.

2-CAR cocrystal evidenced a more intense release of CAR in absolute terms, but a completely different release profile with respect to **2**-THY cocrystal (*Figure 75*). In fact, the release of CAR resulted almost constant during the first 10 h, independently from the set of samples. A considerable difference was observed only after 24 h, with a lower concentration of the irradiated samples. This agrees with the enhanced release promoted by the absorption of UV radiation, as demonstrated in the spectroscopic and structural analyses. In this way, CAR was

more intensely released during the irradiation thus assuming a lower response at the end of the treatment, due to the consumption of the cocrystal. On the other hand, the amplitude of the standard deviations and the limited number of replicates, due to the size capability under the UV lamp, minimize the differences between the two sets.

2-EUG cocrystal exhibited a medium release of EUG, in absolute terms, rather than the previous cocrystals (*Figure 76*). The release profile of the control set linearly decreased during the time with a minimal slope, instead the irradiated set showed a significant decrease which almost halved the EUG response after 24 h. From a comparison of the two sets, the irradiated set always presented lower response values since the 1 h, and huge differences with respect to the control set were observed from 9 h of irradiation. This behaviour is in line with the promoted release of EOs induced by UV radiation, as well as the consumption of the cocrystal that implies lower response values.

In conclusion, **2**-EUG cocrystal evidenced the better results concerning the activation of the cocrystal release upon irradiation, with remarkable differences in particular after 24 h of irradiation. **2**-CAR cocrystal also showed an activation, however minimal differences were observed only after 24 h. Finally, **2**-THY cocrystal exhibited an intense release in the first three hours however no reliable differences were detected between the irradiated and the control sets.

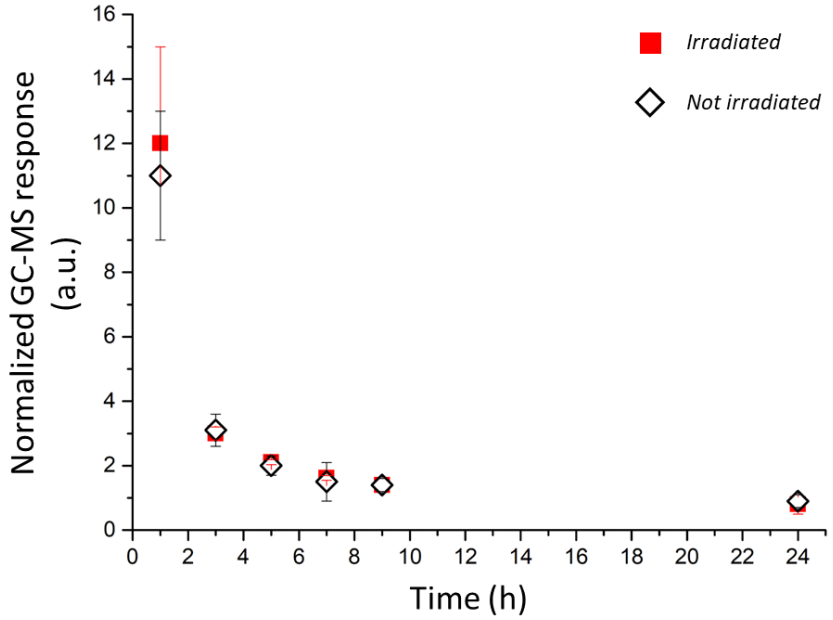

Figure 74. *Normalized HS–GC–MS profiles for* ***2****-THY 1:1 cocrystal as a function of the irradiation time. The results are plotted as mean ± standard deviation (*n *= 2).*

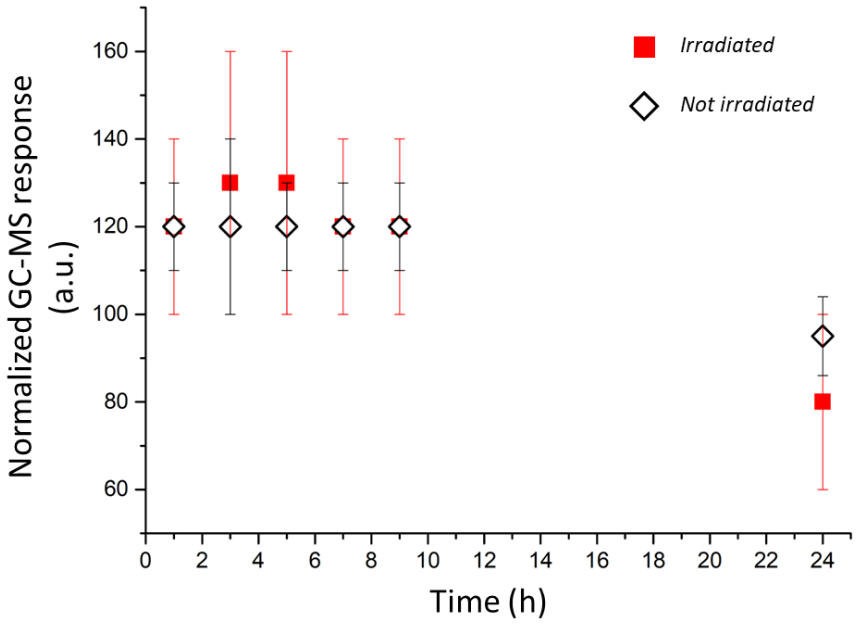

Figure 75. *Normalized HS–GC–MS profiles for* ***2****-CAR 1:1 cocrystal as a function of the irradiation time. The results are plotted as mean ± standard deviation (*n *= 2).*

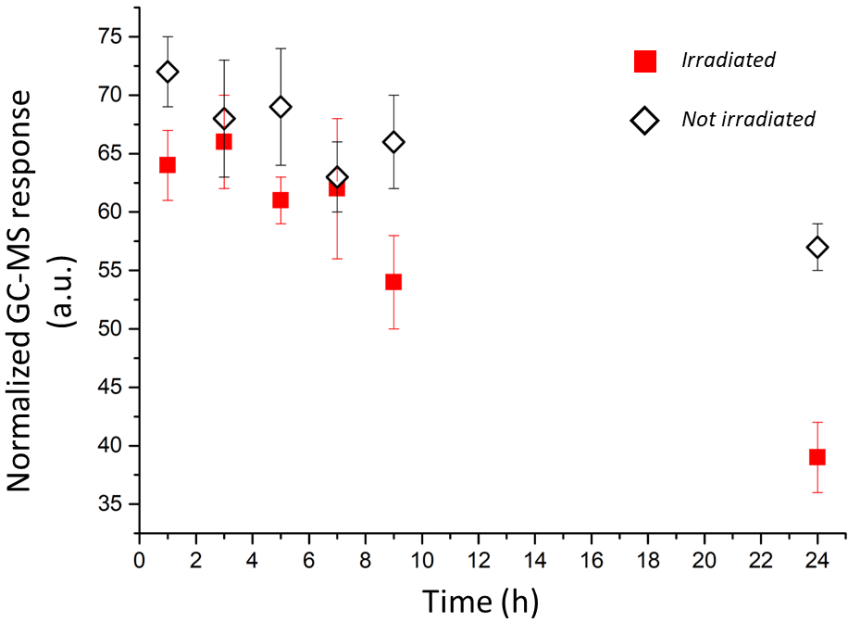

Figure 76. *Normalized HS–GC–MS profiles for* ***2****-EUG 1:1 cocrystal as a function of the irradiation time. The results are plotted as mean ± standard deviation (*n *= 2).*

Bibliography

[1] A. E. Keating, M. A. Garcia-Garibay, in *Org. Inorg. Photochem.*, New York, NY, USA, **1998**, p. 195–248.

[2] G. Kaupp, *Encycl. Phys. Org. Chem. 5 Vol. Set* **2016**, 1–80.

[3] Y. Norikane et al., *Org. Lett.* **2014**, *16*, 5012–5015.

[4] M. Hoshino et al., *J. Am. Chem. Soc.* **2014**, *136*, 9158–9164.

[5] P. Naumov, S. Chizhik, M. K. Panda, N. K. Nath, E. Boldyreva, *Chem. Rev.* **2015**, *115*, 12440–12490.

[6] M. Horie, C. H. Wang, *Mater. Chem. Front.* **2019**, *3*, 2258–2269.

[7] V. Balzani, A. Credi, F. M. Raymo, J. F. Stoddart, *Angew. Chemie Int. Ed.* **2000**, *39*, 3348–3391.

[8] P. Mobian, J.-M. Kern, J.-P. Sauvage, *Angew. Chemie* **2004**, *116*, 2446–2449.

[9] R. Eelkema et al., *Nat. 2006 4407081* **2006**, *440*, 163–163.

[10] M. Irie, S. Kobatake, M. Horichi, *Science (80-.).* **2001**, *291*, 1769–1772.

[11] M. A. Garcia-Garibay, *Angew. Chemie Int. Ed.* **2007**, *46*, 8945–8947.

[12] A. Gonzalez, E. S. Kengmana, M. V. Fonseca, G. G. D. Han, *Mater. Today Adv.* **2020**, *6*, 100058.

[13] B. M. Trost, *Science (80-.).* **1991**, *254*, 1471–1477.

[14] H. Akiyama et al., *ACS Appl. Mater. Interfaces* **2014**, *6*, 7933–7941.

[15] E. N. Cho, D. Zhitomirsky, G. G. D. Han, Y. Liu, J. C. Grossman, *ACS Appl. Mater. Interfaces* **2017**, *9*, 8679–8687.

[16] C. Probst et al., *Adv. Mater.* **2016**, *28*, 2624–2628.

[17] L. G. Nandi et al., *Carbohydr. Polym.* **2017**, *157*, 1548–1556.

[18] H. Koshima, N. Ojima, H. Uchimoto, *J. Am. Chem. Soc.* **2009**, *131*, 6890–6891.

[19] O. S. Bushuyev, A. Tomberg, T. Friščić, C. J. Barrett, *J. Am. Chem. Soc.* **2013**, *135*, 12556–12559.

[20] K. Min Lee, B. M. Lynch, P. Luchette, T. J. White, *J. Polym. Sci. Part A Polym. Chem.* **2014**, *52*, 876–882.

[21] P. Commins, I. T. Desta, D. P. Karothu, M. K. Panda, P. Naumov, *Chem. Commun.* **2016**, *52*, 13941–13954.

[22] Q. Yu et al., *Chem. – A Eur. J.* **2019**, *25*, 5611–5622.

[23] N. Tamai, H. Miyasaka, *Chem. Rev.* **2000**, *100*, 1875–1890.

[24] L. Wang, C. Yi, H. Zou, J. Xu, W. Xu, *J. Phys. Org. Chem.* **2009**, *22*, 888–896.

[25] M. Zhu, L. Yu, *J. Therm. Anal. Calorim.* **2018**, *132*, 463–469.

[26] K. Bujak et al., *Eur. Polym. J.* **2019**, *115*, 173–184.

[27] K. Bujak et al., *Dye. Pigment.* **2019**, *160*, 654–662.

[28] U. Bhattacharjee et al., *ChemPhysChem* **2017**, *18*, 2526–2532.

[29] J. Casellas, C. de Graaf, C. de Graaf, M. Reguero, *Mater. 2017, Vol. 10, Page 1342* **2017**, *10*, 1342.

[30] M. G. Mohamed, J. H. Tu, S. H. Huang, Y. W. Chiang, S. W. Kuo, *RSC Adv.* **2016**, *6*, 51456–51469.

[31] M. Pfletscher, C. Wölper, J. S. Gutmann, M. Mezger, M. Giese, *Chem. Commun.* **2016**, *52*, 8549–8552.

[32] M. D. Koshti M., Sonar J., Sonawane A., Pawar Y., Nagle P., Mahulikar P., *Indian J. Chem. Sect. B* **2007**, *47*, 329–331.

[33] L. Li et al., *http://dx.doi.org/10.1080/15533174.2013.768644* **2013**, *44*, 291–294.

[34] T. S. Basu Baul, A. Chaurasiya, A. Duthie, M. G. Vasquez-Ríos, H. Höpfl, *J. Organomet. Chem.* **2018**, *872*, 87–101.

[35] C. P. Constantin, I. Sava, M. D. Damaceanu, *Macromolecules* **2021**, *54*, 1517–1538.

[36] J. H. Lambert, *Photometria Sive de Mensura et Gradibus Luminis, Colorum et Umbrae*, Augusta, Detleffsen, **1760**.

[37] A. Beer, in *Ann. Der Phys. Und Chemie*, **1852**, pp. 78–88.

[38] F. H. Allen, IUCr, *urn:issn:0108-7681* **2002**, *58*, 380–388.

[39] M. C. Etter, J. C. MacDonald, J. Bernstein, *urn:issn:0108-7681* **1990**, *46*, 256–262.

[40] J. D. Dunitz, G. Filippini, A. Gavezzotti, *Helv. Chim. Acta ±* **2000**, *83*, DOI 10.1002/1522-2675.

[41] A. Gavezzotti, *Model. Simul. Mater. Sci. Eng.* **2002**, *10*, R1.

[42] J. D. Dunitz, G. Filippini, A. Gavezzotti, *Tetrahedron* **2000**, *56*, 6595–6601.

[43] T. Steiner, IUCr, *urn:issn:0108-7681* **2001**, *57*, 103–106.

[44] C. B. Aakeröy, D. J. Salmon, *CrystEngComm* **2005**, *7*, 439–448.

CHAPTER 4

In situ monitoring of cocrystals syntheses

The outcome of a chemical reaction can be easily figured out by performing ex situ measurements on the final product. Crystalline materials, such as cocrystals, are generally characterized through the determination of their physical properties (structural, spectroscopic, thermal, etc.) and their chemical composition. However, the information about the final products is often not sufficient for a fulfilled comprehension of the process and deeper investigations of the mechanistic aspects are required. The reaction path that leads to the formation of a product may often

involve the presence of intermediate species, which are no longer present at the end of the reaction and thus cannot be detected through ex situ analyses. The importance of intermediate species has been come up from the measuring in real time of the reaction course, demonstrating in several fields that intermediate species may influence the final product, the reaction time, and the kinetic of the process[1,2]. Depending on the nature of the chemical species, such as liquid, amorphous, or crystalline, several techniques can be employed with the purpose of monitoring in situ the development of the reaction. The utilization of time-resolved in situ (TRIS) investigations has been constantly growing[3,4], and, in particular, mechanochemical reactions have attracted attention for the capability to pursue different reaction paths and involve different intermediate species[5,6]. Mechanochemical methods are compatible with in situ investigations, even if *ad hoc* experimental setups are usually necessary for employing specific techniques or improving the data quality. For instance, the investigation of mechanochemical reactions that involve crystalline materials can be followed using X-ray powder diffraction, however the choice of the vessel material and the energy radiation is crucial for the processing of the resulting powder patterns[7].

In the last years, mechanochemical cocrystallizations have been largely investigated for the easiness of reaching the cocrystal formation, the potential presence of intermediates, and the possibility to obtain different polymorphic phases[8]. Only a few examples of cocrystals reactions that proceed through liquid intermediates are found[9,10], and their investigation still remains a hard task, especially for the intrinsic problems due to the not perfect mixing and often to the lifetimes of the intermediate species. In the following paragraphs, two cases of study will be proposed concerning the formation of cocrystals through liquid intermediates. In these systems, the mere contact between the crystals of two different coformers generates a metastable liquid phase, from which cocrystallization is initiated. This

liquid phase was demonstrated to be the eutectic binary mixture of the coformers, whose composition (χ_ε) was different from the cocrystal stoichiometry (χ_C) (*Figure 77*). The eutectic composition of coformers is always included within the range of cocrystal existence (χ_m (ε_{AC}) < χ_m (ε_{AB}) < χ_m (ε_{CB}), if it does exist, a region where the cocrystal represents the most stable thermodynamic phase. This means that the eutectic mixture of coformers can spontaneously convert into cocrystal acting as a metastable phase. These considerations are translated in the binary phase diagram by reporting the liquidus curves with either solid or dashed lines to indicate thermodynamic or metastable equilibria (*Figure 77*).

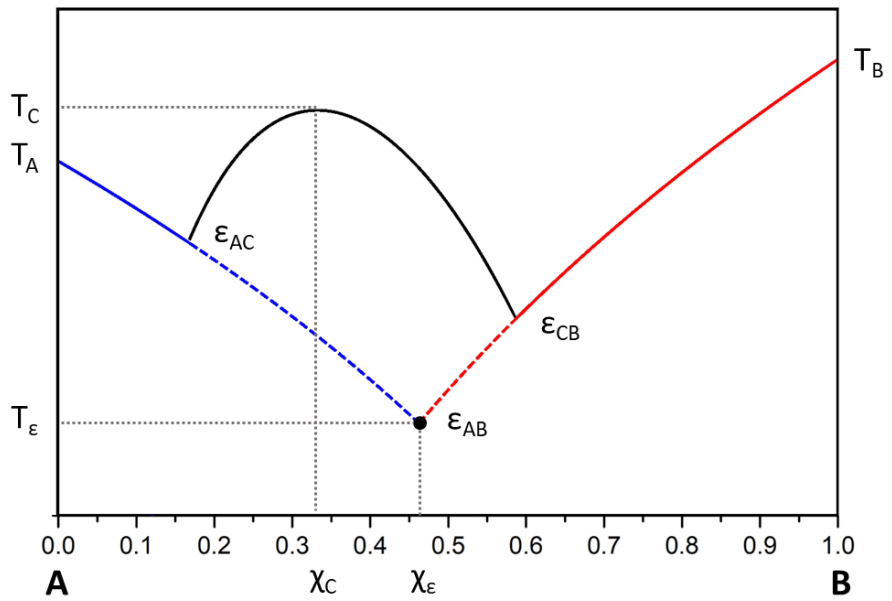

Figure 77. *Representation of a generic binary liquid-solid phase diagram of two compounds (A/B), with a metastable eutectic mixture* ε_{AB} *and a A-B 1:2 cocrystal (C). The liquidus curves of A, B, and cocrystal are depicted in blue, red, and black.* ε_{AC} *and* ε_{CB} *are the eutectic mixtures between respectively A and B with the cocrystal (C).*

The two cases of study that will be discussed are based on thymol (THY) which reacted with hexamethylenetetramine (HMT), giving HMT-THY 1:3 cocrystal[11,12],

or 4,4'-azopyridine (AZO), giving AZO-THY 1:2 cocrystal (*Scheme 3*). The peculiarity of both systems was the extreme reactivity between the coformers, which rapidly formed a metastable liquid intermediate that converted into the cocrystal in a brief time. The cocrystallization processes were evaluated using a multi-techniques approach which included the analyses in situ of the mechanochemical cocrystallizations.

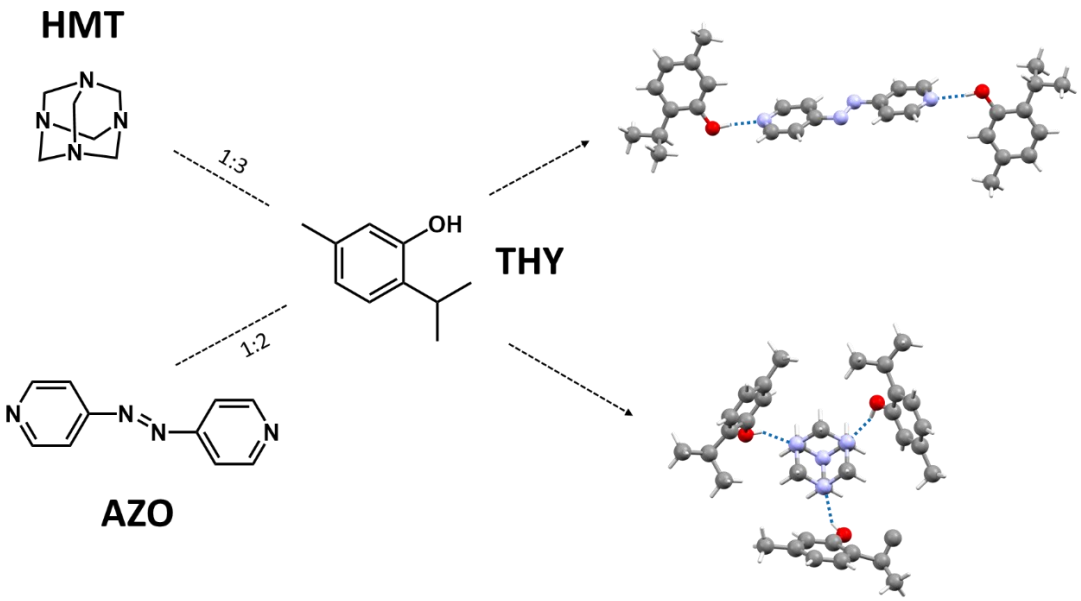

Scheme 3. *Cocrystallization of thymol (THY) with hexamethylenetetramine (HMT) and 4,4'-azopyridine (AZO).*

4.1 TRIS mechanochemical cocrystallizations

The mechanochemical cocrystallizations of HMT-THY and AZO-THY were performed at the BESSY-II synchrotron (Berlin) using the customized setups and experimental conditions described in paragraph 2.4. The reactions were examined with a TRIS-

PXRD monitoring using a low energy synchrotron radiation (0.729 Å). The radiation energy was opportunely selected to easily penetrate the PMMA jar and optimize the spatial resolution of the resulting powder patterns. During the mechanochemical reactions, the incident beam passed through the oscillating jar and diffraction occurred from the sample detected along the optical beam (*Figure 78*). Differently from ideal diffraction, which takes place from a single point, in this case the elongated sample volume gave origin to a broadening, or ultimately splitting, of the diffracted peaks. This phenomenon was further enhanced with the formation of the intermediate liquids, whose sticky nature held the sample to the jar walls. Therefore, the diffracted peaks resulted split into three main contributions: the external contributions due to the sample that adhered to the jar walls ($\overrightarrow{s_1}$ and $\overrightarrow{s_3}$ in *Figure 78*), while the middle contribution was related to the portion of sample in movement within the jar walls ($\overrightarrow{s_2}$ in *Figure 78*).

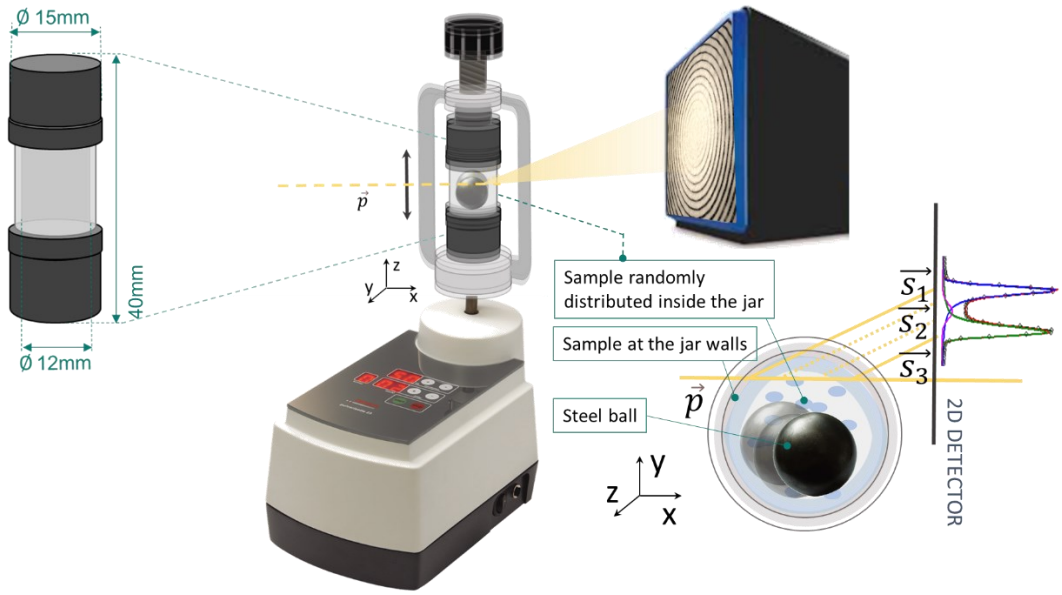

Figure 78. *Schematic representation of the experimental setup used during the TRIS-PXRD monitoring of HMT-THY and AZO-THY mechanochemical cocrystallizations.*

The modelling of this complex instrumental aberration was tackled using an innovative processing of peak position and peak profile, recently reported[7,13]. In these works, the peak position of each component was adapted using a single function that considered the displacement of the sample inside the jar. The peak profile, instead, was modelled by two split TCHZ pseudo-Voigt functions for the two external components, in addition to a Gaussian function for the middle component. With this three-peak model, the split Bragg reflections were adequately refined as a convolution of the three components, each treated as independent.

The evaluation of the reaction course passed through the quantification of all the phases involved in the cocrystallization processes, either crystalline or not. The use of a PMMA jar had as benefit the employing of a low energy radiation but also gave a considerable amorphous background contribution to the powder patterns (*Figure 79*). This latter aspect hindered the phases quantification since the scattering generated from the jar partially covered the diffracted Bragg reflections of the crystalline species. To take this scattering contribution into account, a measurement with an empty PMMA jar (only the two steel balls inside) was performed in the same experimental conditions of the mechanochemical reactions, in order to obtain a representative pattern of the extrinsic background contribution.

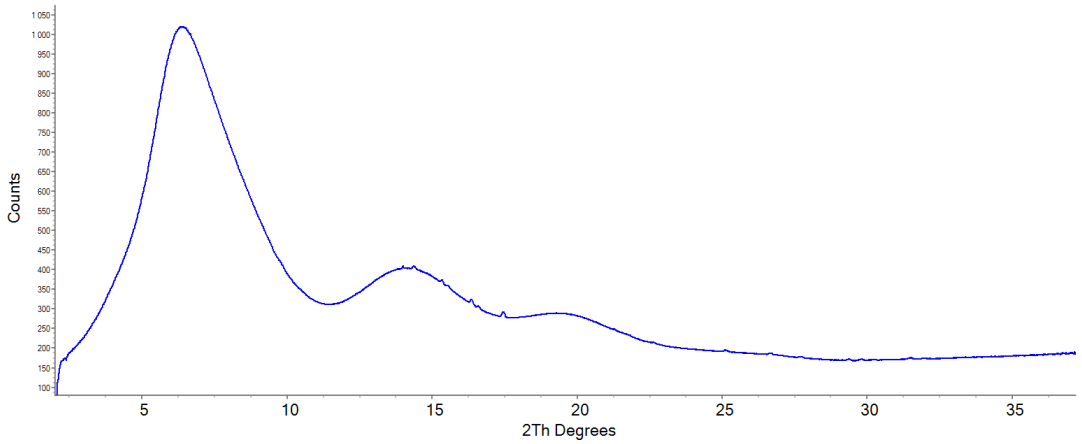

Figure 79. *Experimental pattern of the empty jar with two steel balls inside, corresponding to the extrinsic amorphous background contribution.*

The other amorphous contribution, for both HMT-THY and AZO-THY systems, was given by the liquid intermediate, which continuously was formed and then converted during the mechanochemical reactions. Unlike the jar contribution, the amorphous liquid had a short lifetime and its quantity varied over time. Hence, for its determination, a reaction pattern was chosen in which it was present in large quantity. Both the extrinsic (jar) and intrinsic (liquid intermediate) amorphous background contributions were then extrapolated as "rigid" phases (only scalable) from the representative patterns and used in the overall refinement.

At least, the crystalline phases (*i.e.* coformers and cocrystals) were taken into account. Although their crystal structures were already known, it was necessary to collect a representative pattern for each of them in the same conditions of the mechanochemical reactions, in order to simulate their behaviour. The crystalline phases were included in the PXRD data analyses using cell parameters, fractional coordinates, and temperature factors obtained by Rietveld refinement on the representative patterns. Once all the phases involved were known, the reaction courses were evaluated through a sequential multi-phases Rietveld refinement: the output obtained from the "n-1" scan was used as input for the "n" scan. The three-

peak model was applied by using the new peak split function and peak profile discussed above. The phases quantification was carried out through the sum of the integrated areas associated with all the Bragg reflection of the crystalline phases, while the amorphous amounts were adjusted by a scale factor.

4.2 HMT-THY cocrystallization

The reactivity between HMT and THY was first defined by getting in touch a few crystals of the two coformers on a glass plate and observing the variations upon thermal treatment through Hot Stage microscopy[14]. The stoichiometry of the mixing could not be determined due to the tiny sizes and low amounts of crystals used. The starting temperature was set at 20.0 °C, and then the system was heated up at 1 °C/min. Around 23.7 °C, a liquid phase started to form at the interface between the crystals, which corresponded to the eutectic mixture between the two coformers (*Figure 80*, b). The melting of THY and HMT crystals continued according to their eutectic composition, remaining a liquid phase with a solid residue of HMT at 30 °C (*Figure 80*, d). Afterward, the system was cooled down at 5°C/min and the crystallization of needle-shape crystals occurred at 10.0 °C. These crystals corresponded to a new phase since they started to melt at 42.0 °C, which differs from the melting temperature of coformers. SCXRD analysis revealed that the new phase was HMT-THY 1:3 cocrystal.

The crystal structure of HMT-THY 1:3 cocrystal was already determined[11] and highlights the presence of supra-molecular aggregates with a very high molecular multiplicity (Z'= 4, Z'' =16). These aggregates are formed thanks to the HBs between

one molecule of HMT and three molecules of THY in a pseudo-trigonal arrangement (O···N distances range: 2.745(5) − 2.801(4) Å) (*Scheme 3*).

The melting temperature of HMT-THY 1:3 cocrystal was confirmed by the first endothermic peak at 42.38 °C (*ΔH = 66.61 J/g*), obtained performing a DSC measurement on the pure cocrystal at 5 °C/min (*Figure 81*). In the cooling ramp, a crystallization occurred (*ΔH = -44.07 J/g*), followed by two endothermic peaks in the second heating, probably due to the concomitance of undefined endothermic and exothermic events.

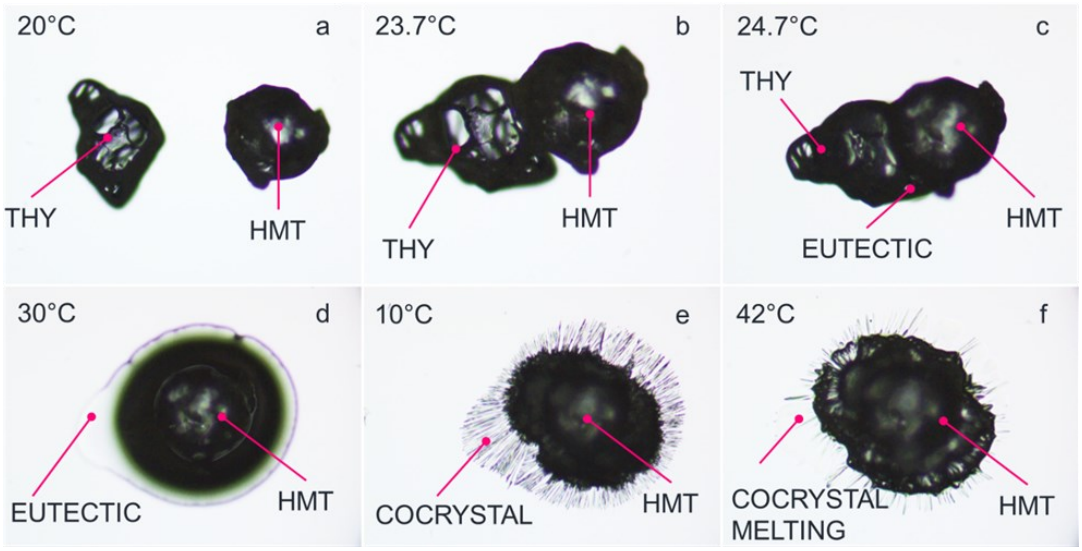

Figure 80. *Solid state reaction between HMT and THY monitored by means of Hotstage microscopy (magnification x100). a) starting condition, separated crystal of THY and HMT. b-d) melting of the eutectic mixture between HMT-THY. e) cocrystal formation from the melt. f) cocrystal melting. Reprinted with permission from Cryst. Growth Des. 2022, 22, 7, 4260–4267. Copyright 2022 American Chemical Society.*

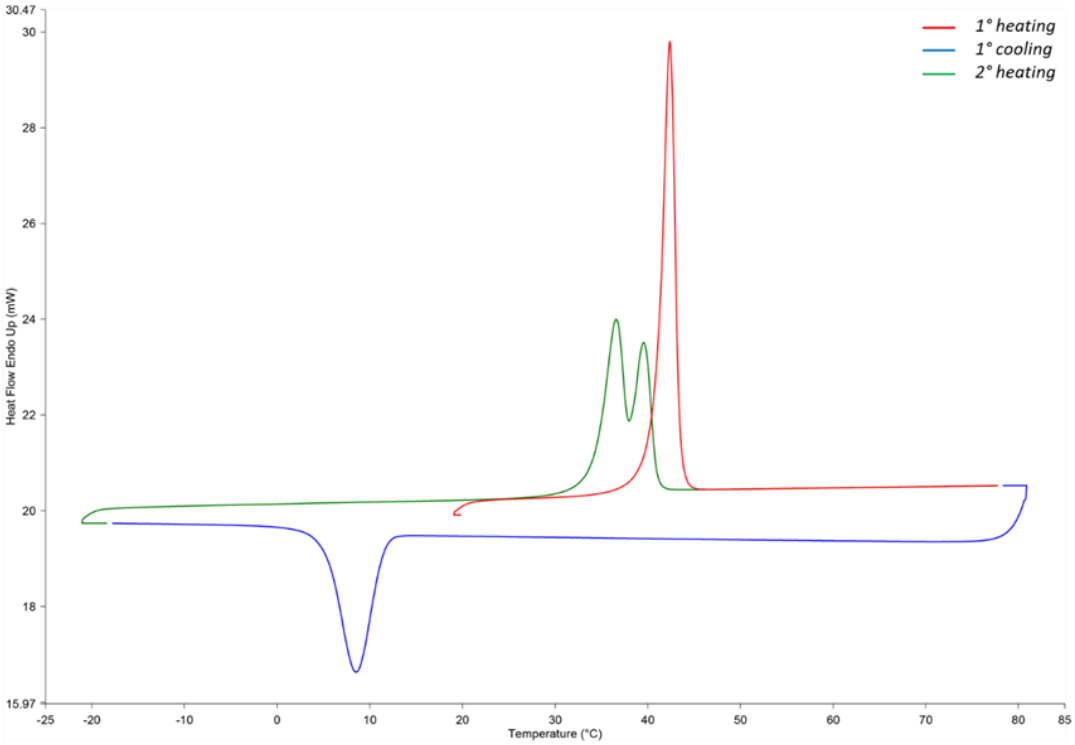

Figure 81. *Thermogram of HMT-THY 1:3 cocrystal. First heating run from 20 °C to 80 °C (red curve), cooling run from 80 °C to -20 °C (blue curve), and second heating run from -20 °C to 80 °C (green curve). Reprinted with permission from Cryst. Growth Des. 2022, 22, 7, 4260–4267. Copyright 2022 American Chemical Society.*

4.2.1 Time-Resolved In Situ Powder X-ray Diffraction

A VT-TRIS-PXRD experiment was carried out to clarify the nature of the thermal events. HMT-THY 1:3 cocrystal was placed on a non-ambient chamber mounted on a laboratory diffractometer (see paragraph 2.4). The experiment was performed in order to replicate the thermal profile of DSC analysis, meanwhile collecting the powder patterns every 3 seconds. At the beginning, the cocrystal was the only

phase present and melted in the first heating at almost 42.0 °C. In the cooling run, a new phase crystallized at 12.0 °C, which remained stable until the second heating run at 39.0 °C, when it melted (*Figure 82*). After the second heating, the sample was thermalized and single crystals were obtained, that corresponded to the native HMT-THY 1:3 cocrystal. This suggested that the thermal profile influences the formation of a metastable phase that can only be isolated by a kinetically controlled cooling ramp.

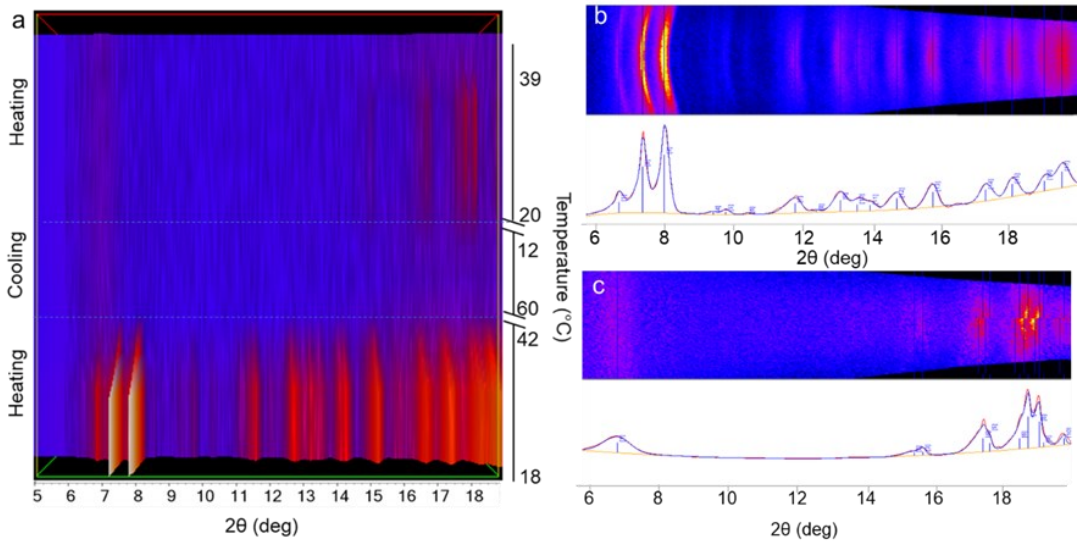

Figure 82. *a) Heatmap plot of PXRD patterns extrapolated by integrating the 2D images collected during the VT-PXRD measurement. b) 2D-PXRD pattern collected at 19.2°C during the first heating run and its integrated 1D-PXRD pattern corresponding to HMT-THY 1:3 cocrystal. c) 2D-PXRD pattern collected at 24°C during the second heating run and its integrated 1D-PXRD pattern corresponding to HMT-THY kinetic phase. Reprinted with permission from Cryst. Growth Des. 2022, 22, 7, 4260–4267. Copyright 2022 American Chemical Society.*

4.2.1 Mechanochemical synthesis

The results of the mechanochemical cocrystallization between HMT and THY are reported in *Figure 83*. The cocrystal was present since the first powder pattern of the reaction indicating the high reactivity of the two coformers. The signals of HMT and THY, in fact, monotonously decrease and reach almost the lowest concentrations already after 3 seconds of reaction. Decrease of coformers amount is accompanied by the formation of the amorphous low melting eutectic phase, whose amount reaches a maximum after 2 seconds. The cocrystal was totally obtained just after 5 seconds and its amount reached a plateau, according to an ultra-fast mechanochemical reaction. These results show the role of the eutectic phase which was originated from the coformers as a metastable phase and rapidly converted into the cocrystal.

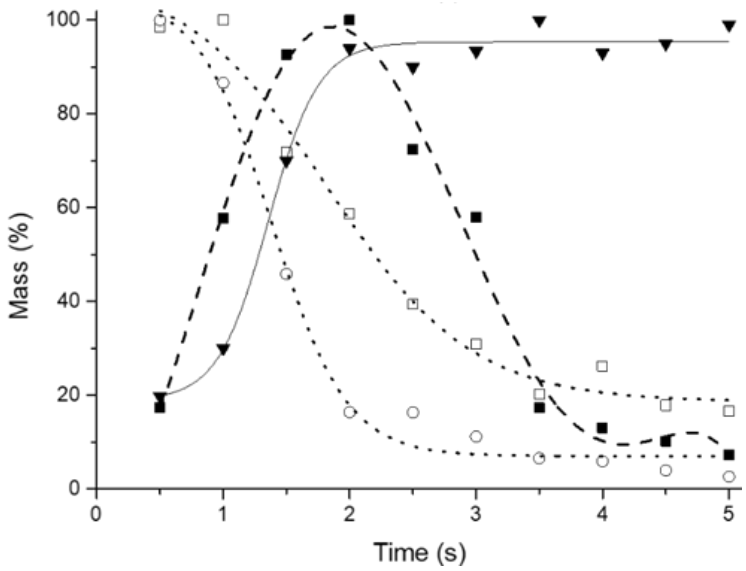

Figure 83. *Semiquantitative phase analysis (sQPA) performed via Rietveld Refinement. Experimental data for cocrystal (▼), eutectic phase (■), THY (□) and HMT (○) were reported as mass % normalized with respect to the maxima of each*

chemical specie. Sigmoidal fit of cocrystal data (solid black line), polynomial fit of the eutectic metastable phase (dashed black line), sigmoidal fit of coformers (dotted black line) as function of the milling time. Reprinted with permission from Cryst. Growth Des. 2022, 22, 7, 4260–4267. Copyright 2022 American Chemical Society.

4.2.2 Binary phase diagram

The composition of the eutectic phase, which plays as intermediate in the cocrystal formation of HMT and THY, was determined through the construction of the solid-liquid binary phase diagram (*Figure 84*). The experimental points of the phase diagram were determined by preparing mixtures of HMT-THY at different composition and then measuring the melting temperature of each mixture by means of DSC analyses.

The liquidus curve of THY was obtained using the Schröder-Laar equation[15] (*Eq. 1*), where χ_m (THY) is the experimental molar ratio of THY in the mixture under investigation, while T_{THY} and ΔH_{THY} are respectively the melting temperature and the enthalpy of fusion of THY as pure component.

The liquidus curve of cocrystal was not calculated using a thermodynamic interpolation since no experimental points can be collected beyond the cocrystal composition (χ_m (HMT) = 0.25). Moreover, a thermodynamic fit requires at least three experimental temperatures (excluding those referring to the pure cocrystal and the eutectic mixture) that would have all been grouped in a narrow range of molar compositions (0.15 < χ_m (HMT) < 0.25). Therefore, the liquidus curve of cocrystal was calculated with a second-order polynomial fit (*Eq. 2*).

$$ln\,\chi_m\,(THY) = \frac{\Delta H°_{THY}}{R}\left(\frac{1}{T_{THY}} - \frac{1}{T_{calc}}\right) \qquad \textit{Eq. 1}$$

$$T_{calc} = a\,(\chi_m\,(HMT))^2 + b\,(\chi_m\,(HMT)) + c \qquad \textit{Eq. 2}$$

χ_m (HMT) represents the experimental molar ratio of HMT, whilst *a*, *b*, *c* are the calculated parameter of the polynomial fit.

The liquidus curve of HMT was not experimentally derived due to its endothermic decomposition which prevents the accurate evaluation of the melting point of binary mixtures with an excess of HMT (χ_m (HMT) > 0.33). A linear fit passing through the pure HMT melting/decomposition and the cocrystal melting represent a first-order approximation guess of the liquidus curve of HMT. The liquidus curves of THY and HMT intersect at the metastable eutectic composition ε_{TH}, which is characterized by a melting point below ambient temperature in the standard laboratory conditions ($T\varepsilon_{TH}$ = 24.38 °C) (*Figure 84*, left).

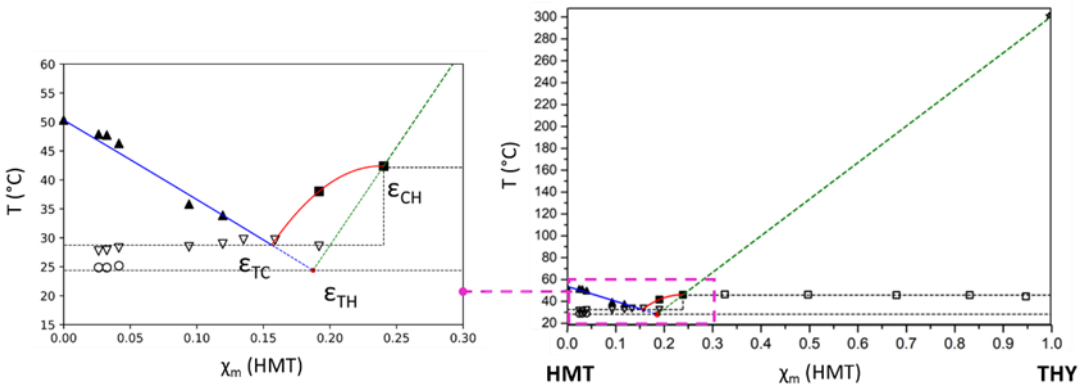

Figure 84. *Left: binary solid-liquid phase diagram of HMT/THY system. Solid lines represent the liquidus curves, dashed black lines represent the solidus curves. HMT, THY, and cocrystal liquidus curves are depicted in green, blu, and red respectively. Right: magnified portion of the binary phase in the range of 0 < χ_m (HMT) < 0.30 and 15°C < T < 60°C. The liquidus curves intersect each other at the eutectic composition ε_{TC} (χ_m (HMT) = 0.156, T_m = 28.75°C) and ε_{TH} (χ_m (HMT) = 0.187, T_m = 24.38°C). The experimental melting points are distinguished depending on the species they refer: ▲ = T_m of THY residue; ■ = T_m of cocrystal residue; ⋆ = $T_{decomposition}$ of HMT; ▽ = T_m of ε_{TC}, ○ = T_m of ε_{TH}.*

As further proof of the eutectic melting temperature, the thermal analyses of mixtures with a large excess of THY (χ_m (THY) < 0.04) showed the presence of a first endothermic peak in the second heating run at 24.86 °C (*Figure 85*), due to the melting of the mixture of two coformers which previously crystallized in the cooling run. This is consistent with the melting temperature of the eutectic mixture determined by the binary phase diagram. In *Figure 85* the experimental melting points of the binary eutectic mixtures are reported as hole circles.

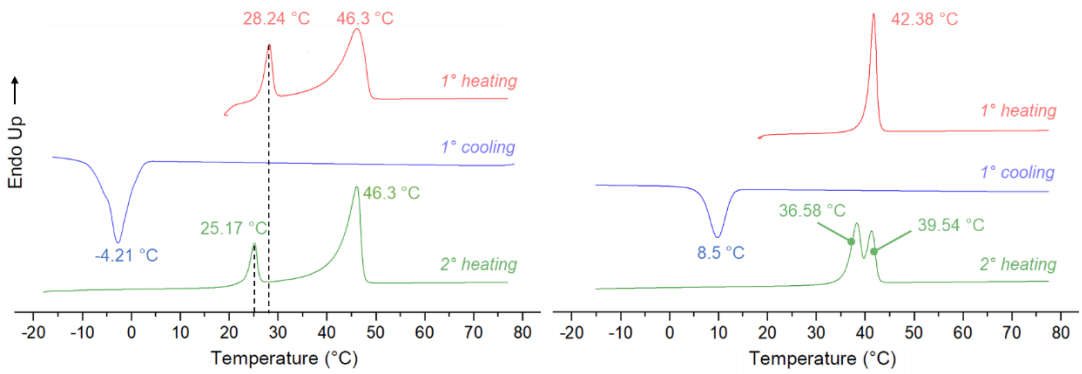

Figure 85. *Thermograms of binary mixtures with χ_m (HMT) = 0.026 (left) and χ_m (HMT) = 0.240 (right) composition. First heating run from 20 °C to 80 °C (red curve), cooling run from 80 °C to -20 °C (blue curve) and second heating run from -20 °C to 80 °C (green curve). Reprinted with permission from Cryst. Growth Des. 2022, 22, 7, 4260–4267. Copyright 2022 American Chemical Society.*

4.3 AZO-THY cocrystallization

The reactivity between AZO and THY was determined by getting in contact the crystals of both coformers on a glass plate and observing the physical variations by optical microscopy (*Figure 86*). At laboratory temperature (25 °C), the mere touch

of coformers crystals brought to the melting of their eutectic mixture and thus the formation of a liquid phase. This metastable liquid spread on the glass surface and dissolved other crystals of both species. After a few seconds from the first contact, a crystallization started from the liquid eutectic phase triggered by the hetero seeding of the residual crystals of both coformers. SCXRD analysis revealed that the new crystalline phase was AZO-THY 1:2 cocrystal (CC **1**).

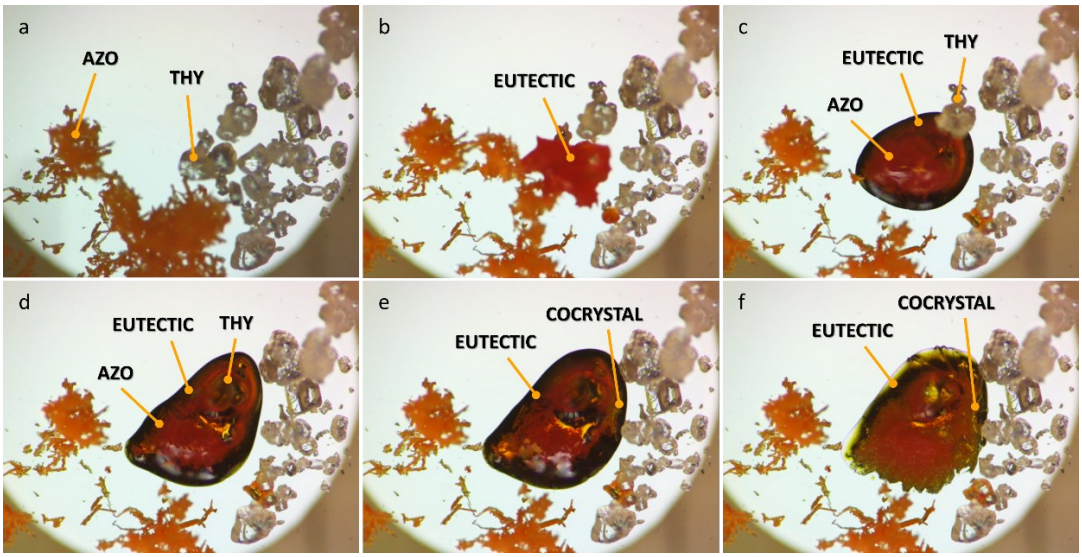

Figure 86. *Solid state reaction between AZO and THY monitored by means of optical microscopy (magnification x30). a) starting condition, separated crystals of AZO and THY. b-d) melting of the eutectic mixture between AZO-THY. e-f) cocrystal formation through hetero seeding.*

Single crystals of CC **1** were obtained through slow solvent evaporation from a solution of $CHCl_3$. CC **1** crystallizes in P-1 space group with a half formula unit in the asymmetric unit (Z = 1, Z' = 0.5, Z'' = 1.5). The inversion center lays on the double bond of the azo groups of AZO molecules, whose pyridinic rings are displayed on different planes with an interplanar distance of 0.253 Å. The phenolic group of THY molecules interacts with the nitrogen atom of pyridine rings via HB interactions

forming trimeric units (O···N: 2.743(4) Å; O-H···N = 174.6°) (*Figure 87*, left). The calculated energy associated with this hydrogen bond synthon was -39.4 kJ/mol, confirming this interaction as the driving force for the crystal packing. Trimers, in their turn, are organized in different offset chains due to the CH··· π (-13.8 kJ/mol) and CH···O (-17.1 kJ/mol) interactions among the *orto*-CH groups of pyridine molecules respectively with the aromatic rings and the O atoms of THY molecules (*Figure 87*, right). The offset chains instead interact through the THY molecules by establishing weak dispersive interactions.

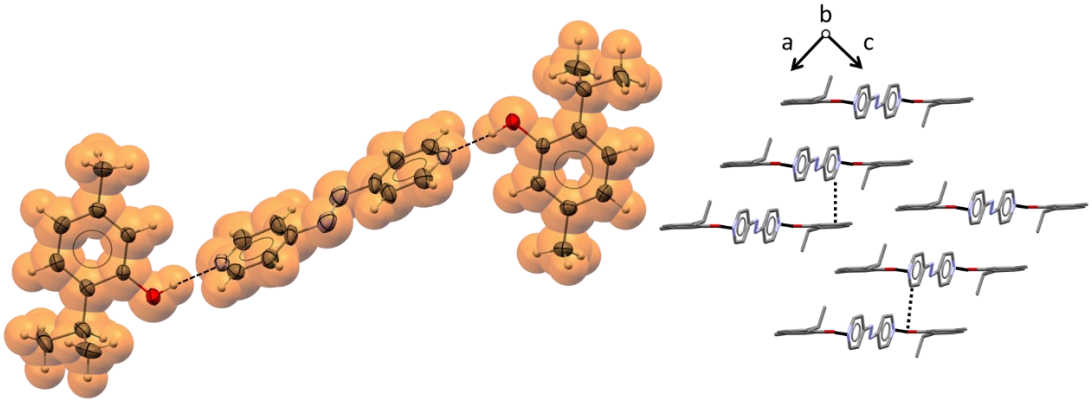

Figure 87. *Left: representation of the trimeric aggregate formed by OH···N hydrogen bond interactions in CC* ***1*** *crystal structure. Hydrogen bonds are depicted with a black dashed line. Right: molecular arrangements in CC* ***1*** *crystal structure driven by hydrogen bonds (solid black lines), CH···π interactions, and CH···O interactions (dotted black lines). Hydrogen atoms are omitted for sake of clarity.*

4.3.1 Mechanochemical synthesis

The results of the in situ monitoring of the mechanochemical cocrystallization between AZO and THY are reported in *Figure 88*. Also in this case, the cocrystal was

present since from the first patterns as symptom of the high reactivity between the coformers. Along with the decrease of coformers quantity, the amorphous eutectic phase was formed, reaching its maximum after 4 seconds, and then converted into CC **1**. This is supported by the complementary trends among all the species involved in the reaction. Nevertheless, the cocrystal formation was not immediate and oscillating trends are observed due to the sticky nature of the liquid eutectic phase. In fact, as soon as it is formed, the metastable liquid tends to adhere to the jar walls, partially dissolving the coformers powders and does not allow a homogenous mixing. When the cocrystal begins to form from the metastable liquid, it is removed from the jar walls thanks to the mechanochemical collisions and then the residual coformers powders, initially dissolved in the liquid phase, are finally mixed. This stepwise mechanism was repeated until the complete formation of the cocrystal and was coherent with the oscillating trends of all the species. The overall reaction ended in 12 seconds.

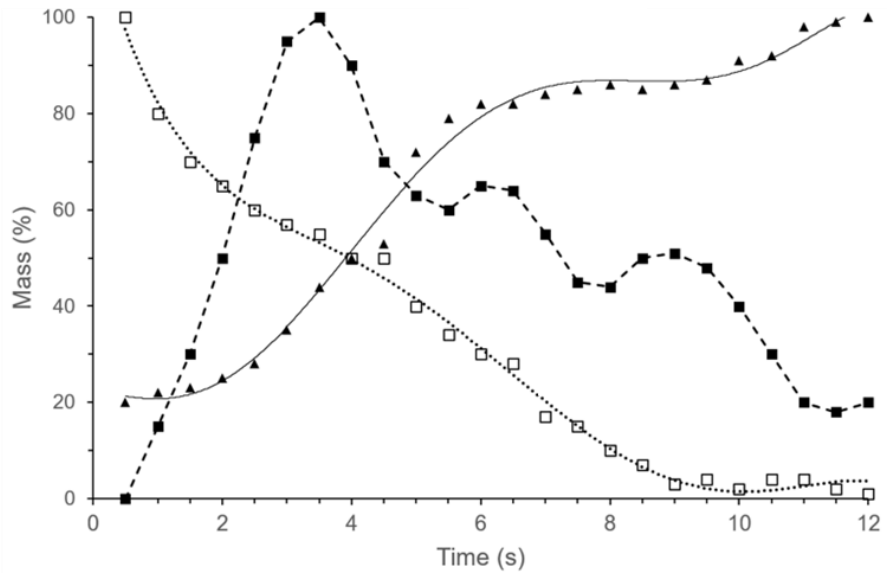

Figure 88. *Semiquantitative phase analysis (sQPA) performed via Rietveld Refinement. Experimental data for cocrystal (▼), eutectic phase (■), and coformers*

(□) were reported as mass % normalized with respect to the maxima of each chemical specie. Sigmoidal fit of cocrystal data (solid black line), polynomial fit of the eutectic metastable phase (dashed black line), and polynomial fit of coformers (dotted black line) as function of the milling time.

4.3.2 Raman spectroscopy

The cocrystallization between AZO and THY was also evaluated through Raman spectroscopy. The Raman spectrum of the liquid eutectic phase is reported in *Figure 89* (a). The metastable liquid was formed by the contact of a few crystals of AZO and THY, and remained inert as long as the hetero seeding was avoided. In order to monitor the cocrystallization process, a small crystal of CC **1**, previously obtained by mechanochemistry, was immersed in the metastable liquid and Raman spectra were acquired every 2 seconds after the seeding.

The first Raman spectrum was measured just after seeding (*Figure 89*, b) and results still comparable with the metastable liquid, while after 2 seconds a drastic decrease of the quasi-elastic scattering occurred (600 - 1600 cm^{-1}) and weak low-frequency bands appeared below 120 cm^{-1}, due to lattice vibrations and indicative of a crystalline phase. After 4 seconds, these lattice vibrations slightly increased up to the complete formation of CC **1**.

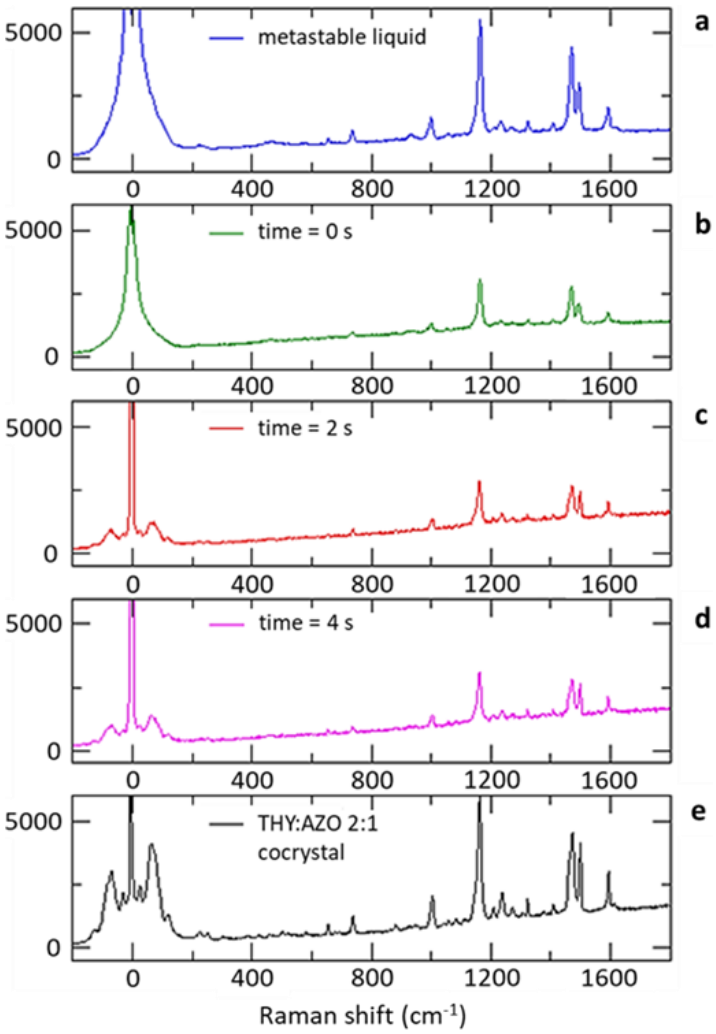

Figure 89. *Comparison of the Raman spectra acquired on the liquid eutectic phase before the hetero seeding (a), when the cocrystallization was triggered (b), after 2 seconds from the trigger (c), and after 4 seconds (d) with the Raman spectra of CC* ***1*** *obtained from mechanochemistry (e).*

4.3.3 Binary phase diagram

THY and AZO present a typical system of congruent mixing but with an unusual number and kind of phases. The thermal analysis of AZO-THY binary mixtures with different stoichiometries have evidenced a new cocrystal with AZO-THY 2:1 (CC **2**) molar ratio and the presence of another polymorph of AZO, already reported in the literature[16]. In *Figure 90* the resulting experimental AZO/THY binary solid-liquid phase diagram is shown. The binary phase diagram is divided into different regions through straight and dotted lines, that correspond to the liquidus and solidus curves. Basically, all these curves describe the region where either solid, liquid, or solid-liquid mixtures are thermodynamically favoured. Respectively, the liquidus curves refer to the coformers, THY (blue) and AZO (orange), and to the cocrystal AZO-THY 1:2 (CC **1**) (red). The two orange liquidus curves are due to the enantiotropic transition of polymorph I of AZO (filled circles)[17] into form II (filled stars), which occurs at 78.62 °C and was recorded for all the mixtures with χ_m (AZO) > 0.80.

The liquidus curve of THY, AZO (I), and AZO (II) were calculated using the Schröder-Laar equation (*Eq. 1*), referred to a pure phase in a binary mixture. The liquidus of CC **1** was instead obtained by means of Prigogine-Defay equation (*Eq. 3*), referred to multi-component crystals with ν_a:ν_b stoichiometry.

$$ln(\chi_a)^{\nu_a}(1-\chi_a)^{\nu_b} - ln(\chi_c)^{\nu_a}(1-\chi_c)^{\nu_b} = \frac{\Delta H^{\circ}_c}{R}\left(\frac{1}{T_a} - \frac{1}{T_{calc}}\right) \qquad \textit{Eq. 3}$$

In this case, AZO (I) was a priori established as “a” component and THY as “b” component, thus leading to $\nu_a = 1$ and $\nu_b = 2$; while χ_c represented the weight of “a” component into the cocrystal stoichiometry (AZO-THY 1:2), therefore $\chi_c = 1/3$.

The liquidus curve of CC **1** intersects the ones of the two coformers at the two eutectic points ε_{TC} (χ_m (AZO) = 0.16, T_m = 30.85 °C) and ε_{CA} (χ_m (AZO) = 0.44, T_m = 48.80 °C). Above the eutectic points, the system turns into a liquid phase, which consists of THY (liquid) and AZO (liquid), in equilibrium with a solid residue. This solid residue represents the excess of one component as compared to the eutectic composition. Hence, between the molar ratio of the two eutectic points, the solid residue consists of CC **1**, while at the extremes of the eutectic points, the excess is due to the coformers. Instead, the intersection of the liquidus of THY and AZO gives the extrapolated ε_{TA} eutectic point (χ_m (AZO) = 0.23, T_m = 21.77 °C), which is below the laboratory temperature (25 °C) thus justifying the existence of the intermediate liquid phase. This intermediate liquid is demonstrated to be metastable since its region of existence is below CC **1** liquidus curve. Moreover, in the region bordered by the liquidus of THY, AZO, and CC **1**, the liquid intermediate can be regarded as a supersaturated solution of CC **1** which may easily convert if opportunely stimulated (*Figure 86*).

All the experimental eutectic melting temperatures are crossed through the dotted solidus curves. So ε_{TA} delimits below the region where both the coformers are solid; while the regions between $\varepsilon_{TA} - \varepsilon_{TC}$ and $\varepsilon_{TA} - \varepsilon_{CA}$ melting temperatures, confined by the coformers liquidus, present CC **1** (solid) in equilibrium with respectively THY (solid) and AZO (solid).

The mixtures with χ_m (AZO) > 0.44, after grinding, revealed the existence of a new cocrystal phase AZO-THY 2:1 (CC **2**). The solidus curve of CC **2** is depicted with a magenta dotted line in *Figure 90*. This new cocrystal resulted stable but melted at the same temperature (T_m = 51.52 °C) in all the experimental mixtures after being subjected to heating. CC **2** thus exhibits an incongruent melting point since its range of stability is below the AZO liquidus curve, which is the most thermodynamic stable

phase in that range. After the incongruent melting, CC **2** decomposed into a liquid phase and an AZO solid residue, with this latter that afterward melted at the corresponding liquidus temperature. Besides, CC **2** should have a proper liquidus curve which would intercept CC **1** and AZO liquidus, but no experimental points were found to determine that curve since its limited extension.

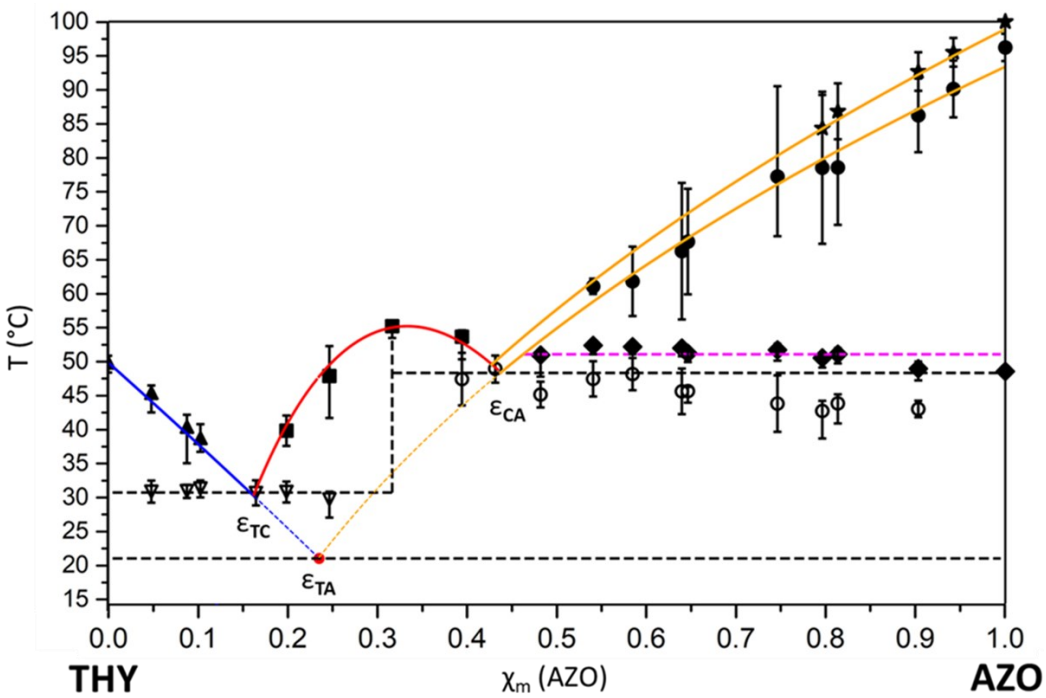

Figure 90. *Binary solid-liquid phase diagram of AZO/THY system. Solid lines represent the liquidus curves, dashed black lines represent the solidus curves. AZO, THY, and CC **1** liquidus curves are depicted respectively in orange, blue, and red, while CC **2** is depicted in magenta. The liquidus curves intersect each other at the eutectic compositions ε_{TC}, ε_{TA}, and ε_{CA}. Each melting point is affected to an error estimated considering as extremes the T_{max} and T_{min} associated to the peak width in experimental DSC thermograms. The experimental melting points are distinguished depending on the species they refer: ▲ = T_m of THY residue; ■ = T_m of CC **1** residue; ● = T_m of AZO(I) residue; ◆: T_m incongruent of CC **2**; ★: T_m of AZO (II) residue; ▽ = T_m of ε_{TC}; ○ = T_m of ε_{CA}, ●: T_m of ε_{TA}.*

4.3.4 Time-Resolved In Situ Powder X-ray Diffraction

The presence of another cocrystal (CC **2**) increased the number of coexisting phases in all the mixtures with χ_m (AZO) > 0.33 and thus the number of thermal events, whose understanding was not straightforward. Therefore, a VT-TRIS-PXRD analysis was performed for one of those mixtures (AZO-THY 2:1 mixture (χ_m (AZO) = 0.67)) adopting a comparable thermal profile with DSC measurements. The sample was investigated in air atmosphere employing a single heating ramp from 20 °C to 120 °C at 5°C/min. In *Figure 91* it is shown the sequence of powder patterns collected at increasing temperatures together with the DSC thermogram of AZO-THY 2:1 mixture. The first pattern was collected before the heating (*Figure 91*, up, blue) and shows the co-presence of CC **1**, CC **2**, and AZO phases in the starting mixture. At 47.8 °C, the Bragg reflections related to CC **1** began to diminish both with AZO reflections, and this up to 51.0 °C, according to the melting of their eutectic mixture ε_{CA} (T_m = 48.80 °C). Meanwhile, the formation of this liquid phase enriched of AZO component promoted the growth of CC **2**, whose Bragg reflections increased in intensity. These phenomena are consistent with the presence of an endothermic peak at 46.16 °C, immediately followed by an exothermic peak at 47.91 °C in the thermal profile (*Figure 91*, down). After these events, the AZO residue and CC **2** remained the only phases still present in the mixture. From 51.0 °C to 52.6 °C, the significant decrease of CC **2** phase was symptomatic of its incongruent melting, confirmed by an endothermic peak at 51.67 °C. All the crystalline phases vanished at 54.2 °C (*Figure 91*, up), although an enlarged endothermic peak associated with the melting of AZO residue occurred between 55-90 °C (*Figure 91*, down). This might be explained considering that eventual AZO residue could be remained on

the bottom of the copper sample holder and thus not be detected during the measurement.

This calorimetric study confirmed that liquid phases act as a medium in cocrystallization processes. Indeed, the two liquid intermediates involved in CC **1** and CC **2** cocrystallization have different compositions, nonetheless their formation turn out as an indispensable step. The main reasons for this evidence are to be found in the increasing of molecular mobility and diffusion, while the rapid conversion into cocrystal can be explained by the stability gain of liquid to solid transformation.

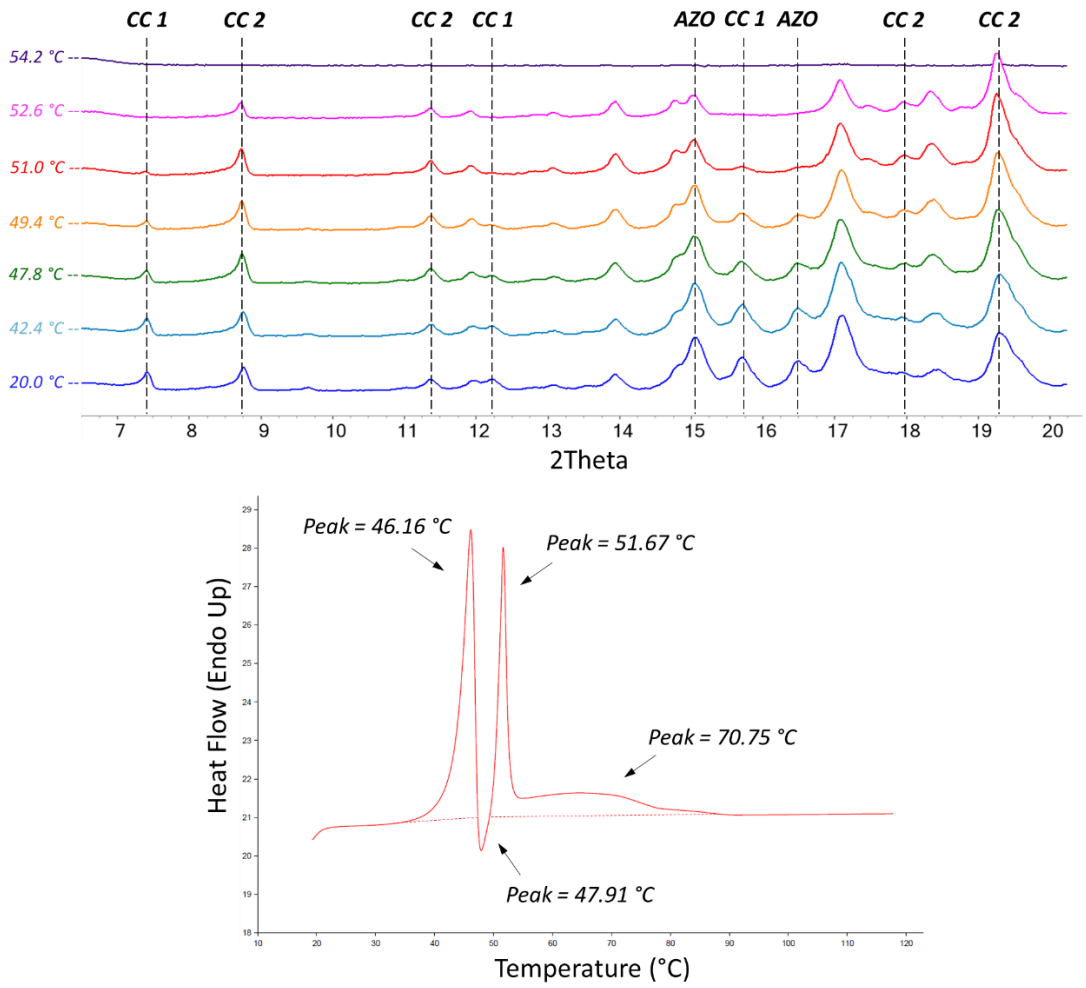

Figure 91. *Up: VT-TRIS-PXRD analysis performed on AZO-THY 2:1 mixture after ~10 min of grinding. Some of the most representative patterns are displayed as function of temperature. Patterns were collected during the single heating ramp (from 20 °C to 120 °C). Dotted vertical lines emphasized some Bragg reflections of the crystalline phases (AZO, CC* ***1****, CC* ***2****) involved during the thermal events. Down: thermogram registered for AZO-THY 2:1 mixture after ~10 min of grinding. The red straight line represents the heat flow while the red dotted line is the calculated baseline. The experiment was performed with a single heating from 20 °C to 120 °C.*

Bibliography

[1] A. Madani, B. Pieber, *ChemCatChem* **2023**, *15*, e202201583.

[2] Y. Zhao et al., *Chem. Rev.* **2023**, *123*, 6257–6358.

[3] S. Beutel, S. Henkel, *Appl. Microbiol. Biotechnol. 2011 916* **2011**, *91*, 1493–1505.

[4] B. F. Gomes, C. M. S. Lobo, L. A. Colnago, *Appl. Sci. 2019, Vol. 9, Page 498* **2019**, *9*, 498.

[5] A. A. L. Michalchuk, F. Emmerling, *Angew. Chemie Int. Ed.* **2022**, *61*, e202117270.

[6] S. Lukin, L. S. Germann, T. Friščić, I. Halasz, *Acc. Chem. Res.* **2022**, *55*, 1262–1277.

[7] G. I. Lampronti et al., *Nat. Commun. 2021 121* **2021**, *12*, 1–9.

[8] S. Lukin et al., *Chem. - A Eur. J.* **2017**, *23*, 13941–13949.

[9] K. Chadwick, R. Davey, W. Cross, *CrystEngComm* **2007**, *9*, 732–734.

[10] N. Biliškov, *Cryst. Growth Des.* **2021**, *21*, 1434–1442.

[11] P. P. Mazzeo et al., *ACS Sustain. Chem. Eng.* **2019**, *7*, 17929–17940.

[12] F. Bianchi et al., *Food Chem.* **2021**, *347*, 129051.

[13] P. P. Mazzeo et al., *Faraday Discuss.* **2023**, *241*, 289–305.

[14] P. P. Mazzeo, M. Prencipe, T. Feiler, F. Emmerling, A. Bacchi, *Cryst. Growth & Des.* **2022**, *22*, 4260–4267.

[15] I. P. and R. Defay, *Chemical Thermodynamics*, Longmans Green, **1954**.

[16] P. P. Mazzeo, C. Carraro, A. Arns, P. Pelagatti, A. Bacchi, *Cryst. Growth Des.* **2020**, *20*, 636–644.

[17] K. M. Hutchins et al., *CrystEngComm* **2016**, *18*, 8354–8357.

CHAPTER 5

Pair distribution function analysis on organic compounds

The correlation between molecular organization and physical properties has been largely discussed in the previous chapters, bringing out the importance of knowing how molecule are arranged in materials. Any compound can always be defined according to the order of its arrangement, thus crystalline, amorphous, and liquid compounds are easily differentiable. To this purpose, X-ray diffraction techniques represent the straightforward way to recognize the presence of long or low order range materials, through the evaluation of the coherent scattering (*i.e*. Thomson scattering), that is responsible for the Bragg peaks. However, a more detailed

information concerning the local arrangement, which involves a few pairs of neighbouring atoms/molecules, also requires the study of the weak diffuse scattering, whose determination usually implies long acquisition times. The diffuse scattering is the result of different crystal defects, such as dislocation, stacking faults, or disorder. The measurement of coherent and diffuse scattering consists in performing a total scattering experiment. PXRD and SCXRD are common examples of total scattering experiments, despite their measurements are usually set up on the maximization of the coherent contribution, acquiring information only about the crystal structure, the phase quantification, and the microstructure. The local organization can be instead determined by the Fourier transformation of the total scattering structure function $S(Q)$[1], thus obtaining the pair distribution function (PDF) $G(r)$:

$$G(r) = \frac{2}{\pi} \int_{Q_{min}}^{Q_{min}} Q[S(Q) - 1] \sin(Qr)\, dQ$$

where $Q = 4\pi\ (sin\ \theta/\lambda)$ is the wave vector with wavelength λ and scattering angle 2θ.

The PDF analysis returns the probability of finding pairs of atoms at a certain distance, and PDF peaks are weighted on the scattering power of each pair. PDF is directly obtained from the experimental powder pattern, after subtracting the background contribution, which is opportunely measured in the same conditions and takes into account sample container, inelastic scattering (Compton), or absorption phenomena. After the background subtraction, the resulting function is normalized by the scattering factors and number of scatters, finally obtaining the total scattering structure function $S(Q)$, which gives $G(r)$[2].

PDF analysis has attracted popularity for the possibility of having access to the structure of small molecular clusters or nanocrystalline materials. The classical application of PDF analysis has regarded the determination of nanoparticles domain

size[3], or the quantification of the amorphous content in a sample[4]. PDF analysis has been largely developed for inorganic materials, instead the study of organic compounds has been delayed due to the intrinsic lower scattering power of the light atoms they are made of. Nevertheless, in the last years several studies have shown even the possibility to solve the crystal structure of organic compounds through a PDF fit[5,6], without prior indexing[7], or using the Artificial Intelligence (AI)[8]. The PDF analysis of organic compounds has been also used to determine the orientational disorder[9], or to evaluate the effects on the local structure due to the micronization and amorphization[10]. All these results required the use of synchrotron X-ray sources; however, in the last years laboratory sources have been improved by permitting successful accomplishments for the easier topics[11,12].

In the previous chapter, the low melting eutectics of two binary mixtures were found to be involved into the cocrystals formation, acting as intermediates for the cocrystal nucleation. Although the eutectic compositions were closer to the cocrystals stoichiometries, the investigations did not allow to draw conclusions concerning the local arrangements of the eutectic mixtures, whose compositions exclusively depend on the thermodynamics of the binary mixtures. Indeed, the eutectic composition is the intersection of the liquidus curves of the two components, that are determined by the enthalpy of fusions and melting temperatures (*Eq.1* and *Eq.3*) rather than the interactions among components. Here another example of cocrystallization will be proposed, passing through a low melting eutectic mixture and involving the essential oil thymol (THY) and the coformer pyrazine (PYR) (*Scheme 4*). However, in this case, the liquid intermediate was metastable enough to be analysed for a long time without converting into the PYR-THY 1:2 cocrystal[13]. The purpose of this study was thus to perform PDF analyses on both the eutectic mixture and the cocrystal, in order to compare their local arrangements and eventually find a pre-organization in the liquid

intermediate, such as to justify its role into the cocrystal formation. The measurements were performed on a laboratory diffractometer, using the experimental conditions described in the paragraph 2.5.

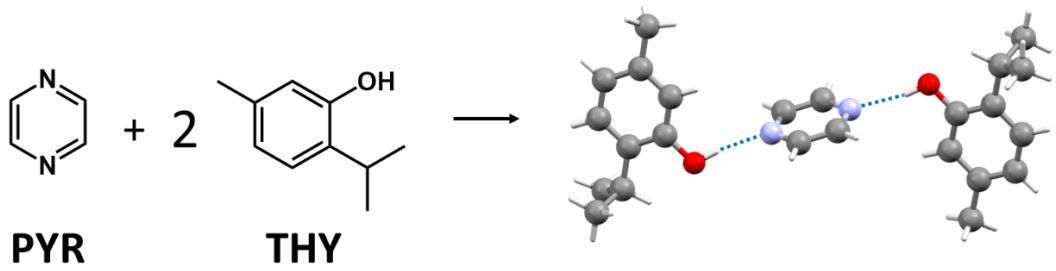

Scheme 4. *Cocrystallization of thymol (THY) with pyrazine (PYR).*

5.1 Binary phase diagram of PYR-THY

The eutectic composition of the PYR-THY system was determined by constructing their binary phase diagram. The experimental melting points were measured by performing DSC analyses on PYR-THY binary mixtures at different stoichiometries. In this case, considering the low T_m of the eutectic ε_{CP} (*Figure 92*), all the mixtures were prepared grinding the reactants at low temperature (below 10 °C) using a Retsch MM 500 ball mill, and then thermalizing the mixtures at 5 °C for 24 hours before the DSC analysis.

The liquidus curves of PYR and THY were calculated according to the Schröder-Laar equation (*Eq. 1*), referred to a pure phase in a binary mixture, while the cocrystal liquidus was obtained by means of the Prigogine-Defay equation (*Eq. 3*).

The liquidus curve of cocrystal intersects the ones of the two coformers at the two eutectic points ε_{TC} (χ_m (PYR) = 0.15, T_m = 36.50 °C) and ε_{CP} (χ_m (PYR) = 0.58, T_m = 10.51 °C). The slight uncertainty of the experimental melting temperatures for

χ_m (PYR) > 0.60 is due to the difficulty of maintaining those binary mixtures at the same composition (cocrystal + pyrazine), considering the low temperature of ε_{CP} and the rapid sublimation of PYR. Instead, the intersection of the liquidus of THY and PYR gives the extrapolated ε_{TP} eutectic point (χ_m (PYR) = 0.58, T_m = -12.97 °C), which is significantly below the laboratory temperature (25 °C). However, differently from HMT-THY and AZO-THY systems, in this case the eutectic composition results far from the cocrystal stoichiometry (χ_m (PYR) = 0.33).

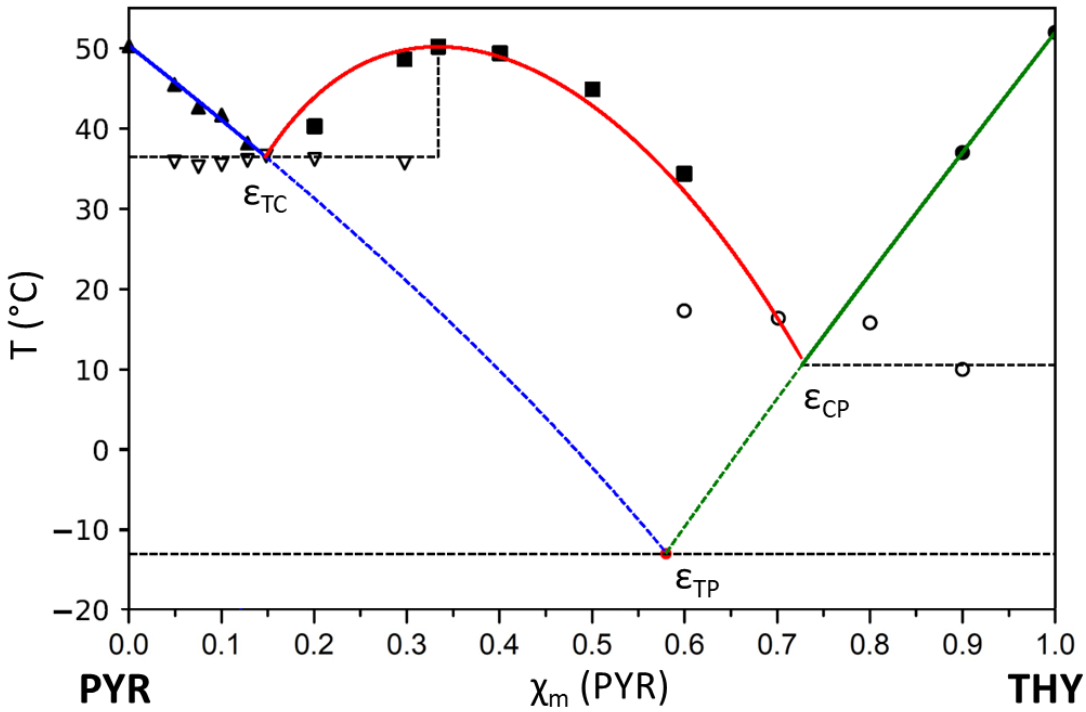

Figure 92. *Binary solid-liquid phase diagram of PYR/THY system. Solid lines represent the liquidus curves, dashed black lines represent the solidus curves. PYR, THY, and cocrystal liquidus curves are depicted respectively in green, blue, and red. The liquidus curves intersect each other in the eutectic compositions ε_{TC}, ε_{TP}, and ε_{CP}. The experimental melting points are distinguished depending on the species they refer: ▲ = T_m of THY residue; ■ = T_m of cocrystal residue; ● = T_m of PYR residue; ▽ = T_m of ε_{TC}; ○ = T_m of ε_{CP}, ●: T_m of ε_{TP}.*

5.2 Rietveld refinement on PYR-THY system

The experimental powder patterns of coformers and cocrystal collected during the total scattering measurements were checked to confirm the crystal phases and evaluate the experimental conditions, before being processed to obtain the PDFs. As a general consideration, all the powder patterns show a weak scattering power with detectable peaks until 2θ = 20°, except for pyrazine whose Bragg peaks are found until 2θ = 45°. This is due to the low scattering power of the light atoms in the system, and to the low crystallinity of the compounds. The presence of Bragg peaks at high 2θ is crucial to obtain a PDF with high resolution, which is expressed in terms of Q_{max} according to the wave vector definition $Q = 4\pi\ (sin\ \theta/\lambda)$. The theoretical resolution should be Q_{max} = 20.36 $Å^{-1}$, for θ = 65°, however the last Bragg peaks remodulate the value at Q_{max} = 3.90 $Å^{-1}$, which is definitely low but sufficient to discriminate a crystalline compound (cocrystal) from an amorphous one (liquid eutectic phase).

The Rietveld refinement of PYR (*Figure 93*) confirms the presence of the expected PYR phase, nonetheless all the Bragg peaks with 2θ > 14° exhibit a strong aberration due to the intrinsic nature of the sample and its preparation. In fact, PYR sublimes at ambient temperature (25 °C) and tends to aggregate even after grinding, thus making the filling of capillaries more complicated. Therefore, the resulting powder pattern evidence preferred orientations and strong aberrations due to the lack of homogeneity of the sample.

The powder pattern of THY is instead in agreement with the known crystalline phase, as supported by the difference curve shown in *Figure 94*.

At last, the Rietveld refinement of PYR-THY 1:2 cocrystal reveals the simultaneous presence of cocrystal and THY phase, with the latter probably formed during the

data collection (*Figure 95-96*). Indeed, the long exposure time of the experiment and the energy of radiation could have induced the cocrystal disruption and the release of the coformers. Although both the coformers are extremely volatile, the absence of PYR can be related to its faster sublimation process.

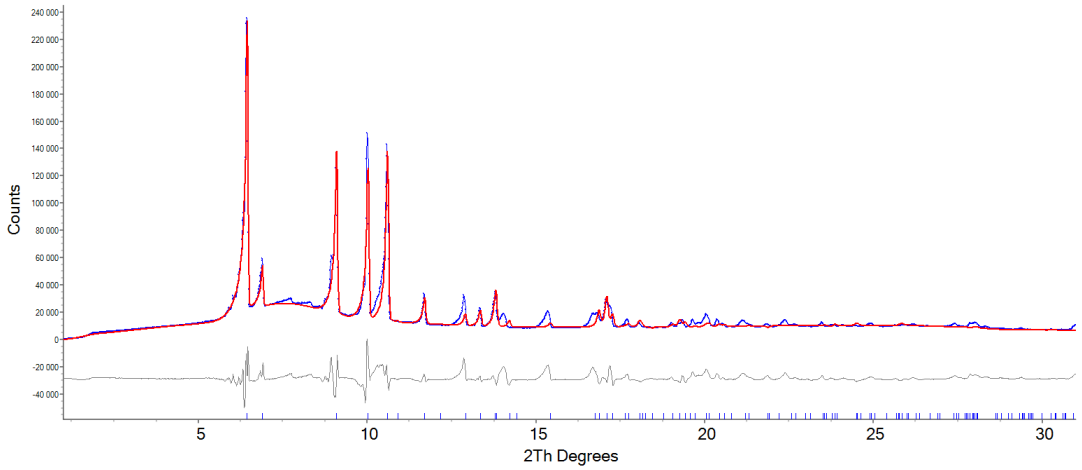

Figure 93. *Rietveld fit of PYR (red line) against experimental data (blue dots). Tick marks indicate calculated reflection positions. Ycalc-Yobs residual curve is reported in grey.*

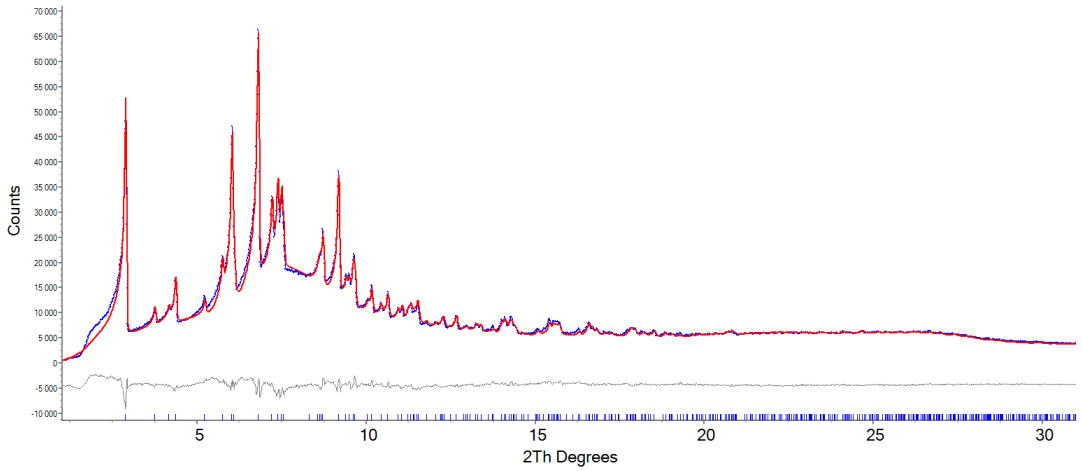

Figure 94. *Rietveld fit of THY (red line) against experimental data (blue dots). Tick marks indicate calculated reflection positions. Ycalc-Yobs residual curve is reported in grey.*

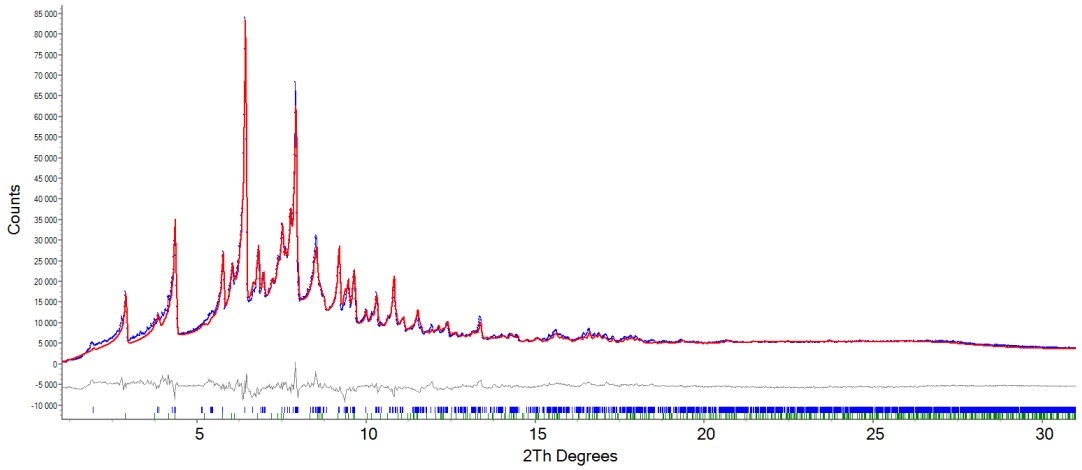

Figure 95. *Rietveld fit of PYR-THY 1:2 cocrystal (red line) against experimental data (blue dots). Multi-phases refinement was performed since an amount of THY was found. Tick marks indicate calculated reflection positions. Ycalc-Yobs residual curve is reported in grey.*

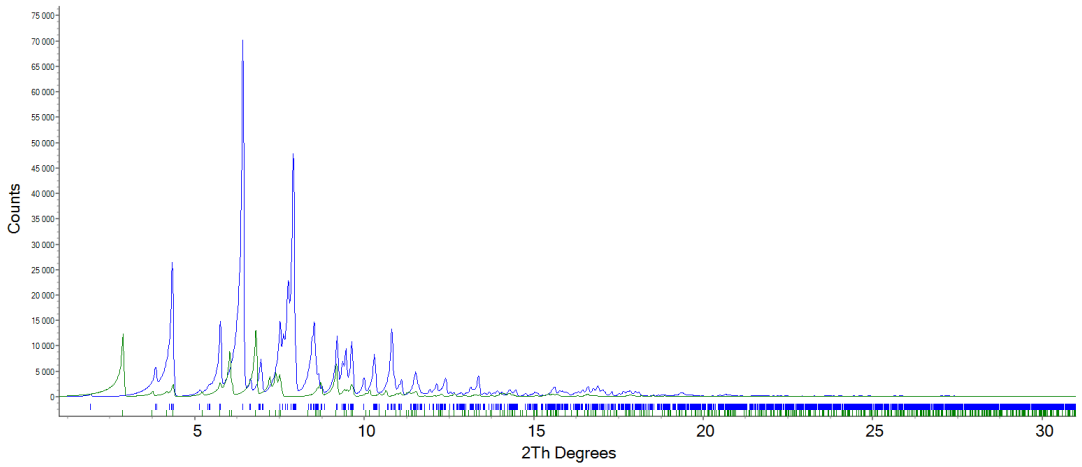

Figure 96. *Representation of PYR-THY 1:2 cocrystal (blue) and THY (green) in multi-phases Rietveld fit of PYR-THY 1:2 cocrystal reported in Figure 94. Tick marks indicate calculated reflection positions.*

5.3 PDF analysis on PYR-THY system

The processing of total scattering powder patterns was performed adopting a Q_{max} of 3.90 Å^{-1} for THY, cocrystal, and the liquid eutectic phase, while a resolution of 8.60 Å^{-1} was chosen for PYR. Even though the PDF analysis of coformers was not necessary in order to compare the local structure of cocrystal and liquid eutectic, on the other hand it helped to evaluate the reliability of the data.

The $G(r)$ function of PYR (*Figure 97*) was obtained by correcting the total scattering function $S(Q)$ with a polynomial function of six order according to the relation:

$$r_{poly} = \pi n / Q_{maxinst}$$

where n is the polynomial order and $Q_{maxinst}$ is the maximal resolution according to the experimental conditions (20.36 Å^{-1}).

The resulting r_{poly} = 0.93 expresses a low-r bound threshold of reliable $G(r)$ values.

The first peak of $G(r)$ function of PYR correctly corresponds to the average length of C-C and C-N bonds of PYR molecules (1.323 Å), while the second peak refers to the intramolecular distances between atoms separated by two bonds (2.412 Å). The crystallinity of PYR is confirmed by the repetition of $G(r)$ peaks with a periodicity of 9.314 Å, which corresponds to the length of the a-axis cell, however incorrect values are observed after two unit cells (*Figure 97*, *dotted line*). Moreover, the periodicity along b-axis and c-axis is not appreciable probably due to the lower axis lengths that are more influenced by the aberrations found in the experimental powder pattern for high 2θ values.

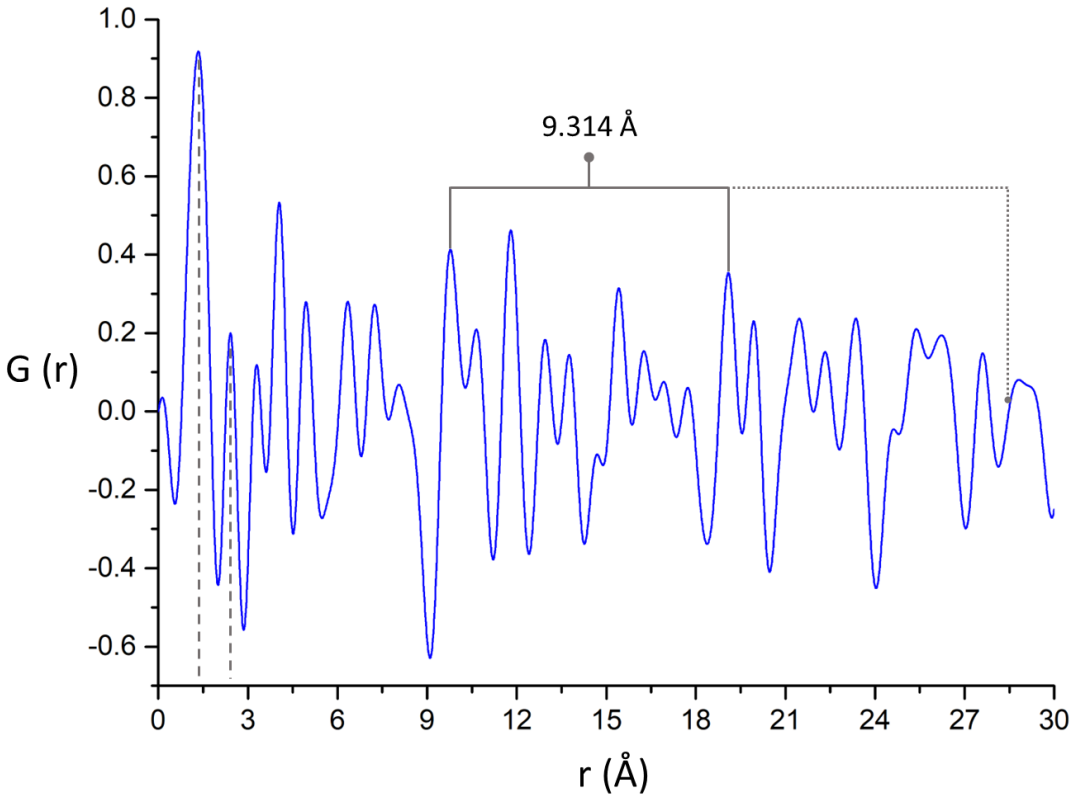

Figure 97. *Pair distribution function (PDF) of PYR. Dashed lines highlight the PDF peaks, while straight and dotted lines the periodicity along the a-axis.*

The PDF fit of PYR (*Figure 98*) was performed by imposing bond and angle constraints with a rigid body model. The fit agrees with the considerations on $G(r)$

function, in fact the peak position of the first two peaks, and the others at a distance of 9.314 Å within two unit cells, are correctly generated. Instead, all the other peaks, and thus the information along the b- and c-axis, are mistaken, and this influences even the fit of the correct peaks since the peak width was badly described.

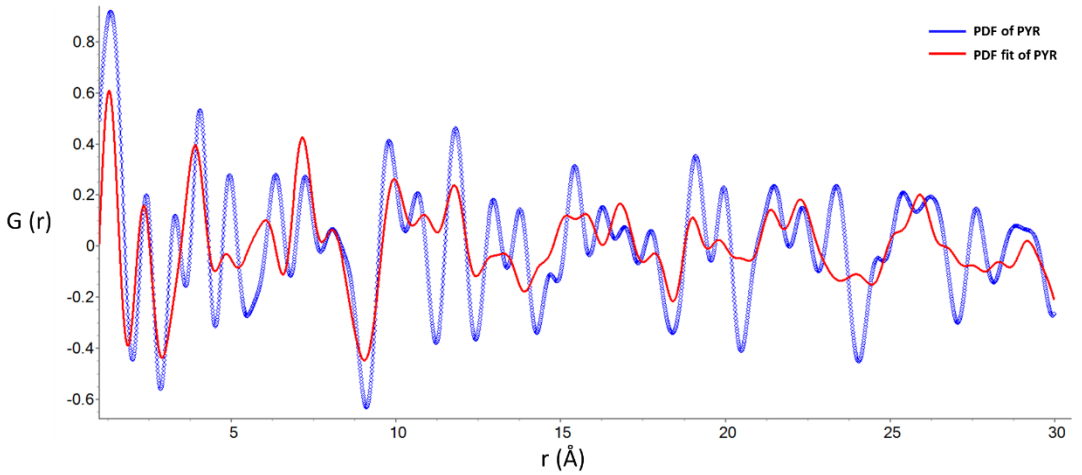

Figure 98. *PDF fit (red) of PYR against experimental PDF (blue).*

The $G(r)$ function of THY (*Figure 99*) was obtained using r_{poly} =0.91 and clearly exhibits a low resolution, as shown by the large width of the peaks, with Q_{max} = 3.90 Å^{-1}, against 8.60 Å^{-1} for PYR. Nonetheless, the first peak of $G(r)$ has a reasonable value (1.384 Å), which is included within the range of C-C aromatic bonds and C-O bond lengths (1.381-1.394 Å). The low resolution also influences the damping of $G(r)$ function since no reliable peaks are observed after 2θ = 20 Å (*Figure 99*). Even though the profile of $G(r)$ resembles that of a nanocrystalline material, in this case the peaks after 2θ = 20 Å are the result of the noise collected at high 2θ values, where the intensities of the Bragg and diffuse peaks are extremely low. Therefore, the damping is main consequence of the weak power scattering of THY, and in minor quantity of its low crystallinity. The periodicity of THY crystal structure is not appreciable considering the shortest axes cell have a length of 14.73 Å. In addition,

it is worth noting that the intermolecular distance of HBs (2.703 Å) is not related to any peak in the $G(r)$ function, since the extremely low resolution does not allow to perceive more than two peaks in the range 1-3 Å.

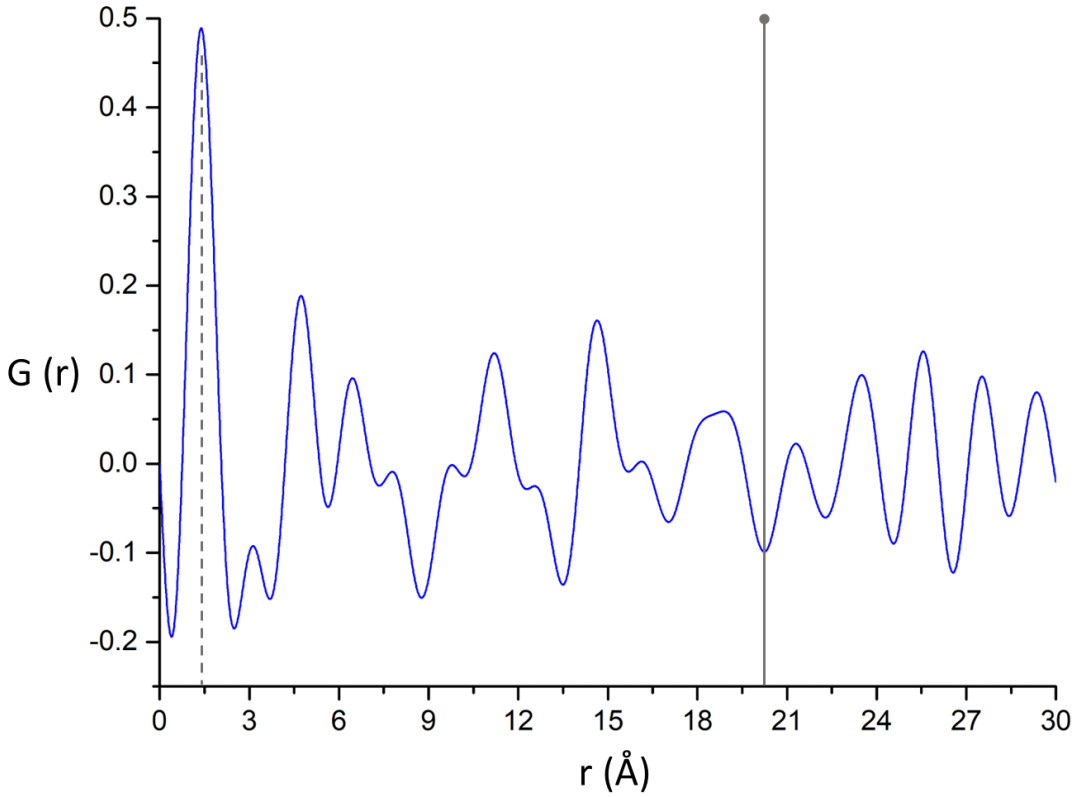

Figure 99. *Pair distribution function (PDF) of THY. The dashed line highlights the first PDF peak, while the straight line the range of reliable peaks (0-20 Å).*

The PDF of THY (*Figure 100*) was performed using a rigid body model and gives a much better outcome than for PYR. The main issue of the fit is related to the peak width, expression of the thermal motion and taken into account by means of the isotropic thermal parameters (Beq). In the case of organic compounds, the thermal motion of atoms within the same molecule is correlated, giving sharper peaks due to the strength of covalent bonds[14]. Instead, the intermolecular interactions, and thus the intermolecular pairs, are less correlated than intramolecular ones, with the

result of broader peaks. Therefore, the peak width was modelled using two different Beq parameters for intra and inter pairs. Nonetheless, there is always a range in the $G(r)$ function where inter and intra peaks are superimposed, making difficult the discrimination of the two contributions. In this specific case, the low resolution of $G(r)$ function further hinders the PDF fit because of the broad peaks.

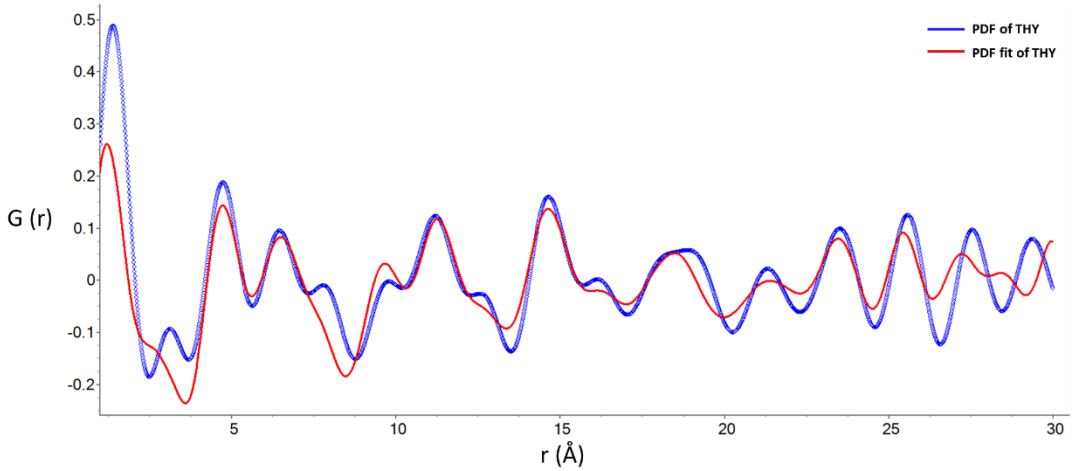

Figure 100. *PDF fit (red) of THY against experimental PDF (blue).*

The $G(r)$ function of PYR-THY 1:2 cocrystal (*Figure 101*) was obtained using r_{poly} = 0.90 and the same Q_{max} of THY (3.9 $Å^{-1}$). The first peak falls at 1.334 Å, which is the average length of C-C and C-N bonds of PYR, and the pronounced peak width also suggests the presence of C-C and C-O bonds of THY molecules. However, the other peaks do not correspond to relevant atom pairs, considering that the residual amount of THY found through the Rietveld refinement altered the $G(r)$ peaks. The low scattering power of cocrystal is confirmed by the maxima of the peaks, similar to THY, while the crystallinity is maintained within the range 0-30 Å. Even in this case, the region of the HBs (2.7-2.8 Å) cannot be appreciated due to the low resolution of the measurement.

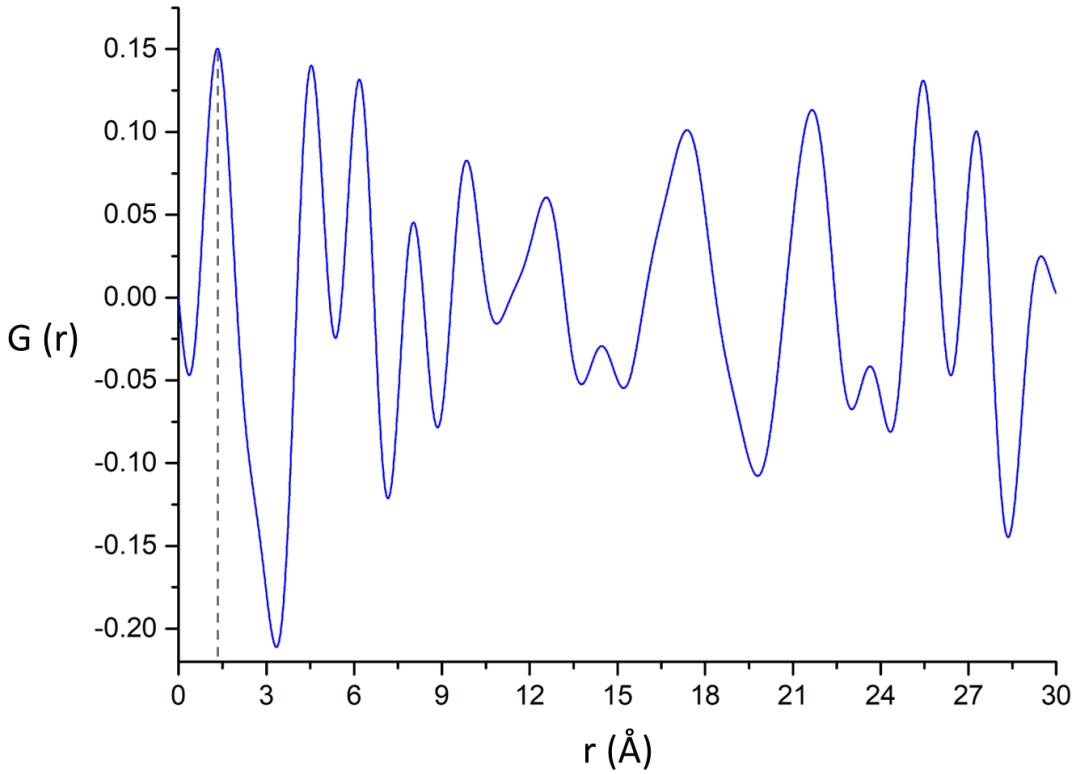

Figure 101. *Pair distribution function (PDF) of PYR-THY 1:2 cocrystal. The dashed line highlights the first PDF peak.*

The PDF of PYR-THY 1:2 cocrystal (*Figure 102*) was performed using a rigid body model and maintaining the same proportion between cocrystal and THY phases, previously determined by Rietveld refinement. Even adopting different Beq parameters for intra and intermolecular pairs, the peak width was not opportunely modelled. While the peak position of the peaks below 10 Å was partially satisfied, instead serious issues were addressed in the region over 10 Å. The reason has to be found in the lower power of scattering and crystallinity of the residual THY, compared to cocrystal, as showed in the $G(r)$ function of THY (*Figure 99*). Indeed, it is likely that THY mostly contributes to the $G(r)$ function for r < 10 Å, while beyond this threshold its contribution is equivalent to noise. This means that the THY and cocrystal should have two different damping functions, but the low resolution and

the high number of refinable parameters complicated the handling of the refinement.

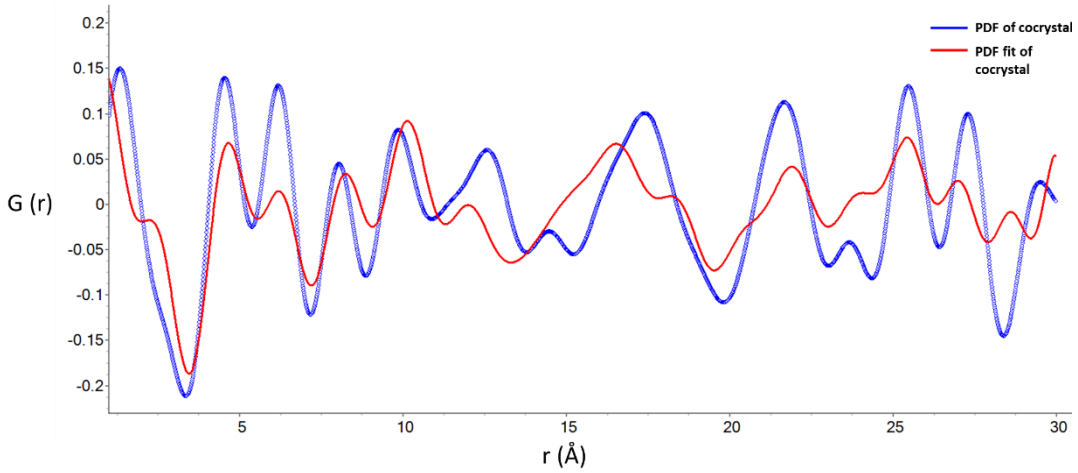

Figure 102. *PDF fit (red)of PYR-THY 1:2 cocrystal against experimental PDF (blue).*

The $G(r)$ function of the liquid eutectic phase was processed with the same resolution of cocrystal (Q_{max} = 3.9 Å^{-1}), in order to be easily compared, and with r_{poly} = 0.91. By superimposing the $G(r)$ functions of cocrystal and liquid eutectic a great similarity is pointed out (*Figure 103*). The first peaks are almost overlapped, even though the liquid eutectic shows a slightly lower value (1.320 Å), which is more similar to the distances of C-C and C-N pairs of PYR, due to the higher concentration of PYR in the eutectic composition rather than into the cocrystal. Also the others PDF peaks are quite comparable, however the information concerning the local arrangement, particularly in the region where intra and intermolecular pairs are overlapped, is not accessible due to the lower resolution. On the other hand, it is evident that the liquid eutectic has a short range order since the PDF function rapidly damps after 10.5 Å. It is interesting that this value is in the range of distances between pairs of atoms belonging to two neighbouring molecules, either THY-THY or PYR-THY, in cocrystal structure[13]. This might mean that the distance between whatever couple of neighbouring molecules in the liquid eutectic is similar to

distance between neighbouring molecules into cocrystal, with the difference that no periodic arrangement involving more distant molecules is already formed in the eutectic mixture, as confirmed by the damping of the eutectic PDF.

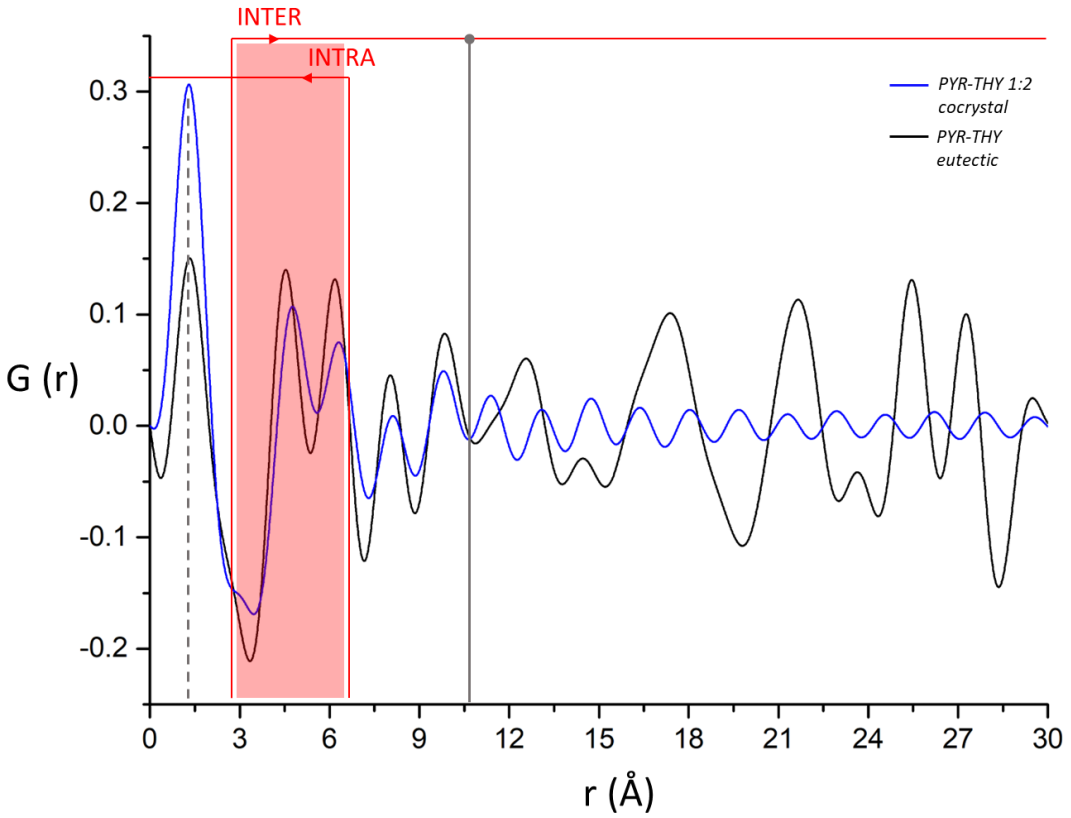

Figure 103. *Comparison of the pair distribution function (PDF) of PYR-THY 1:2 cocrystal (blue) and the metastable liquid eutectic phase (black). The dashed grey line highlights the first PDF peak of the eutectic phase, while the grey straight line the short range order. Red arrows indicate the intra and inter pairs distances within the cocrystal structure.*

In conclusion, the data quality of the experimental powder patterns and their low resolution are strongly influenced by the weak power of scattering and the low crystallinity of the compounds. According to these experimental conditions, it was possible to identify the first peaks of PDFs, that were related to the bond distances,

while no reliable information regarding the local arrangement was found, particularly in the case of cocrystal. In order to improve these issues, a total scattering experiment using synchrotron radiation is necessary, even to reduce the exposure time and avoid the cocrystal disruption.

Bibliography

[1] T. Egami, S. Billinge, *Underneath the Bragg Peaks*, Elsevier, **2012**.

[2] M. W. Terban, S. J. L. Billinge, *Chem. Rev.* **2022**, *122*, 1208–1272.

[3] R. B. Neder, V. I. Korsunskiy, *J. Phys. Condens. Matter* **2005**, *17*, S125.

[4] J. Peterson et al., *J. Appl. Crystallogr.* **2013**, *46*, 332–336.

[5] D. Prill, P. Juhás, S. J. L. Billinge, M. U. Schmidt, *Acta Crystallogr. Sect. A Found. Adv.* **2016**, *72*, 62–72.

[6] C. Schlesinger et al., *IUCrJ* **2022**, *9*, 406–424.

[7] Carina Schlesinger, S. Habermehl, D. Prill, *J. Appl. Crystallogr.* **2021**, *54*, 776–786.

[8] L. Yang, P. Juhás, M. W. Terban, M. G. Tucker, S. J. L. Billinge, *Acta Crystallogr. Sect. A Found. Adv.* **2020**, *76*, 395–409.

[9] C. Schlesinger, S. M. Hammer, T. E. Gorelik, M. U. Schmidt, *Acta Crystallogr. Sect. B Struct. Sci. Cryst. Eng. Mater.* **2020**, *76*, 353–365.

[10] M. W. Terban et al., *Mol. Pharm.* **2020**, *17*, 2370–2389.

[11] S. L. J. Thomae et al., *Rev. Sci. Instrum.* **2019**, *90*, DOI 10.1063/1.5093714/283175.

[12] D. Tsymbarenko, D. Grebenyuk, M. Burlakova, M. Zobel, *J. Appl. Crystallogr.* **2022**, *55*, 890–900.

[13] F. Montisci et al., *ACS Sustain. Chem. Eng.* **2022**, DOI 10.1021/ACSSUSCHEMENG.2C01257.

[14] D. Prill, P. Juhás, M. U. Schmidt, S. J. L. Billinge, *J. Appl. Crystallogr.* **2015**, *48*, 171–178.

CHAPTER 6

Conclusions

Along this thesis, the theme of cocrystallization has been largely developed leading to a further comprehension of the phenomenon and significant results in terms of potential application. Once selected the most promising active ingredients, cocrystallization has been proven as an efficient strategy to improve the physical properties of these molecules. In total, 23 new cocrystals were obtained using mechanochemistry, most of them containing thymol, carvacrol, and eugenol. The melting points of cocrystals were found generally between the melting points of the coformers. This was sufficient to sensibly stabilize essential oils such as

carvacrol or eugenol, which are liquid at ambient conditions, while a cocrystal based on thymol even exhibited a melting point higher of both coformers. The properties of cocrystals were also influenced by the synthesis of opportune azopyridinic coformers, which were designed to establish heteromeric interactions with the selected active ingredients. It has been demonstrated that the azopyridinic coformers interact with UV radiation even within the cocrystal structure, modifying the release of essential oils. Although the mechanism of interaction was supposed to be the trans-to-cis isomerization, after the irradiation no proofs of cis azopyridinic isomer were detected. The cocrystal **2**-EUG 1:1 has shown a higher response upon irradiation with a significant loss of eugenol after 24 hours.

The mechanism of cocrystalizzation was also investigated by an in situ monitoring of the process with a multi-technique approach. Two cases of cocrystallization were evaluated, characterized by the formation of a liquid intermediate from which the cocrystal crystallized. The analyses of the mechanochemical reactions and the construction of the binary phase diagrams have demonstrated that the liquid intermediates represent the eutectic mixtures between the coformers. These have shown a melting point below the laboratory temperature (25 °C) and have been revealed as the fundamental step in the cocrystal formation. In addition, the compositions of the eutectic phases have been found similar to the cocrystals stoichiometries. The in situ investigation has been fundamental for the comprehension of cocrystals mechanisms.

The reason behind the role of liquid eutectic phases in cocrystals formation was further deepened with the pair distribution function (PDF) analysis. A case of study based on a metastable eutectic composition was investigated showing a similarity between the pair distribution functions of the cocrystal and the liquid eutectic phase. PDF analysis revealed to be a useful tool to distinguish amorphous from

crystalline compounds, however laboratory measurements did not allow the extraction of reliable information concerning the local arrangement, while the employment of a synchrotron source would allow to reduce the acquisition time and increase the resolution of the PDFs, to appreciate the local structures.

ABBREVIATIONS

API, active pharmaceutical ingredient
AZO, 4,4'-azopyridine
AZP, azopyridinic
CAR, carvacrol
CCDC, Cambridge crystallographic data centre
CSD, Cambridge structural database
CSP, crystal structure prediction
DSC, differential scanning calorimetry
EO, essential oil
EUG, eugenol
FDA, food and drug administration
GRAS, generally recognized as safe
HB, hydrogen bond
HMT, hexamethylenetetramine
ILAG, ion- and liquid-assisted grinding
MEP, molecular electrostatic potential
NMR, nuclear magnetic resonance
PDF, pair distribution function
POLAG, polymer-assisted grinding
PMMA, poly (methyl methacrylate)
PXRD, powder X-ray diffraction
PYR, pyrazine
QSAR, quantitative structure-activity relationship
QSPR, quantitative structure-property relationship
SCXRD, single crystal X-ray diffraction
TJP, β-thujaplicin
THY, thymol
TRIS, time-resolved in situ
VAG, vapour-assisted grinding
VAN, vanillin
VT-PXRD, variable-temperature powder X-ray diffraction

APPENDIX A

AZOPYRIDINIC COFORMERS

A.1 ^{1}H NMR Spectra

^{1}H NMR spectra were collected on a Bruker Advance 400 spectrometer using standard Bruker sequences. Chemical shifts are reported in ppm referred to residual solvent protons (DMSO, d^6, $CDCl_3$).

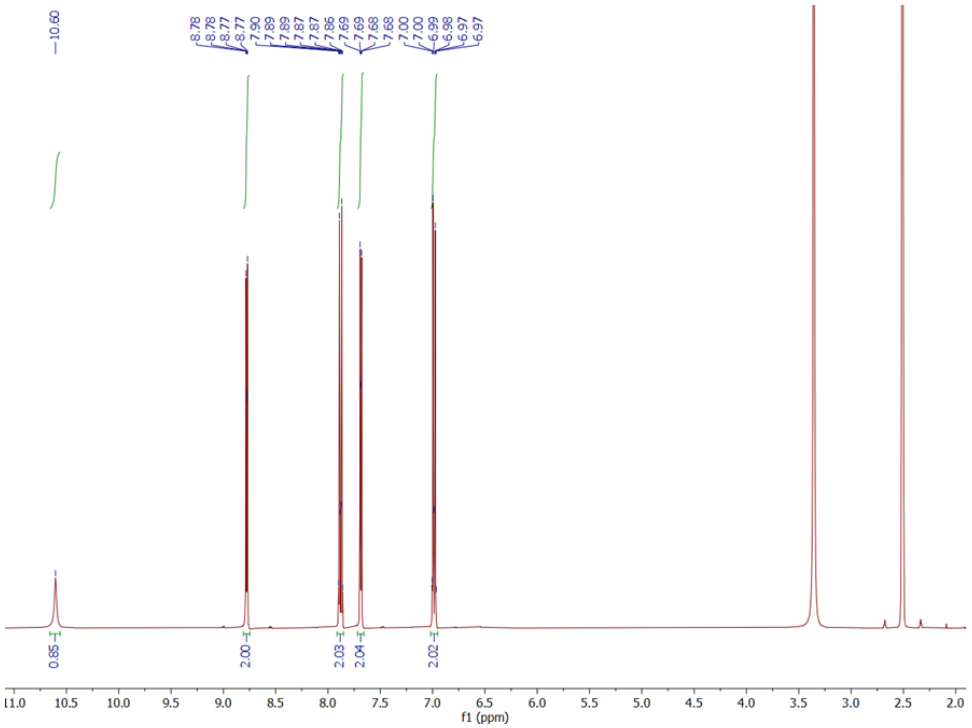

Figure A1.1 *^{1}H NMR spectrum of AZP **1** in DMSO. Not integrated peaks correspond respectively to residual H_2O (δ 3.30) and DMSO signal (δ 2.50).*

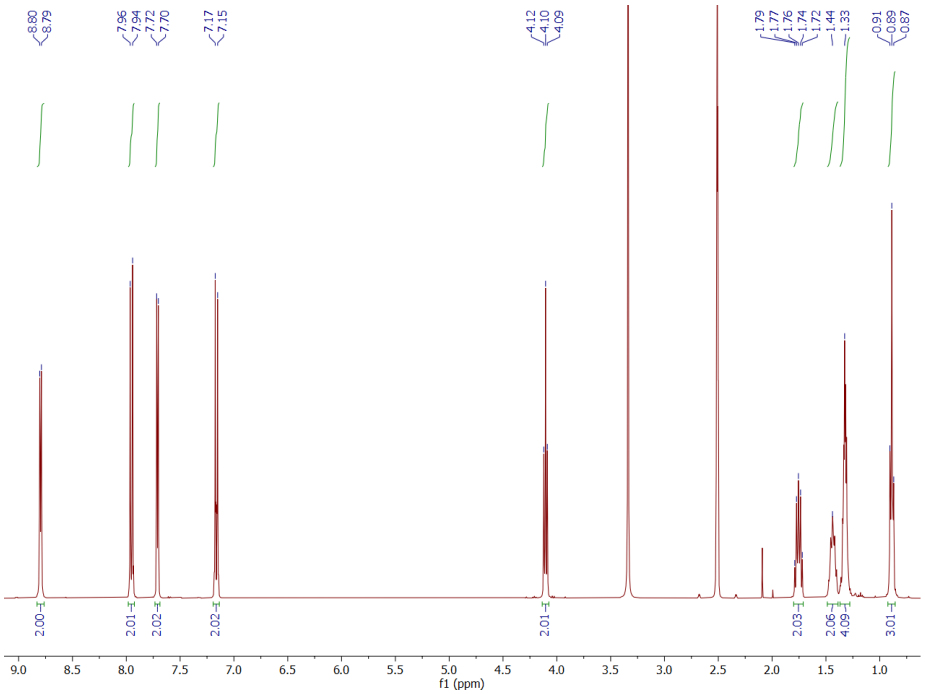

Figure A1.2 *^{1}H NMR spectrum of AZP **2** in DMSO. Not integrated peaks correspond respectively to residual H_2O (δ 3.30) and DMSO signal (δ 2.50).*

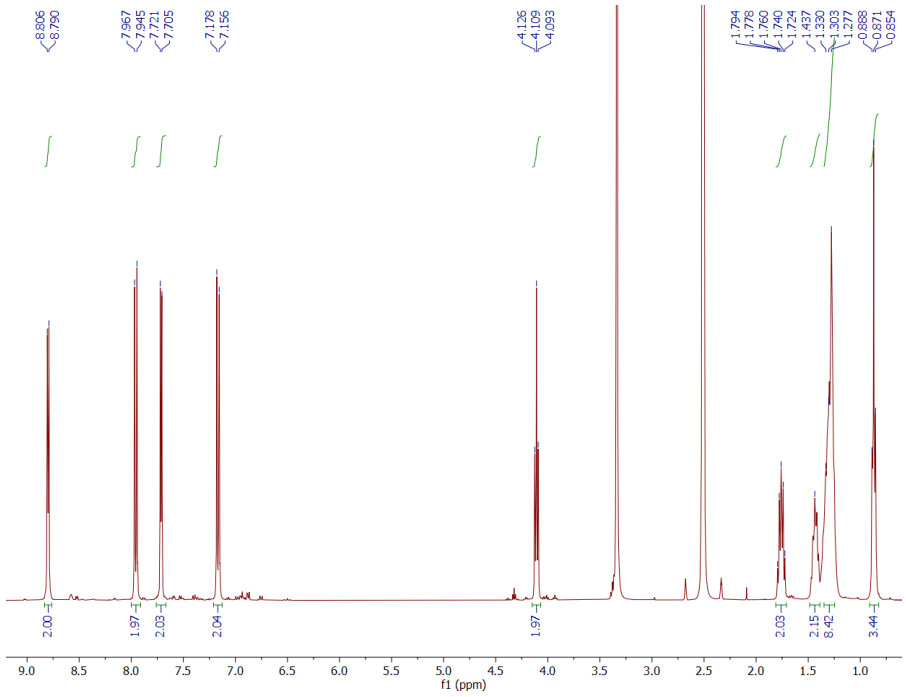

Figure A1.3 *^{1}H NMR spectrum of AZP **3** in DMSO. Not integrated peaks correspond respectively to residual H_2O (δ 3.30) and DMSO signal (δ 2.50).*

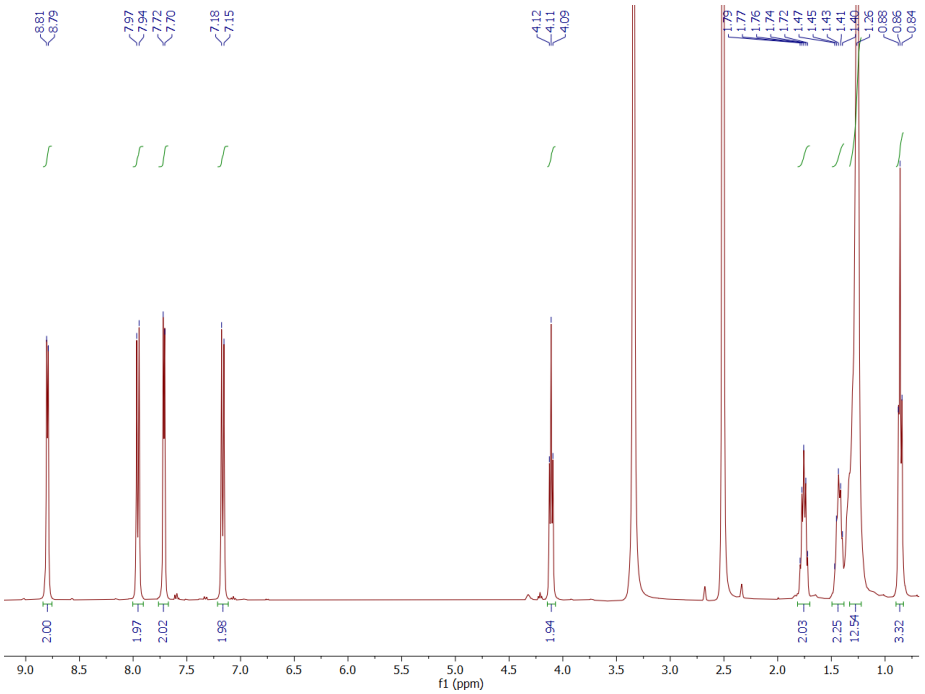

Figure A1.4 *^{1}H NMR spectrum of AZP **4** in DMSO. Not integrated peaks correspond respectively to residual H_2O (δ 3.30) and DMSO signal (δ 2.50).*

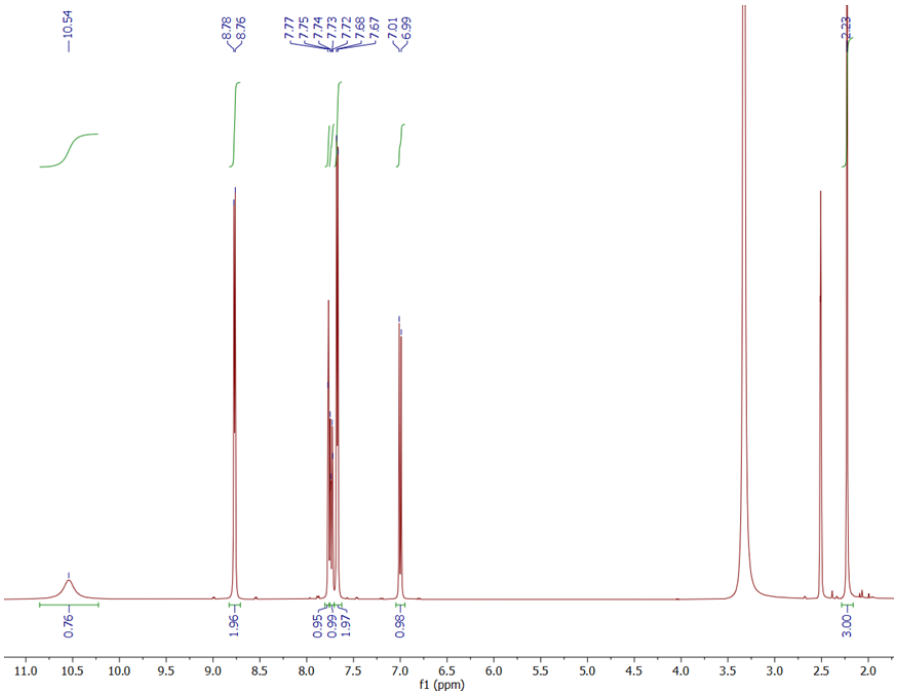

Figure A1.5 *^{1}H NMR spectrum of AZP **5** in DMSO. Not integrated peaks correspond respectively to residual H_2O (δ 3.30) and DMSO signal (δ 2.50).*

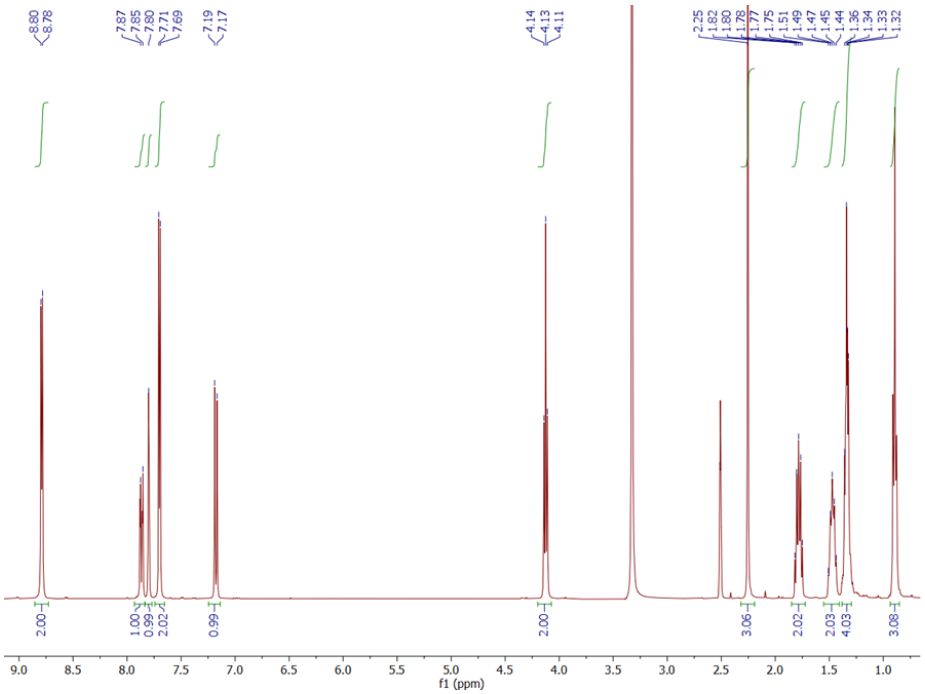

Figure A1.6 *^{1}H NMR spectrum of AZP **6** in DMSO. Not integrated peaks correspond respectively to residual H_2O (δ 3.30) and DMSO signal (δ 2.50).*

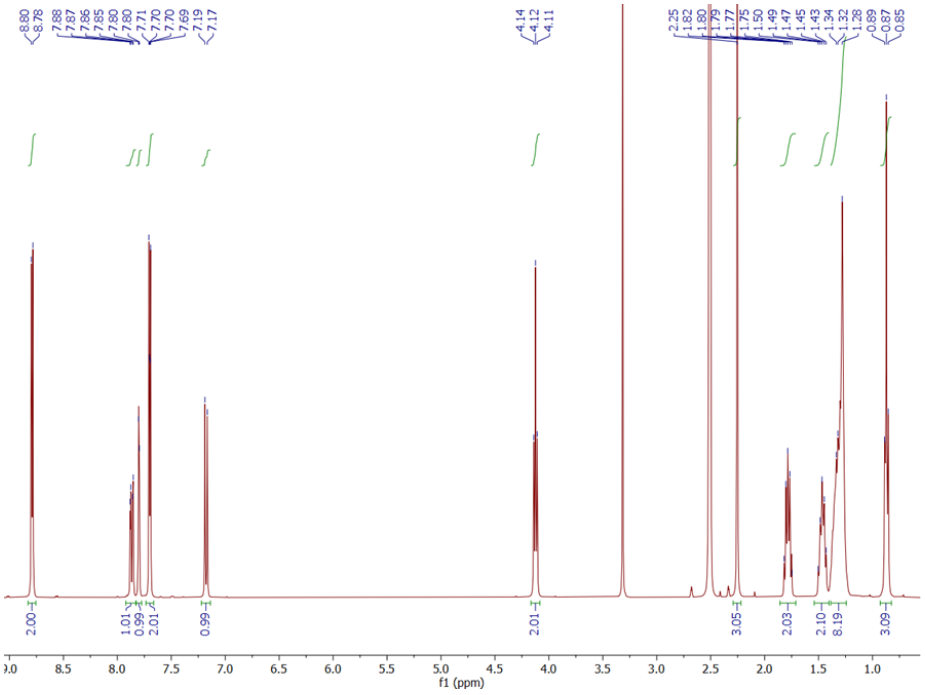

Figure A1.7 *^{1}H NMR spectrum of AZP **7** in DMSO. Not integrated peaks correspond respectively to residual H_2O (δ 3.30) and DMSO signal (δ 2.50).*

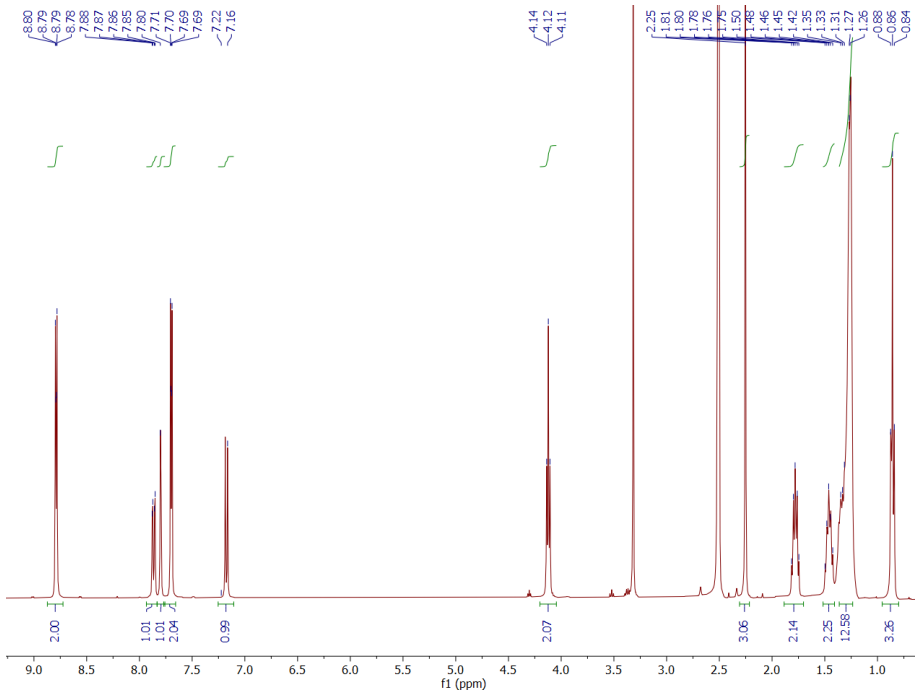

Figure A1.8 *^{1}H NMR spectrum of AZP **8** in DMSO. Not integrated peaks correspond respectively to residual H_2O (δ 3.30) and DMSO signal (δ 2.50).*

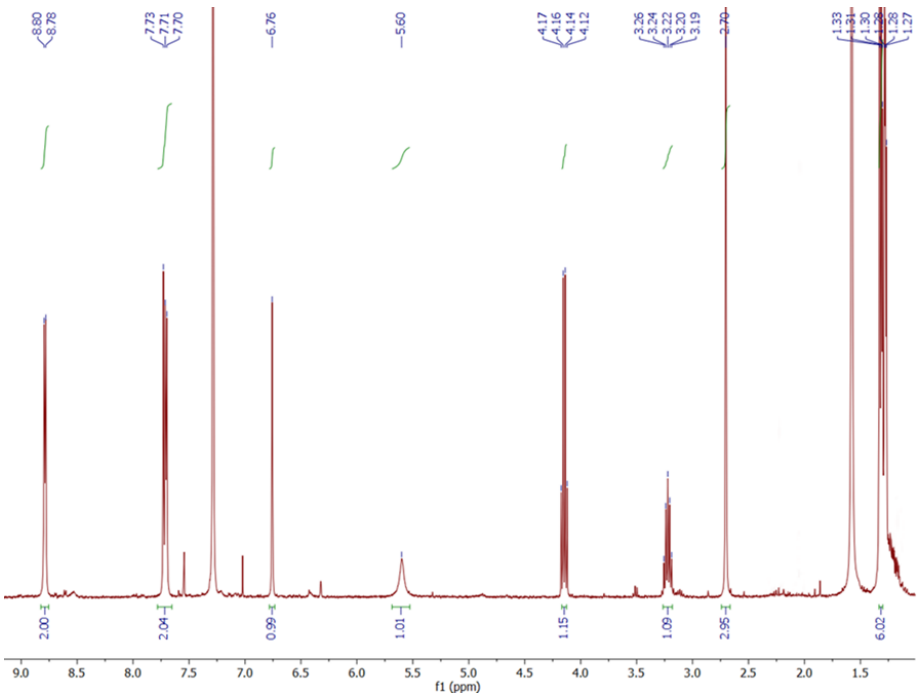

Figure A1.9 *^{1}H NMR spectrum of AZP **9** in DMSO. Not integrated peaks correspond respectively to residual H_2O (δ 3.30) and DMSO signal (δ 2.50).*

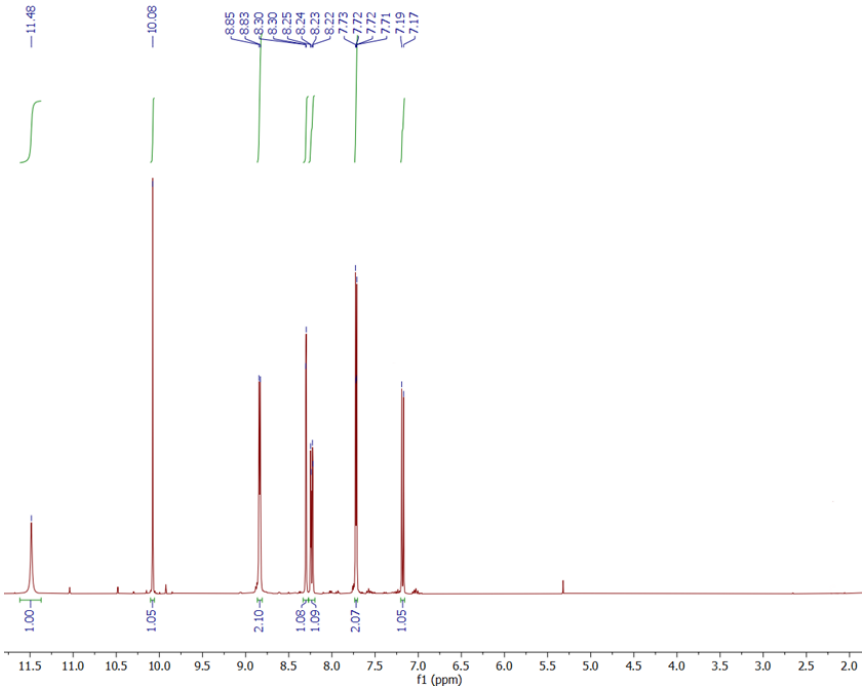

Figure A1.10 *^{1}H NMR spectrum of AZP **10** in DMSO. Not integrated peaks correspond to $CDCl_3$ signal (δ 7.26).*

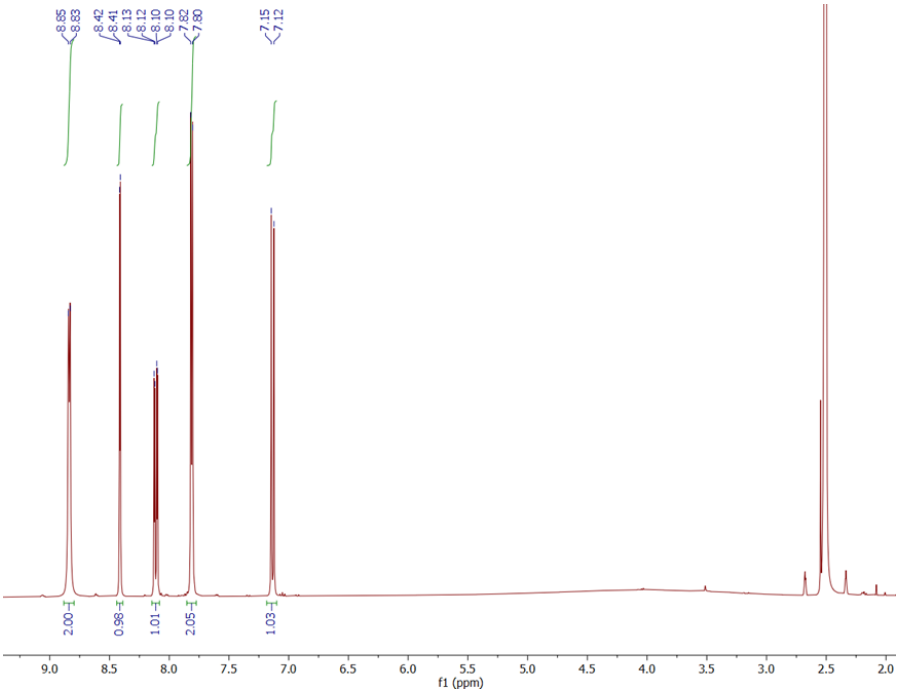

Figure A1.11 *^{1}H NMR spectrum of AZP **11** in DMSO. Not integrated peaks correspond to $CDCl_3$ signal (δ 7.26).*

A.2 X-ray Powder Patterns

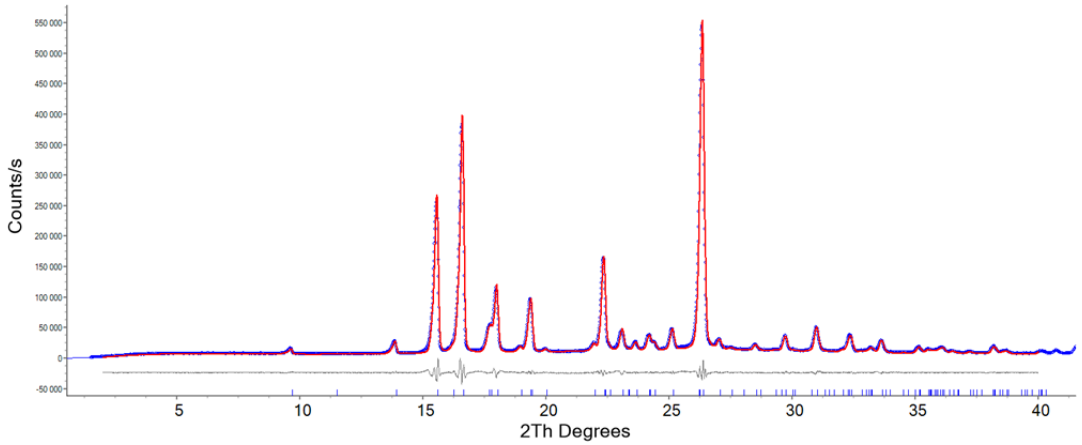

Figure A2.1 *Pawley fit of AZP* ***1a*** *(red line) against experimental data (blue dots). Tick marks indicate calculated reflection positions. Ycalc-Yobs residual curve is reported in grey.*

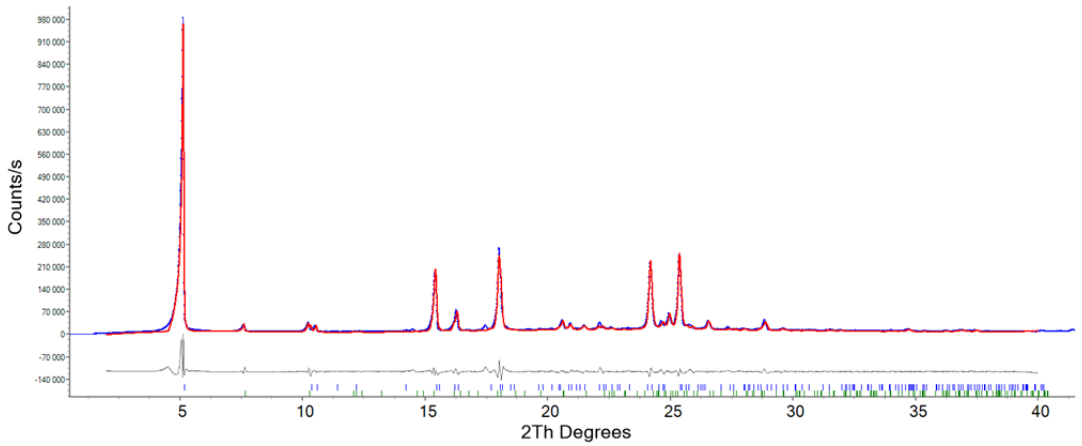

Figure A2.2 *Pawley fit of AZP* ***2*** *(red line) against experimental data (blue dots). Multi-phases refinement was performed since a small amount of* ***2b*** *was formed by grinding* ***2a*** *at laboratory condition (22 °C, 1 atm). Tick marks indicate calculated reflection positions. Ycalc-Yobs residual curve is reported in grey.*

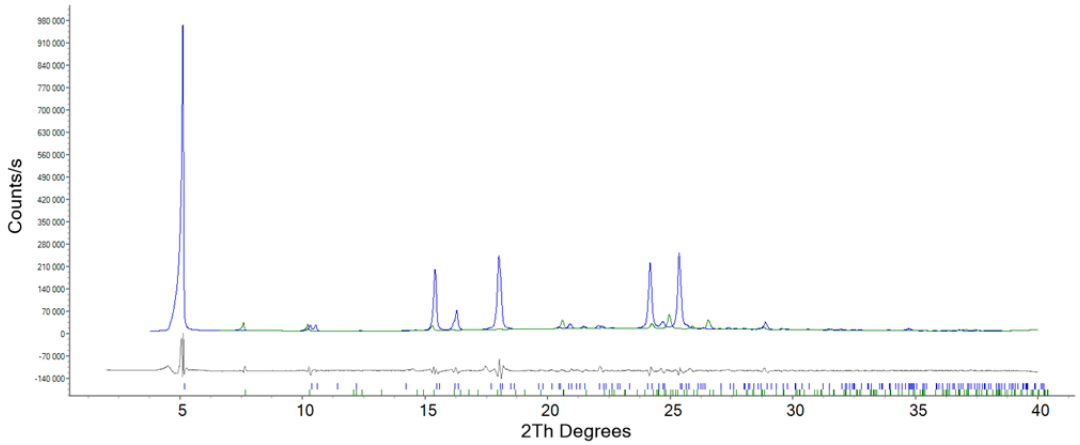

Figure A2.3 *Representation of* ***2a*** *(blue) and* ***2b*** *(green) in multi phases Pawley fit of AZP* ***2*** *reported in Figure A2.2. Tick marks indicate calculated reflection positions.*

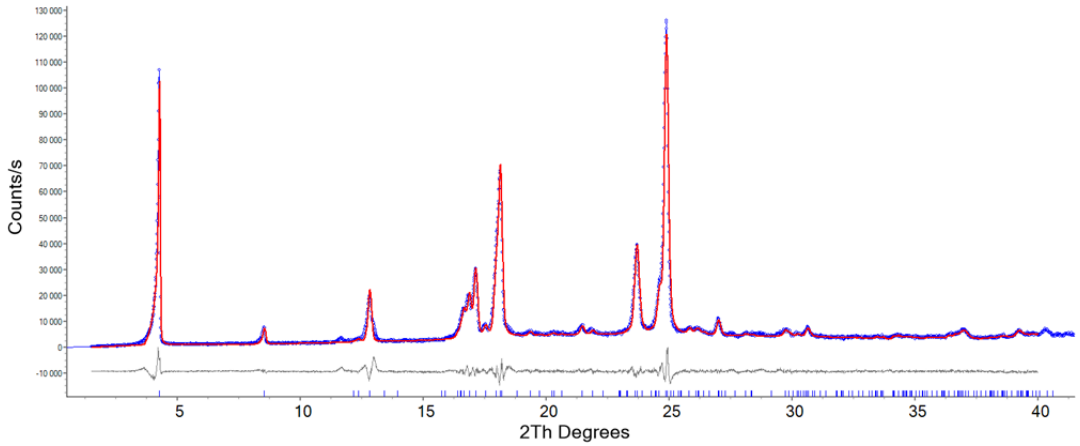

Figure A2.4 *Pawley fit of AZP* ***3*** *(red line) against experimental data (blue dots). Tick marks indicate calculated reflection positions. Ycalc-Yobs residual curve is reported in grey.*

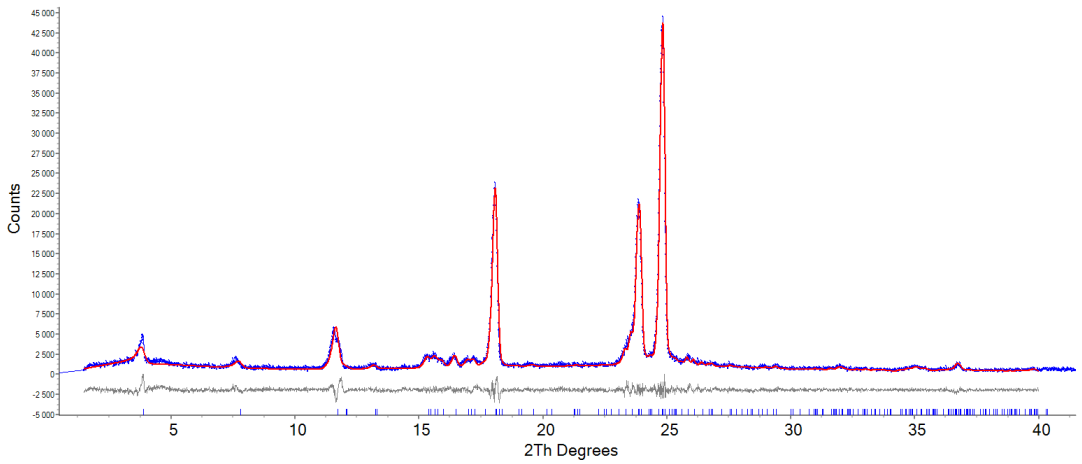

Figure A2.5 *Pawley fit of AZP* ***4*** *(red line) against experimental data (blue dots). Tick marks indicate calculated reflection positions. Ycalc-Yobs residual curve is reported in grey.*

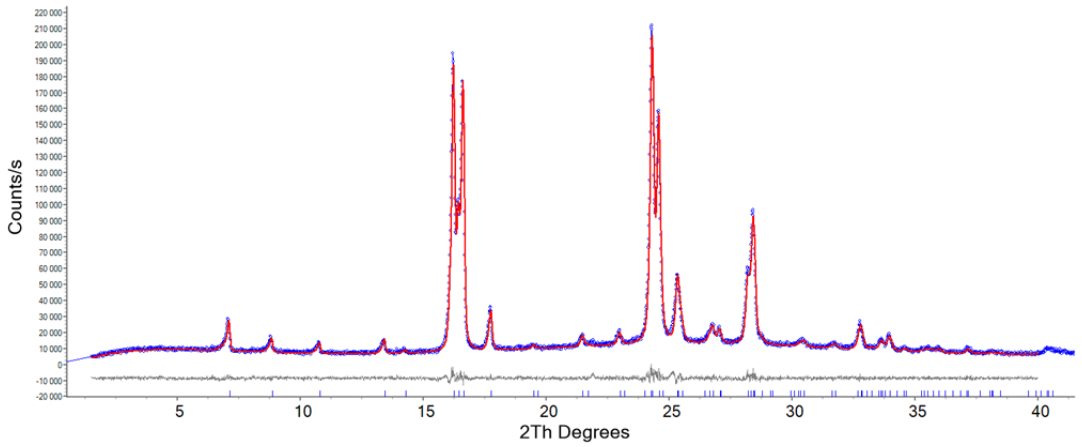

Figure A2.6 *Pawley fit of AZP* ***5*** *(red line) against experimental data (blue dots). Tick marks indicate calculated reflection positions. Ycalc-Yobs residual curve is reported in grey.*

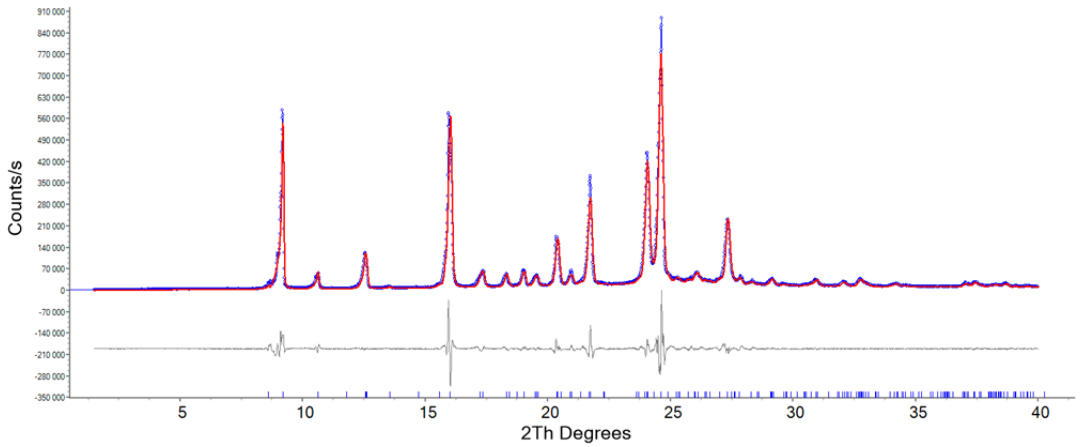

Figure A2.7 *Pawley fit of AZP* ***6b*** *(red line) against experimental data (blue dots). Tick marks indicate calculated reflection positions. Ycalc-Yobs residual curve is reported in grey.*

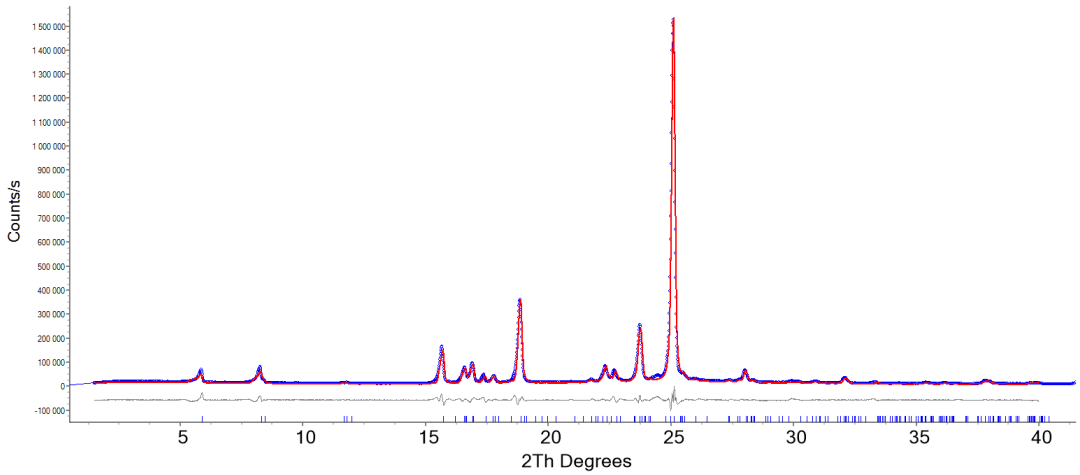

Figure A2.8 *Pawley fit of AZP* ***7c*** *(red line) against experimental data (blue dots). Tick marks indicate calculated reflection positions. Ycalc-Yobs residual curve is reported in grey.*

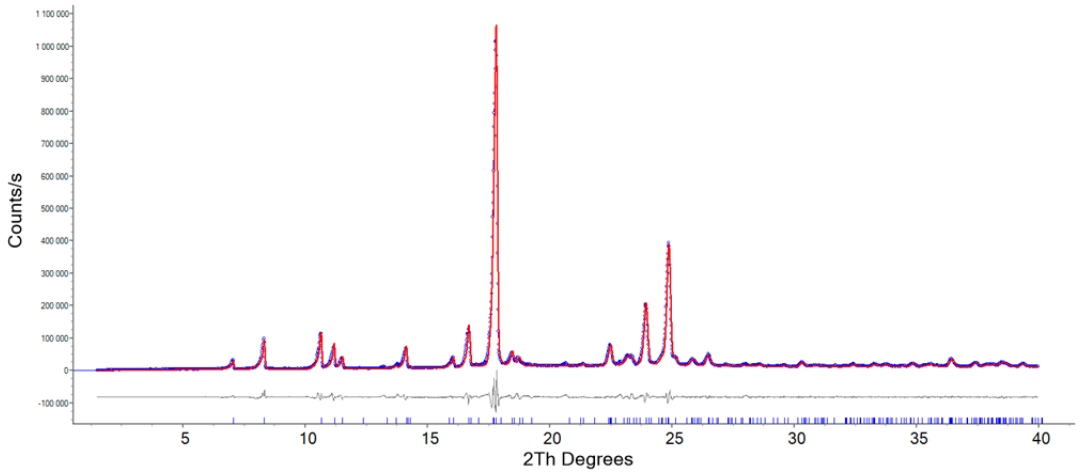

Figure A2.9 *Pawley fit of AZP* ***8*** *(red line) against experimental data (blue dots). Tick marks indicate calculated reflection positions. Ycalc-Yobs residual curve is reported in grey.*

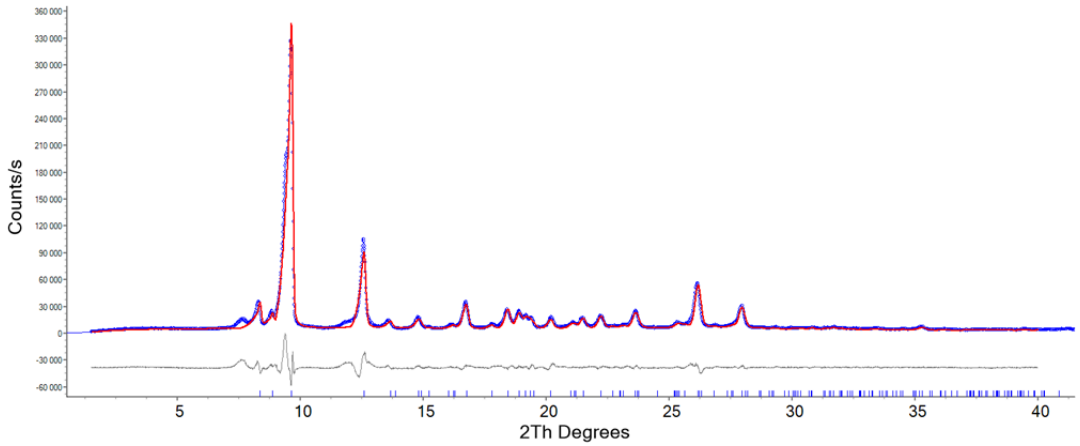

Figure A2.10 *Pawley fit of AZP* ***9*** *(red line) against experimental data (blue dots). Tick marks indicate calculated reflection positions. Ycalc-Yobs residual curve is reported in grey.*

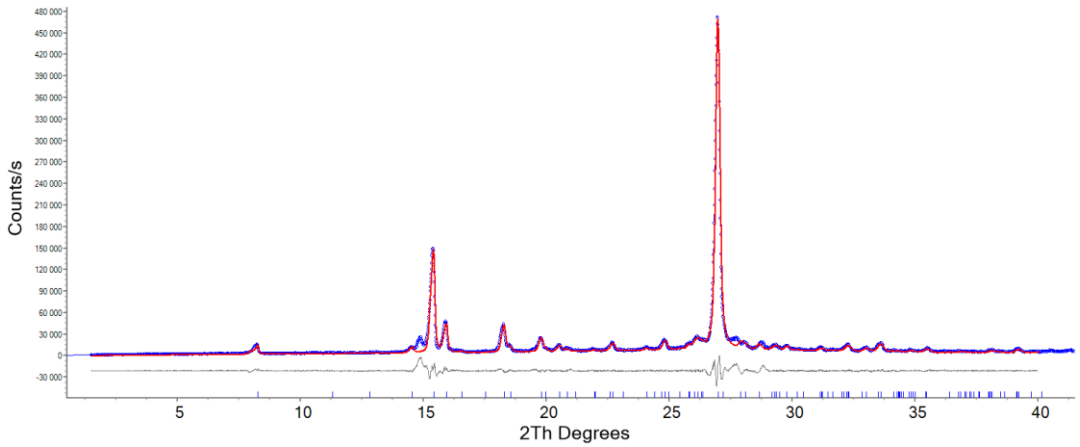

Figure A2.11 *Pawley fit of AZP* ***10*** *(red line) against experimental data (blue dots). Tick marks indicate calculated reflection positions. Ycalc-Yobs residual curve is reported in grey.*

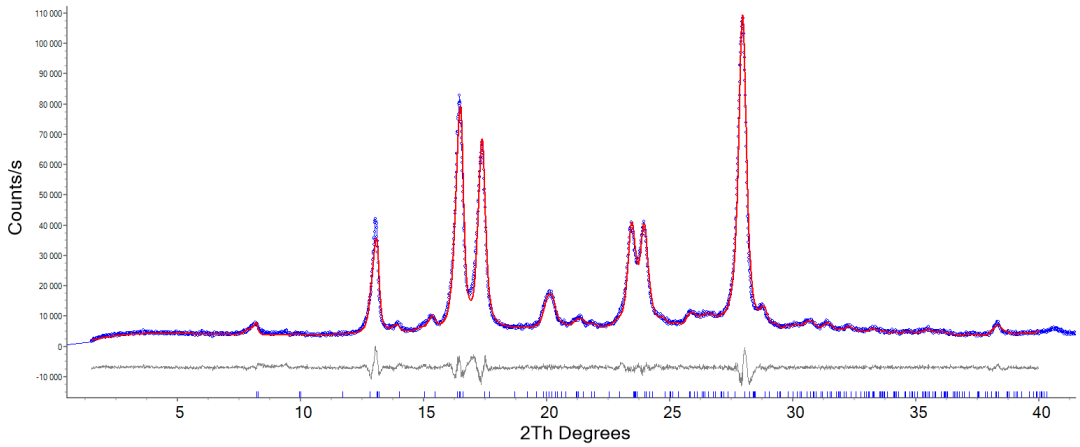

Figure A2.12 *Pawley fit of AZP* ***11*** *(red line) against experimental data (blue dots). Tick marks indicate calculated reflection positions. Ycalc-Yobs residual curve is reported in grey.*

A.3 DSC Thermograms

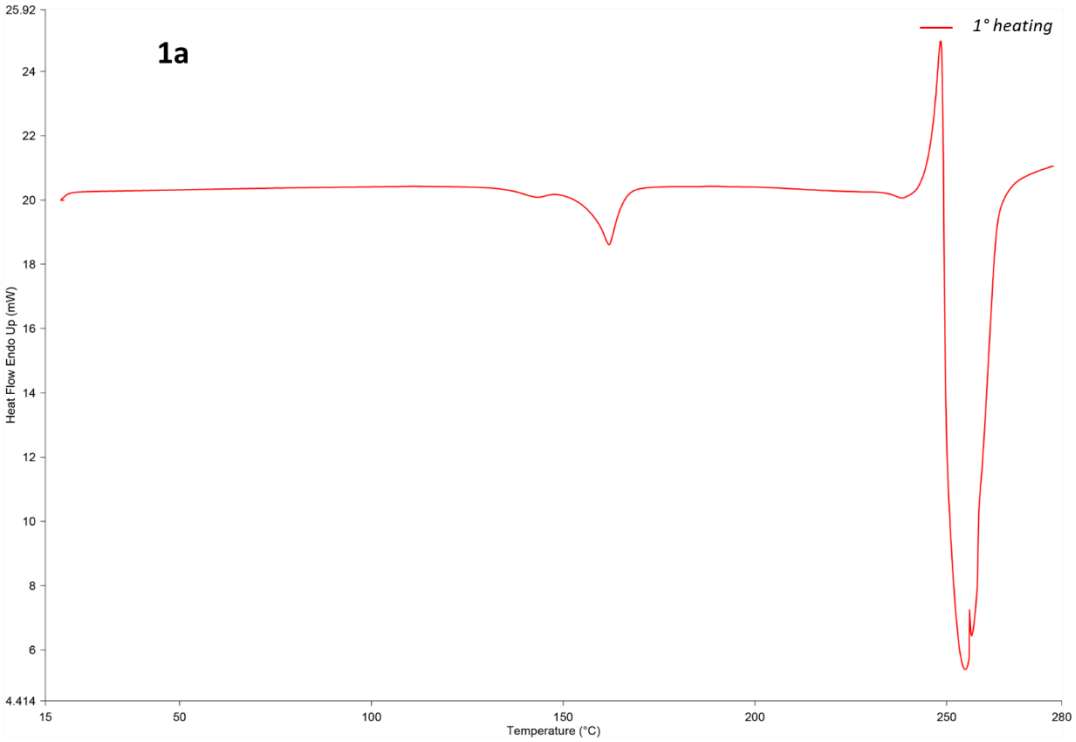

Figure A3.1 *Thermogram of AZP* ***1a****. Heating run from 20 °C to 280 °C at 5 °C/min (red curve). No additional thermal treatments were performed due to unusual exothermic and endothermic peaks related to the decomposition of the sample.*

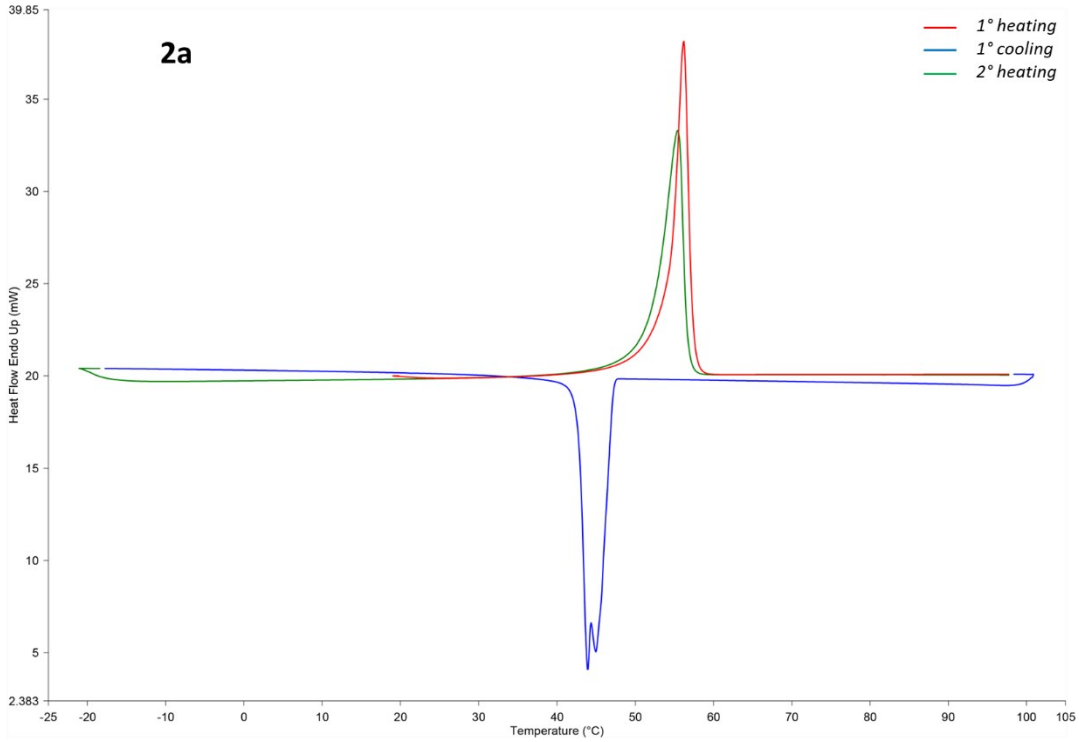

Figure A3.2 *Thermogram of AZP* ***2a****. First heating run from 20 °C to 100 °C (red curve), cooling run from 100 °C to -20 °C (blue curve) and second heating run from -20 °C to 100 °C (green curve). The whole firing profile was performed at 5°C/min. The endothermic peaks shown in the heating runs refer to the melting of* ***2a****, while the exothermic peak in the cooling run refers to its recrystallization.*

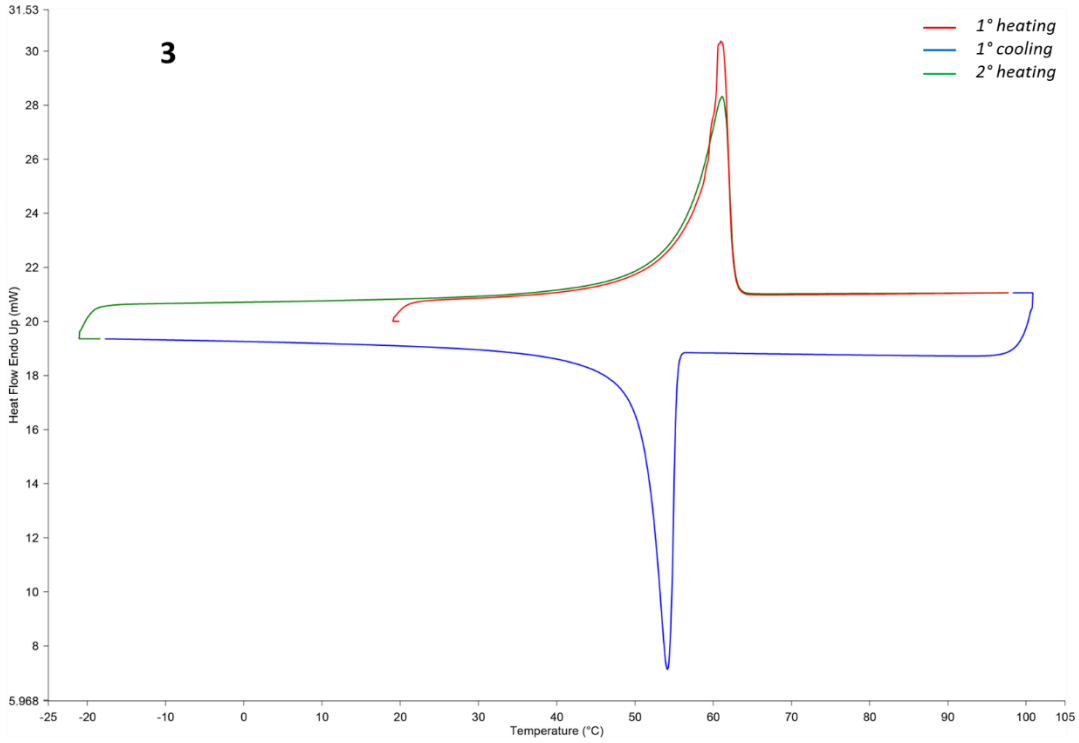

Figure A3.3 *Thermogram of AZP **3**. First heating run from 20 °C to 100 °C (red curve), cooling run from 100 °C to -20 °C (blue curve) and second heating run from -20 °C to 100 °C (green curve). The whole firing profile was performed at 5°C/min. The endothermic peaks shown in the heating runs refer to the melting of **3**, while the exothermic peak in the cooling run refers to its recrystallization.*

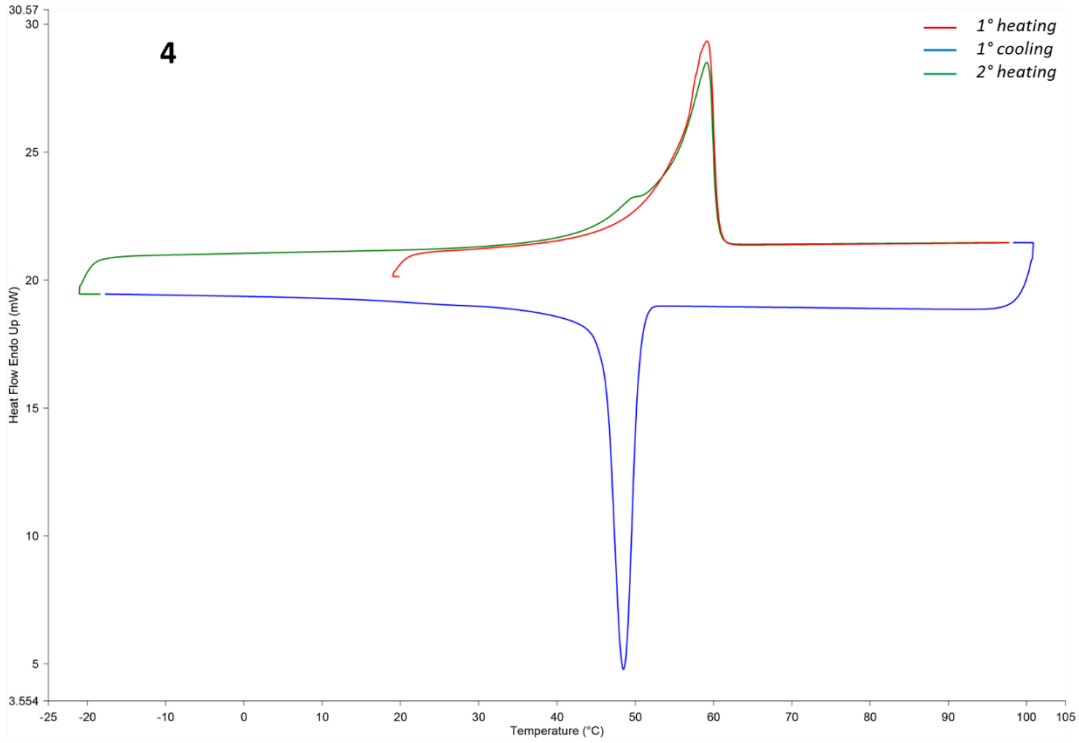

Figure A3.4 *Thermogram of AZP* ***4****. First heating run from 20 °C to 100 °C (red curve), cooling run from 100 °C to -20 °C (blue curve) and second heating run from -20 °C to 100 °C (green curve). The whole firing profile was performed at 5°C/min. The endothermic peaks shown in the heating runs refer to the melting of* ***4****, while the exothermic peak in the cooling run refers to its recrystallization.*

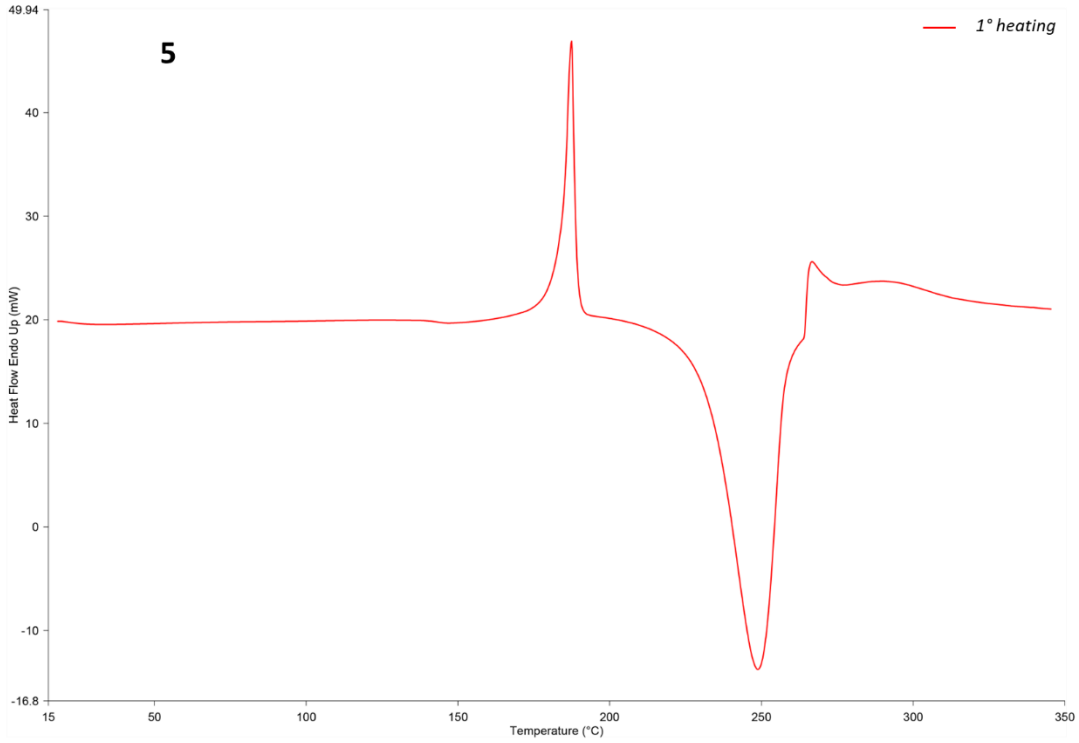

Figure A3.5 *Thermogram of* ***5****. Heating run from 20 °C to 345 °C at 5 °C/min (red curve). No additional thermal treatments were performed due to unusual exothermic and endothermic peaks related to the decomposition of the sample.*

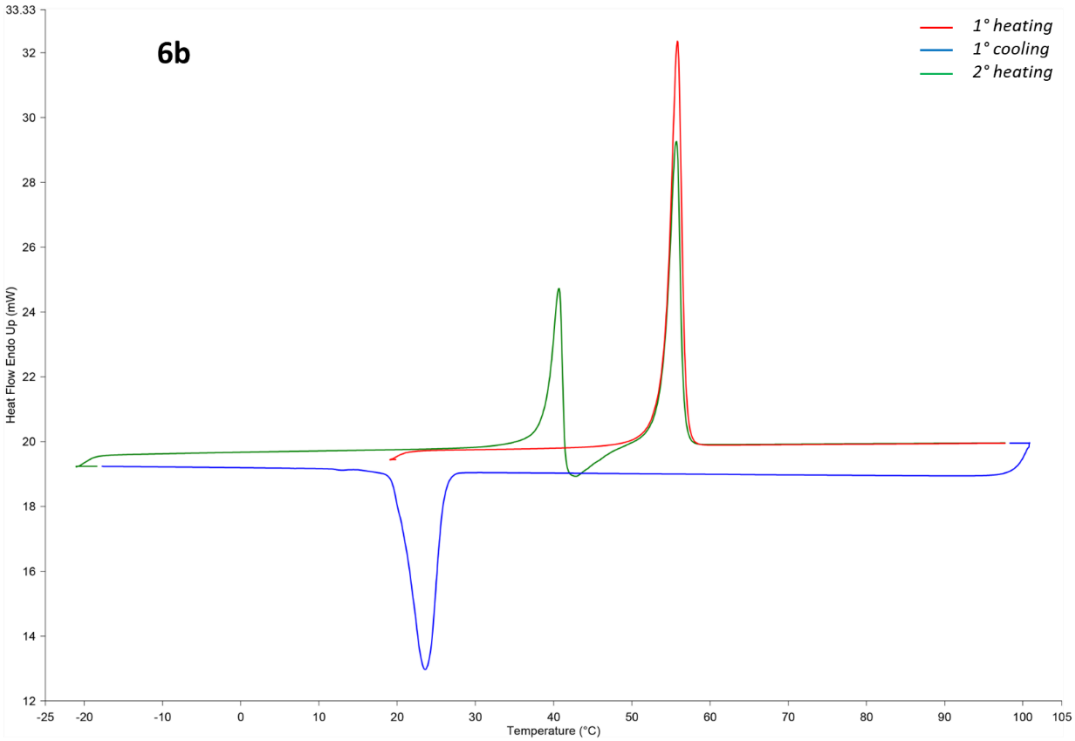

Figure A3.6 *Thermogram of AZP* ***6b****. First heating run from 20 °C to 100 °C (red curve), cooling run from 100 °C to -20 °C (blue curve) and second heating run from -20 °C to 100 °C (green curve). The whole firing profile was performed at 5°C/min. The endothermic peak shown in the first heating run refers to the melting of* ***6b****. In the cooling run the crystallization of polymorph* ***6c*** *occurred, as confirmed by VT-PXRD experiment of* ***6b*** *that was performed in the same conditions. In the second heating run the melting of* ***6c*** *is partially overlapped to an exothermic peak due to the recrystallization of* ***6b*** *from the melt, in turn followed by the second endothermic peak referred to the melting of* ***6b****.*

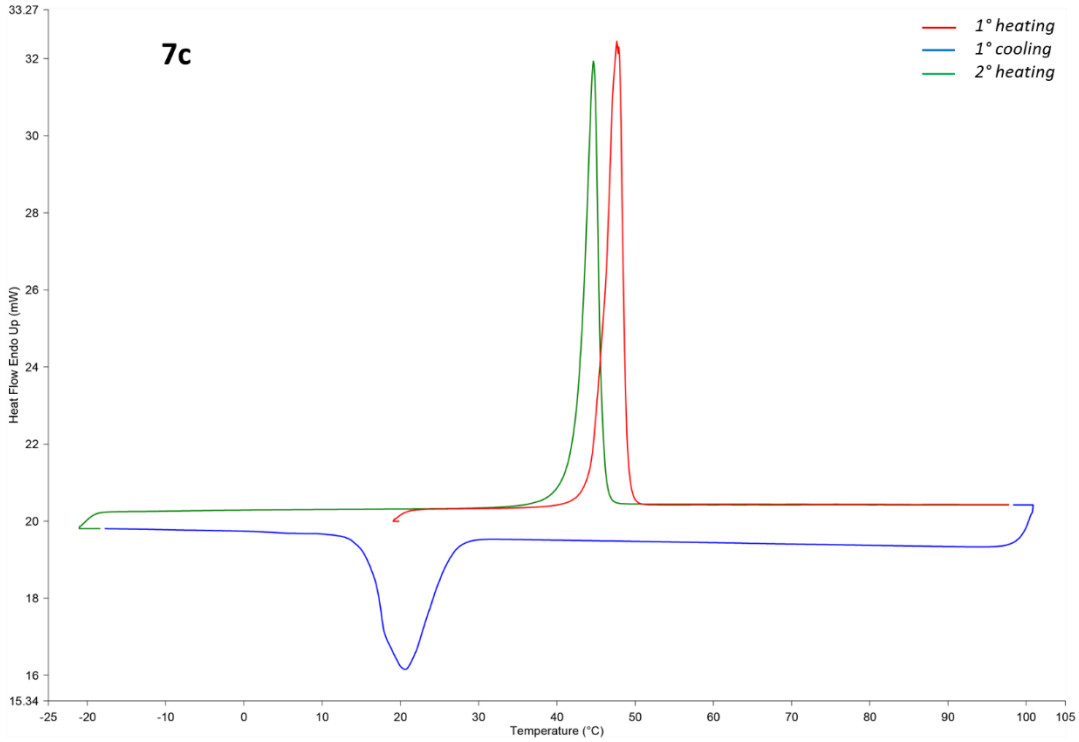

Figure A3.7 *Thermogram of AZP* ***7c****. First heating run from 20 °C to 100 °C (red curve), cooling run from 100 °C to -20 °C (blue curve) and second heating run from -20 °C to 100 °C (green curve). The whole firing profile was performed at 5°C/min. The endothermic peak shown in the first heating run refers to the melting of* ***7c****, while the endothermic peak shown in the second heating run is due to the melting of* ***7b*** *polymorph, which crystallized from the melt in the cooling run.*

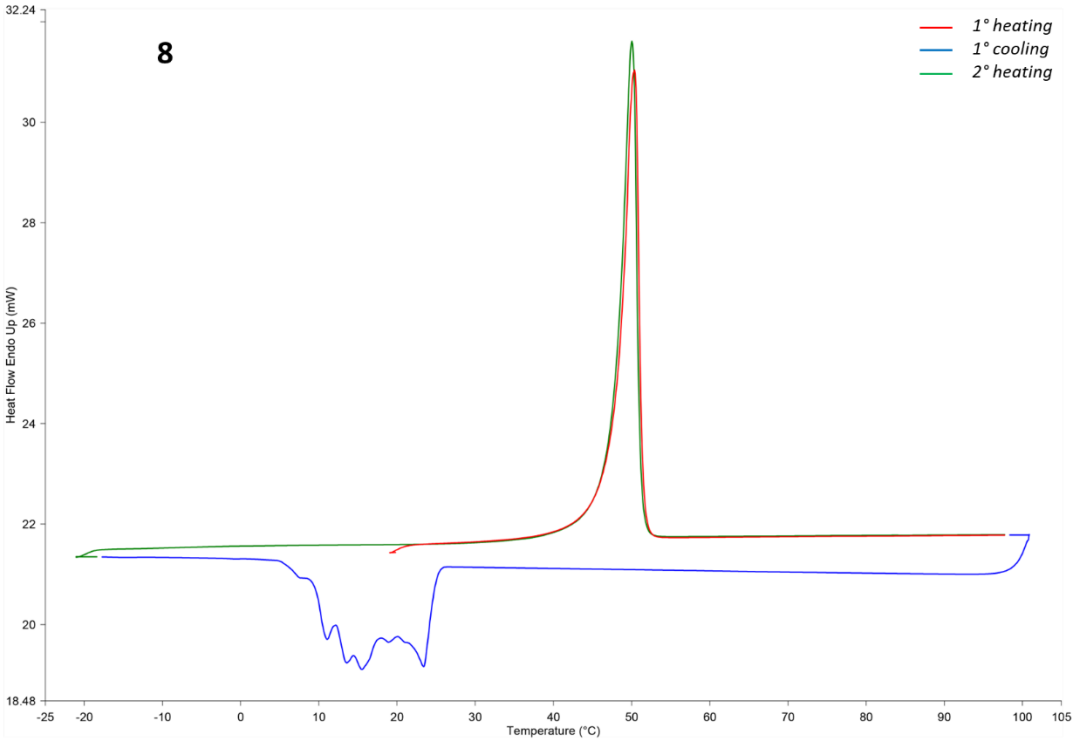

Figure A3.8 *Thermogram of AZP* ***8****. First heating run from 20 °C to 100 °C (red curve), cooling run from 100 °C to -20 °C (blue curve) and second heating run from -20 °C to 100 °C (green curve). The whole firing profile was performed at 5°C/min. The endothermic peaks shown in the heating runs refer to the melting of* ***8****, while the exothermic peak in the cooling run refers to its recrystallization.*

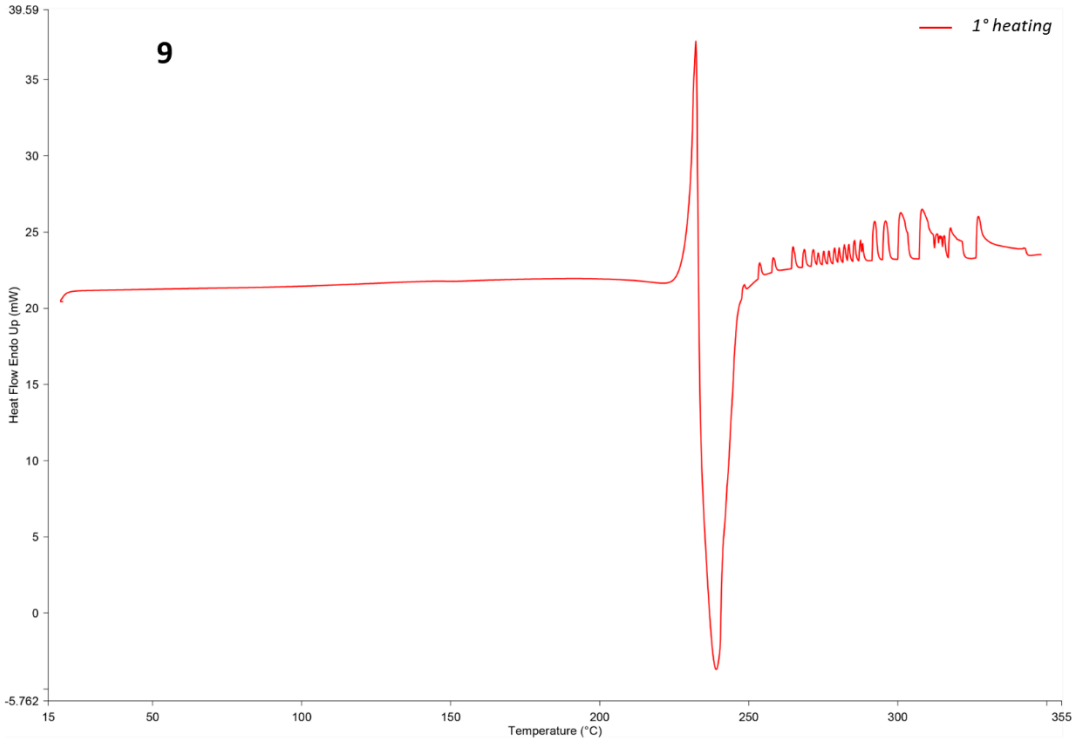

Figure A3.9 *Thermogram of AZP* ***9****. Heating run from 20 °C to 350 °C at 5 °C/min (red curve). No additional thermal treatments were performed due to unusual exothermic and endothermic peaks related to the decomposition of the sample.*

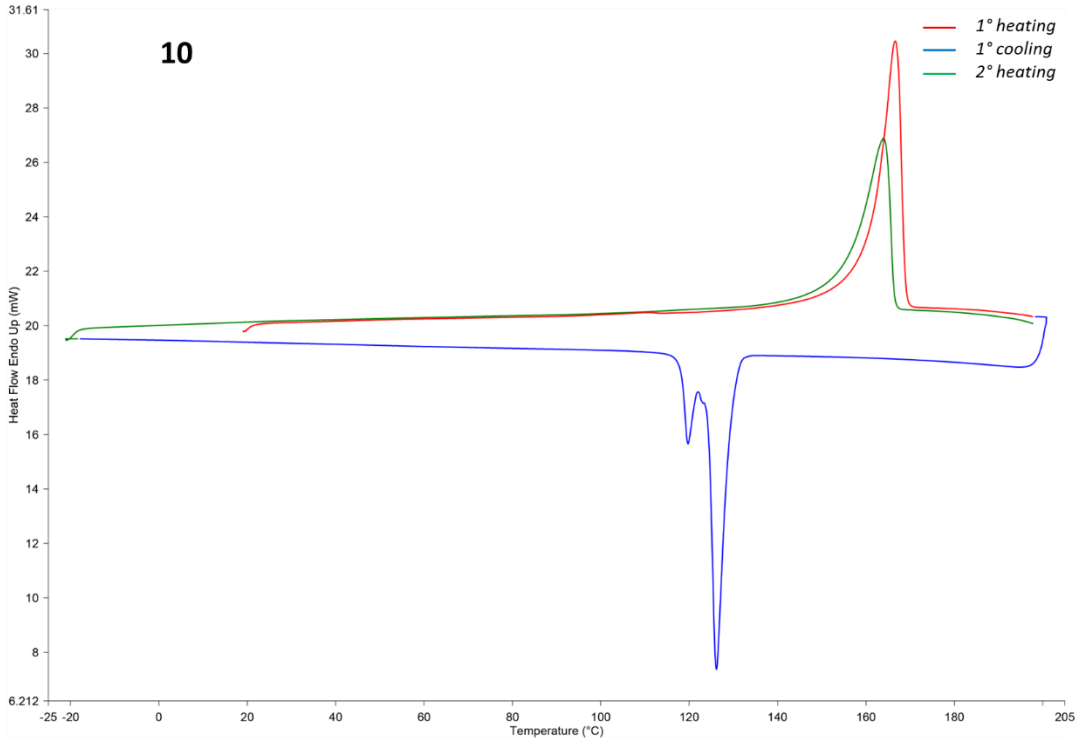

Figure A3.10 *Thermogram of AZP* ***10****. First heating run from 20 °C to 200 °C (red curve), cooling run from 200 °C to -20 °C (blue curve) and second heating run from -20 °C to 200 °C (green curve). The whole firing profile was performed at 5°C/min. The endothermic peak shown in the first heating run refers to the melting of* ***10****, while the endothermic peak shown in the second heating run is due to the melting of a different polymorph, which crystallized from the melt in the cooling run and it has not been identified.*

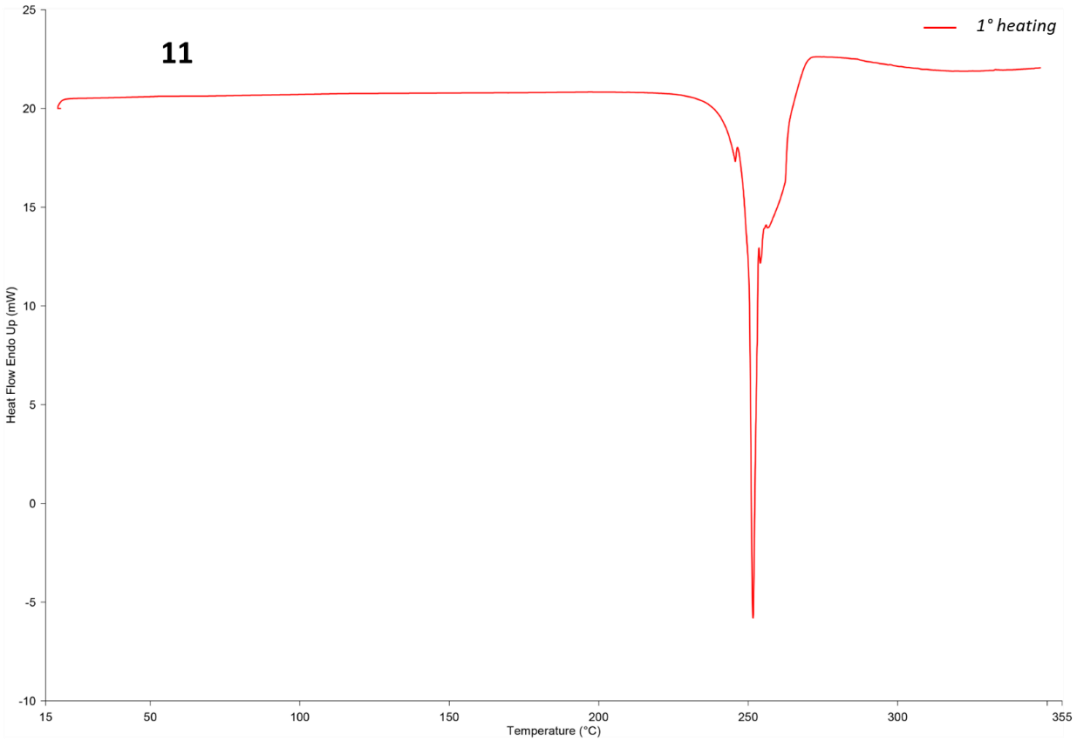

Figure A3.11 *Thermogram of* ***11****. Heating run from 20 °C to 350 °C at 5 °C/min (red curve). No additional thermal treatments were performed due to unusual exothermic peaks related to the decomposition of the sample.*

Table A3.1 *Summary of the thermal events that occurred during DSC measurements of AZP coformers (**1**-**11**).*

AZP	Run		Thermal event	Temperature (°C)	ΔH (J/g)
1a	First heating	1st peak	Exothermic	161.93	-82.78
		2nd peak	Endothermic	--	--
		3rd peak	Exothermic	--	--
2a	First heating	1st peak	Endothermic	56.22	114.14
	First cooling	1st peak	Exothermic	43.90	-110.94
	Second heating	1st peak	Endothermic	55.40	109.48
3	First heating	1st peak	Endothermic	60.96	110.53
	First cooling	1st peak	Exothermic	54.18	-110.32
	Second heating	1st peak	Endothermic	61.17	109.16
4	First heating	1st peak	Endothermic	59.22	115.46
	First cooling	1st peak	Exothermic	48.47	-114.55
	Second heating	1st peak	Endothermic	59.17	109.91
5	First heating	1st peak	Endothermic	187.44	148.14
		2nd peak	Exothermic	--	--
6b	First heating	1st peak	Endothermic	55.83	123.89
	First cooling	1st peak	Exothermic	23.56	-113.97
	Second heating	1st peak	Endothermic	40.72	45.51
		2nd peak	Exothermic	42.83	-18.38
		3rd peak	Endothermic	55.72	91.51
7c	First heating	1st peak	Endothermic	47.67	156.54
	First cooling	1st peak	Exothermic	20.59	-120.90
	Second heating	1st peak	Endothermic	44.68	134.93
8	First heating	1st peak	Endothermic	50.39	142.25
	First cooling	1st peak	Exothermic	15.48	-132.86
	Second heating	1st peak	Endothermic	50.04	143.93
9	First heating	1st peak	Endothermic	--	--
		2nd peak	Exothermic	--	--
10	First heating	1st peak	Endothermic	166.62	152.24
	First cooling	1st peak	Exothermic	126.17	-117.52
	Second heating	1st peak	Endothermic	163.94	122.92
11	First heating	1st peak	Exothermic	--	--

A.4 Crystallographic data

Table A4.1 *Crystallographic data and structure refinement of AZP coformers (**1**-**11**).*

Identification code	**1b**	**2a**	**2b**	**3**
Empirical formula	$C_{11}H_9N_3O$	$C_{17}H_{21}N_3O$	$C_{17}H_{21}N_3O$	$C_{19}H_{25}N_3O$
Temperature (K)	200	200	150	200
Crystal system	Triclinic	Triclinic	Triclinic	Triclinic
Space group	P-1	P-1	P-1	P-1
a (Å)	6.0269 (2)	5.5105 (2)	7.5535 (5)	5.7846 (2)
b (Å)	7.8108 (3)	8.3169 (3)	8.9622 (5)	7.8315 (3)
c (Å)	20.8246 (8)	17.3527 (6)	11.9979 (8)	20.7931 (7)
α (°)	80.919 (3)	84.829 (2)	88.496 (5)	82.799 (3)
β (°)	82.295 (3)	82.068 (2)	72.993 (5)	88.762 (3)
γ (°)	83.759 (3)	84.234 (2)	81.453 (5)	71.300 (3)
Volume (Å^3)	955.44 (6)	781.33 (5)	767.94 (9)	885.03 (6)
Z, Z'	4, 2	2, 1	2, 1	2, 1
ρ_{calc} /g cm^{-3}	1.385	1.204	1.225	1.169
Independent reflections	3899 R_{int} = 0.1050, R_{sigma} = 0.0558	3169 R_{int} = 0.0396, R_{sigma} = 0.0277	3075 R_{int} = 0.1292, R_{sigma} = 0.1118	3390 R_{int} = 0.0953, R_{sigma} = 0.0841
Goodness-of-fit on F^2	1.032	1.033	1.003	0.987
Final R indexes [all data]	R1 = 0.1128, wR2 = 0.1848	R1 = 0.0591, wR2 = 0.1151	R1 = 0.1503, wR2 = 0.1929	R1 = 0.1405, wR2 = 0.1794

Table A4.1 Continued *Crystallographic data and structure refinement of AZP coformers (**1-11**).*

Identification code	**4**	**5**	**6a**	**6b**
Empirical formula	$C_{21}H_{29}N_3O$	$C_{12}H_{11}N_3O$	$C_{18}H_{23}N_3O$	$C_{18}H_{23}N_3O$
Temperature (K)	200	200	200	294
Crystal system	Triclinic	Orthorhombic	Triclinic	Triclinic
Space group	P-1	$P2_12_12_1$	P-1	P-1
a (Å)	5.8740 (7)	5.8802 (2)	8.5964 (5)	8.811 (5)
b (Å)	7.7066 (9)	7.2283 (2)	9.6278 (5)	10.052 (9)
c (Å)	22.845 (3)	24.4050 (6)	10.8129 (6)	10.431 (10)
α (°)	98.249 (8)	90	94.652 (2)	87.36 (3)
β (°)	92.464 (10)	90	101.482 (2)	80.41 (3)
γ (°)	106.596 (9)	90	100.282 (2)	72.17 (3)
Volume (Å^3)	977.0 (2)	1037.31(5)	856.59 (8)	867.2 (12)
Z, Z'	2, 1	4, 1	2, 1	2, 1
ρ_{calc} ***/g cm^{-3}***	1.154	1.365	1.153	1.139
Independent reflections	3370 R_{int} = 0.1412, R_{sigma} = 0.1904	1969 R_{int} = 0.1057, R_{sigma} = 0.0616	3526 R_{int} = 0.0664, R_{sigma} = 0.0449	3550 R_{int} = 0.1587, R_{sigma} = 0.1422
Goodness-of-fit on F^2	0.969	1.037	1.035	1.083
Final R indexes [all data]	R1 = 0.2661, wR2 = 0.2857	R1 = 0.0785, wR2 = 0.1350	R1 = 0.0690, wR2 = 0.1234	R1 = 0.2490, wR2 = 0.2585

Table A4.1 Continued *Crystallographic data and structure refinement of AZP coformers (**1-11**).*

Identification code	**6c**	**7a**	**7b**	**7c**
Empirical formula	$C_{18}H_{23}N_3O$	$C_{20}H_{27}N_3O$	$C_{20}H_{27}N_3O$	$C_{20}H_{27}N_3O$
Temperature (K)	200	200	200	200
Crystal system	Triclinic	Triclinic	Monoclinic	Triclinic
Space group	P-1	P-1	C2/c	P-1
a (Å)	11.2264 (7)	8.588 (2)	11.7823 (12)	5.5160 (2)
b (Å)	11.4415 (7)	10.141 (3)	16.1939 (17)	11.0854 (3)
c (Å)	14.1166 (6)	12.337 (3)	20.073 (2)	15.9449 (5)
α (°)	95.707 (4)	68.551 (9)	90	70.467 (2)
β (°)	111.170 (4)	75.401 (7)	99.021 (7)	82.934 (2)
γ (°)	91.643 (5)	76.240 (10)	90	85.713 (2)
Volume (Å^3)	1678.40 (17)	955.0 (5)	3782.5 (7)	911.30 (5)
Z, Z'	4, 2	2, 1	8, 1	2, 1
ρ_{calc} /g cm^{-3}	1.177	1.132	1.143	1.186
Independent reflections	6478 R_{int} = 0.1141, R_{sigma} = 0.1167	3914 R_{int} = 0.0497, R_{sigma} = 0.0255	3590 R_{int} = 0.1042, R_{sigma} = 0.0555	3384 R_{int} = 0.0352, R_{sigma} = 0.0360
Goodness-of-fit on F^2	1.01	1.045	1.022	1.06
Final R indexes [all data]	R1 = 0.1679, wR2 = 0.2117	R1 = 0.0568, wR = 0.1228	R1 = 0.1322, wR2 = 0.2308	R1 = 0.0554, wR2 = 0.1244

Table A4.1 Continued *Crystallographic data and structure refinement of AZP coformers (**1-11**).*

Identification code	**8**	**9**	**10**	**11**
Empirical formula	$C_{22}H_{31}N_3O$	$C_{22}H_{31}N_3O$	$C_{12}H_9N_3O_2$	$C_{24}H_{18}N_6O_6$
Temperature (K)	200	200	200	200
Crystal system	Triclinic	Triclinic	Monoclinic	Triclinic
Space group	P-1	P-1	$P2_1/c$	P-1
a (Å)	7.7945 (5)	7.7945 (5)	10.6267 (4)	8.9655 (8)
b (Å)	10.8973 (9)	10.8973 (9)	11.4122 (4)	11.0432 (7)
c (Å)	12.4671 (10)	12.4671 (10)	8.6275 (3)	11.3429 (10)
α (°)	92.324 (3)	92.324 (3)	90	74.442 (7)
β (°)	91.120 (2)	91.120 (2)	96.327 (3)	79.434 (7)
γ (°)	104.493 (2)	104.493 (2)	90	88.293 (7)
Volume (Å^3)	1023.92 (14)	1023.92 (14)	1039.92 (6)	1063.32 (16)
Z, Z'	2, 1	2, 1	4, 1	4, 2
ρ_{calc} /g cm^{-3}	1.147	1.147	1.451	1.519
Independent reflections	3906 R_{int} = 0.0924, R_{sigma} = 0.0434	3906 R_{int} = 0.0924, R_{sigma} = 0.0434	2114 R_{int} = 0.0758, R_{sigma} = 0.0422	4011 R_{int} = 0.0760, R_{sigma} = 0.0520
Goodness-of-fit on F^2	1.037	1.037	1.017	1.024
Final R indexes [all data]	R1 = 0.0759, wR2 = 0.1163	R1 = 0.0759, wR2 = 0.1163	R1 = 0.0772, wR2 = 0.1416	R1 = 0.0871, wR2 = 0.1638

APPENDIX B

COCRYSTALS BASED ON ESSENTIAL OILS

B.1 X-ray Powder Patterns

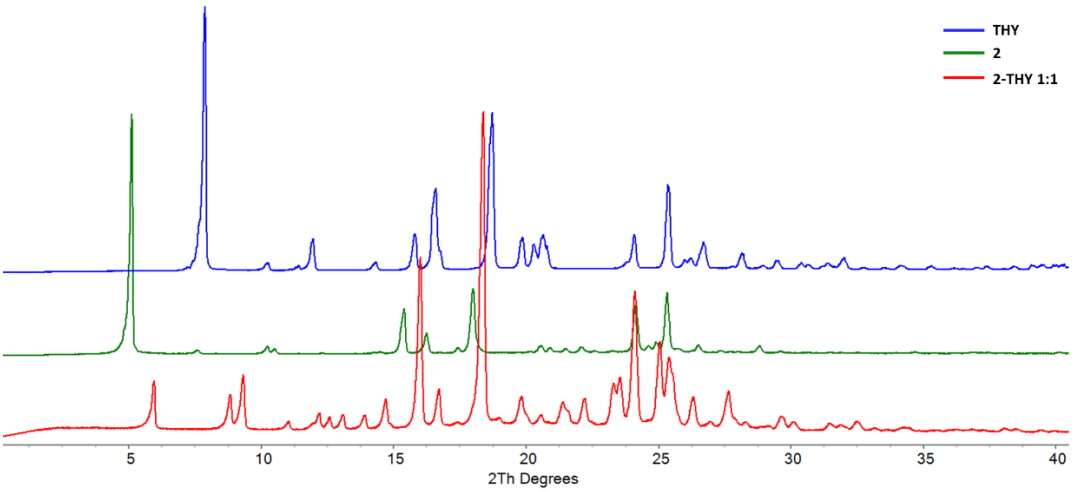

Figure B1.1 *Comparison of the experimental powder patterns of THY, AZP* ***2****, and the mixture* ***2****-THY 1:1 obtained after grinding. The mixture does not show any traces of coformers and corresponds to their cocrystal.*

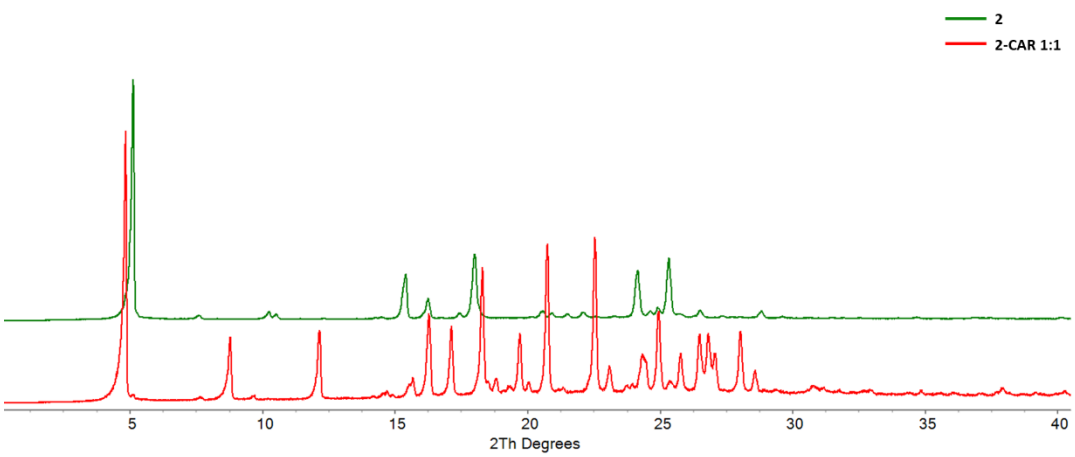

Figure B1.2 *Comparison of the experimental powder patterns of AZP* ***2****, and the mixture* ***2****-CAR 1:1 obtained after grinding. The mixture does not show any traces of coformers and corresponds to their cocrystal.*

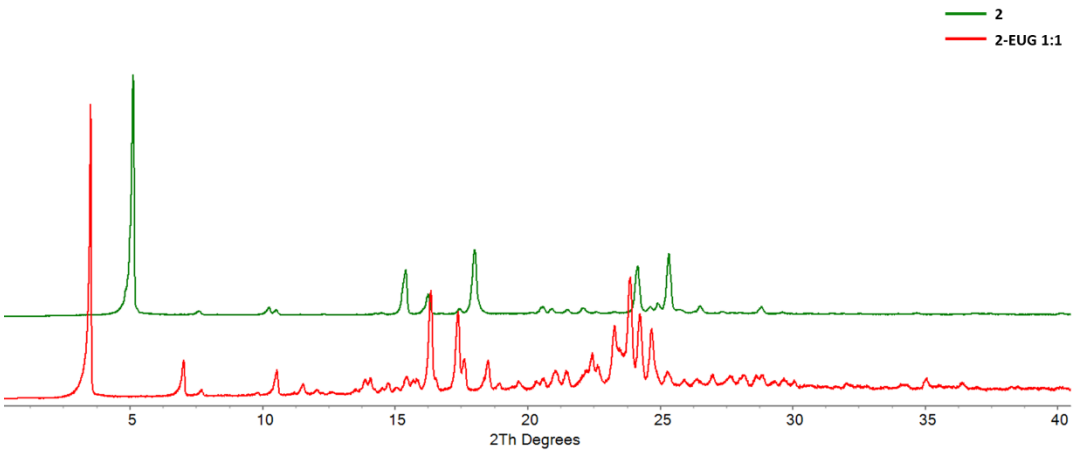

Figure B1.3 *Comparison of the experimental powder patterns of AZP* ***2****, and the mixture* ***2****-EUG 1:1 obtained after grinding. The mixture does not show any traces of coformers and corresponds to their cocrystal.*

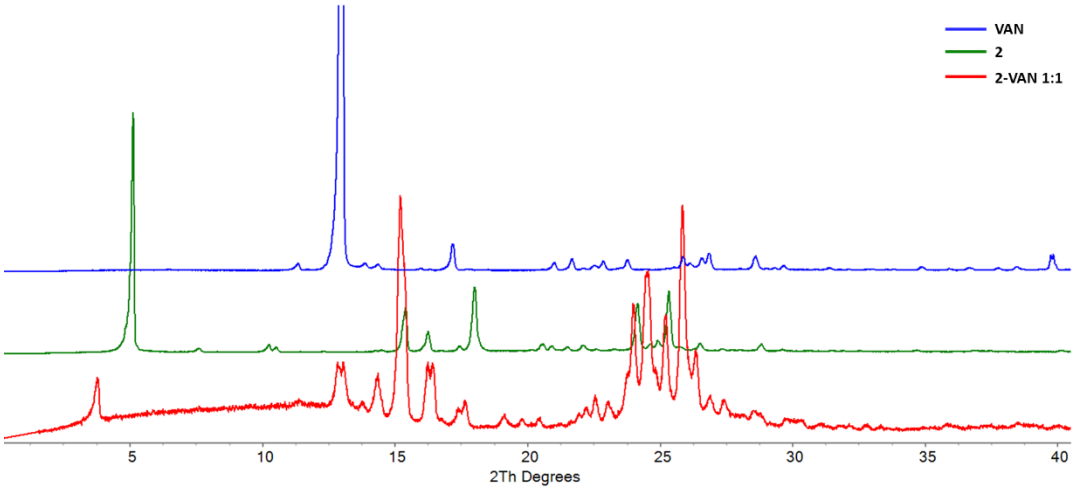

Figure B1.4 *Comparison of the experimental powder patterns of VAN, AZP* ***2****, and the mixture* ***2****-VAN 1:1 obtained after grinding. The mixture mainly corresponds to the cocrystal, however a small amount of VAN remained.*

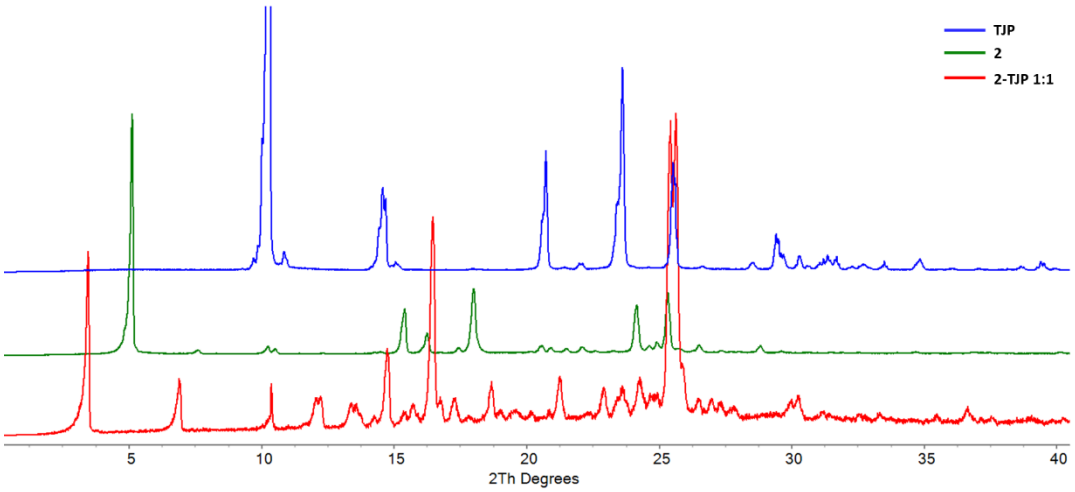

Figure B1.5 *Comparison of the experimental powder patterns of TJP, AZP* ***2****, and the mixture* ***2****-TJP 1:1 obtained after grinding. The mixture does not show any traces of coformers and corresponds to their cocrystal.*

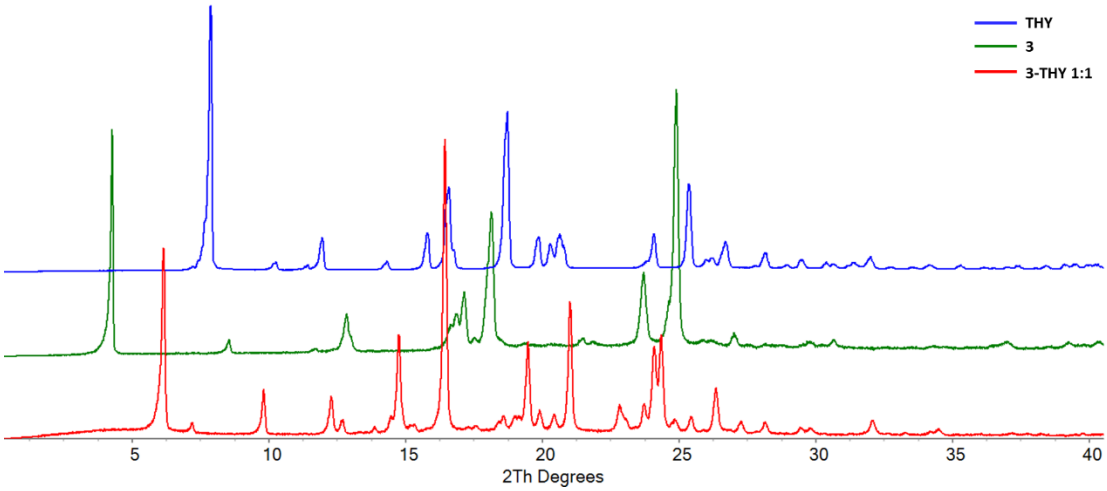

Figure B1.6 *Comparison of the experimental powder patterns of THY, AZP **3**, and the mixture **3**-THY 1:1 obtained after grinding. The mixture does not show any traces of coformers and corresponds to their cocrystal.*

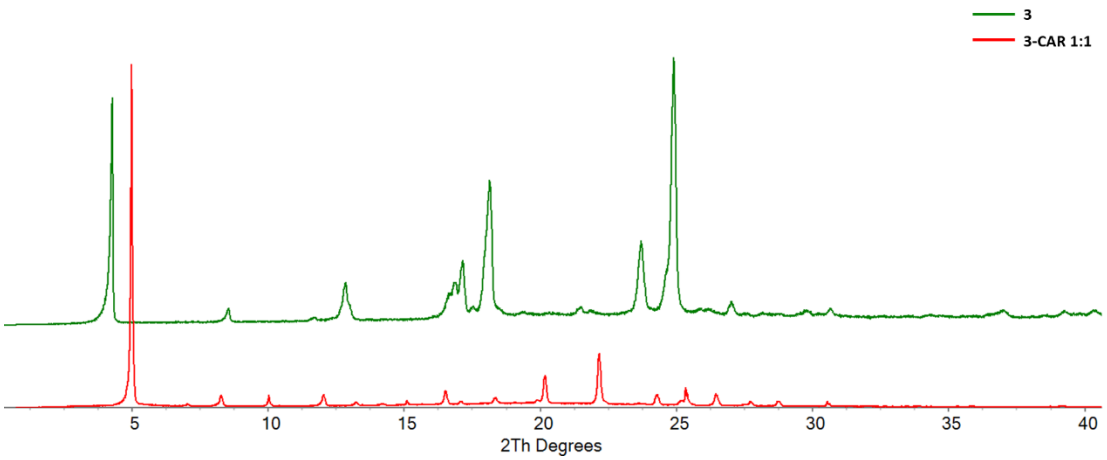

Figure B1.7 *Comparison of the experimental powder patterns of AZP **3**, and the mixture **3**-CAR 1:1 obtained after grinding. The mixture does not show any traces of coformers and corresponds to their cocrystal.*

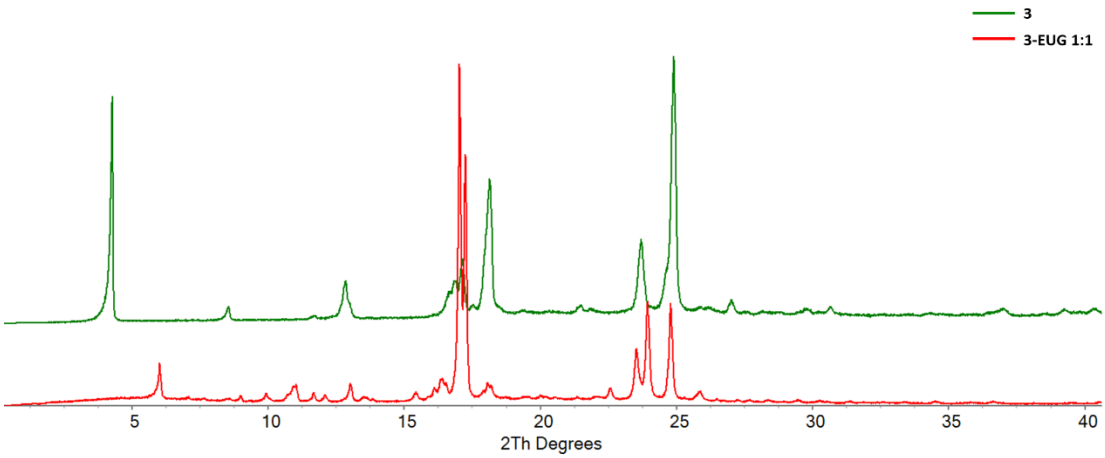

Figure B1.8 *Comparison of the experimental powder patterns of AZP* ***3****, and the mixture* ***3****-EUG 1:1 obtained after grinding. The mixture does not show any traces of coformers and corresponds to their cocrystal.*

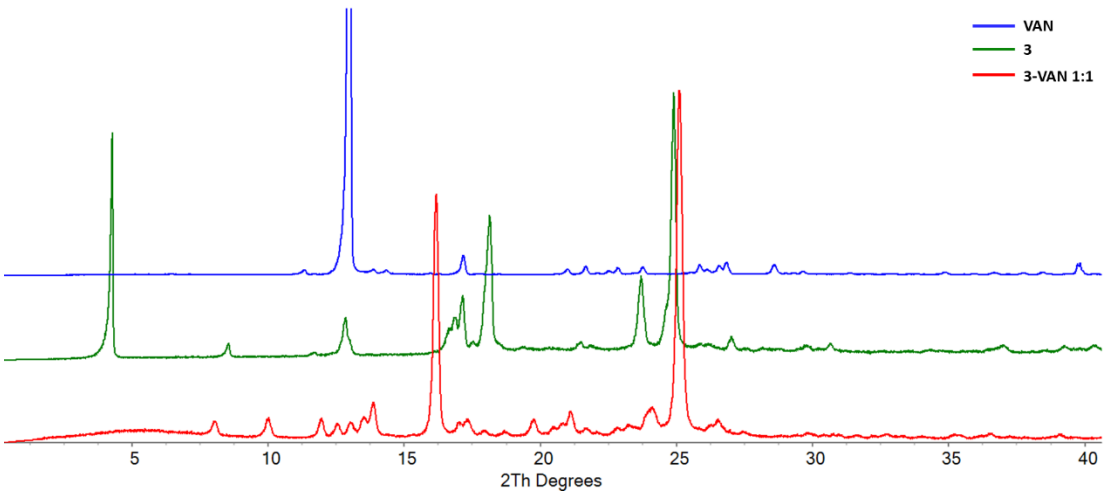

Figure B1.9 *Comparison of the experimental powder patterns of VAN, AZP* ***3****, and the mixture* ***3****-VAN 1:1 obtained after grinding. The mixture does not show any traces of coformers and corresponds to their cocrystal.*

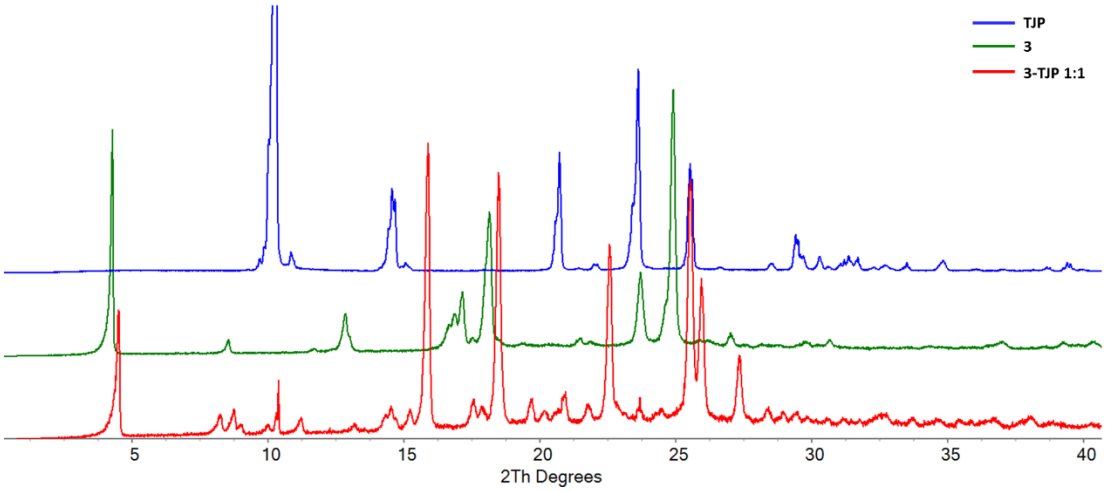

Figure B1.10 *Comparison of the experimental powder patterns of TJP, AZP* ***3****, and the mixture* ***3****-TJP 1:1 obtained after grinding. The mixture overall corresponds to the cocrystal, however a tiny amount of TJP remained.*

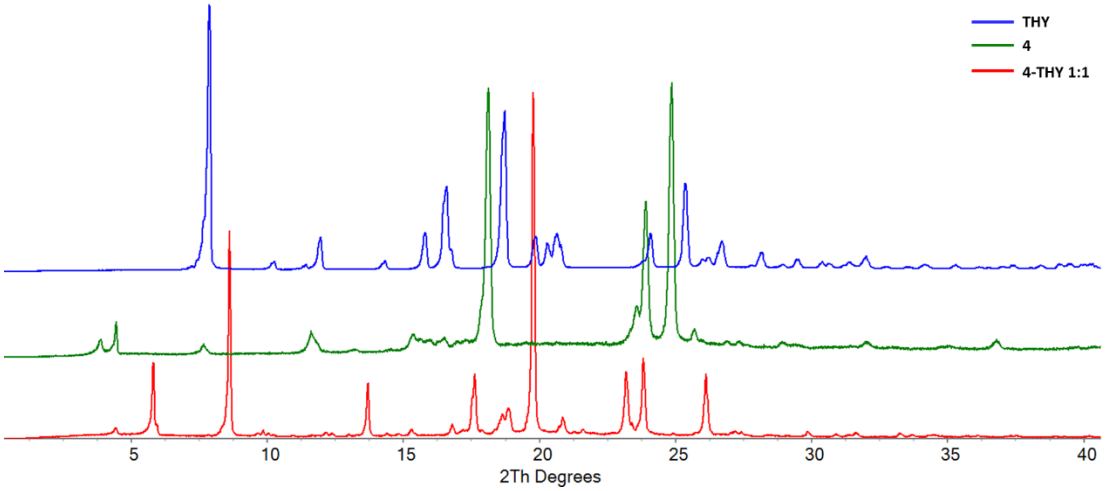

Figure B1.11 *Comparison of the experimental powder patterns of THY, AZP* ***4****, and the mixture* ***4****-THY 1:1 obtained after grinding. The mixture does not show any traces of coformers and corresponds to their cocrystal.*

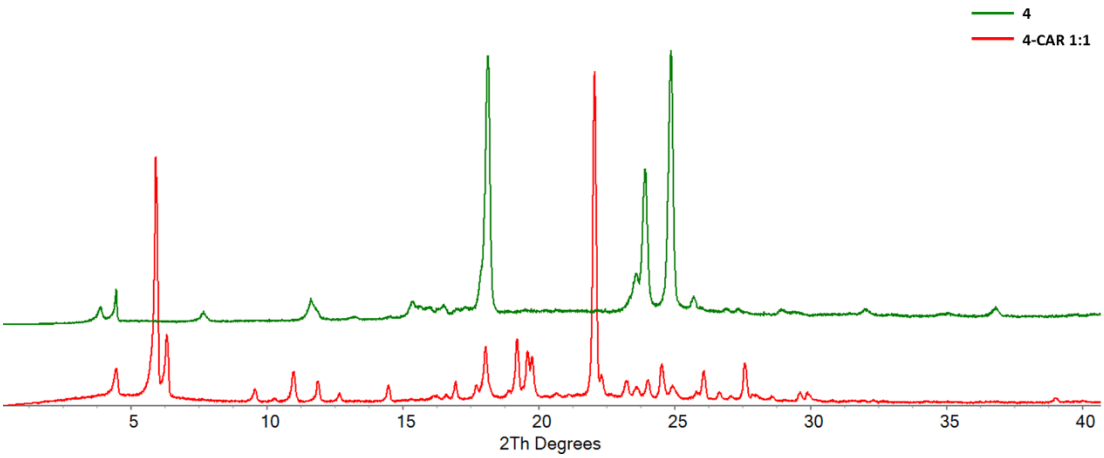

Figure B1.12 *Comparison of the experimental powder patterns of AZP* ***4****, and the mixture* ***4****-CAR 1:1 obtained after grinding. The mixture does not show any traces of coformers and corresponds to their cocrystal.*

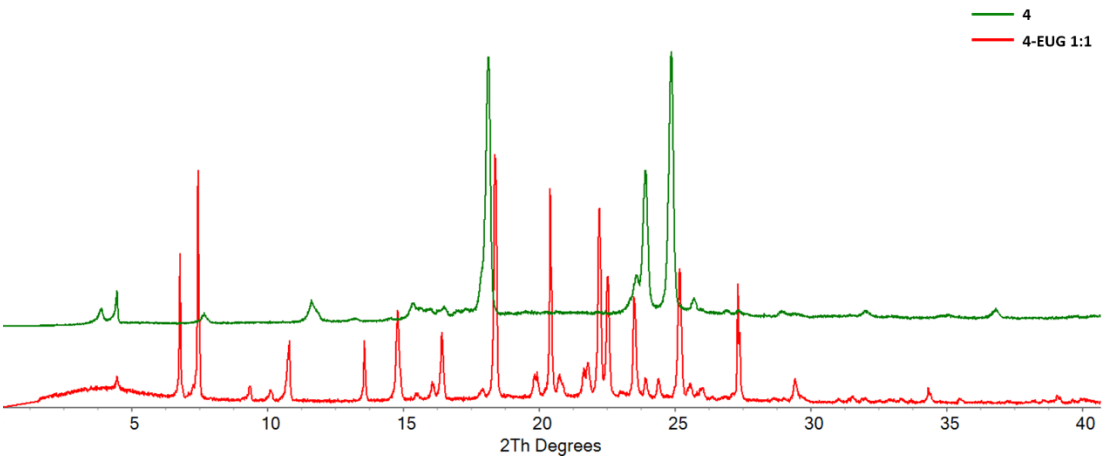

Figure B1.13 *Comparison of the experimental powder patterns of AZP* ***4****, and the mixture* ***4****-EUG 1:1 obtained after grinding. The mixture does not show any traces of coformers and corresponds to their cocrystal.*

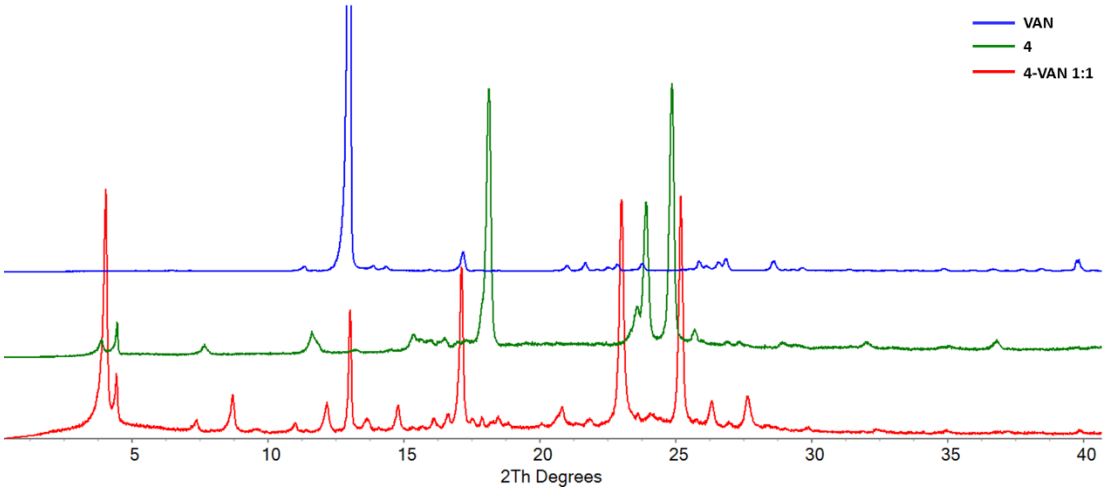

Figure B1.14 *Comparison of the experimental powder patterns of VAN, AZP* ***4****, and the mixture* ***4****-VAN 1:1 obtained after grinding. The mixture does not show any traces of coformers and corresponds to their cocrystal.*

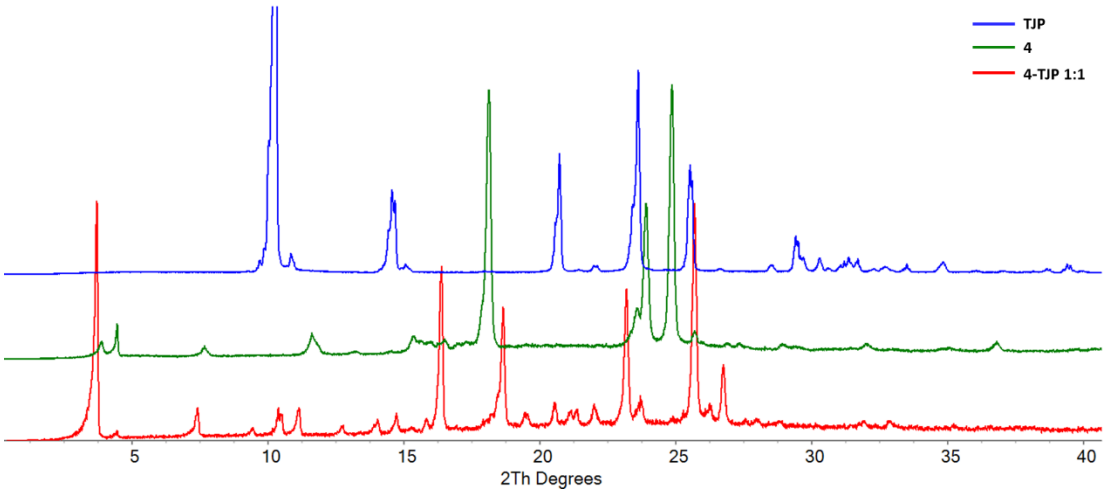

Figure B1.15 *Comparison of the experimental powder patterns of TJP, AZP* ***4****, and the mixture* ***4****-TJP 1:1 obtained after grinding. The mixture does not show any traces of coformers and corresponds to their cocrystal.*

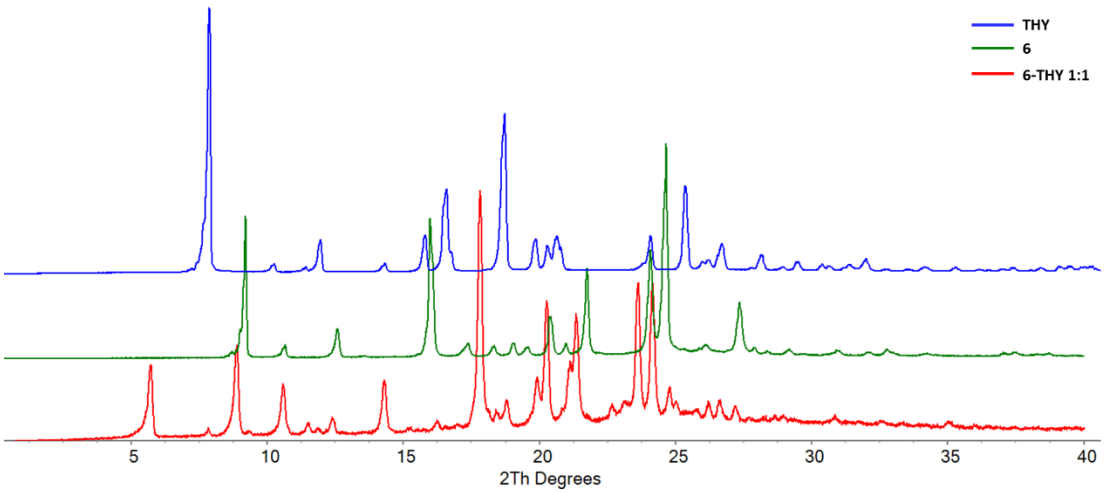

Figure B1.16 *Comparison of the experimental powder patterns of THY, AZP* ***6****, and the mixture* ***6****-THY 1:1 obtained after grinding. The mixture does not show any traces of coformers and corresponds to their cocrystal.*

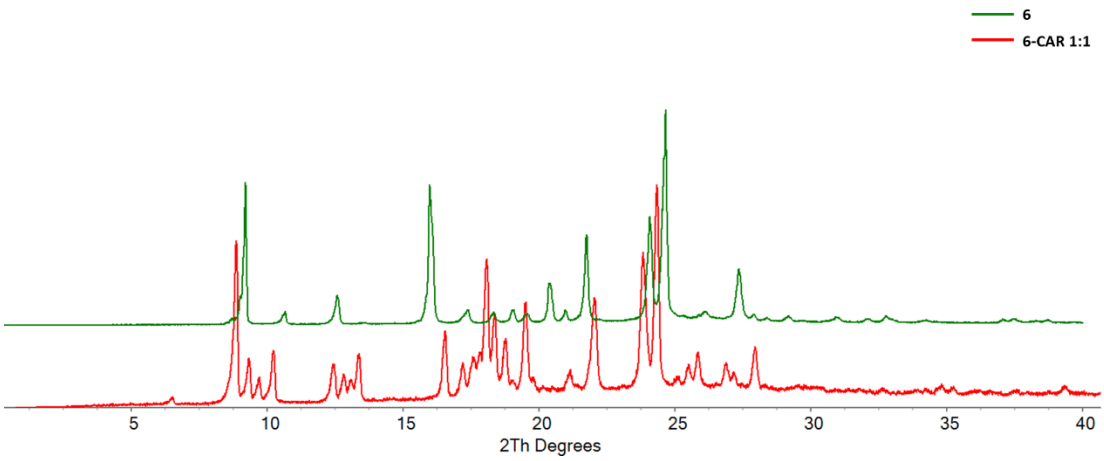

Figure B1.17 *Comparison of the experimental powder patterns of AZP* ***6****, and the mixture* ***6****-CAR 1:1 obtained after grinding. The mixture does not show any traces of coformers and corresponds to their cocrystal.*

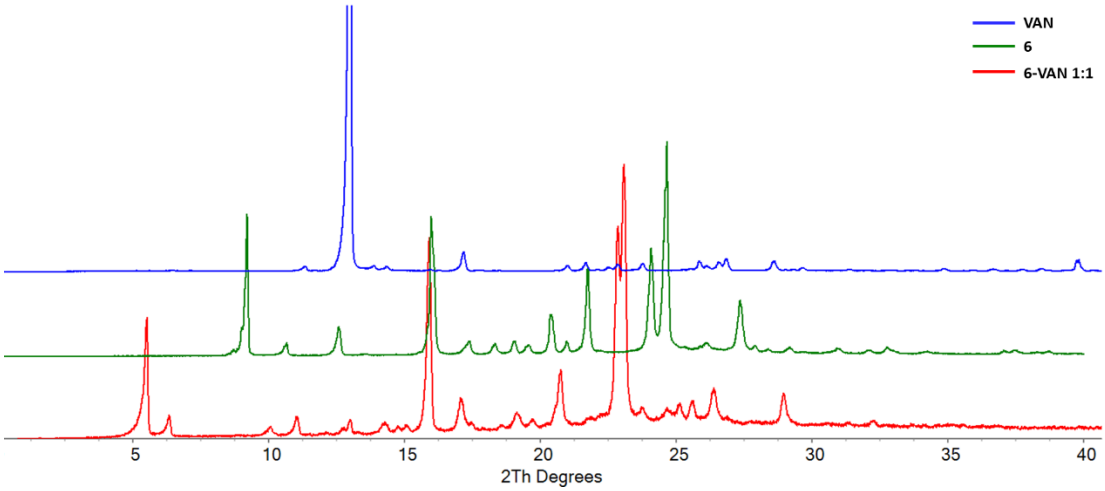

Figure B1.18 *Comparison of the experimental powder patterns of VAN, AZP* ***6****, and the mixture* ***6****-VAN 1:1 obtained after grinding. The mixture does not show any traces of coformers and corresponds to their cocrystal.*

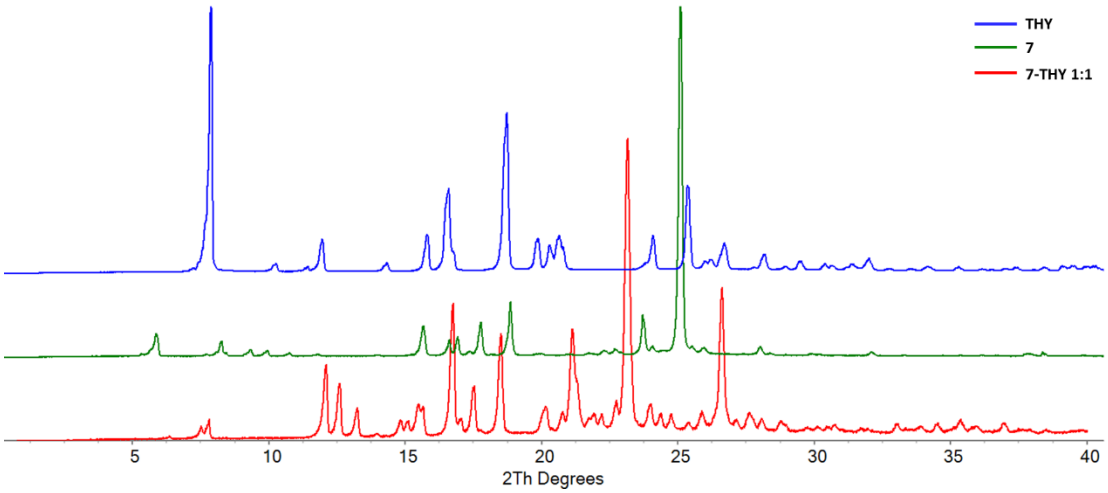

Figure B1.19 *Comparison of the experimental powder patterns of THY, AZP* ***7****, and the mixture* ***7****-THY 1:1 obtained after grinding. The mixture does not show any traces of coformers and corresponds to their cocrystal.*

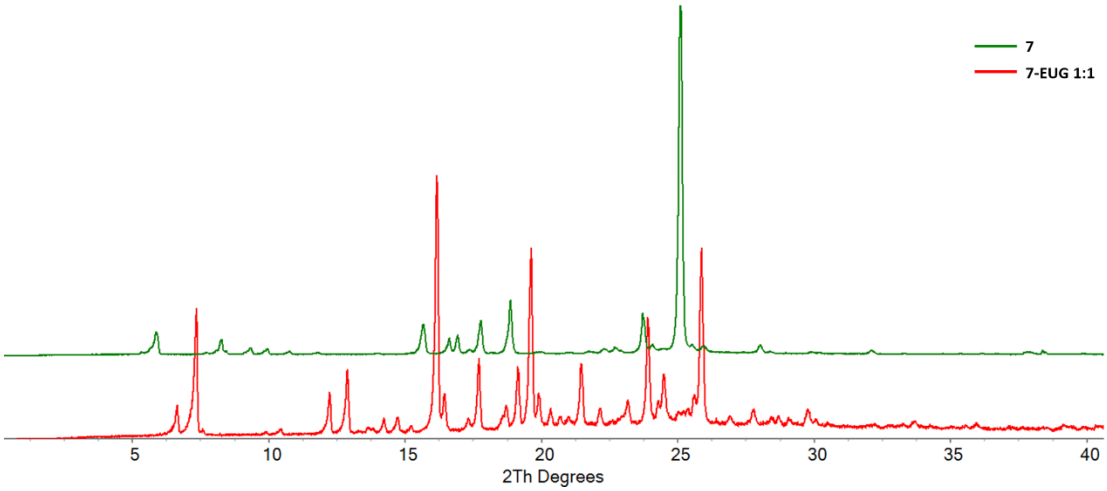

Figure B1.20 *Comparison of the experimental powder patterns of AZP **7**, and the mixture **7**-EUG 1:1 obtained after grinding. The mixture does not show any traces of coformers and corresponds to their cocrystal.*

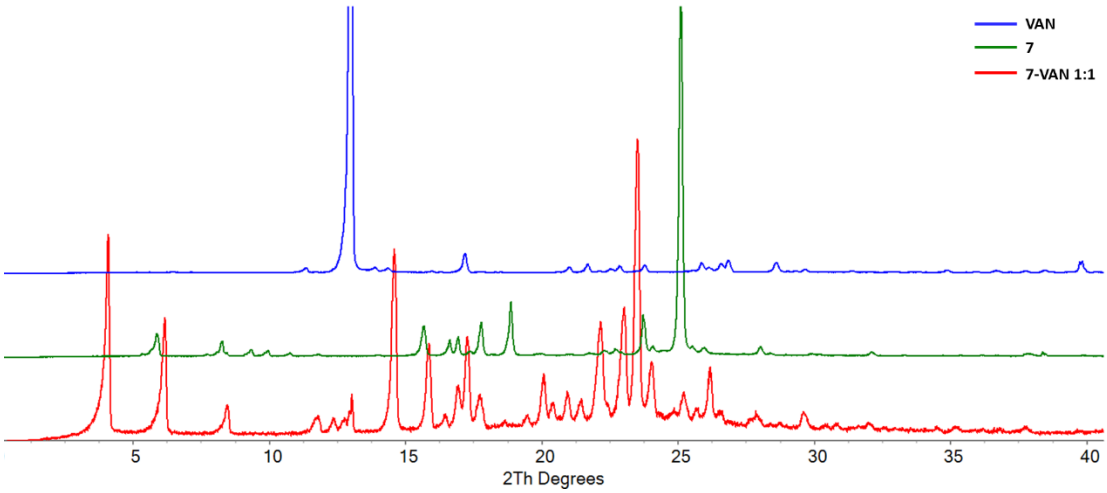

Figure B1.21 *Comparison of the experimental powder patterns of VAN, AZP **7**, and the mixture **7**-VAN 1:1 obtained after grinding. The mixture does not show any traces of coformers and corresponds to their cocrystal.*

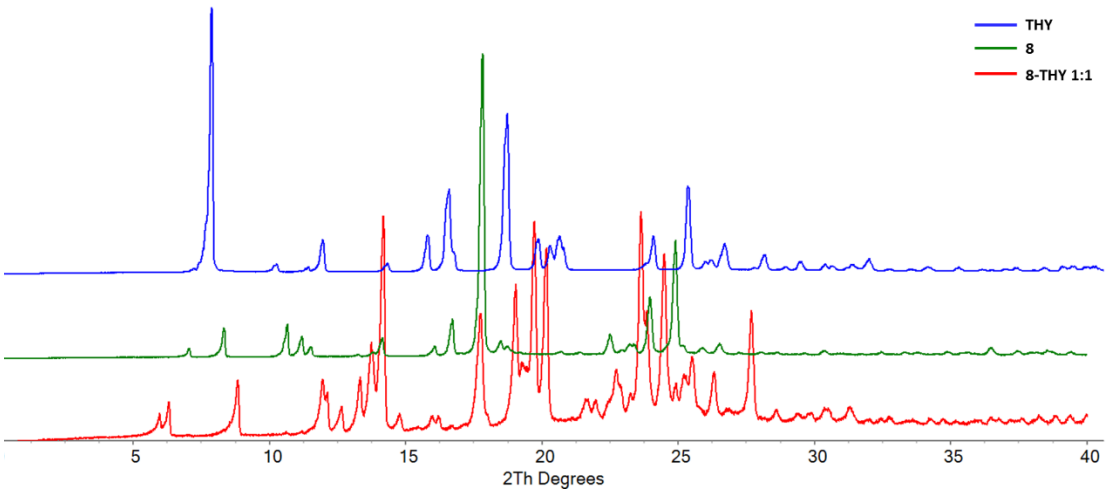

Figure B1.22 *Comparison of the experimental powder patterns of THY, AZP* ***8****, and the mixture* ***8****-THY 1:1 obtained after grinding. The mixture does not show any traces of coformers and corresponds to their cocrystal.*

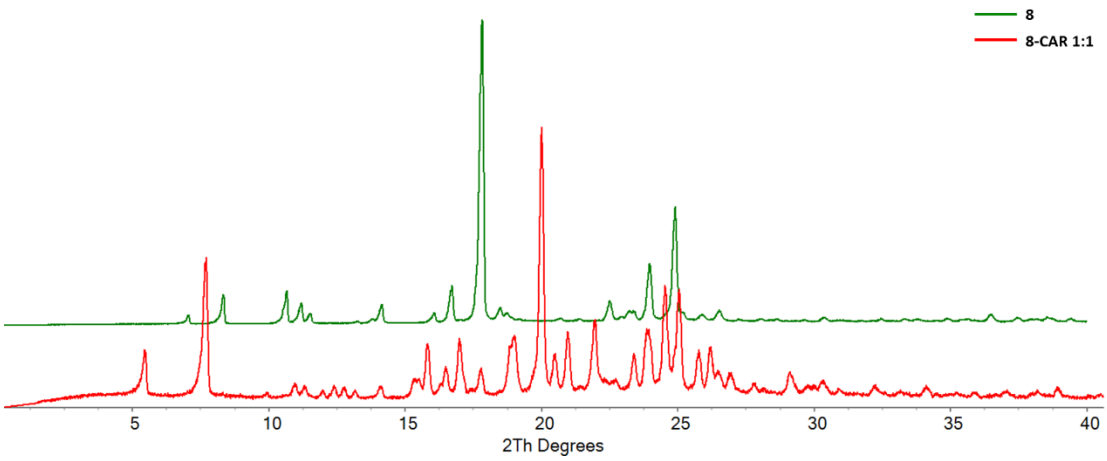

Figure B1.23 *Comparison of the experimental powder patterns of AZP* ***8****, and the mixture* ***8****-CAR 1:1 obtained after grinding. The mixture does not show any traces of coformers and corresponds to their cocrystal.*

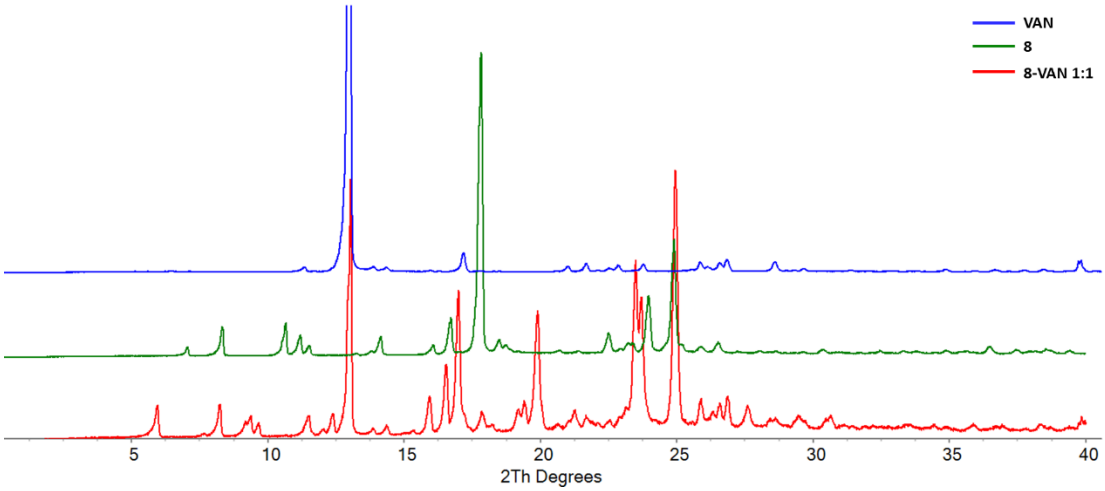

Figure B1.24 *Comparison of the experimental powder patterns of VAN, AZP* ***8****, and the mixture* ***8****-VAN 1:1 obtained after grinding. The mixture does not show any traces of coformers and corresponds to their cocrystal.*

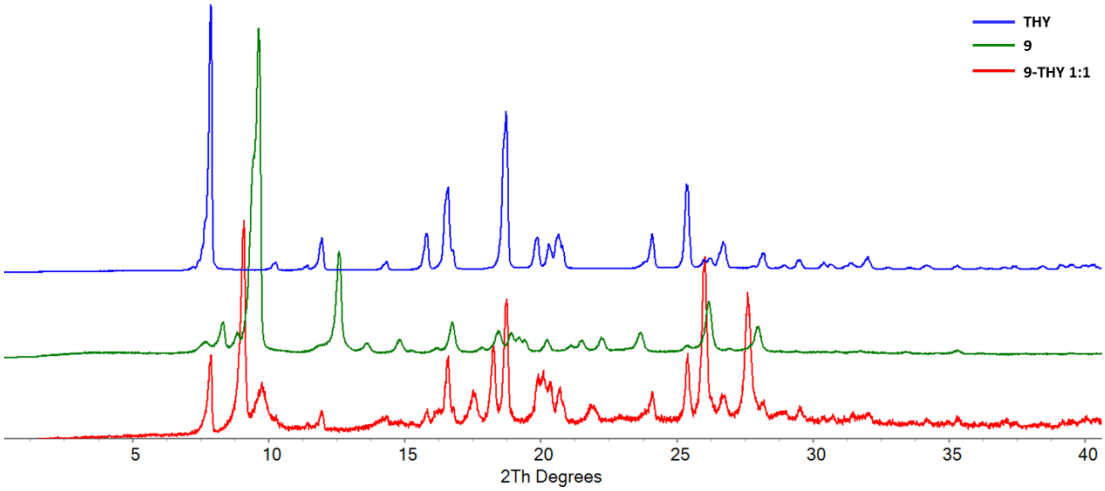

Figure B1.25 *Comparison of the experimental powder patterns of THY, AZP* ***9****, and the mixture* ***9****-THY 1:1 obtained after grinding. The mixture shows traces of THY even after longer grinding time or addition of a few drops of solvent. Nevertheless, the main phase corresponds to the cocrystal.*

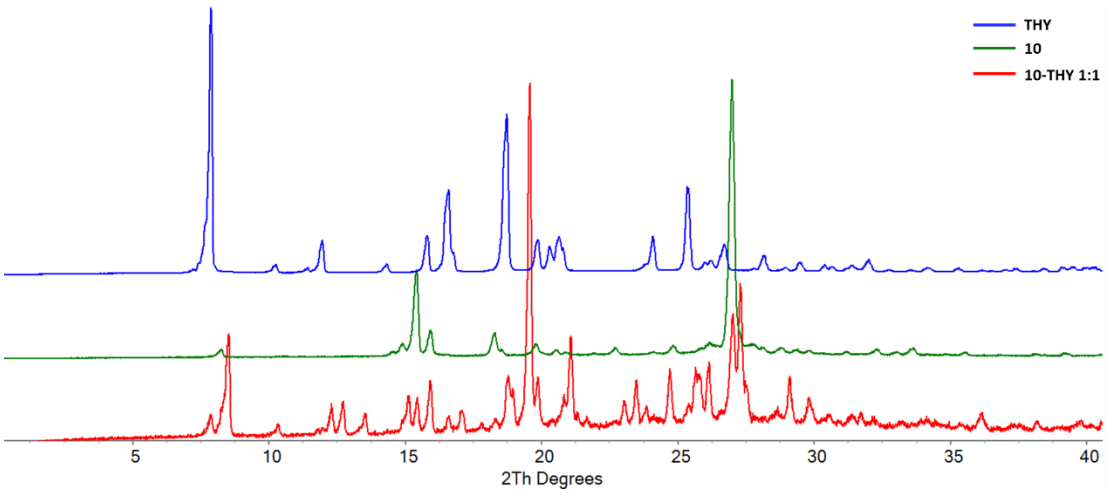

Figure B1.27 *Comparison of the experimental powder patterns of THY, AZP* ***10****, and the mixture* ***10****-THY 1:1 obtained after grinding. The mixture shows traces of THY even after longer grinding time or addition of a few drops of solvent. Nevertheless, the main phase corresponds to the cocrystal.*

B.2 DSC Thermograms

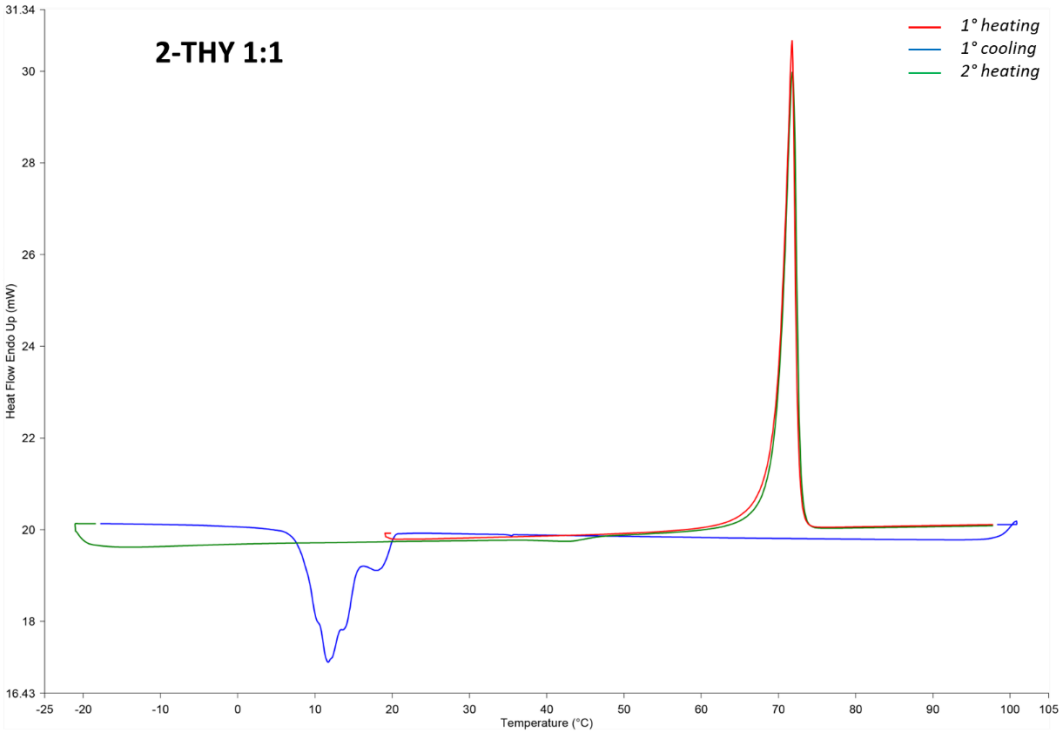

Figure B2.1 *Thermogram of **2**-THY 1:1. First heating run from 20 °C to 100 °C (red curve), cooling run from 100 °C to -20 °C (blue curve) and second heating run from -20 °C to 100 °C (green curve). The whole firing profile was performed at 5°C/min. The endothermic peaks shown in the heating runs refer to the melting of **2**-THY 1:1, while the exothermic peak in the cooling run refers to cocrystal recrystallization. A glass transition was recorded at 44.55 °C.*

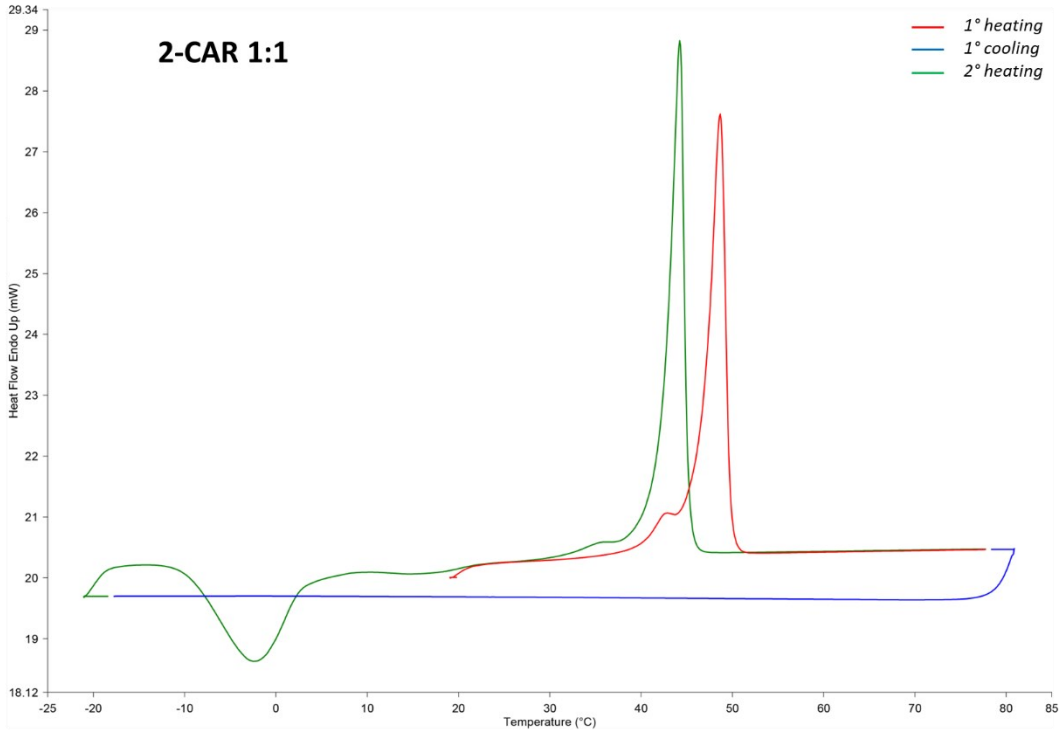

Figure B2.2 *Thermogram of **2**-CAR 1:1. First heating run from 20 °C to 80 °C (red curve), cooling run from 80 °C to -20 °C (blue curve) and second heating run from -20 °C to 80 °C (green curve). The whole firing profile was performed at 5°C/min. The endothermic peaks shown in the heating runs refer to the melting of **2**-CAR 1:1, while the endothermic peak shown in the second heating run is due to the melting of a different polymorph, which crystallized from the melt in the cooling run. A small amount of **2** was probably present in the starting mixture as confirmed by the smaller endothermic peak in the first heating run. Also, a partial recrystallization of **2** likely occurred due to the smaller endothermic peak in the second heating run.*

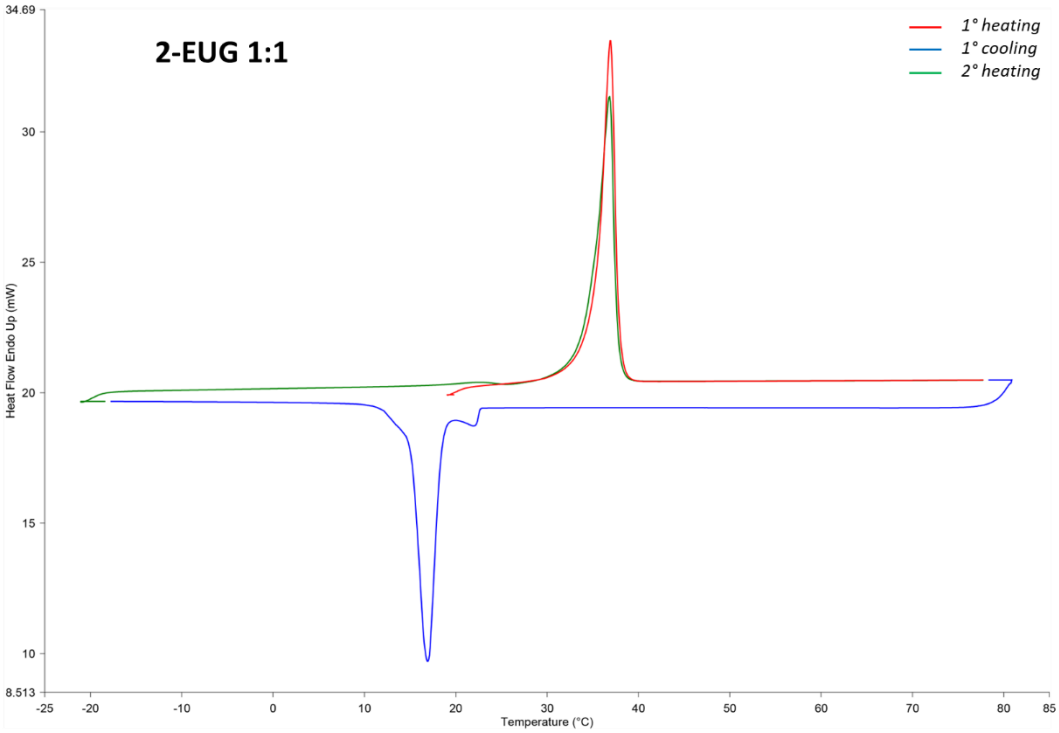

Figure B2.3 *Thermogram of **2**-EUG 1:1. First heating run from 20 °C to 80 °C (red curve), cooling run from 80 °C to -20 °C (blue curve) and second heating run from -20 °C to 80 °C (green curve). The whole firing profile was performed at 5°C/min. The endothermic peaks shown in the heating runs refer to the melting of **2**-EUG 1:1, while the exothermic peak in the cooling run refers to cocrystal recrystallization.*

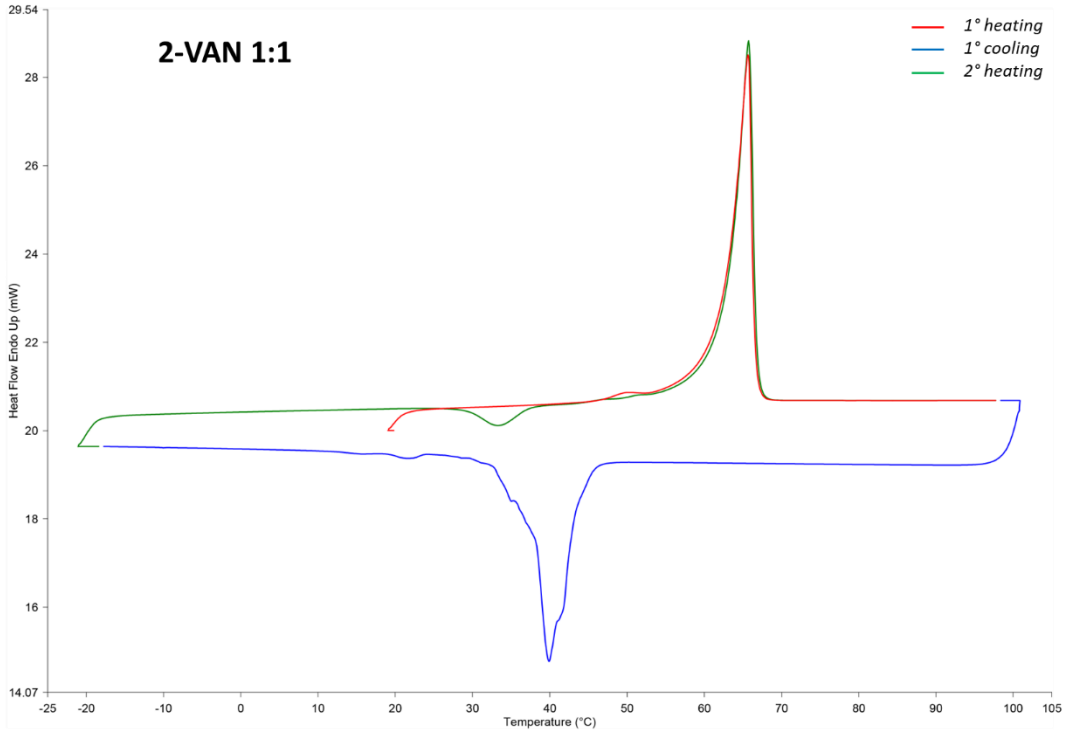

Figure B2.4 *Thermogram of* ***2****-VAN 1:1. First heating run from 20 °C to 100 °C (red curve), cooling run from 100 °C to -20 °C (blue curve) and second heating run from -20 °C to 100 °C (green curve). The whole firing profile was performed at 5°C/min. The endothermic peaks shown in the heating runs refer to the melting of* ***2****-VAN 1:1, while the exothermic peaks in the cooling run and in the second heating run refer to cocrystal recrystallization. A tiny amount of vanillin was probably present in the starting mixture as confirmed by the smaller endothermic peak in the first heating run.*

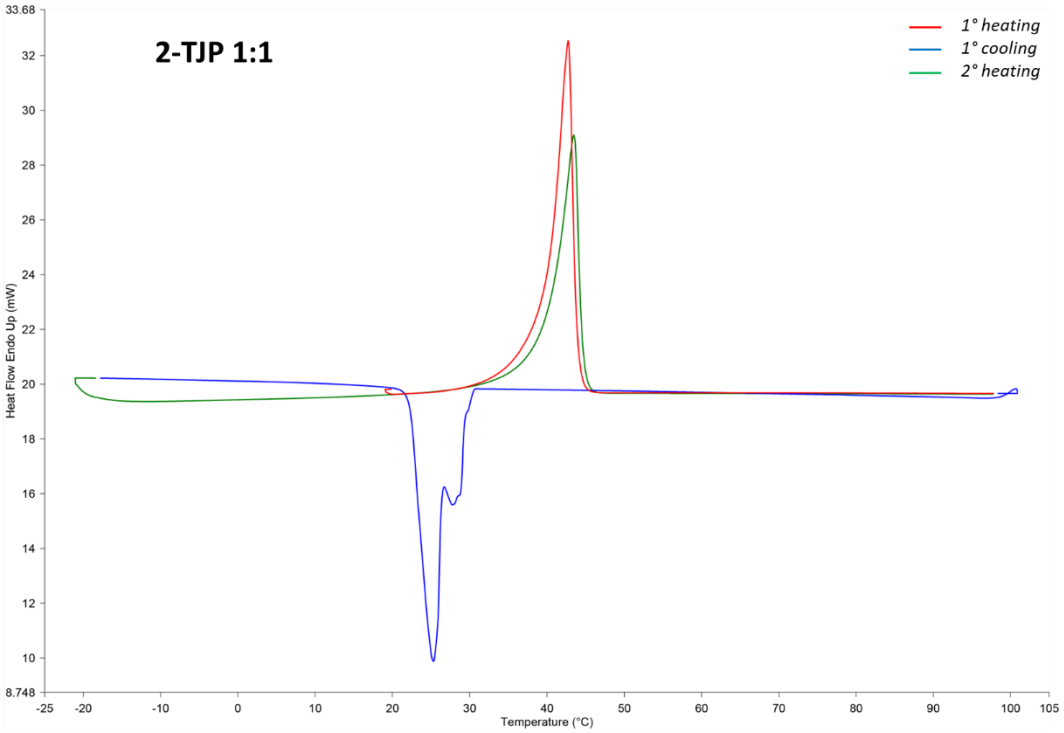

Figure B2.5 *Thermogram of **2**-TJP 1:1. First heating run from 20 °C to 100 °C (red curve), cooling run from 100 °C to -20 °C (blue curve) and second heating run from -20 °C to 100 °C (green curve). The whole firing profile was performed at 5°C/min. The endothermic peaks shown in the heating runs refer to the melting of **2**-TJP 1:1, while the exothermic peak refers to cocrystal recrystallization.*

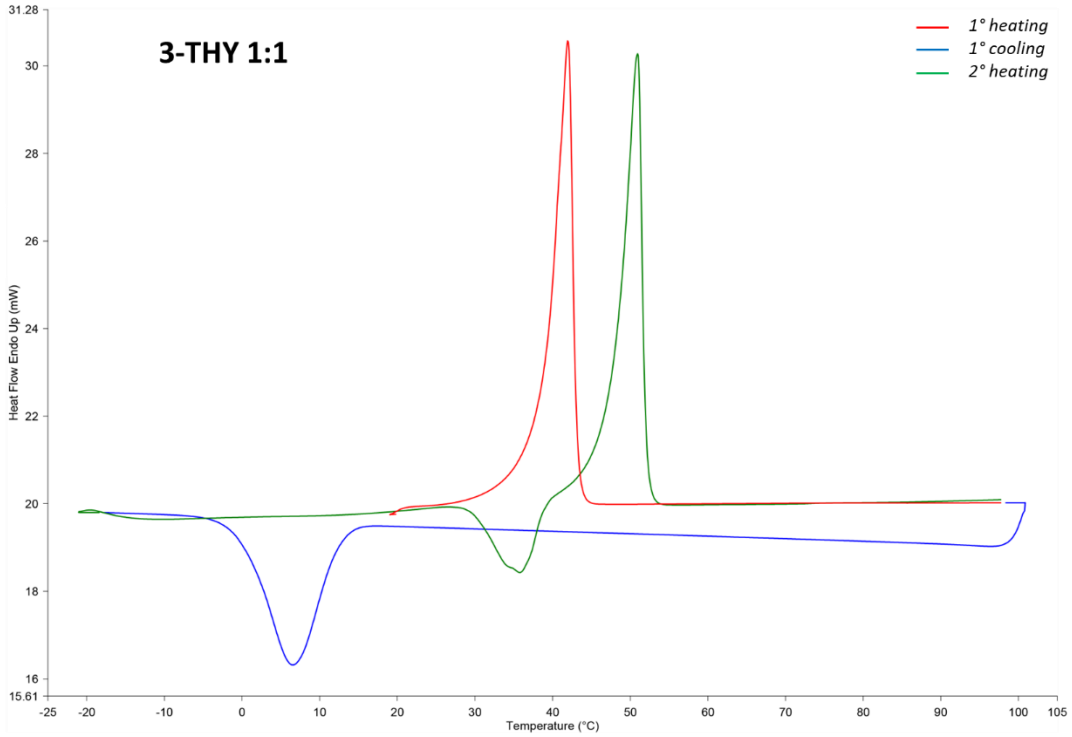

Figure B2.6 *Thermogram of **3**-THY 1:1. First heating run from 20 °C to 100 °C (red curve), cooling run from 100 °C to -20 °C (blue curve) and second heating run from -20 °C to 100 °C (green curve). The whole firing profile was performed at 5°C/min. The endothermic peak shown in the first heating run refers to the melting of **3**-THY 1:1, while the endothermic peak shown in the second heating run is due to the melting of another polymorph, which crystallized from the melt.*

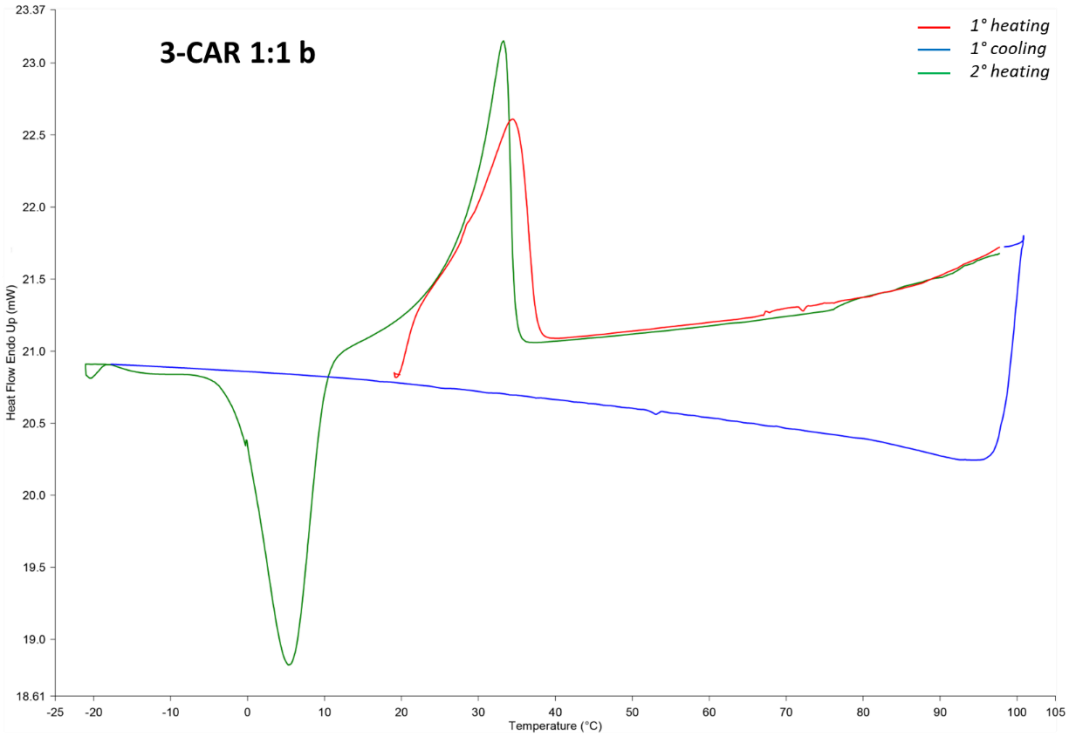

Figure B2.7 *Thermogram of **3**-CAR 1:1 **b**. First heating run from 20 °C to 100 °C (red curve), cooling run from 100 °C to -20 °C (blue curve) and second heating run from -20 °C to 100 °C (green curve). The whole firing profile was performed at 5°C/min. The endothermic peak shown in the first heating run refers to the melting of **3**-CAR 1:1, while the endothermic peak shown in the second heating run is due to the melting of a different polymorph, which crystallized from the melt.*

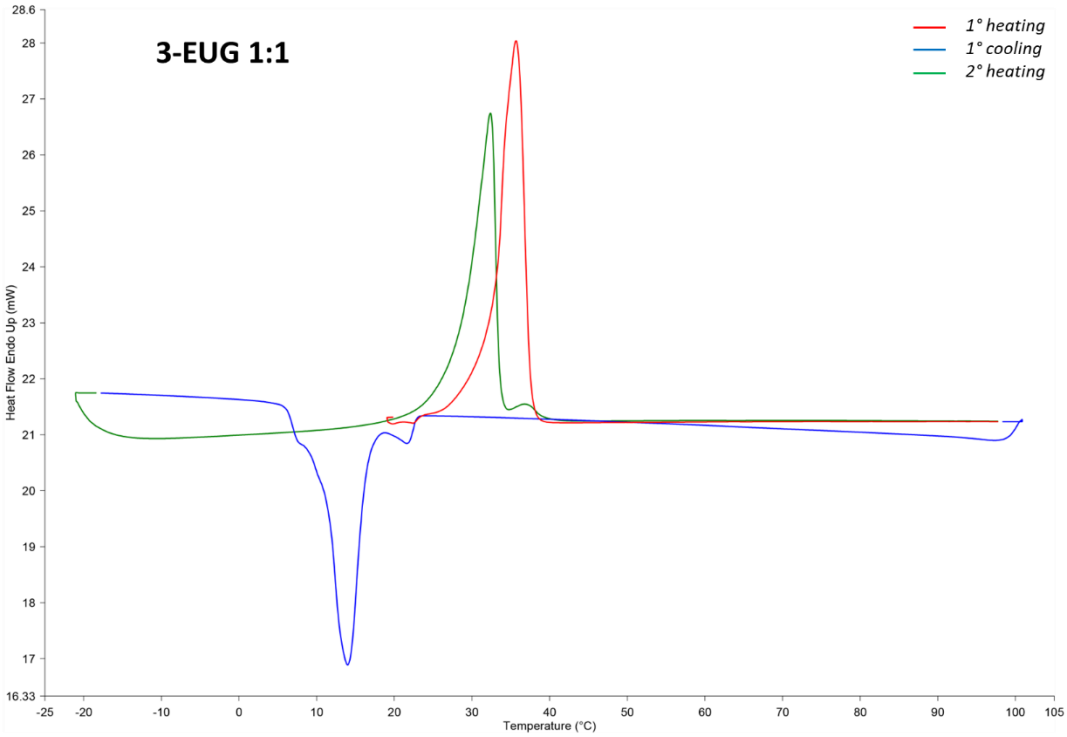

Figure B2.8 *Thermogram of **3**-EUG 1:1. First heating run from 20 °C to 100 °C (red curve), cooling run from 100 °C to -20 °C (blue curve) and second heating run from -20 °C to 100 °C (green curve). The whole firing profile was performed at 5°C/min. The endothermic peak shown in the first heating run refers to the melting of **3**-EUG 1:1. In the second heating run the melting of a different polymorph is partially overlapped to an exothermic peak due to the recrystallization of **3**-EUG 1:1 cocrystal, in turn followed by the second endothermic peak referred to the melting of **3**-EUG 1:1.*

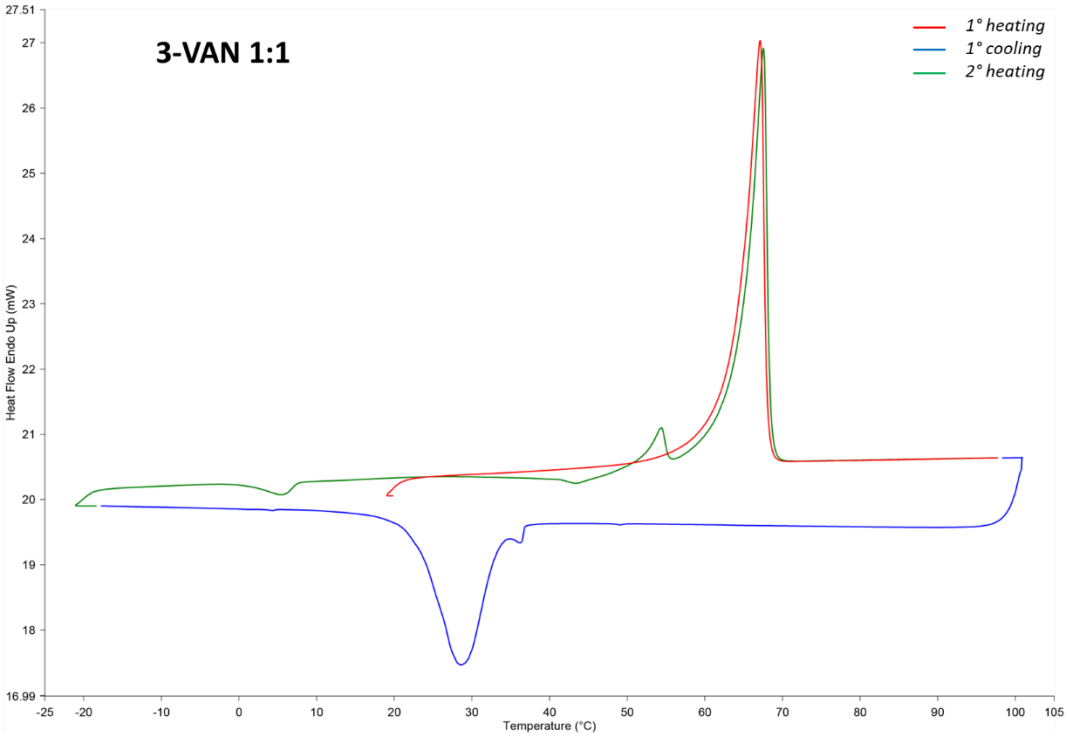

Figure B2.9 *Thermogram of **3**-VAN 1:1. First heating run from 20 °C to 100 °C (red curve), cooling run from 100 °C to -20 °C (blue curve) and second heating run from -20 °C to 100 °C (green curve). The whole firing profile was performed at 5°C/min. The endothermic peaks shown in the heating runs refer to the melting of **3**-VAN 1:1, while the exothermic peak refers mainly to cocrystal recrystallization. A small amount of coformers recrystallized from melt as confirmed by the smaller endothermic peak in the second heating run.*

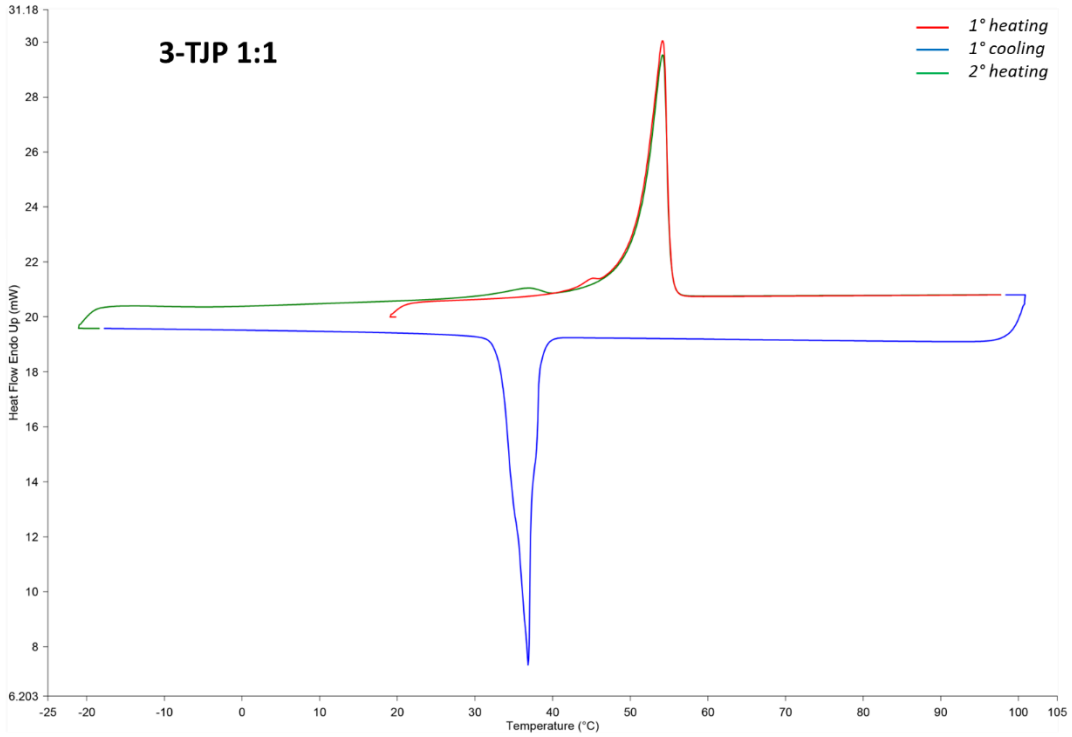

Figure B2.10 *Thermogram of **3**-TJP 1:1. First heating run from 20 °C to 100 °C (red curve), cooling run from 100 °C to -20 °C (blue curve) and second heating run from -20 °C to 100 °C (green curve). The whole firing profile was performed at 5°C/min. The endothermic peaks shown in the heating runs refer to the melting of **3**-TJP 1:1, while the exothermic peak in the cooling run refers to cocrystal recrystallization. A tiny amount of β-thujaplicin was probably present in the starting mixture, as confirmed by the smaller endothermic peak in the first heating run, that recrystallized in the second heating run as confirmed by the smaller endothermic peak.*

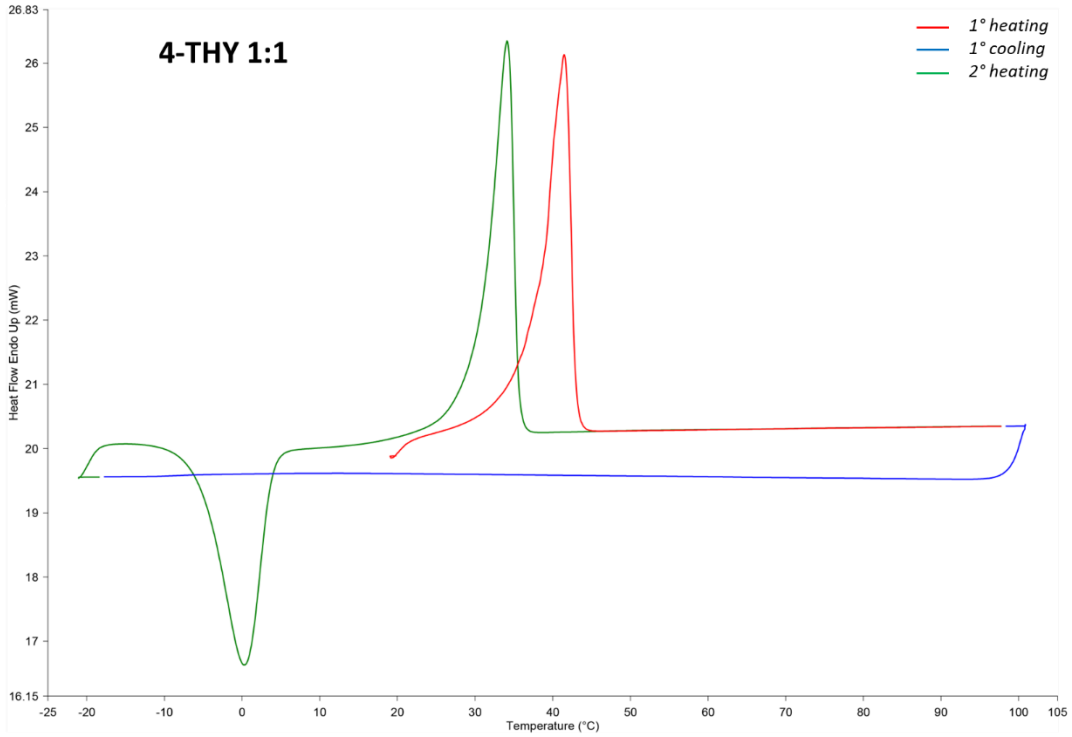

Figure B2.11 *Thermogram of **4**-THY 1:1. First heating run from 20 °C to 100 °C (red curve), cooling run from 100 °C to -20 °C (blue curve) and second heating run from -20 °C to 100 °C (green curve). The whole firing profile was performed at 5°C/min. The endothermic peak shown in the first heating run refers to the melting of **4**-THY 1:1, while the endothermic peak shown in the second heating run is due to the melting of another polymorph, which crystallized from the melt.*

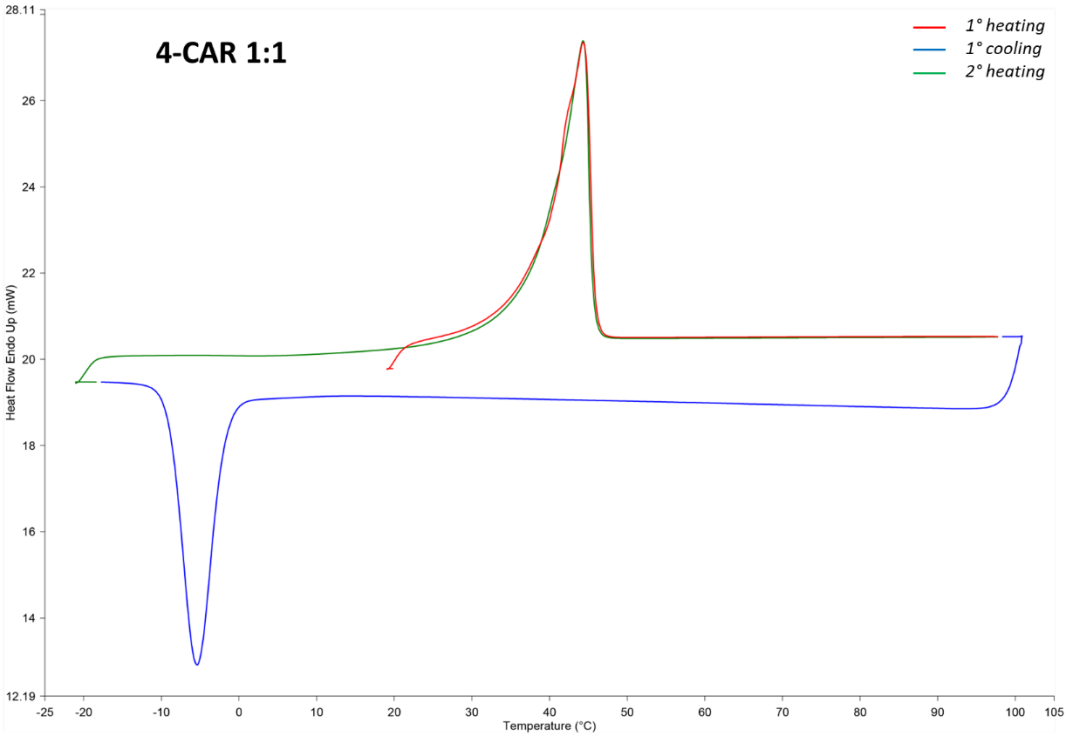

Figure B2.12 *Thermogram of **4**-CAR 1:1. First heating run from 20 °C to 100 °C (red curve), cooling run from 100 °C to -20 °C (blue curve) and second heating run from -20 °C to 100 °C (green curve). The whole firing profile was performed at 5°C/min. The endothermic peaks shown in the heating runs refer to the melting of **4**-CAR 1:1, while the exothermic peak in the cooling run refers to cocrystal recrystallization.*

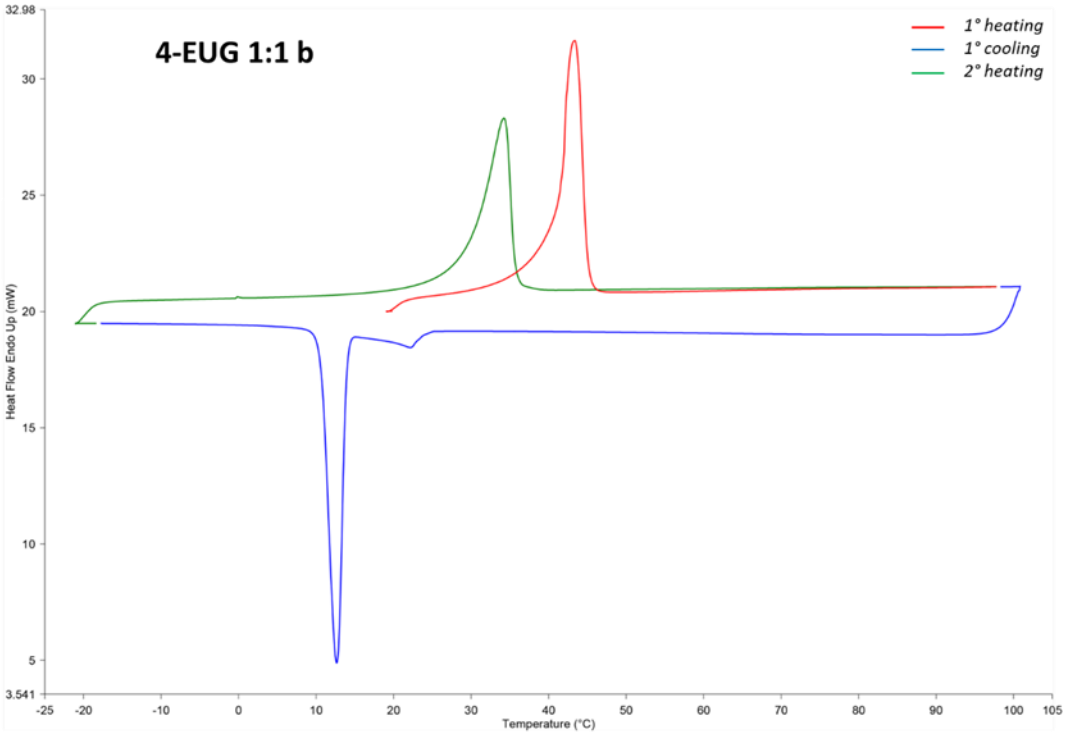

Figure B2.13 *Thermogram of **4**-EUG 1:1 **b**. First heating run from 20 °C to 100 °C (red curve), cooling run from 100 °C to -20 °C (blue curve) and second heating run from -20 °C to 100 °C (green curve). The whole firing profile was performed at 5°C/min. The endothermic peak shown in the first heating run refers to the melting of **4**-EUG 1:1, while the endothermic peak shown in the second heating run is due to the melting of another polymorph, which crystallized from the melt.*

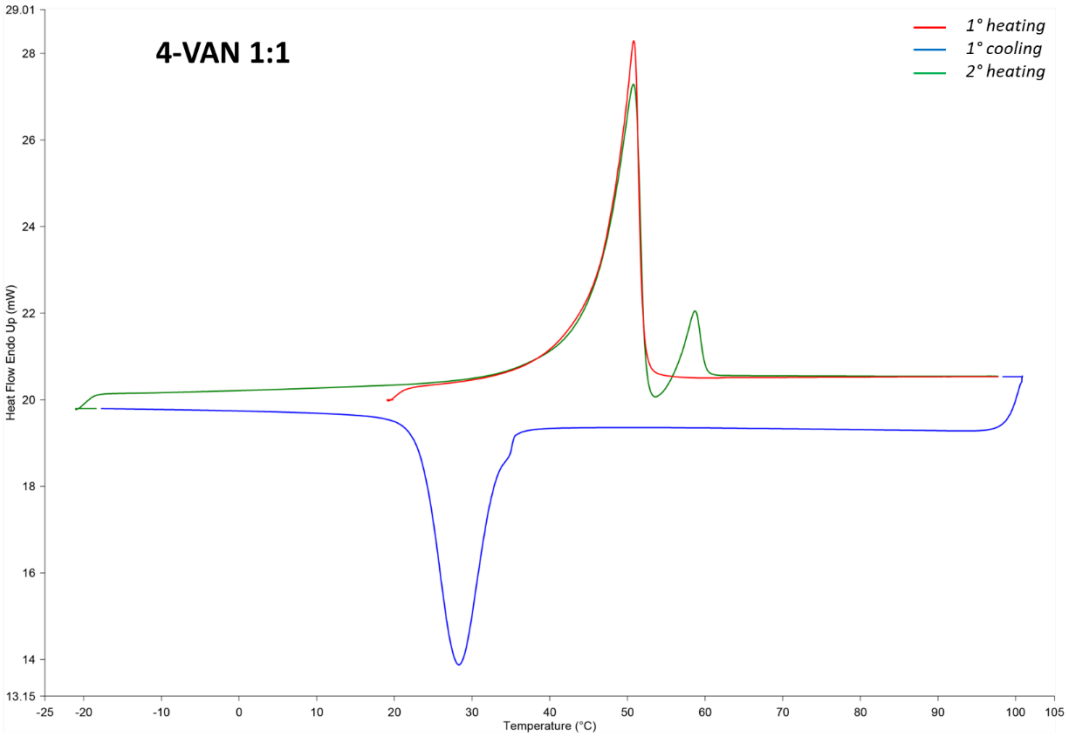

Figure B2.14 *Thermogram of **4**-VAN 1:1. First heating run from 20 °C to 100 °C (red curve), cooling run from 100 °C to -20 °C (blue curve) and second heating run from -20 °C to 100 °C (green curve). The whole firing profile was performed at 5°C/min. The endothermic peak shown in the first heating run refer to the melting of **4**-VAN 1:1, while the exothermic peak in the cooling run refers to cocrystal recrystallization. In the second heating run the melting of **4**-VAN 1:1 is followed by an exothermic peak due to the crystallization of a different polymorph or the coformer AZP **4**, which in turn melted as shown by the second endothermic peak.*

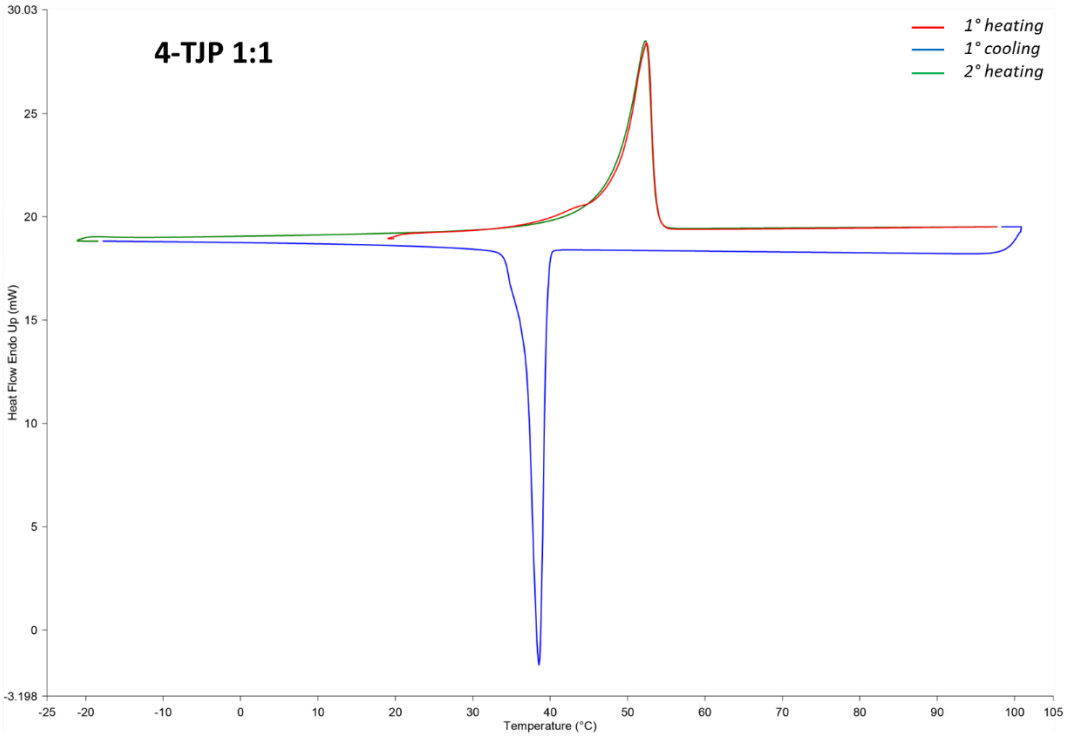

Figure B2.15 *Thermogram of **4**-TJP 1:1. First heating run from 20 °C to 100 °C (red curve), cooling run from 100 °C to -20 °C (blue curve) and second heating run from -20 °C to 100 °C (green curve). The whole firing profile was performed at 5°C/min. The endothermic peaks shown in the heating runs refer to the melting of **4**-TJP 1:1, while the exothermic peak in the cooling run refers to cocrystal recrystallization.*

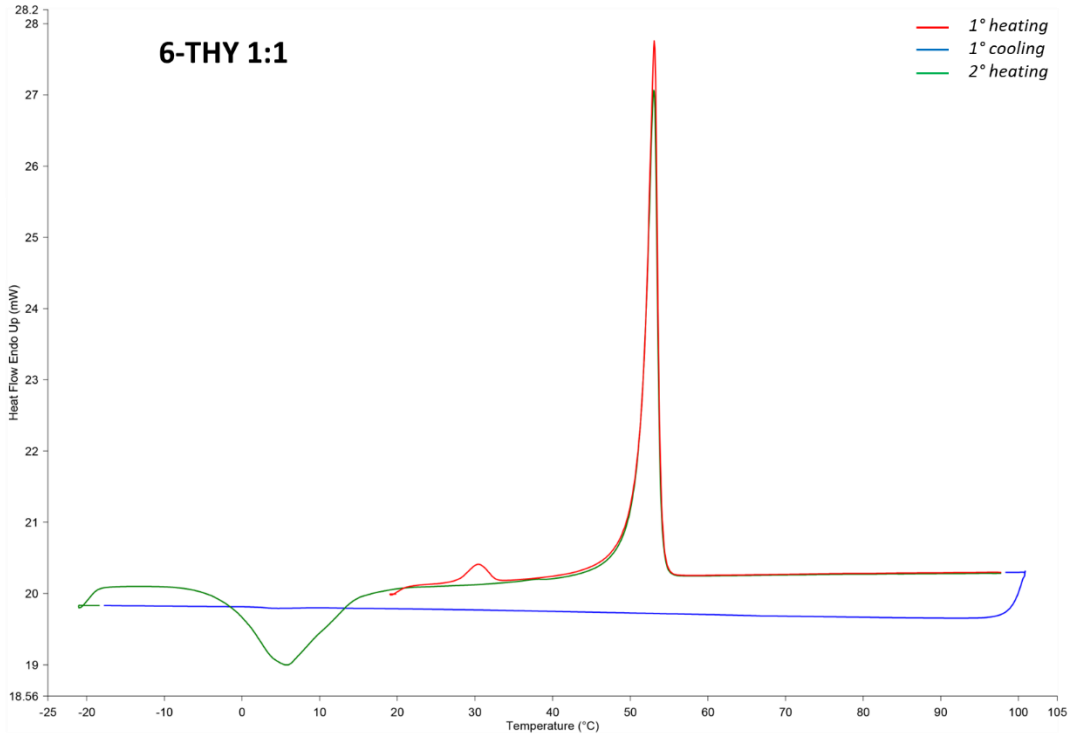

Figure B2.16 *Thermogram of **6**-THY 1:1. First heating run from 20 °C to 100 °C (red curve), cooling run from 100 °C to -20 °C (blue curve) and second heating run from -20 °C to 100 °C (green curve). The whole firing profile was performed at 5°C/min. The first endothermic peak shown in the heating run is probably due to an enantiomeric transition, followed by a second endothermic peak which refer to the melting of **6**-THY 1:1, also present in the second heating run. The exothermic peak refers instead to cocrystal recrystallization.*

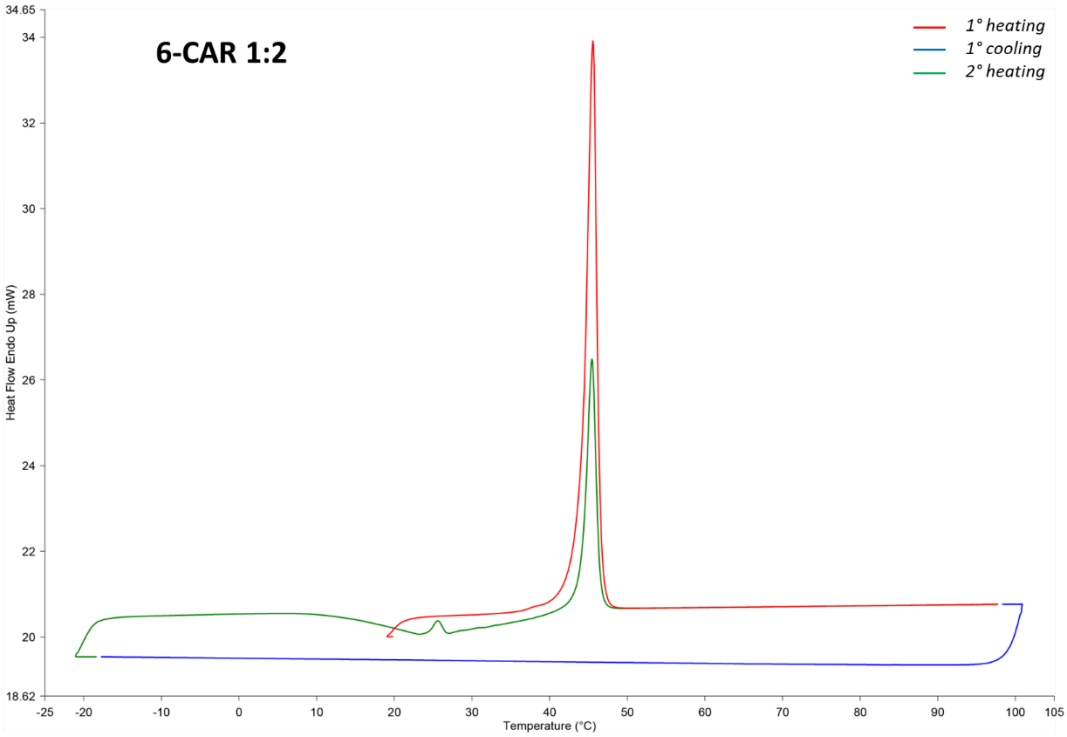

Figure B2.17 *Thermogram of **6**-CAR 1:2. First heating run from 20 °C to 100 °C (red curve), cooling run from 100 °C to -20 °C (blue curve) and second heating run from -20 °C to 100 °C (green curve). The whole firing profile was performed at 5°C/min. The endothermic peaks shown in the heating runs refer to the melting of **6**-CAR 1:1, while the exothermic peak in the cooling run refers to cocrystal recrystallization.*

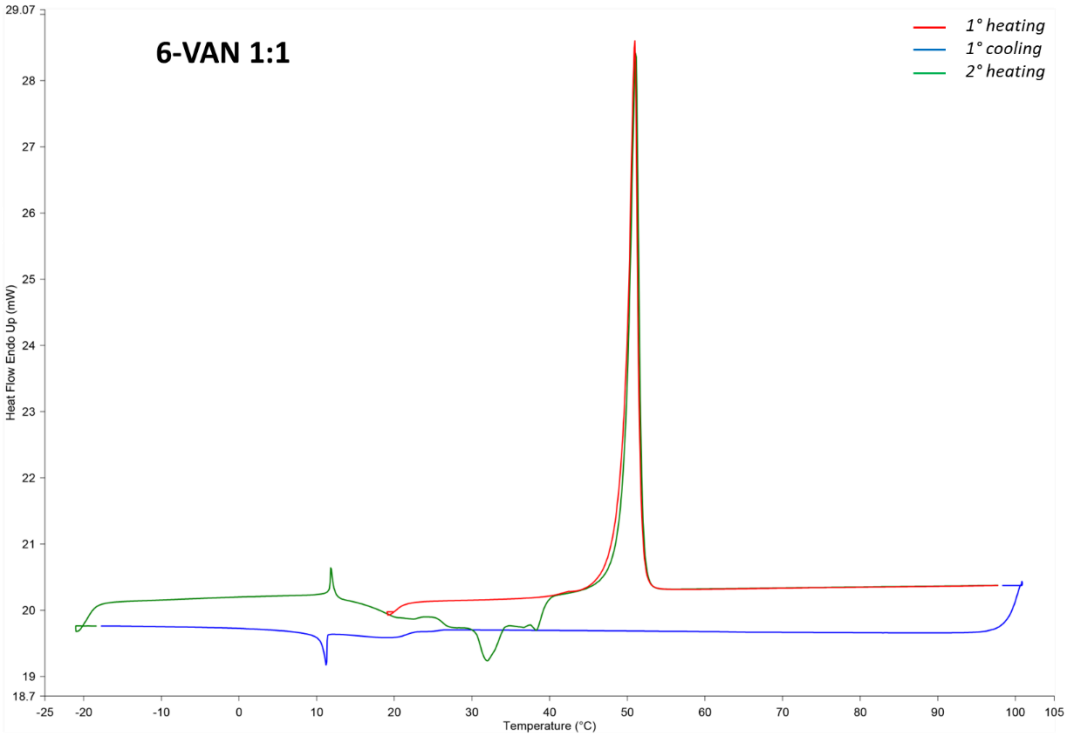

Figure B2.18 *Thermogram of **6**-VAN 1:1. First heating run from 20 °C to 100 °C (red curve), cooling run from 100 °C to -20 °C (blue curve) and second heating run from -20 °C to 100 °C (green curve). The whole firing profile was performed at 5°C/min. The endothermic peaks shown in the heating runs refer to the melting of **6**-VAN 1:1, while the exothermic peaks refer to cocrystal recrystallization.*

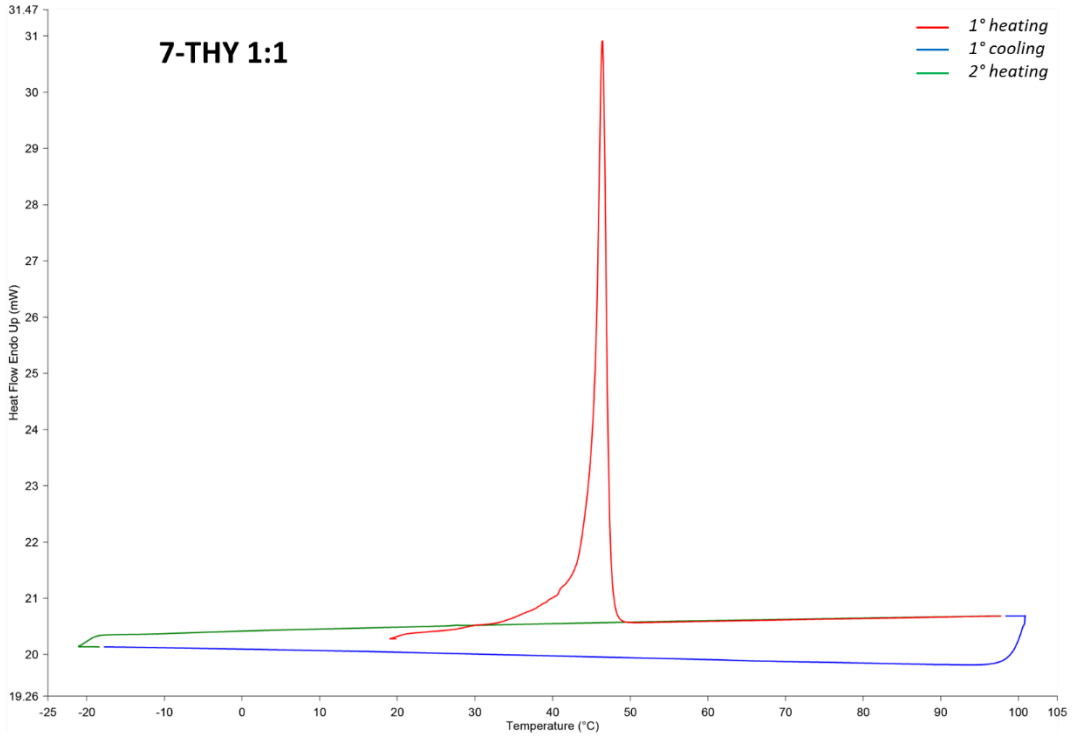

Figure B2.19 *Thermogram of **7**-THY 1:1. First heating run from 20 °C to 100 °C (red curve), cooling run from 100 °C to -20 °C (blue curve) and second heating run from -20 °C to 100 °C (green curve). The whole firing profile was performed at 5°C/min. The endothermic peak shown in the first heating run refers to the melting of **7**-THY 1:1 cocrystal.*

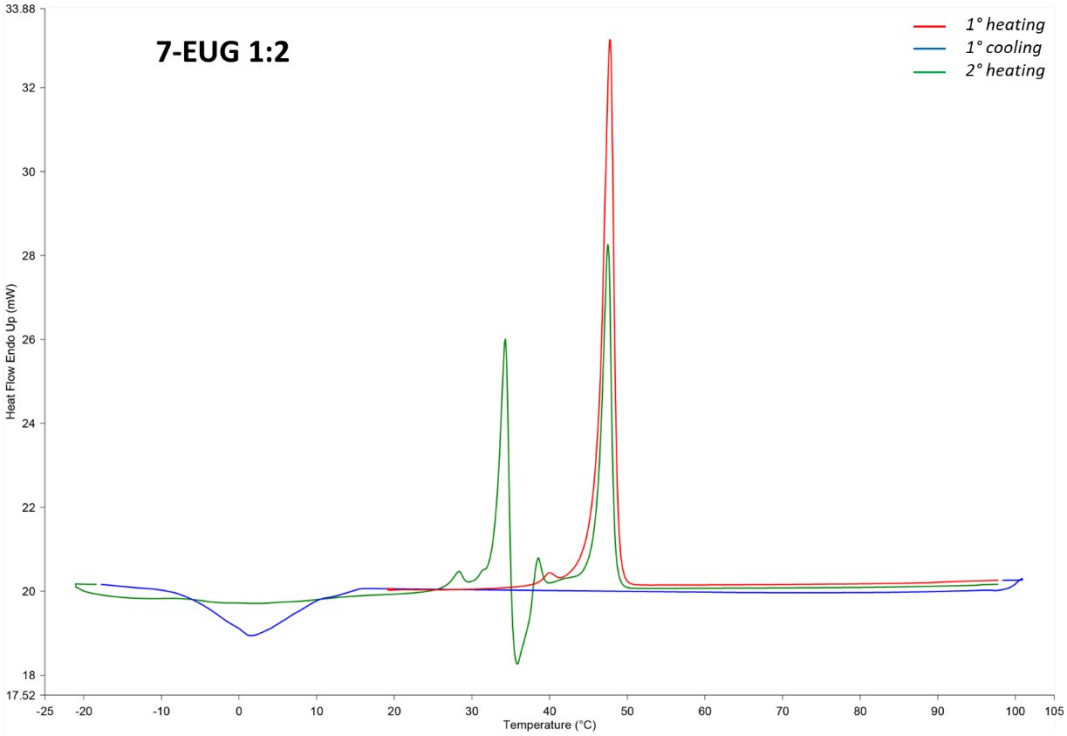

Figure B2.20 *Thermogram of **7**-EUG 1:2. First heating run from 20 °C to 100 °C (red curve), cooling run from 100 °C to -20 °C (blue curve) and second heating run from -20 °C to 100 °C (green curve). The whole firing profile was performed at 5°C/min. The endothermic peak shown in the first heating run refer to the melting of **7**-EUG 1:2, while the exothermic peak in the cooling run refers to the crystallization of a different polymorph. In the second heating run, the first endothermic peak is due to the melting of the new phase, followed by an exothermic peak due to the crystallization of **7**-EUG 1:2, which in turn melted as confirmed by the second endothermic peak. A tiny amount of **7** was probably present in the starting mixture as confirmed by the smaller endothermic peak in the first heating run.*

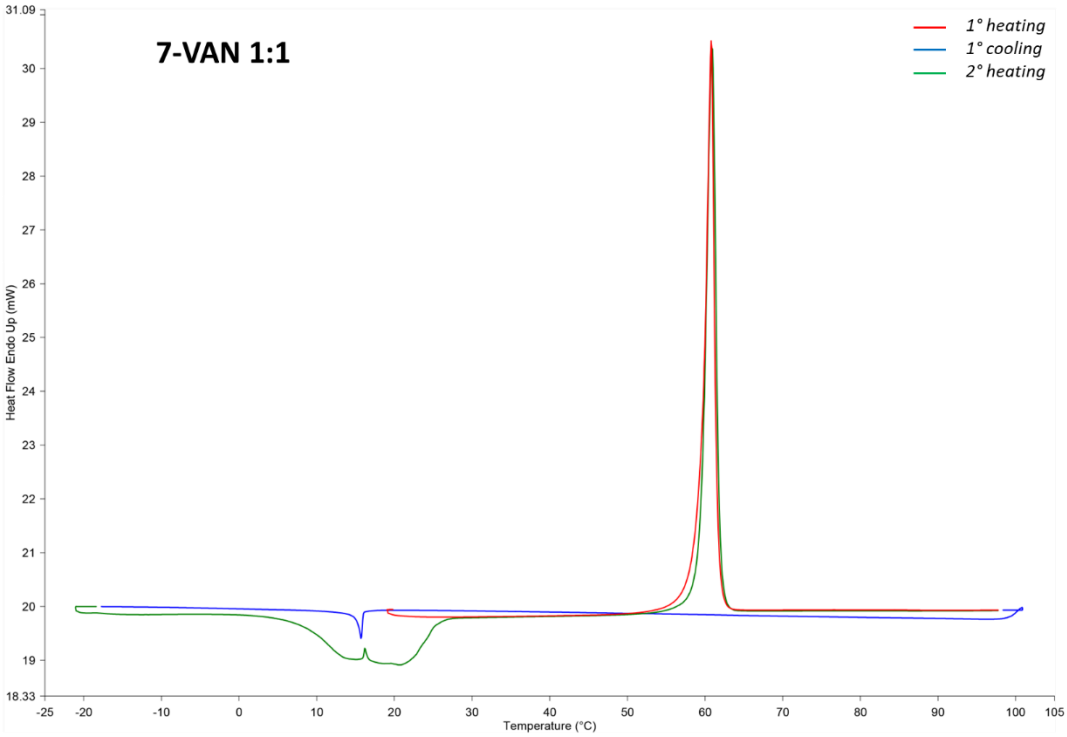

Figure B2.21 *Thermogram of **7**-VAN 1:1. First heating run from 20 °C to 100 °C (red curve), cooling run from 100 °C to -20 °C (blue curve) and second heating run from -20 °C to 100 °C (green curve). The whole firing profile was performed at 5°C/min. The endothermic peaks shown in the heating runs refer to the melting of **7**-VAN 1:1, while the exothermic peaks refer to cocrystal recrystallization.*

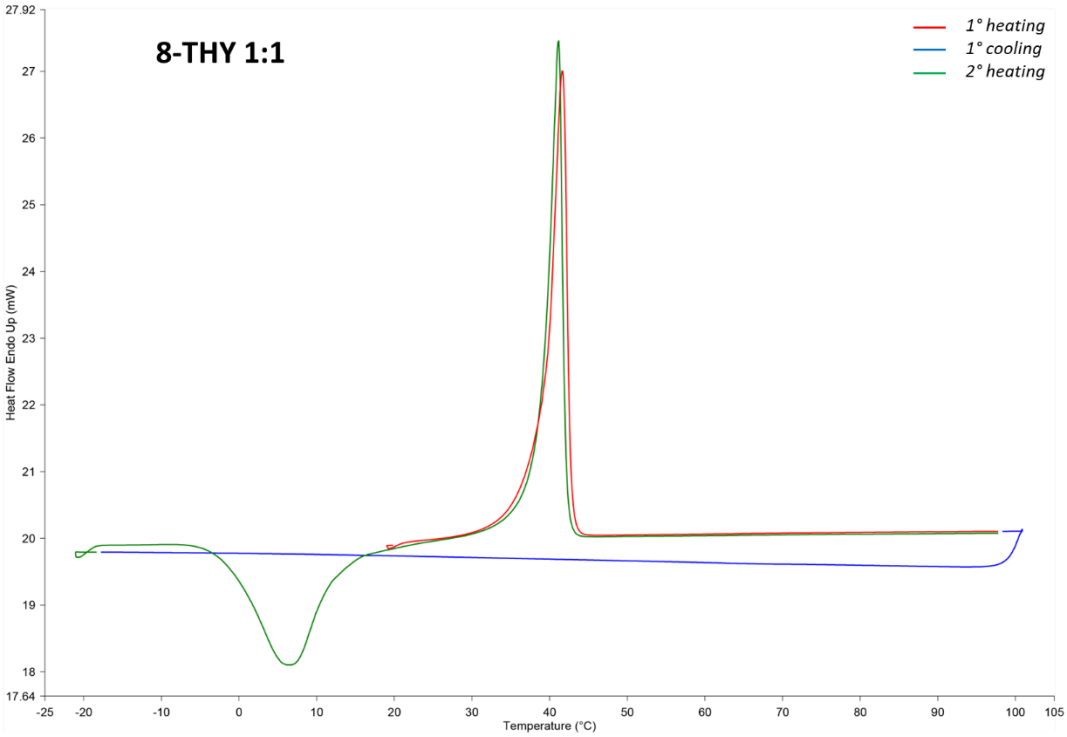

Figure B2.22 *Thermogram of **8**-THY 1:1. First heating run from 20 °C to 100 °C (red curve), cooling run from 100 °C to -20 °C (blue curve) and second heating run from -20 °C to 100 °C (green curve). The whole firing profile was performed at 5°C/min. The endothermic peaks shown in the heating runs refer to the melting of **8**-THY 1:1, while the exothermic peak refers to cocrystal recrystallization.*

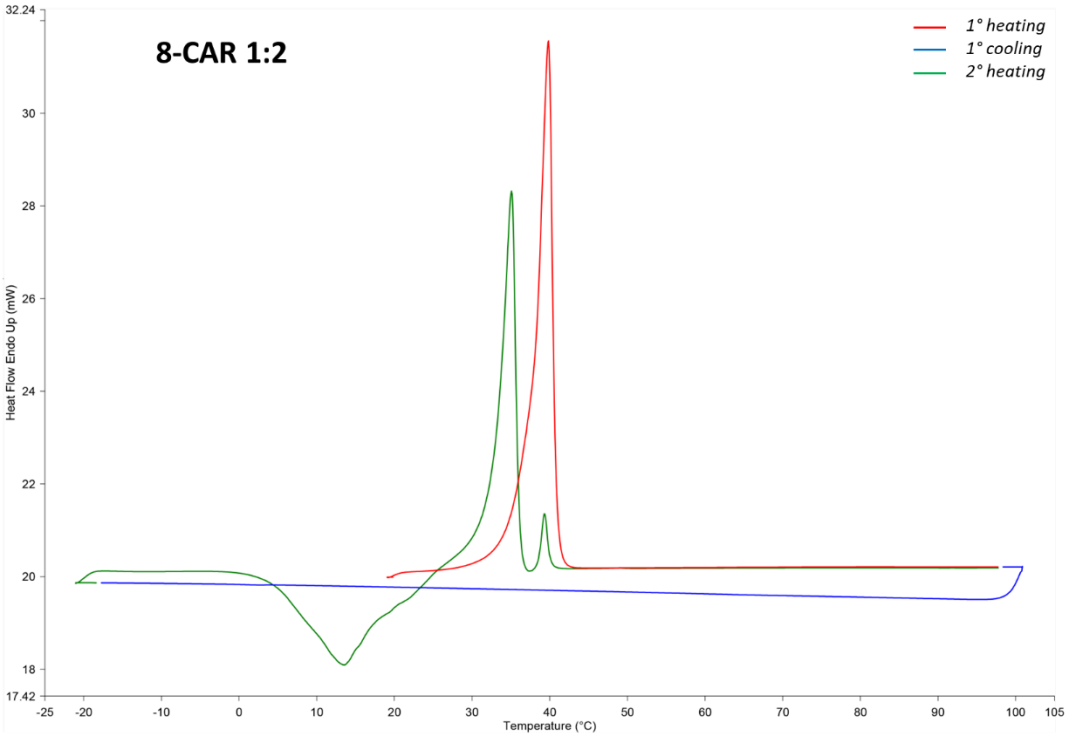

Figure B2.23 *Thermogram of **8**-CAR 1:2. First heating run from 20 °C to 100 °C (red curve), cooling run from 100 °C to -20 °C (blue curve) and second heating run from -20 °C to 100 °C (green curve). The whole firing profile was performed at 5°C/min. The endothermic peak shown in the first heating run refers to the melting of **8**-CAR 1:2. In the second heating run the melting of a different polymorph is partially overlapped to an exothermic peak due to the recrystallization of **8**-CAR 1:2 cocrystal, in turn followed by the second endothermic peak referred to the melting of **8**-CAR 1:2.*

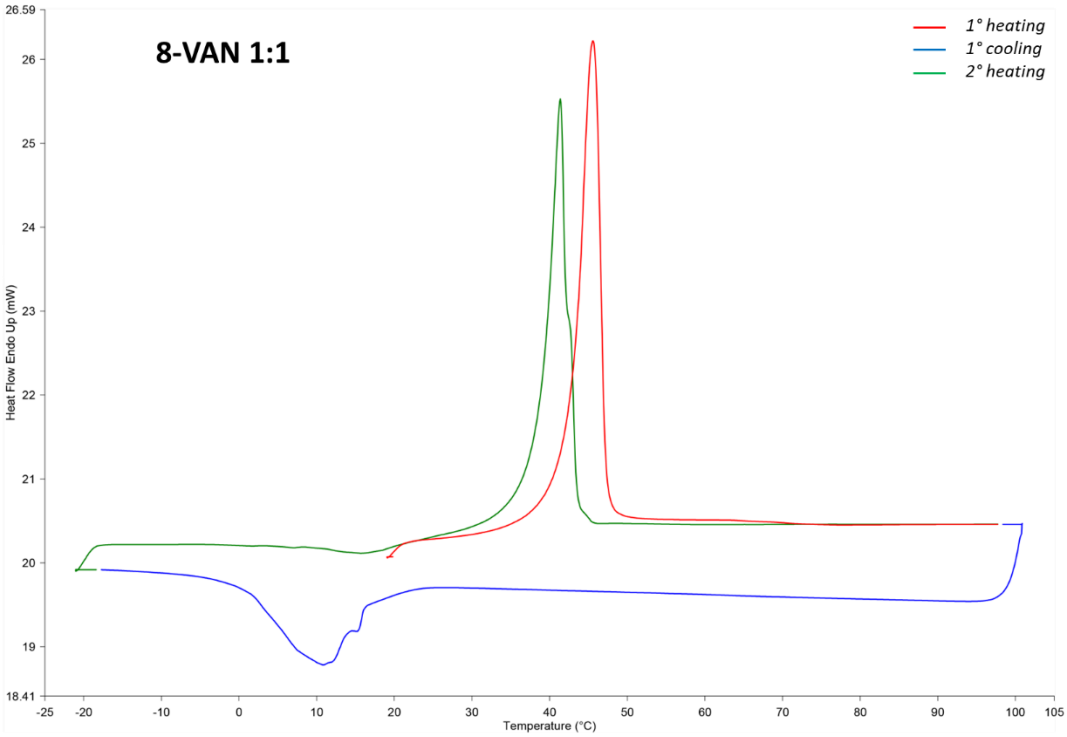

Figure B2.24 *Thermogram of **8**-VAN 1:1. First heating run from 20 °C to 100 °C (red curve), cooling run from 100 °C to -20 °C (blue curve) and second heating run from -20 °C to 100 °C (green curve). The whole firing profile was performed at 5°C/min. The endothermic peak shown in the first heating run refers to the melting of **8**-VAN 1:1, while the endothermic peak shown in the second heating run is due to the melting of another polymorph, which crystallized from the melt.*

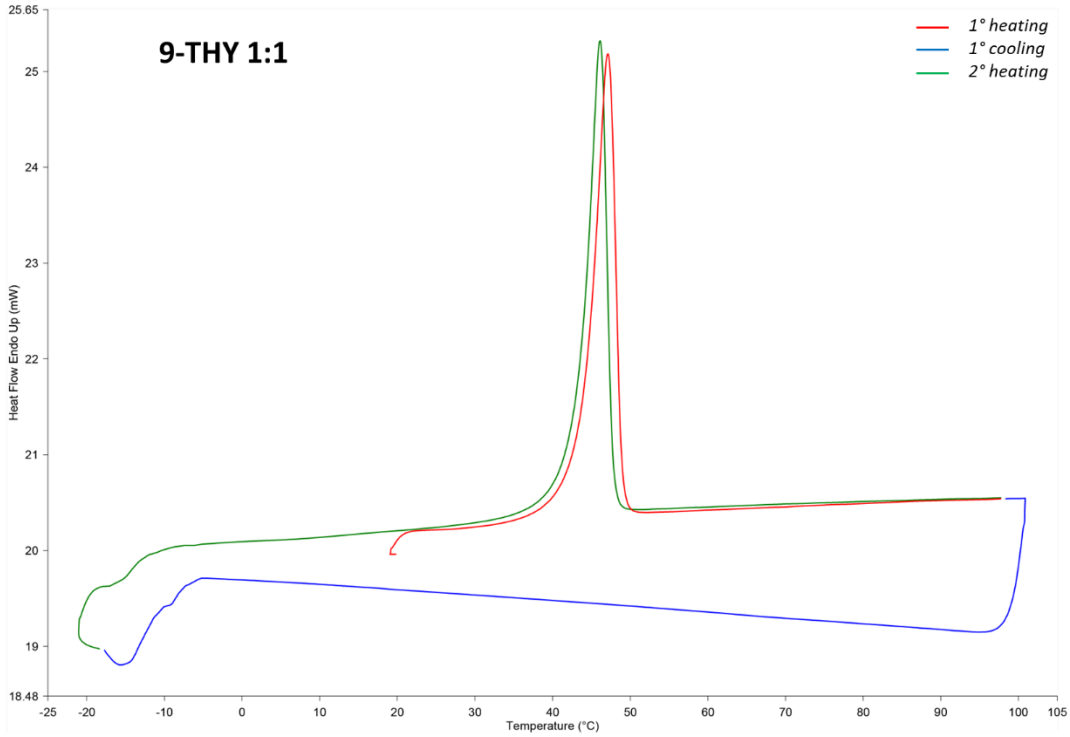

Figure B2.25 *Thermogram of **9**-THY 1:1. First heating run from 20 °C to 100 °C (red curve), cooling run from 100 °C to -20 °C (blue curve) and second heating run from -20 °C to 100 °C (green curve). The whole firing profile was performed at 5°C/min. The endothermic peak shown in the first heating run refers to the melting of **9**-THY 1:1, while the endothermic peak shown in the second heating run is due to the melting of another polymorph, which crystallized from the melt.*

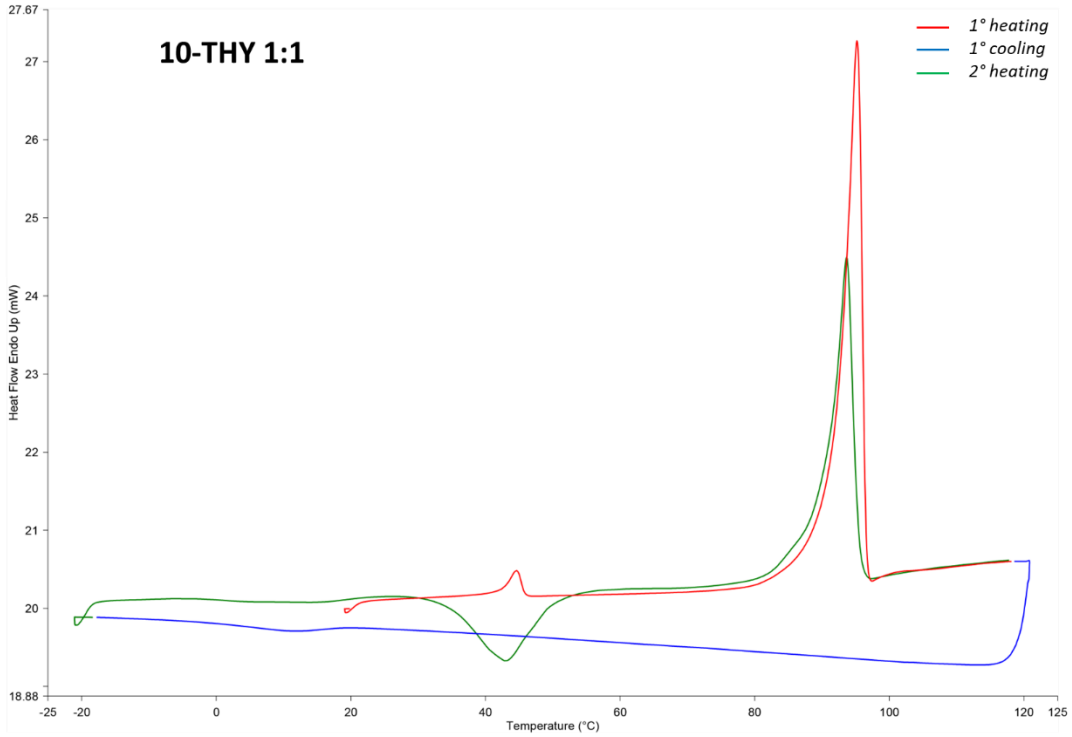

Figure B2.26 *Thermogram of* ***10****-THY 1:1. First heating run from 20 °C to 100 °C (red curve), cooling run from 100 °C to -20 °C (blue curve) and second heating run from -20 °C to 100 °C (green curve). The whole firing profile was performed at 5°C/min. The first endothermic peak shown in the heating run is probably due to an enantiomeric transition, followed by a second endothermic peak which refer to the melting of* ***10****-THY 1:1, also present in the second heating run. The exothermic peaks refer instead to cocrystal recrystallization.*

Table B2.1 *Summary of the thermal events occurred during DSC measurements for cocrystals based on AZP coformers and essential oils.*

Cocrystals	*Run*		*Thermal event*	*Temperature (°C)*	*ΔH (J/g)*
2-THY 1:1	First heating	1st peak	Endothermic	71.78	121.59
	First cooling	1st peak	Exothermic	11.74	-89.52
	Second heating	1st peak	Endothermic	71.80	120.37
2-CAR 1:1	First heating	1st peak	Endothermic	42.55	1.21
		2nd peak	Endothermic	48.68	97.31
	Second heating	1st peak	Exothermic	-2.41	-76.88
		2nd peak	Endothermic	35.22	0.69
		3rd peak	Endothermic	44.23	99.20
2-EUG 1:1	First heating	1st peak	Endothermic	36.89	111.39
	First cooling	1st peak	Exothermic	16.88	-103.36
	Second heating	1st peak	Endothermic	36.85	107.43
2-VAN 1:1	First heating	1st peak	Endothermic	49.81	1.14
		2nd peak	Endothermic	65.66	123.48
	First cooling	1st peak	Exothermic	39.87	-104.62
	Second heating	1st peak	Exothermic	33.32	-10.04
		2nd peak	Endothermic	65.73	122.60
2-TJP 1:1	First heating	1st peak	Endothermic	42.75	102.40
	First cooling	1st peak	Exothermic	25.29	-86.16
	Second heating	1st peak	Endothermic	43.47	81.98
3-THY 1:1	First heating	1st peak	Endothermic	41.94	98.07
	First cooling	1st peak	Exothermic	6.41	-69.62
	Second heating	1st peak	Exothermic	35.85	-24.78
		2nd peak	Endothermic	50.95	93.53
3-CAR 1:1	First heating	1st peak	Endothermic	34.45	37.12
	Second heating	1st peak	Exothermic	5.35	-43.98
		2nd peak	Endothermic	33.28	37.20
3-EUG 1:1	First heating	1st peak	Endothermic	35.68	82.64
	First cooling	1st peak	Exothermic	14.02	-72.02
	Second heating	1st peak	Endothermic	32.38	66.66
3-VAN 1:1	First heating	1st peak	Endothermic	67.18	115.04
	First cooling	1st peak	Exothermic	28.57	-82.96
	Second heating	1st peak	Exothermic	5.48	-3.94
		2nd peak	Exothermic	43.65	-12.97
		3rd peak	Endothermic	54.38	4.31
		4th peak	Endothermic	67.52	103.64

Table B2.1 Continued *Summary of the thermal events occurred during DSC measurements for cocrystals based on AZP coformers and essential oils.*

Cocrystals	*Run*		*Thermal event*	*Temperature (°C)*	*ΔH (J/g)*
3-TJP 1:1	First heating	1st peak	Endothermic	44.96	0.59
		2nd peak	Endothermic	54.13	118.47
	First cooling	1st peak	Exothermic	36.84	-114.80
	Second heating	1st peak	Endothermic	36.80	3.64
		2nd peak	Endothermic	54.14	118.06
4-THY 1:1	First heating	1st peak	Endothermic	41.45	88.43
	Second heating	1st peak	Exothermic	0.30	-68.85
		2nd peak	Endothermic	34.12	78.80
4-CAR 1:1	First heating	1st peak	Endothermic	44.34	88.58
	First cooling	1st peak	Exothermic	-5.43	-65.65
	Second heating	1st peak	Endothermic	44.34	83.55
4-EUG 1:1	First heating	1st peak	Endothermic	43.43	94.05
	First cooling	1st peak	Exothermic	12.64	-81.39
	Second heating	1st peak	Endothermic	34.24	78.19
4-VAN 1:1	First heating	1st peak	Endothermic	50.82	89.61
	First cooling	1st peak	Exothermic	28.29	-85.21
	Second heating	1st peak	Endothermic	50.76	75.60
		2nd peak	Exothermic	53.65	-4.05
		3rd peak	Endothermic	58.70	6.62
4-TJP 1:1	First heating	1st peak	Endothermic	52.47	99.99
	First cooling	1st peak	Exothermic	38.57	-99.84
	Second heating	1st peak	Endothermic	52.30	93.81
6-THY 1:1	First heating	1st peak	Endothermic	30.48	3.63
		2nd peak	Endothermic	53.09	83.95
	First cooling	1st peak	Exothermic	5.75	-58.93
	Second heating	1st peak	Endothermic	53.03	77.69
6-CAR 1:2	First heating	1st peak	Endothermic	45.56	85.98
	Second heating	1st peak	Exothermic	23.32	-31.32
		2nd peak	Endothermic	45.45	32.07
6-VAN 1:1	First heating	1st peak	Endothermic	50.99	80.15
	First cooling	1st peak	Exothermic	11.20	-7.86
	Second heating	1st peak	Endothermic	11.81	1.13
		2nd peak	Exothermic	32.00	-59.31
		3rd peak	Endothermic	51.07	75.74
7-THY 1:1	First heating	1st peak	Endothermic	46.45	107.68

Table B2.1 Continued *Summary of the thermal events occurred during DSC measurements for cocrystals based on AZP coformers and essential oils.*

Cocrystals	*Run*		*Thermal event*	*Temperature (°C)*	*ΔH (J/g)*
7-EUG 1:2	First heating	1st peak	Endothermic	39.98	1.16
		2nd peak	Endothermic	47.73	126.10
	First cooling	1st peak	Exothermic	1.62	-61.55
	Second heating	1st peak	Endothermic	34.29	47.88
		2nd peak	Exothermic	35.86	-15.60
		3rd peak	Endothermic	47.50	69.97
7-VAN 1:1	First heating	1st peak	Endothermic	60.79	99.93
	First cooling	1st peak	Exothermic	20.67	-65.93
	Second heating	1st peak	Exothermic	15.69	-3.09
			Endothermic	60.87	97.81
8-THY 1:1	First heating	1st peak	Endothermic	41.60	108.44
	First cooling	1st peak	Exothermic	6.69	-92.48
	Second heating	1st peak	Endothermic	98.72	98.72
8-CAR 1:2	First heating	1st peak	Endothermic	39.85	124.31
	Second heating	1st peak	Exothermic	13.44	-88.63
		2nd peak	Endothermic	35.07	86.78
		3rd peak	Endothermic	39.30	5.08
8-VAN 1:1	First heating	1st peak	Endothermic	45.62	97.75
	First cooling	1st peak	Exothermic	10.79	-54.77
	Second heating	1st peak	Exothermic	15.73	-5.37
		2nd peak	Endothermic	41.38	88.15
9-THY 1:1	First heating	1st peak	Endothermic	47.13	36.35
	First cooling	1st peak	Exothermic	46.14	/
	Second heating	1st peak	Endothermic	50.76	34.16
10-THY 1:1	First heating	1st peak	Endothermic	44.65	2.62
		2nd peak	Endothermic	95.18	86.46
	Second heating	1st peak	Exothermic	43.01	-27.64
		2nd peak	Endothermic	93.65	60.29

B.3 Crystallographic data

Table B3.1 *Crystallographic data and structure refinement of cocrystals based on AZP coformers and essential oils.*

Identification code	**2-THY**	**3-THY**	**7-THY**
Empirical formula	$C_{27}H_{35}N_3O_2$	$C_{29}H_{39}N_3O_2$	$C_{30}H_{41}N_3O_2$
Temperature (K)	200	200	200
Crystal system	Monoclinic	Triclinc	Triclinic
Space group	$P2_1/c$	P-1	P-1
a (Å)	10.392 (8)	7.8390 (6)	8.0621 (5)
b (Å)	29.55 (3)	12.3821 (7)	12.8403 (7)
c (Å)	8.616 (7)	14.1916 (10)	15.0618 (7)
α (°)	90	85.140 (2)	66.561 (3)
β (°)	107.884 (15)	82.368 (3)	82.740 (3)
γ (°)	90	82.106 (2)	75.641 (3)
Volume (Å^3)	2518 (4)	1349.24 (16)	1385.17 (14)
Z, Z', Z''	4, 1, 2	2, 1, 2	4, 2, 2
ρ_{calc} /g cm^{-3}	1.144	1.136	1.14
Independent reflections	5147 R_{int} = 0.0468, R_{sigma} = 0.0204	5561 R_{int} = 0.0987, R_{sigma} = 0.0856	5624 R_{int} = 0.0518, R_{sigma} = 0.0390
Goodness-of-fit on F^2	1.07	1.02	1.028
Final R indexes [all data]	R1 = 0.0590, wR2 = 0.1132	R1 = 0.1341, wR2 = 0.1483	R1 = 0.0689, wR2 = 0.1293

Table B3.1 Continued *Crystallographic data and structure refinement of cocrystals based on AZP coformers and essential oils.*

Identification code	**3-CAR**	**2-EUG**	**4-EUG**
Empirical formula	$C_{29}H_{39}N_3O_2$	$C_{27}H_{33}N_3O_3$	$C_{62}H_{82}N_6O_6$
Temperature (K)	200	150	200
Crystal system	Monoclinic	Monoclinic	Triclinic
Space group	$P2_1/n$	$P2_1/c$	P-1
a (Å)	5.8257 (4)	7.753 (3)	10.655 (6)
b (Å)	40.423 (3)	50.384 (19)	12.926 (7)
c (Å)	23.5267 (16)	13.110 (5)	22.607 (12)
α (°)	90	90	92.47 (3)
β (°)	94.247 (4)	104.072 (12)	100.23 (8)
γ (°)	90	90	109.68 (5)
Volume (Å^3)	5525.2 (7)	4968 (3)	2866.9 (2)
Z, Z', Z''	8, 2, 4	8, 2, 4	4, 2, 4
ρ_{calc} /g cm^{-3}	1.11	1.197	1.167
Independent reflections	10430 R_{int} = 0.1136, R_{sigma} = 0.0897	10137 R_{int} = 0.2757, R_{sigma} = 0.1857	11807 R_{int} = 0.2760, R_{sigma} = 0.2760
Goodness-of-fit on F^2	1.015	1.448	0.992
Final R indexes [all data]	R1 = 0.1624, wR2 = 0.2042	R1 = 0.2830, wR2 = 0.5444	R1 = 0.3167, wR2 = 0.2923

APPENDIX C

IN SITU MONITORING OF COCRYSTAL SYNTHESIS

C.1 DSC measurements

Table C1.1 *Summary of thermal events occurred during DSC measurements for HMT-THY binary mixtures.*

HMT-THY molar ratio	***Run***		***Thermal event***	***Temperature (°C)***	***ΔH (J/g)***
χ_{HMT} = 0.000 (THY)	First heating	1st peak	Endothermic	47.94 [a]	135.84
	First cooling	1st peak	Exothermic	-10.37 [b]	-90.44
	Second heating	1st peak	Endothermic	47.69 [a]	133.92
χ_{HMT} = 0.026	First heating	1st peak	Endothermic	26.21 [a]	10.64
		2nd peak	Endothermic	47.67 [b]	109.22
	First cooling	1st peak	Exothermic	-1.97 [b]	-93.81
	Second heating	1st peak	Endothermic	23.57 [a]	7.37
		2nd peak	Endothermic	47.97	111.85
χ_{HMT} = 0.032	First heating	1st peak	Endothermic	25.99 [a]	12.50
		2nd peak	Endothermic	47.73 [b]	105.00
	First cooling	1st peak	Exothermic	-2.42 [b]	-91.77
	Second heating	1st peak	Endothermic	22.82 [a]	9.21
		2nd peak	Endothermic	47.89 [b]	105.17
χ_{HMT} = 0.048	First heating	1st peak	Endothermic	26.43 [a]	19.97
		2nd peak	Endothermic	46.30 [b]	92.15
	First cooling	1st peak	Exothermic	-4.20 [b]	-84.08
	Second heating	2nd peak	Endothermic	23.38 [a]	15.11
			Endothermic	46.35 [b]	95.35
χ_{HMT} = 0.113	First heating	1st peak	Endothermic	27.03 [a]	48.42
		2nd peak	Endothermic	35.81 [b]	34.65
χ_{HMT} = 0.131	First heating	1st peak	Endothermic	27.27 [a]	58.56
		2nd peak	Endothermic	33.88 [b]	25.18
χ_{HMT} = 0.135	First heating	1st peak	Endothermic	27.35 [a]	87.83
	Second heating	1st peak	Exothermic	8.33 [b]	-29.58
		2nd peak	Endothermic	31.62 [b]	30.01

Table C1.1 Continued *Summary of thermal events occurred during DSC measurements for HMT-THY binary mixtures.*

HMT-THY molar ratio	***Run***		***Thermal event***	***Temperature (°C)***	***ΔH (J/g)***
χ_{HMT} = 0.159	First heating	1st peak	Endothermic	26.75 [a]	77.82
	Second heating	1st peak	Exothermic	-3.20 [b]	-64.14
		2nd peak	Endothermic	31.77 [b]	71.30
χ_{HMT} = 0.192	First heating	1st peak	Endothermic	26.99 [a]	37.91
		2nd peak	Endothermic	38.02 [b]	35.49
	First cooling	1st peak	Exothermic	1.87 [b]	-20.27
	Second heating	1st peak	Exothermic	10.83 [b]	-23.72
		2nd peak	Endothermic	35.37 [b]	77.17
χ_{HMT} = 0.225	First heating	1st peak	Endothermic	22.59 [a]	1.18
		2nd peak	Endothermic	41.70 [b]	56.31
	First cooling	1st peak	Exothermic	10.77 [b]	-41.93
	Second heating	1st peak	Endothermic	39.04 [b]	48.12
χ_{HMT} = 0.240	First heating	1st peak	Endothermic	40.79 [a]	66.61
	First cooling	1st peak	Exothermic	8.50 [b]	-44.07
	Second heating	1st peak	Endothermic	36.58 [b]	59.99
χ_{HMT} = 0.327	First heating	1st peak	Endothermic	41.55 [a]	66.01
χ_{HMT} = 0.500	First heating	1st peak	Endothermic	41.24 [a]	52.32
χ_{HMT} = 0.681	First heating	1st peak	Endothermic	40.30 [a]	32.52
χ_{HMT} = 0.832	First heating	1st peak	Endothermic	39.73 [a]	18.15
χ_{HMT} = 0.949	First heating	1st peak	Endothermic	38.12 [a]	8.47
χ_{HMT} = 1.000 (HMT)	First heating	1st peak	Endothermic	--	--

Table C1.2 *Summary of thermal events occurred during DSC measurements for AZO-THY binary mixtures.*

AZO-THY molar ratio	*Run*		*Thermal event*	*Temperature (°C)*	*ΔH (J/g)*
χ_{AZO} = 0.000 (THY)	First heating	1st peak	Endothermic	47.94	135.84
	First cooling	1st peak	Exothermic	-10.37	-90.44
	Second heating	1st peak	Endothermic	47.69	133.92
χ_{AZO} = 0.048	First heating	1st peak	Endothermic	31.51	15.63
		2nd peak	Endothermic	45.91	85.31
	First cooling	1st peak	Exothermic	-13.96	-4.62
	Second heating	1st peak	Exothermic	-15.53	-55.26
		2nd peak	Endothermic	46.14	84.09
χ_{AZO} = 0.088	First heating	1st peak	Endothermic	31.60	35.44
		2nd peak	Endothermic	41.05	65.86
	Second heating	1st peak	Exothermic	-1.78	-55.36
		2nd peak	Endothermic	41.70	54.88
χ_{AZO} = 0.103	First heating	1st peak	Endothermic	31.98	36.32
		2nd peak	Endothermic	39.32	54.32
χ_{AZO} = 0.165	First heating		Endothermic	31.31	79.84
χ_{AZO} = 0.199	First heating	1st peak	Endothermic	31.47	61.85
		2nd peak	Endothermic	40.39	11.92
χ_{AZO} = 0.247	First heating	1st peak	Endothermic	30.39	87.83
		2nd peak	Endothermic	49.48	39.79
	Second heating	1st peak	Exothermic	31.06	-10.25
		2nd peak	Endothermic	47.29	9.55
χ_{AZO} = 0.317	First heating	1st peak	Endothermic	55.62	91.14
	Second heating	1st peak	Exothermic	11.94	-68.92
		2nd peak	Endothermic	53.41	82.22
χ_{AZO} = 0.394	First heating	1st peak	Endothermic	47.49	10.53
		2nd peak	Endothermic	54.08	92.07
	Second heating	1st peak	Exothermic	19.86	-81.78
		2nd peak	Endothermic	multiple peaks	87.58
χ_{AZO} = 0.431	First heating	1st peak	Endothermic	49.42	105.00
	Second heating	1st peak	Exothermic	13.71	-80.08
		2nd peak	Endothermic	44.10	91.91
χ_{AZO} = 0.482	First heating	1st peak	Endothermic	45.49	5.69
		2nd peak	Endothermic	50.28	94.40
	Second heating	1st peak	Exothermic	22.18	-73.89
		2nd peak	Endothermic	multiple peaks	79.62
χ_{AZO} = 0.541	First heating	1st peak	Endothermic	47.52	3.28
		2nd peak	Endothermic	52.82	80.26
		3rd peak	Endothermic	61.42	19.36
	First cooling	1st peak	Exothermic	23.55	-21.64
	Second heating	1st peak	Exothermic	4.33	-56.83
		2nd peak	Endothermic	44.45	14.37
		3rd peak	Exothermic	46.66	-3.21
		4th peak	Endothermic	56.10	85.26

Table C1.2 Continued *Summary of thermal events occurred during DSC measurements for AZO-THY binary mixtures.*

AZO-THY molar ratio	*Run*		*Thermal event*	*Temperature (°C)*	*ΔH (J/g)*
χ_{AZO} = 0.584	First heating	1st peak	Endothermic	48.50	4.27
		2nd peak	Endothermic	73.77	52.63
		3rd peak	Endothermic	62.16	28.51
	First cooling	1st peak	Exothermic	33.32	-25.85
	Second heating	1st peak	Exothermic	6.40	-52.16
		2nd peak	Endothermic	45.34	16.82
		3rd peak	Exothermic	47.00	-5.71
		4th peak	Endothermic	multiple peaks	80.31
χ_{AZO} = 0.639	First heating	1st peak	Endothermic	52.42	57.94
		2nd peak	Endothermic	66.55	39.74
	First cooling	1st peak	Exothermic	45.69	-36.13
	Second heating	1st peak	Exothermic	9.63	-41.87
		2nd peak	Endothermic	46.12	29.71
		3rd peak	Exothermic	48.07	-2.18
		4th peak	Endothermic	multiple peaks	61.77
χ_{AZO} = 0.646	First heating	1st peak	Endothermic	46.16	48.65
		2nd peak	Endothermic	47.91	-2.52
		3rd peak	Exothermic	51.67	25.61
		4th peak	Endothermic	67.95	32.92
	First cooling	1st peak	Exothermic	42.88	-37.66
	Second heating	1st peak	Exothermic	8.31	-45.21
		2nd peak	Endothermic	45.24	24.52
		3rd peak	Exothermic	46.99	-2.95
		4th peak	Endothermic	multiple peaks	75.24
χ_{AZO} = 0.746	First heating	1st peak	Endothermic	43.87	0.79
		2nd peak	Endothermic	52.16	44.10
		3rd peak	Endothermic	77.44	69.50
	First cooling	1st peak	Exothermic	62.11	-58.30
	Second heating	1st peak	Exothermic	15.10	-32.04
		2nd peak	Endothermic	25.38	46.12
		3rd peak	Endothermic	multiple peaks	79.89
χ_{AZO} = 0.796	First heating	1st peak	Endothermic	43.27	5.04
		2nd peak	Endothermic	51.00	29.25
		3rd peak	Endothermic	84.49	82.35
	First cooling	1st peak	Exothermic	69.61	-70.92
	Second heating	1st peak	Exothermic	19.21	-27.20
		2nd peak	Endothermic	45.13	20.02
		3rd peak	Endothermic	multiple peaks	93.64
χ_{AZO} = 0.813	First heating	1st peak	Endothermic	44.37	6.77
		2nd peak	Endothermic	51.54	24.74
		3rd peak	Endothermic	78.76 86.94	86.36
	First cooling	1st peak	Exothermic	71.17	-73.27
	Second heating	1st peak	Exothermic	18.16	-22.99
		2nd peak	Endothermic	45.73	22.99
		3rd peak	Endothermic	multiple peaks	84.91

Table C1.2 Continued *Summary of thermal events occurred during DSC measurements for AZO-THY binary mixtures.*

AZO-THY molar ratio	***Run***		***Thermal event***	***Temperature (°C)***	***ΔH (J/g)***
χ_{AZO} = 0.903	First heating	1st peak	Endothermic	49.43	14.14
		2nd peak	Endothermic	86.35 92.74	102.42
	First cooling	1st peak	Exothermic	83.70	-94.86
	Second heating	1st peak	Endothermic	43.55	1.70
		2nd peak	Endothermic	93.72	98.13
χ_{AZO} = 0.942	First heating	1st peak	Endothermic	49.04	9.08
		2nd peak	Endothermic	90.20 95.54	114.21
	First cooling	1st peak	Exothermic	84.57	-100.37
	Second heating	1st peak	Endothermic	97.54	101.88
χ_{AZO} = 1.000 (AZO)	First heating	1st peak	Endothermic	78.62	1.51
		2nd peak	Endothermic	97.30	131.20
	First cooling	1st peak	Exothermic	87.64	-117.37
	Second heating	1st peak	Endothermic	73.45	1.21
		2nd peak	Endothermic	96.25 100.56	119.21

C.2 Crystallographic data

Table C2.1 *Crystallographic data and structure refinement of AZO-THY 1:2 cocrystal.*

Identification code	**AZO-THY**
Empirical formula	$C_{30}H_{36}N_4O_2$
Temperature (K)	189.99
Crystal system	Triclinic
Space group	P-1
a (Å)	6.625 (5)
b (Å)	9.306 (8)
c (Å)	11.539 (10)
α (°)	90.560 (19)
β (°)	91.28 (2)
γ (°)	104.027 (15)
Volume (Å^3)	690.0 (10)
Z, Z', Z''	1, 0.5, 1.5
ρ_{calc} /g cm^{-3}	1.166
Independent reflections	3866 R_{int}= 0.1126, R_{sigma}= 0.1479
Goodness-of-fit on F^2	1.038
Final R indexes [all data]	R1 = 0.2292, wR2 = 0.2346

C.3 Python scripts

Binary solid-liquid phase diagram of HMT-THY

```
import numpy as np

import matplotlib.pyplot as plt

import scipy.interpolate

from shapely.geometry import  LineString

import pandas as pd


#Standard temperature of melting determined selecting the endothermic peak of the pure phases

#Enthalphy of melting extracted plotting 1/T (experimental melting temperature of component) against ln X (molar fraction of component)

Tm_std_thy = 50.33

dH_calc_thy = 6396


#Experimental molar fraction for different stoichiometry

Xm = np.array([0.02624, 0.03241, 0.04147, 0.09416, 0.11947, 0.13510, 0.15881, 0.19179, 0.22529, 0.24034, 0.32687, 0.49887, 0.68147, 0.83267, 0.94881])


#Experimental mole fractions with pure phase molar fractions (0,1), necessary for plotting also pure phases temperatures

Xm_pure = Xm

Xm_pure = np.insert(Xm_pure, 0, 0)

Xm_pure = np.append(Xm_pure, [1])


#experimental eutectic THY-cocrystal melting temperatures

f_peak = np.array([-20, 27.72, 27.82, 28.24, 28.43, 28.92, 29.68, 29.61, 28.52, -20, -20, 42.85, 42.6, 42.12, 42.19, 40.96, -20])


#experimental solid residue melting temperature

s_peak = np.array([50.33, 47.89, 47.73, 46.3, 35.81, 33.88, -20, -20, 38.02, 41.70, 42.38, -20, -20, -20, -20, -20, -20])


#experimental eutectic HMT-THY melting temperatures
```

```
t_peak = np.array([-20, 24.87, 24.86, 25.17, -20, -20, -20, -20, -20, -20, -20, -20, -20, -20, -20, -20, -20])


#Calculated melting temperatures

Tm_calc_thy = []

Tm_calc_cocr = []

Tm_calc_hmt = []


for i in Xm:

    calc_thy = (1/(-(np.log(1-i)*8.31446/ dH_calc_thy) + ((1/( Tm_std_thy + 273.15))))) - 273.15

    Tm_calc_thy.append(calc_thy)

    calc_hmt = (-39.12759 + 339.12759*(i))

    Tm_calc_hmt.append(calc_hmt)

    calc_cocr = (-69.83774 + 938.11857*(i) -1962.5396*(i**2))

    Tm_calc_cocr.append(calc_cocr)


#New molar fraction range needed for accurate interpolation

Xm_new = np.linspace(0,1,1000)


#DataFrame

data = pd.DataFrame(data = np.column_stack((Xm_pure, f_peak, s_peak, t_peak)))

Xm_1 = pd.DataFrame(data=np.column_stack((Xm, Tm_calc_cocr, Tm_calc_hmt, Tm_calc_thy)))


#Interpolation of calculated melting temperatures discrete points

interp1 = scipy.interpolate.InterpolatedUnivariateSpline(Xm, Tm_calc_thy)

interp2 = scipy.interpolate.InterpolatedUnivariateSpline(Xm, Tm_calc_hmt)

interp3 = scipy.interpolate.InterpolatedUnivariateSpline(Xm, Tm_calc_cocr)


#Intersections of interpolated curves

line_1 = LineString(np.column_stack((Xm, interp1(Xm))))

line_2 = LineString(np.column_stack((Xm, interp2(Xm))))

line_3 = LineString(np.column_stack((Xm, interp3(Xm))))

intersection_tc = line_1.intersection(line_3)
```

```
intersection_ch = line_2.intersection(line_3)

intersection_th = line_1.intersection(line_2)

x_tc = intersection_tc[0].x

y_tc = intersection_tc[0].y

x_ch = intersection_ch[1].x

y_ch = intersection_ch[1].y

x_th = intersection_th.x

y_th = intersection_th.y


step1 = 0

step2_a = 0

step2_b = 0

step3 = 0


#x-axis, y-axis, plot features

fig = plt.figure(dpi=4000)

ax = plt.axis((0,1,15,305))

plt.xlabel("Xm")

plt.ylabel("T")

plt.scatter(x_th, y_th, c="red", s=10)

plt.scatter(0.997, 301.16, marker='*', color="None", edgecolor="black", s=20)

plt.hlines(y=y_th, xmin=0.0005, xmax=0.9995, linewidth=0.7, linestyles='--', colors='k')

plt.hlines(y=y_tc, xmin=0.0005, xmax=x_ch, linewidth=0.7, linestyles='--', colors='k')

plt.hlines(y=42.144, xmin=x_ch, xmax=0.9995, linewidth=0.7, linestyles='--', colors='k')

plt.vlines(x_ch, y_tc, y_ch, linewidth=0.7, linestyles='--', colors='k')


#plot of experimental temperatures with different markers associated to each phase

plt.scatter(data.iloc[:9, 0:1], data.iloc[:9, 1:2], marker='v', color="None", edgecolor="black", s=20)

plt.scatter(data.iloc[:6, 0:1], data.iloc[:6, 2:3], marker='^', color="black", s=20).set_clip_on(False)

plt.scatter(data.iloc[8:11, 0:1], data.iloc[8:11, 2:3], marker='s', color="black", s=20)

plt.scatter(data.iloc[1:4, 0:1], data.iloc[1:4, 3:4], color="none", edgecolor="black", s=20)

plt.scatter(data.iloc[10:, 0:1], data.iloc[10:, 1:2], marker='s', color="None", edgecolor="black", s=20)
```

```
#plot of interpolated curves in different ranges with different dotting
for j in Xm_new:
    if j <= x_tc:
        step1 = np.linspace(0,j,100)
        plt.plot(step1, interp1(step1), 'k-', linewidth=1, color='blue')
    elif j >= x_tc and j <= x_th:
        step2_a = np.linspace(x_tc,j,100)
        plt.plot(step2_a, interp1(step2_a), 'k--', linewidth=0.7, color='blue')
        plt.plot(step2_a, interp3(step2_a), 'k-', linewidth=1, color='red')
    elif j >= x_th and j <= x_ch:
        step2_b = np.linspace(x_th,j,100)
        plt.plot(step2_b, interp2(step2_b), 'k--', linewidth=0.7, color='green')
        plt.plot(step2_b, interp3(step2_b), 'k-', linewidth=1, color='red')
    elif j >= x_ch:
        step3 = np.linspace(x_ch,j,100)
        plt.plot(step3, interp2(step3), 'k--', linewidth=1, color='green')

fig.savefig("Binary phase diagram HMT-THY.pdf")
plt.close("all")
plt.close()
```

Binary solid-liquid phase diagram of AZO-THY

```
import numpy as np
import matplotlib.pyplot as plt
import matplotlib.ticker as ticker
import scipy.interpolate
from shapely.geometry import  LineString
import pandas as pd

#Standard temperature of melting determined selecting the endothermic peak of the pure phases
```

#Enthalphy of melting extracted plotting 1/T (experimental melting temperature of component) against ln X (molar fraction of component)

Tm_std_thy = 50.33

Tm_std_azo_I = 93.43

Tm_std_azo_II = 98.92

Tm_std_cocr_1_2 = 55.62

Tm_std_cocr_2_1 = 52.79

dH_calc_thy = 7446

dH_calc_azo_I = 18202

dH_calc_azo_II = 17378

dH_calc_cocr_1_2 = 8884

dH_calc_cocr_2_1 = 36729

#Experimental molar fraction for different stoichiometry

Xm = np.array([0.048136667, 0.087771608, 0.102813365, 0.164706393, 0.198715633, 0.246588325, 0.316572168, 0.394354019, 0.431481028, 0.481928687, 0.540528895, 0.584492958, 0.639485687, 0.64619165, 0.746019357, 0.796048716, 0.813310599, 0.903050886, 0.942156003])

#Experimental mole fractions with pure phase molar fractions (0,1), necessary for plotting also pure phases temperatures

Xm_pure = Xm

Xm_pure = np.insert(Xm_pure, 0, 0)

Xm_pure = np.append(Xm_pure, [1])

#experimental eutectic melting temperatures

f_peak = np.array([-20, 31.51, 31.6, 31.98, 31.31, 31.47, 30.39, -20, 47.91, 49.42, 45.66, 47.94, 48.64, 46.12, 46.16, 44.34, 43.27, 44.37, 43.55, -20, -20])

#experimental solid residue melting temperature

s_peak = np.array([50.33, 45.91, 40.97, 39.32, -20, 40.39, 48.36, 55.62, 54.08, -20, 51.41, 52.82, 52.63, 52.42, 51.67, 52.16, 51, 51.54, 49.43, -20, 49.04])

#experimetal azopyridine(I) residue melting temperature

t_peak = np.array([-20, -20, -20, -20, -20, -20, -20, -20, -20, -20, -20, 61.42, 62.16, 66.55, 67.95, 77.44, 78.71, 78.76, 86.35, 90.2, 96.25])

```
#experimetal azopyridine(I) residue melting temperature

fo_peak = np.array([-20, -20, -20, -20, -20, -20, -20, -20, -20, -20, -20, -20, -20, -20, -20, -20, 84.49, 86.94, 92.74, 95.54, 100])


#uncertainities on experimental eutectic melting temperatures

err_f = np.array([[0, 1.62, 1.01, 1.31, 1.81, 1.55, 2.66, 0, 3.83, 2.03, 1.87, 2.57, 2.35, 3.32, 1.69, 4.12, 4.02, 2.92, 1.2, 0, 0],

[0, 1.61, 0.91, 1.17, 1.85, 1.51, 1.11, 0, 3.83, 1.92, 1.87, 2.57, 2.35, 3.32, 0.62, 4.12, 1.47, 1.32, 1.2, 0, 0]])


#uncertainities on experimental solid residue melting temperature

err_s = np.array([[1.47, 2.85, 5.32, 2.01, 0, 2.22, 6.12, 1.71, 3.29, 0, 3.13, 1.3, 1.11, 1.17, 1.27, 1.56, 1.4, 1.34, 1.71, 3.21, 0],

[0.99, 1.07, 1.74, 2.01, 0, 2.22, 4.36, 0.59, 0.93, 0, 0.62, 0.72, 0.55, 0.57, 0.75, 0.92, 0.79, 0.88, 1.02, 2.02, 0]])


#uncertainities on experimental azopyridine(I) residue melting temperature

err_t = np.array([[0, 0, 0, 0, 0, 0, 0, 0, 0, 0, 0, 1.12, 5.06, 9.95, 7.69, 8.71, 11.08, 8.38, 5.37, 4.14, 1.99],

[0, 0, 0, 0, 0, 0, 0, 0, 0, 0, 0, 1.12, 5.06, 9.95, 7.69, 13.15, 11.08, 8.38, 5.37, 4.14, 1.99]])


#uncertainities on experimental azopyridine(II) residue melting temperature

err_fo = np.array([0, 0, 0, 0, 0, 0, 0, 0, 0, 0, 0, 0, 0, 0, 0, 0, 4.84, 4.07, 2.81, 2.09, 1.75])


#Calculated melting temperatures

Tm_calc_thy = []

Tm_calc_azo_I = []

Tm_calc_azo_II = []

Tm_calc_cocr_1_2 = []


for i in Xm:

    calc_thy = (1/(-(np.log(1-i)*8.31446/dH_calc_thy) + ((1/(Tm_std_thy + 273.15))))) - 273.15

    Tm_calc_thy.append(calc_thy)

    calc_azo_I = (1/(-(np.log(i)*8.31446/dH_calc_azo_I) + ((1/(Tm_std_azo_I + 273.15))))) - 273.15

    Tm_calc_azo_I.append(calc_azo_I)

    calc_azo_II = (1/(-(np.log(i)*8.31446/dH_calc_azo_II) + ((1/(Tm_std_azo_II + 273.15))))) - 273.15

    Tm_calc_azo_II.append(calc_azo_II)

    calc_cocr_1_2 = (1/(((-np.log(i*((1-i)**2)) + np.log((1/3)*((2/3)**2)))*8.31446/dH_calc_cocr_1_2) +
((1/(Tm_std_cocr_1_2 + 273.15))))) - 273.15
```

```
    Tm_calc_cocr_1_2.append(calc_cocr_1_2)


#New molar fraction range needed for accurate interpolation

Xm_new = np.linspace(0,1,100)


#DataFrame

data = pd.DataFrame(data = np.column_stack((Xm_pure, f_peak, s_peak, t_peak, fo_peak)))

Xm_1 = pd.DataFrame(data=np.column_stack((Xm, Tm_calc_thy, Tm_calc_azo_I, Tm_calc_azo_II, Tm_calc_cocr_1_2)))


#Interpolation of calculated melting temperatures discrete points

interp1 = scipy.interpolate.InterpolatedUnivariateSpline(Xm, Tm_calc_thy)

interp2 = scipy.interpolate.InterpolatedUnivariateSpline(Xm, Tm_calc_azo_I)

interp3 = scipy.interpolate.InterpolatedUnivariateSpline(Xm, Tm_calc_azo_II)

interp4 = scipy.interpolate.InterpolatedUnivariateSpline(Xm, Tm_calc_cocr_1_2)


#Intersections of interpolated curves

line_1 = LineString(np.column_stack((Xm, interp1(Xm))))

line_2 = LineString(np.column_stack((Xm, interp2(Xm))))

line_3 = LineString(np.column_stack((Xm, interp3(Xm))))

line_4 = LineString(np.column_stack((Xm, interp4(Xm))))

intersection_tc1 = line_1.intersection(line_4)

intersection_c1a = line_4.intersection(line_2)

intersection_ta = line_1.intersection(line_2)

intersection_c1a2 = line_3.intersection(line_4)

x_tc1 = intersection_tc1[0].x

y_tc1 = intersection_tc1[0].y

x_c1a = intersection_c1a[1].x

y_c1a = intersection_c1a[1].y

x_c1a2 = intersection_c1a2[1].x

y_c1a2 = intersection_c1a2[1].y

x_ta = intersection_ta.x

y_ta = intersection_ta.y
```

```
x_c2a = 0.4631000711606675

y_c2a = 51.524


step1 = 0

step2_a = 0

step2_b = 0

step3 = 0

step4 = 0


#x-axis, y-axis, plot features

fig = plt.figure(dpi=4000)

ax = plt.axis((0,1,15,100))

plt.xlabel("Xm")

plt.ylabel("T")

plt.scatter(x_ta, y_ta, c="red", s=10)

plt.hlines(y=31.37666667, xmin=0.005, xmax=0.316572168, linewidth=1, linestyles='--', colors='k')

plt.hlines(y=48.80325465, xmin=0.316572168, xmax=0.995, linewidth=1, linestyles='--', colors='k')

plt.hlines(y=51.524, xmin=0.4631000711606675, xmax=0.995, linewidth=1, linestyles='--', colors='magenta')

plt.vlines(0.316572168, 31.37666667, 55.62, linewidth=1, linestyles='--', colors='k')

plt.hlines(y=y_ta, xmin=0.005, xmax=0.995, linewidth=1, linestyles='--', colors='k')


#plot of experimental temperatures with different markers associated to each phase

plt.scatter(data.iloc[:8, 0:1], data.iloc[:8, 1:2], marker='v', color="None", edgecolor="black", s=20)

plt.errorbar(data.iloc[:8, 0:1].values, data.iloc[:8, 1:2].values, yerr=err_f[:, :8], linestyle="None", ecolor="black",
elinewidth=0.5, capsize=1.5)

plt.scatter(data.iloc[:5, 0:1], data.iloc[:5, 2:3], marker='^', color="black", s=20).set_clip_on(False)

plt.errorbar(data.iloc[:5, 0:1].values, data.iloc[:5, 2:3].values, yerr=err_s[:, :5], linestyle="None", ecolor="black",
elinewidth=0.5, capsize=1.5)

plt.scatter(data.iloc[5:10, 0:1], data.iloc[5:10, 2:3], marker='s', color="black", s=20)

plt.errorbar(data.iloc[5:10, 0:1].values, data.iloc[5:10, 2:3].values, yerr=err_s[:, 5:10], linestyle="None", ecolor="black",
elinewidth=0.5, capsize=1.5)

plt.scatter(data.iloc[8:, 0:1], data.iloc[8:, 1:2], color="none", edgecolor="black", s=20)

plt.errorbar(data.iloc[8:, 0:1].values, data.iloc[8:, 1:2].values, yerr=err_f[:, 8:], linestyle="None", ecolor="black",
elinewidth=0.5, capsize=1.5)
```

```
plt.scatter(data.iloc[10:, 0:1], data.iloc[10:, 2:3], marker='D', color="black", s=20).set_clip_on(False)

plt.errorbar(data.iloc[10:, 0:1].values, data.iloc[10:, 2:3].values, yerr=err_s[:, 10:], linestyle="None", ecolor="black",
elinewidth=0.5, capsize=1.5)

plt.scatter(data.iloc[10:, 0:1], data.iloc[10:, 3:4], color="black", s=20).set_clip_on(False)

plt.errorbar(data.iloc[10:, 0:1].values, data.iloc[10:, 3:4].values, yerr=err_t[:, 10:], linestyle="None", ecolor="black",
elinewidth=0.5, capsize=1.5)

plt.scatter(data.iloc[10:, 0:1], data.iloc[10:, 4:5], marker='*', color="black", s=30).set_clip_on(False)

plt.errorbar(data.iloc[10:, 0:1].values, data.iloc[10:, 4:5].values, yerr=err_fo[10:], linestyle="None", ecolor="black",
elinewidth=0.5, capsize=1.5)


#plot of interpolated curves in different ranges with different dotting

for j in Xm_new:

    if j <= x_tc1:

        step1 = np.linspace(0,j,100)

        plt.plot(step1, interp1(step1), 'k-', linewidth=1, color='blue')

    elif j >= x_tc1 and j <= x_ta:

        step2_a = np.linspace(x_tc1,j,100)

        plt.plot(step2_a, interp1(step2_a), 'k--', linewidth=0.7, color='blue')

        plt.plot(step2_a, interp4(step2_a), 'k-', linewidth=1, color='red')

    elif j >= x_ta and j <= x_c1a:

        step2_b = np.linspace(x_ta,j,100)

        plt.plot(step2_b, interp2(step2_b), 'k--', linewidth=0.7, color='orange')

        plt.plot(step2_b, interp4(step2_b), 'k-', linewidth=1, color='red')

    elif j >= x_c1a:

        step3 = np.linspace(x_c1a,j,100)

        step4 = np.linspace(x_c1a2,j,100)

        plt.plot(step3, interp2(step3), 'k-', linewidth=1, color='orange')

        plt.plot(step4, interp3(step4), 'k-', linewidth=1, color='orange')


fig.savefig("Binary phase diagram AZO-THY.pdf")

plt.close("all")

plt.close()
```

APPENDIX D

PAIR DISTRIBUTION FUNCTION ANALYSIS ON ORGANIC COMPOUNDS

D.1 DSC measurements

Table D1.1 *Summary of thermal events occurred during DSC measurements for PYR-THY binary mixtures.*

PYR-THY molar ratio	***Run***		***Thermal event***	***Temperature (°C)***	***ΔH (J/g)***
χ_{PYR} = 0.000 (THY)	First heating	1st peak	Endothermic	47.94	135.84
	First cooling	1st peak	Exothermic	-10.37	-90.44
	Second heating	1st peak	Endothermic	47.69	133.92
χ_{PYR} = 0.049	First heating	1st peak	Endothermic	35.85	32.43
		2nd peak	Endothermic	45.44	99.49
	First cooling	1st peak	Exothermic	-8.21	-95.76
	Second heating	1st peak	Endothermic	35.27	30.35
		2nd peak	Endothermic	45.79	97.01
χ_{PYR} = 0.075	First heating	1st peak	Endothermic	35.28	38.73
		2nd peak	Endothermic	42.67	78.44
	First cooling	1st peak	Exothermic	not defined	/
	Second heating	1st peak	Exothermic	not defined	/
		2nd peak	Endothermic	34.77	35.42
		3rd peak	Endothermic	43.15	72.33
χ_{PYR} = 0.100	First heating	1st peak	Endothermic	35.56	19.97
		2nd peak	Endothermic	41.76	92.15
	First cooling	1st peak	Exothermic	-4.20 [b]	-84.08
	Second heating	2nd peak	Endothermic	23.38	15.11
			Endothermic	46.35	95.35
χ_{PYR} = 0.128	First heating	1st peak	Endothermic	36.03	113.38
		2nd peak	Endothermic	38.21	
	Second heating	1st peak	Exothermic	-10.12	-77.10
		2nd peak	Endothermic	35.76 38.92	110.23

Table D1.1 Continued *Summary of thermal events occurred during DSC measurements for PYR-THY binary mixtures.*

PYR-THY molar ratio	Run		Thermal event	Temperature (°C)	ΔH (J/g)
χ_{PYR} = 0.148	First heating	1st peak	Endothermic	36.59	113.34
	First cooling	1st peak	Exothermic	not defined	/
	Second heating	1st peak	Exothermic	not defined	/
		2nd peak	Endothermic	36.66	111.45
χ_{PYR} = 0.200	First heating	1st peak	Endothermic	36.37	112.39
	First cooling	1st peak	Exothermic	not defined	/
	Second heating	1st peak	Exothermic	not defined	/
		2nd peak	Exothermic	36.21	100.55
χ_{PYR} = 0.298	First heating	1st peak	Endothermic	35.64	18.82
	First cooling	1st peak	Exothermic	23.28	-95.66
		2nd peak	Exothermic	-6.64	-11.53
	Second heating	1st peak	Endothermic	35.10	19.94
		2nd peak	Endothermic	48.80	100.19
χ_{PYR} = 0.334	First heating	1st peak	Endothermic	34.24	2.43
		2nd peak	Endothermic	50.21	113.43
	First cooling	1st peak	Exothermic	21.44	-104.88
	Second heating	1st peak	Endothermic	33.90	1.53
		2nd peak	Endothermic	50.24	113.02
χ_{PYR} = 0.400	First heating	1st peak	Endothermic	49.41	119.08
	First cooling	1st peak	Exothermic	20.92	-108.91
	Second heating	1st peak	Endothermic	49.56	115.61
χ_{PYR} = 0.500	First heating	1st peak	Endothermic	44.94	115.40
	First cooling	1st peak	Exothermic	15.75	-113.08
	Second heating	1st peak	Endothermic	25.47	1.83
		2nd peak	Endothermic	multiple peaks	117.45
χ_{PYR} = 0.600	First heating	1st peak	Endothermic	44.94	115.40
	Second heating	1st peak	Exothermic	-18.38	-106.58
		2nd peak	Endothermic	16.20	93.08
χ_{PYR} = 0.700	First heating	1st peak	Endothermic	16.37	110.41
	First cooling	1st peak	Exothermic	1.55	-39.25
	Second heating	1st peak	Endothermic	14.88	36.54
χ_{PYR} = 0.800	First heating	1st peak	Endothermic	15.98 multiple peaks	213.18
	First cooling	1st peak	Exothermic	18.61	-16.61
				-7.36	-10.63
	Second heating	1st peak	Endothermic	15.86	10.51
χ_{PYR} = 0.900	First heating	1st peak	Endothermic	9.84	26.22
				37.02	79.74
	First cooling	1st peak	Exothermic	21.01	-73.98
	Second heating	1st peak	Endothermic	28.69	63.50

Table D1.1 Continued *Summary of thermal events occurred during DSC measurements for PYR-THY binary mixtures.*

PYR-THY molar ratio	***Run***		***Thermal event***	***Temperature (°C)***	***ΔH (J/g)***
χ_{PYR} = *1.000 (PYR)*	First heating	1st peak	Endothermic	27.37	10.70
		2nd peak	Endothermic	52.14	151.20
	First cooling	1st peak	Exothermic	42.62	-151.28
		2nd peak	Exothermic	20.04	-8.04
	Second heating	1st peak	Endothermic	28.38	10.57
		2nd peak	Endothermic	52.01	151.41

D.2 Python script

Binary solid-liquid phase diagram of PYR-THY

```
import numpy as np

import matplotlib.pyplot as plt

import scipy.interpolate

from shapely.geometry import  LineString

import pandas as pd


#Standard temperature of melting determined selecting the endothermic peak of the pure phases

#Enthalphy of melting extracted plotting 1/T (experimental melting temperature of component) against ln X (molar fraction of component)

Tm_std_thy = 50.33

Tm_std_pyr = 52.00

Tm_std_cocr = 50.21

dH_calc_thy = 9607

dH_calc_pyr = 5909

dH_calc_cocr = 19686


#Experimental molar fraction for different stoichiometry

Xm = np.array([0.04899, 0.07484, 0.09995, 0.12782, 0.14813, 0.20036, 0.29755, 0.33381, 0.40042, 0.50049, 0.59941, 0.70098, 0.80000, 0.89980])


#Experimental mole fractions with pure phase molar fractions (0,1), necessary for plotting also pure phases temperatures

Xm_pure = Xm

Xm_pure = np.insert(Xm_pure, 0, 0)

Xm_pure = np.append(Xm_pure, [1])


#experimental eutectic melting temperatures

f_peak = np.array([-40, 35.85, 35.25, 35.5, 36.03, 36.59, 36.15, 35.7, 34.3, -40, -40, 17.3, 16.37, 15.8, 9.99, -40])
```

```
#experimental solid residue melting temperature

s_peak = np.array([50.33, 45.5, 42.67, 41.7, 38.2, -40, 40.27, 48.65, 50.21, 49.41, 44.9, 34.38, -40, -40, 37.02, 52])


#Calculated melting temperatures

Tm_calc_thy = []

Tm_calc_cocr = []

Tm_calc_pyr = []


for i in Xm:

    calc_thy = (1/(-(np.log(1-i)*8.31446/dH_calc_thy) + ((1/(Tm_std_thy + 273.15))))) - 273.15

    Tm_calc_thy.append(calc_thy)

    calc_pyr = (1/(-(np.log(i)*8.31446/dH_calc_pyr) + ((1/(Tm_std_pyr + 273.15))))) - 273.15

    Tm_calc_pyr.append(calc_pyr)

    calc_cocr = (1/(((-np.log(i*((1-i)**2)) + np.log((1/3)*((2/3)**2)))*8.31446/dH_calc_cocr) + ((1/(Tm_std_cocr + 273.15))))) -
273.15

    Tm_calc_cocr.append(calc_cocr)


#New molar fraction range needed for accurate interpolation

Xm_new = np.linspace(0,1,1000)


#DataFrame

data = pd.DataFrame(data = np.column_stack((Xm_pure, f_peak, s_peak)))

Xm_1 = pd.DataFrame(data=np.column_stack((Xm, Tm_calc_cocr, Tm_calc_pyr, Tm_calc_thy)))


#Interpolation of calculated melting temperatures discrete points

interp1 = scipy.interpolate.InterpolatedUnivariateSpline(Xm, Tm_calc_thy)

interp2 = scipy.interpolate.InterpolatedUnivariateSpline(Xm, Tm_calc_pyr)

interp3 = scipy.interpolate.InterpolatedUnivariateSpline(Xm, Tm_calc_cocr)


#Intersections of interpolated curves

line_1 = LineString(np.column_stack((Xm, interp1(Xm))))

line_2 = LineString(np.column_stack((Xm, interp2(Xm))))

line_3 = LineString(np.column_stack((Xm, interp3(Xm))))
```

```
intersection_tc = line_1.intersection(line_3)

intersection_cp = line_2.intersection(line_3)

intersection_tp = line_1.intersection(line_2)

x_tc = intersection_tc.x

y_tc = intersection_tc.y

x_cp = intersection_cp.x

y_cp = intersection_cp.y

x_tp = intersection_tp.x

y_tp = intersection_tp.y


step1 = 0

step2_a = 0

step2_b = 0

step3 = 0


#x-axis, y-axis, plot features

fig = plt.figure(dpi=4000)

ax = plt.axis((0,1,-20,55))

plt.xlabel("Xm")

plt.ylabel("T")

plt.scatter(x_tp, y_tp, c="red", s=10)

plt.hlines(y=y_tp, xmin=0.0005, xmax=0.9995, linewidth=0.7, linestyles='--', colors='k')

plt.hlines(y=y_tc, xmin=0.0005, xmax=0.33381, linewidth=0.7, linestyles='--', colors='k')

plt.hlines(y=y_cp, xmin=x_cp, xmax=0.9995, linewidth=0.7, linestyles='--', colors='k')

plt.vlines(0.33381, y_tc, 50.21 , linewidth=0.7, linestyles='--', colors='k')


#plot of experimental temperatures with different markers associated to each phase

plt.scatter(data.iloc[:8, 0:1], data.iloc[:8, 1:2], marker='v', color="None", edgecolor="black", s=20)

plt.scatter(data.iloc[:5, 0:1], data.iloc[:5, 2:3], marker='^', color="black", s=20).set_clip_on(False)

plt.scatter(data.iloc[5:12, 0:1], data.iloc[5:12, 2:3], marker='s', color="black", s=20)

plt.scatter(data.iloc[14:, 0:1], data.iloc[14:, 2:3], color="black", edgecolor="black", s=20)

plt.scatter(data.iloc[11:, 0:1], data.iloc[11:, 1:2], color="None", edgecolor="black", s=20)
```

```
#plot of interpolated curves in different ranges with different dotting
for j in Xm_new:
    if j <= x_tc:
        step1 = np.linspace(0,j,100)
        plt.plot(step1, interp1(step1), 'k-', linewidth=1, color='blue')
    elif j >= x_tc and j <= x_tp:
        step2_a = np.linspace(x_tc,j,100)
        plt.plot(step2_a, interp1(step2_a), 'k--', linewidth=0.7, color='blue')
        plt.plot(step2_a, interp3(step2_a), 'k-', linewidth=1, color='red')
    elif j >= x_tp and j <= x_cp:
        step2_b = np.linspace(x_tp,j,100)
        plt.plot(step2_b, interp2(step2_b), 'k--', linewidth=0.7, color='green')
        plt.plot(step2_b, interp3(step2_b), 'k-', linewidth=1, color='red')
    elif j >= x_cp:
        step3 = np.linspace(x_cp,j,100)
        plt.plot(step3, interp2(step3), 'k-', linewidth=1, color='green')

fig.savefig("Binary phase diagram PYR-THY.pdf")
plt.close("all")
plt.close()
```